Corrosion inhibition of mild steel in corrosive mediums using bio-extracts and epoxy coating

Thesis submitted in partial fulfillment of the requirements for the degree of

DOCTOR OF PHILOSOPHY

by

Anil Kumar

(Roll No.: 196107102)

Department of Chemical Engineering

Indian Institute of Technology Guwahati,

Guwahati–781039, Assam, India

November 2025

Corrosion inhibition of mild steel in corrosive mediums using bio-extracts and epoxy coating

Anil Kumar

Dedicated

to

My parents

And

My mentor

DEPARTMENT OF CHEMICAL ENGINEERING

INDIAN INSTITUTE OF TECHNOLOGY GUWAHATI

STATEMENT

I do hereby declare that the content embodied in this thesis entitled "**CORROSION INHIBITION OF MILD STEEL IN CORROSIVE MEDIUMS USING BIO-EXTRACTS AND EPOXY COATING"** is the result of investigations carried out by me at Department of Chemical Engineering, Indian Institute of Technology Guwahati, Guwahati, India, under the guidance of Prof. Chandan Das. In keeping with the general practice of reporting scientific observations, due acknowledgments have been made wherever the work described is based on the findings of other investigators.

Date: Anil Kumar

DEPARTMENT OF CHEMICAL ENGINEERING

INDIAN INSTITUTE OF TECHNOLOGY GUWAHATI

CERTIFICATE

This is to certify that the thesis entitled **"CORROSION INHIBITION OF MILD STEEL IN CORROSIVE MEDIUMS USING BIO-EXTRACTS AND EPOXY COATING"** submitted by **Mr. Anil Kumar (Roll No.: 196107102)**, a research scholar in the Department of Chemical Engineering, Indian Institute of Technology Guwahati, for the award of the degree of Doctor of Philosophy, is a record of the original research work carried out by him under my supervision and guidance. The thesis has fulfilled all requirements as per the regulations of the institute and in my opinion has reached the standard needed for submission. The work documented in this thesis has not been submitted to any other University or Institute for the award of any degree.

Prof. Chandan Das

Professor

Department of Chemical Engineering

Indian Institute of Technology Guwahati

Guwahati - 781039, Assam, India

Date:

Acknowledgments

It is my great privilege to sincerely thank the people who have supported me throughout my doctoral dissertation.

First and foremost, I would like to express my deepest gratitude to my supervisor, **Prof. Chandan Das**, for his continuous guidance, support, and motivation during my Ph.D. research. I am deeply thankful to him for giving me the golden opportunity to work in his laboratory and take care of all the facilities to carry out my research. His guidance helped me throughout the research and writing of this thesis. His suggestions, encouragement, and support were crucial to the completion of my Ph.D. thesis. Without his precious support, it would not be possible to complete this research. I am grateful for his advice, great ideas, and scientific discussions, which are part of this thesis.

I would like to acknowledge my sincere gratitude to my honorable doctoral committee members, **Dr. Prasanna Venkatesh Rajaraman** and **Prof. Animes Kumar Golder**, Department of Chemical Engineering, and **Prof. Bulu Pradhan**, Department of Civil Engineering. Their intuitive revision of my work, valuable advice, and constructive suggestions during my research progress kept the flow of my research work in the right direction. I express my gratitude to **Prof. Subrata Kumar Majumder**, Head of the Department of Chemical Engineering, for his benevolent support. Furthermore, I would like to thank all other faculty members and staff members of the Department of Chemical Engineering for their invaluable support during my research.

I would like to acknowledge the Aries Engineer, Maharashtra, India, for metal fabrication, Subodh Technologists Metallurgical & Corrosion Testing Laboratory, Maharashtra, India for their assistance in salt spray test, and also acknowledge **Dr. Partho Sarathi Gooh Pattader** (Department of Chemical Engineering) for providing goniometer to

perform contact angle measurements. I sincerely acknowledge Central Workshop (Department of Mechanical Engineering), Analytical Lab (Department of Chemical Engineering), and Central Instruments Facility, IIT Guwahati, for providing me the facility of high-end and sophisticated instruments that were necessary for this work.

I earnestly thank my seniors, juniors, interns, and labmates: Dr. Sujoy Bose, Dr. Amit Baran Das, Dr. Arijit Das, Dr. Kibrom Alebel Gebru, Dr. Abhishek Shukla, Dr. Sushma Chakraborty, Dr. Kulbhushan Samal, Dr. Aritra Das, Dr. Abhradip Pal, Dr. Anirban Chowdhury, Dr. Shashank Shrivastava, Dr. Gunolla Nagendra Prasad, Mr. Ajay Kumar Shakya, Mr. Bharat Bhushan Negi, Mrs. Aswani K Viswanath, Mr. Raj kumar, Mr. Pramod chowdhury, Mrs. Antaripa Saha, Mr. Mondam Sasi Kumar, Mr. Keneniah Elfred Jyrwa, Mrs. Zakia Farhat, and Mrs. Brohmani Bhatacharya for providing a collaborative research environment. I sincerely appreciate the help, guidance, and love received from all of them. I am highly thankful to my friends Mr. Chandra Bhan, Mr. Ravi Vashisht, Dr. Nikhil Rahul Dhongde, Dr. Sayani Adhikari, Dr. Nipu Kumar Das, Mr. Mrinal Kanti Dolai, and Mr. Biswajit Bhattacharjya, for their support and care.

Finally, and most importantly, I would like to remember my parents and family for their never-ending love, support, and patience. It is their numerous personal sacrifices that have enabled me to reach this juncture in life. Simple thanks is not enough to convey my deep respect and gratitude towards my family.

I thank the Almighty for His blessings He has bestowed upon me and for giving me the strength and wisdom to achieve this academic goal.

Anil Kumar

Abstract

Recently, corrosion has become a major concern at local and industrial scales, which hampers their conventional production unit. Corrosion is the destruction or deterioration of material because of electrochemical and chemical reactions with its environment. It causes significant financial losses as well as harmful effects on the environment. Mild steel (MS) is frequently used as a construction material in several industries (marine, oil and gas industry, petrochemicals, chemical refineries, automobile industries, reinforced concrete structures, and automobiles) due to its following properties: strong mechanical durability, easy processing, and low cost. However, unfortunately, MS has a greater propensity to corrode in the acidic medium due to its lower corrosion resistance. Hence, it is very necessary to use suitable approaches to protect the MS in corrosive environments. In this present work, green corrosion inhibitors (objectives 1, 2, 3, and 4) and epoxy coating (EP) reinforced with RGO-ZnO-PANI nanocomposite (objective 5) were used to protect the MS in 1 M HCl and 3.5% NaCl, respectively. Therefore, the entire work of this thesis has been divided into five major parts.

In the first part of the present study, chayote extracts were used to protect MS in 1 M HCl solution. Herein, a novel and eco-friendly corrosion inhibitor using *Sechium edule* (chayote) fruit extract is developed. The chemistry of chayote extract was investigated by Fourier transform infrared (FTIR) and Ultraviolet-Visible (UV-Vis) spectroscopies. The anti-corrosive effectiveness of prepared chayote extracts was evaluated using weight loss and electrochemical techniques. Results of potentiodynamic polarization indicated that the chayote extracts were highly effective, with protection efficiencies of 85.72% and 76.82% at the concentration of 2000 mg L^{-1} of prepared chayote fruit extract in water at pH 3 (CEPH3) and at the original pH 5.2 (CE), respectively. The shift in corrosion potential (E_{corr}) was less than 85 mV with respect to the corrosion potential of the blank, revealing that both chayote extracts

behaved as a mixed type of inhibitor. Langmuir adsorption isotherm showed the best fit for the adsorption studies. The free energies (ΔG°_{ads}) obtained from tests were found to be -53.046 kJ mol^{-1} (CE) and -50.278 kJ mol^{-1} (CEPH3), demonstrating prepared chayote extracts adsorbed onto the metal surface by the chemical adsorption process. Thermodynamic parameters (activation energy, enthalpy, and entropy) were obtained from 303 K to 323 K, indicating that corrosion is spontaneous and endothermic. Outcomes of FESEM, AFM, EDX, and XRD analysis showed that a protective layer was formed on the surface of mild steel (MS) in the presence of chayote extracts.

In the second part of the present study, a novel ecofriendly inhibitor was prepared from *Praecitrullus fistulosus* (tinda fruit and peel) for mild steel (MS) corrosion in 1 M HCl. The presence of phenol, 3,5-bis (1,1-dimethyl ethyl)-, 9-octadecenoic acid, methyl ester, hexadecanoic acid 15-methyl-, methyl ester, 9, 12-octadecadienoic acid, methyl ester, 9, 12, 15-octadecatrienoic acid, methyl ester, (Z,Z,Z-), ascorbic acid, and phytol were identified as major constituent through LC-MS analysis of tinda extracts. The existence of these compounds was further confirmed through FTIR analysis, which shows the presence of various functional groups, such as -OH, C=O, C-O-C, C=C, and aromatic rings in the tinda extracts. Electrochemical and gravimetric analyses were used to investigate the inhibitory effect of tinda extracts. Outcomes of Tafel analysis revealed that both tinda extracts significantly reduced the corrosion current as compared to blank and achieved 83.73% and 87.59 % inhibition efficiencies at 200 mg L^{-1} of tinda peel extract (TPE) and tinda fruit extract (TFE), respectively. The change in corrosion potential (E_{corr}) was within an ± 85 mV range compared to that of the uninhibited system, indicating that both tinda extracts demonstrated a mixed-type inhibition behavior. During adsorption studies, the best fit was obtained for the Langmuir adsorption model. The obtained values of standard Gibbs free energy (ΔG^{o}_{ads}) for TPE and TFE lie between -20 and -40 kJ mol^{-1} but close to -20 kJ mol^{-1}, which reveals the preferential physical

adsorption of the extracts on the metal surface. Thermodynamic parameters, including activation energy, enthalpy, and entropy, were computed across the temperature range of 303 to 323 K, suggesting that corrosion occurs spontaneously by the endothermic process. FESEM analysis depicted that inhibited systems exhibited smooth and crack-free surfaces as compared to blank systems. AFM images demonstrated that surface roughness was significantly reduced for the inhibited system. In EDX analysis, the weight percentage of Cl was reduced in the presence of tinda extracts as compared to blank, and in XRD analysis, the iron chloride ($FeCl_2$) peak did not appear in the presence of inhibitor, but it was in the uninhibited system. All surface-related findings signify that tinda extracts are adsorbed on the MS surface and form a protective layer that separates the metal from the corrosive solution.

In the third part of the present study, a novel environment-friendly corrosion inhibitor was developed from *Phaseolus lunatus* peel and seeds, and their chemistry was studied by liquid chromatography-mass spectrometry (LC-MS) and fourier transform infrared spectroscopy (FTIR) analyses. The inhibitory effect of *Phaseolus lunatus* peel extracts (PLPE) and *Phaseolus lunatus* seed extract (PLSE) on mild steel (MS) degradation in 1 M HCl was explored by electrochemical and weight loss methods. Findings show that the anticorrosive behavior of PLPE and PLSE was enhanced with rising their doses and declined with temperature elevation. The maximum inhibition efficiencies during Tafel analysis, 85.69 % and 90.78 %, were obtained at 200 mg L^{-1} of PLPE and PLSE, separately. In the inhibited system, E_{corr} (corrosion potential) exhibited a positive shift (< ± 85 mV) as compared to the blank system, which means the inhibitor works as a mix-type of inhibitor. PLPE and PLSE followed the Langmuir adsorption isotherm. The values of ΔG^{o}_{ads} were computed, which indicated the preferential physisorption of *Phaseolus lunatus* extracts on MS. Several kinetic and thermodynamic parameters (E_a, ΔH, and ΔS) were evaluated for elevating the temperature from 303 to 323 K, signifying the spontaneous degradation of MS through the endothermic

process. Moreover, field emission scanning electron microscopy (FESEM) revealed smooth, crack-free surfaces in the presence of inhibitors compared to the blank, and atomic force microscopy (AFM) showed reduced surface roughness in the inhibited system. Energy-dispersive X-ray spectroscopy (EDX) revealed a lower Cl wt% in the presence of *Phaseolus lunatus* extracts, while X-ray diffraction (XRD) showed the absence of $FeCl_2$ peaks in the inhibited system. These findings indicate that extract molecules adsorb on the MS surface, forming a protective layer that inhibits corrosion.

In the fourth part of the present study, *Duranta erecta* plant organs were used to develop *Duranta erecta* fruit extract (DEFE) and *Duranta erecta* leaves extract (DELE). These extracts were characterized by LC-MS and FTIR analyses and employed to mitigate the MS deuteriation in 1 M HCl. The inhibitive effect was scrutinized by weight loss and electrochemical methods. Outcomes revealed that *Duranta erecta* extracts are good inhibitors for MS corrosion in HCl. The corrosion inhibitory effect of both DEFE and DELE was increased with their dosage up to 200 mg L^{-1} but decreased with temperature. The highest corrosion inhibitory efficacies of about 90.8 % and 91.8 % were recorded at 200 mg L^{-1} of DEFE and DELE, respectively. Adsorption of *Duranta erecta* extracts over the MS surface was accomplished through Langmuir adsorption. The values of ΔG^{o}_{ads} were -29.00 kJ mol^{-1} and -29.90 kJ mol^{-1} for inhibited MS corrosion with DEFE and DELE, respectively, confirming that they favored physical adsorption (mix-type adsorption) over the MS surface. Some thermodynamic parameters (E_a, ΔH, and ΔS) were determined from PDP data of the following temperature range: 303 to 323 K, which implies the spontaneous degradation of MS through an endothermic process. Acid attack on the metal surface was studied using FESEM, EDX, and AFM analysis, which qualitatively confirmed the findings of the corrosion test.

In the fifth part of the present study, a novel corrosion-resistant RGO-ZnO-PANI nanocomposite was successfully synthesized by decorating ZnO nanorods onto reduced

graphene oxide (RGO) via ultrasonication, followed by polyaniline (PANI) wrapping and incorporated into the epoxy matrix through the solution blending method. Coating morphology, chemical structure, thermal stability, and wettability were analyzed through Field emission scanning electron microscopy (FESEM), Fourier transform infrared spectroscopy (FTIR), Thermogravimetric analysis (TGA), and contact measurements. Among all coatings (EP, EP/RGO, EP/RGO-ZnO, and EP/RGO-ZnO-PANI), the EP/RGO-ZnO-PANI coating exhibited the smoothest surface, highest thermal stability, and enhanced hydrophobicity. The anticorrosive behavior of mild steel (MS) coated with epoxy-based nanocomposite coatings was evaluated using potentiodynamic polarization (PDP), electrochemical impedance spectroscopy (EIS), and salt spray tests. PDP results displayed that the EP/RGO-ZnO-PANI coating provided the highest corrosion protection efficiency (99.98 %) in a 3.5 wt% NaCl solution. EIS and salt spray tests (ASTM B117) analysis confirmed superior long-term corrosion resistance of the ternary composite coating over 45 days immersion in 3.5% NaCl and 1000 h exposure to 5 wt% NaCl, respectively, compared to other coatings. These findings suggested that the synthesized ternary composite is a potential candidate for corrosion protection applications.

Keywords*:* Mild steel; Corrosion; Corrosion inhibitor; Tinda fruit**;** *Phaseolus lunatus; Duranta erecta*: Electrochemical impedance spectroscopy; Potentiodynamic polarization; Tafel curve; Adsorption studies; Inhibition efficiency; Corrosion mechanism; Tafel analysis; Anti-corrosive coating; Epoxy coating; Salt spray test

Nomenclature

Abbreviation

Symbol	Abbreviation
AFM	Atomic force microscopy
CE	Chayote extract
CPE	Constant phase element
EP	Epoxy
DEFE	*Duranta erecta* fruit extract
DELE	*Duranta erecta* leaves extract
EDX	Energy Dispersive X-ray
EIS	Electrochemical impedance spectroscopy
FESEM	Field Emission Scanning Electron Microscopy
LC-MS	Liquid chromatography-mass spectroscopy
MS	Mild steel
OCP	Open circuit potential
PDP	Potentiodynamic polarization test
PLPE	*Phaseolus lunatus* peel extract
PLSE	*Phaseolus lunatus* seed extract
TFE	Tinda fruit extract
TPE	Tinda peel extract
XRD	X-ray diffraction

Notations

Symbol	Nomenclature
A	Effective area (cm^2)
A	Exponential factor
b_a	Anodic slope (V $decade^{-1}$)
b_c	Cathodic slope (V $decade^{-1}$)
C_{dl}	Capacitance of the effective layer (µF cm^{-2})
C_R	Corrosion rate having a unit of (mmpy)

C_{water}	Concentration of water (g L^{-1})
E	Applied potential (V)
E_{corr}	Corrosion potential (V)
i	Measured current density (µA cm^{-2})
i_{corr}	Corrosion current density (µA cm^{-2})
i^{o}_{corr}	Corrosion current density in the absence of inhibitor (µA cm^{-2})
i^{o}_{corr}	Corrosion current density in the presence of inhibitor (µA cm^{-2})
K_{ads}	Adsorption equilibrium constant (L g^{-1})
n	Phase shift
R	Universal gas constant (8.314 J mol^{-1} K^{-1})
R^2	Linear regression coefficient
R_S	Solution resistance (Ω cm^2)
R_{ct}	Charge-transfer resistance (Ω cm^2)
R^{i}_{ct}	Charge transfer resistance in the presence of inhibitor (Ω cm^2)
R^{0}_{ct}	Charge transfer resistance in the absence of inhibitor (Ω cm^2)
t	Exposure time (h)
W	Weight loss (g)
w_o	Weight loss of the MS sample in the absence of inhibitor (g)
w_i	Weight loss of the MS sample in the presence of inhibitor (g)
Y_0	Amplitude comparable to capacitance or modulus of CPE (µMho cm^{-2})
Z_{CPE}	Impedance of the CPE (Ω cm^2)
ΔG°_{ads}	Standard Gibbs free energy (kJ mol^{-1})
θ	Surface coverage
$\mu_{CR}\%$	Corrosion inhibition efficiency
$\mu_{R_{ct}}\%$	Inhibition efficiency calculated from R^{i}_{ct} and R^{0}_{ct}
$\mu_P\%$	Inhibition efficiency calculated from i^{i}_{corr} and i^{0}_{corr}
ρ	Density of the MS (g cm^{-3})
ω	Angular frequency (rad sec^{-1})

Table of Contents

List of Tables

List of Figures

Chapter 1:

Introduction and literature review

Introduction and literature review

This chapter presents a quick overview of conventional, non-eco-friendly corrosion inhibitors and anti-corrosive coatings. It also highlights the growing need for green alternatives and novel anticorrosive coating with enhanced anti-corrosive properties. Additionally, the global impact of corrosion is discussed, emphasizing its adverse effects on humans and the environment. This chapter also reviews recent advancements and experimental approaches that have been used to mitigate corrosion. Some recent efforts to use natural extracts as corrosion inhibitors and epoxy-based coatings are also discussed.

1.1 Corrosion

Corrosion is the destruction or deterioration of metal because of electrochemical and chemical reactions with its environment. It is an undesirable natural process that converts the metals into unwanted substances during exposure to the corrosive environment. It leads to various social consequences, such as plant shutdowns due to equipment failures, reduced operational efficiency, safety hazards, environmental impact, economic losses, decreased public trust, and increased maintenance requirements, etc. in several industries (aerospace, automotive, and petroleum industries) (K O et al., 2019; Verma et al., 2024). According to the report of NACE 2013, corrosion poses a significant global economic challenge, with annual losses estimated at around US$ 2.5 trillion, which was approximately 3.4% of the global Gross Domestic Product (GDP) (Koch et al., 2016; News, 2019). India incurs an annual economic loss of about 4-5% of its GDP due to corrosion.

1.1.1 Classification of corrosion

Corrosion is classified into two categories based on the environmental condition of metallic structures: Wet and dry corrosion. Wet corrosion occurs when metal comes into contact with a liquid, typically an aqueous solution or an electrolyte. It is the most widespread and destructive form of corrosion, responsible for the majority of corrosion-related damage. Wet corrosion is commonly seen everywhere around us. For example, corrosion of steel is caused by water. Dry corrosion occurs when metal interacts with surrounding air in the absence of moisture. It is primarily driven by atmospheric gases such as oxygen, hydrogen, hydrogen sulfide, and nitrogen, as well as halogens and certain inorganic vapors. Generally, dry corrosion is less harmful than wet corrosion, but it can be severe at higher temperatures. The presence of even a small amount of moisture can change the corrosion picture completely. For example, dry chlorine is practically non-corrosive to ordinary steel, but moist chlorine dissolved in water

is highly corrosive and attacks most common metals and alloys (Fontana et al., 1979; Landolt, 2007).

In addition, according to electrochemical theory, metal corrosion in aqueous environments is induced by simultaneous oxidation and reduction reactions that occur on metal surfaces. For an immersed metal in a corrosive electrolyte, metal deterioration caused by corrosion leads to the formation of distinct potential zones, disrupting the crystalline lattice structure (Landolt, 2007). This potential difference leads to the formation of anodic and cathodic sites on the metal surface. Oxidation occurs at the anode, where metal atoms lose electrons, which then travel through an electronic conductor to the cathodic site, where they are consumed during the reduction reaction (Roberge, 2000). These electrochemical processes drive corrosion, leading to material deterioration. The fundamental chemical reactions occurring at the anodic and cathodic regions are given below (Hart, 2023). At anode: In aqueous solution, metal undergoes oxidation to form respective ions.

$$M \rightarrow M^{+n} + ne^{-} \quad (1.1)$$

At Cathode: Multiple reduction processes occur that mainly depend on the nature of the corrosive electrolyte.

(a) In de-aerated acidic corrosive solutions, H_2 gas is formed as follows:

$$2H^{+} + 2e^{-} \rightarrow H_2 \quad (1.2)$$

(b) In aerated acidic corrosive solutions, oxygen is reduced as follows:

$$4H^{+} + O_2 + 4e^{-} \rightarrow 2H_2O \quad (1.3)$$

(c) In de-aerated neutral or alkaline corrosive electrolytes, OH^- ions are formed

$$2H_2O + 2e^{-} \rightarrow 2OH^{-} + H_2 \quad (1.4)$$

(d) In aerated neutral or alkaline corrosive electrolytes, OH^- ions are formed with the liberation of H_2 gas.

$$2H_2O + O_2 + 4e^- \rightarrow 4OH^- \quad (1.5)$$

During the metal immersion in the corrosive solution, metal ions and OH^- are formed at the anode and cathode, respectively. These ions diffuse toward and form an insoluble metal oxide. Over the steel surface, this process constructs a ferric oxide layer, which is well known as rust (Edition, 2004).

1.2 Types of corrosion

1.2.1 Uniform corrosion

The uniform attack is the most common form of corrosion. It is usually characterized by a chemical or electrochemical reaction that proceeds uniformly over the exposed surface or extensive area. The metal becomes thinner and eventually fails (Fig. 1.1 (a)).

1.2.2 Galvanic corrosion

A potential difference usually exists between two dissimilar metals when immersed in a corrosive or conductive solution. If these metals are placed in contact or otherwise electrically connected, this potential difference produces electron flow between them. Corrosion of the less corrosion-resistant metal is usually increased, and the attack on more resistant material is decreased compared with the behavior of these metals when they are not in contact. In this case, less resistant metal becomes anodic, and more resistant metal becomes cathodic. Usually, the cathode or cathodic metal corrodes very little or not in this type of couple. Because of the electric currents and dissimilar metals involved, this form of corrosion is called galvanic or two-metal corrosion (Fig. 1.1 (b)).

1.2.3 Crevice corrosion

Intensive localized corrosion frequently occurs within crevices and other shielded areas on metal surfaces exposed to corrosive solutions. This type of attack is usually associated with small volumes of stagnant solution caused by holes, gasket surfaces, lap joints, surface deposits, and crevices under bolt and rivet heads. As a result, this form of corrosion is called crevice corrosion or, sometimes, deposit or gasket corrosion (Fig. 1.1 (c))

1.2.4 Pitting corrosion

Pitting is a form of extremely localized attack that results in holes in the metal. These holes may be small or large in diameter, but they are relatively small in most cases. Pits are sometimes isolated or so close together that they look like a rough surface. Generally, a pit may be described as a cavity or hole with a surface diameter about the same as or less than the depth. It causes equipment to fail because of perforation, with only a small weight loss percentage for the entire structure (Fig. 1.1 (d)).

1.2.5 Intergranular corrosion

A uniform attack typically occurs when a metal corrodes because grain boundaries are slightly more reactive than the grains themselves. In this case, corrosion occurred severely along the grain boundaries while the grains remained almost unaffected. It is known as intergranular corrosion. This type of corrosion can be triggered by the presence of impurities or excess of alloy elements or by the depletion of elements at the grain boundaries (Fig. 1.1 (e)).

1.2.6 Exfoliation corrosion

Exfoliation corrosion is a form of selective corrosion that progresses along multiple planes parallel to the direction of rolling or extrusion. The schematic of this corrosion is shown in (Fig. 1.1 (f))

1.2.7 Erosion corrosion

Erosion corrosion is the acceleration or increase in the rate of deterioration or attack on a metal because of relative movement between a corrosive fluid and the metal surface. Generally, this movement is quite rapid, and mechanical wear effects or abrasion are involved. Metal is removed from the surface either as dissolved ions or as solid corrosion products that are mechanically swept away by the flowing medium (Fig. 1.1 (g)).

1.2.8 Stress corrosion

Stress corrosion cracking (SCC) refers to the formation of cracks in a material due to the combined influence of tensile stress and exposure to a corrosive environment. Many investigators have classified all cracking failures occurring in a corrosive medium as stress corrosion cracking, including failures due to hydrogen embrittlement (Fig. 1.1 (h)).

1.2.9 Microbial induced corrosion

Microbial activity can create acidic environments through changes in pH and oxygen levels. Sulfate-reducing bacteria, such as Desulfovibrio, produce hydrogen sulfide (H_2S), which can dissolve in water and lead to the formation of sulfuric acid. Microbial corrosion is not induced by an easy chemical interaction between metal and water but rather by bacteria and fungi altering the environment (Fig. 1.1 (a)) (Mahmoud et al., 2021).

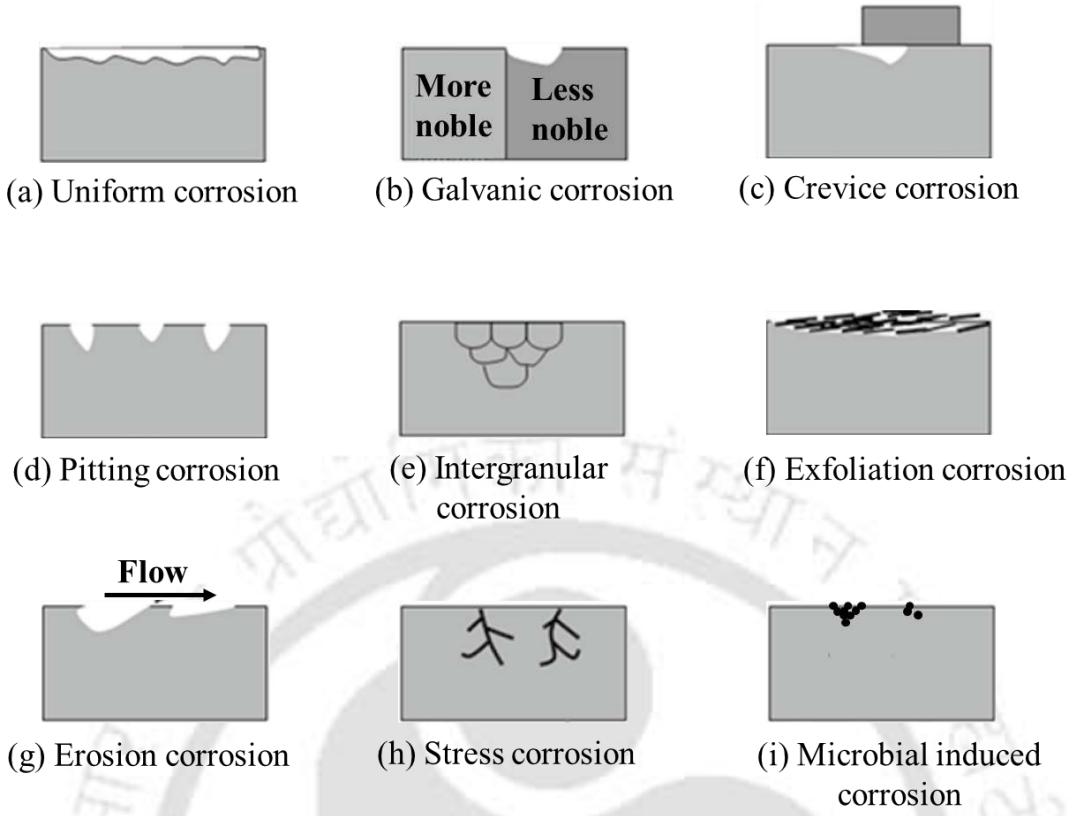

Fig. 1.1 Types of corrosion.

1.3 Major tragedies due to corrosion

In the last few decades, many industrial and non-industrial accidents happened due to corrosion, like the Bhopal gas tragedy in 1984, Carlsbad pipeline explosion in 2000, Prudhoe Bay oil spill in 2006, Guadalajara sewer explosions in 1992, Accident of the Aloha Airlines flight Boeing 737, in 1988, Sinking of the Tongan inter-island ferry ‘‘Princess Ashika’’in 2009, and etc.

1.3.1 Chemical plant explosion in Bhopal

It was the worst corrosion-related disaster regarding human death, injury, and subsequent health problems. Investigation revealed that steel pipes corroded and water leaked into tanks containing methyl isocyanate. The iron corrosion products provided a catalyst for a

reaction, which blew apart the plant, allowing the methylisocyanate and other toxic gases to escape, killing over 8000 people. Since then, an additional 15,000 have died due to the explosion, and an estimated 500,000 others are suffering from gas-related disorders (C M Hansson, 2011). The chemical plant after the explosion is shown in Fig.1.2 (a).

1.3.2 Guadalajara sewer explosions in Mexico

The explosions took place in Guadalajara on 22 April 1992, in the downtown district of Analko. Almost 8 km of streets were destroyed. Officially, by the Lloyd's of London accounting, 252 people were killed, nearly 1,500 were injured, and 15,000 people were homeless. The sewer explosion was traced to the water pipe installation, which had been placed above the gas installations several years before the explosion. The corrosion of the water pipes caused water leaks out of them, which subsequently caused the corrosion of the gas pipes and gas leaks in the sewers (Petrovic, 2016)**.** The destroyed street of Guadalajara sewer explosions is shown in Fig. 1.2 (b).

1.3.3 Carls bad gas pipeline explosion

On August 19, 2000, a 76 cm diameter natural gas transmission pipeline operated by the El Paso Natural Gas Company ruptured adjacent to the Pecos River near Carlsbad, New Mexico. The released gas ignited and burned for 55 minutes. During this accident, twelve persons were killed, and escaping gas created a crater 16 meters wide and blew out three large pieces of the pipeline. One of the pieces showed significantly more corrosion damage than the other one (Petrovic, 2016). The created creata and pitting corrosion on the piece of a pipeline are shown in Fig. 1.2 (c).

1.3.4 Prudhoe bay oil spill

One of the worst oil leaks occurred on March 2, 2006, when approximately 1 million liters of crude oil leaked from a corroded transit pipeline in Northern Alaska. The leak's location was in a culvert surrounding the transit line as it passes under a caribou crossing (C M Hansson, 2011). Oil leaked over snow is shown in Fig. 1.2 (d).

1.3.5 Accident of Boeing 737 from Aloba Airlines

After reaching the cruising altitude of 24,000 feet (approximately 8,000 meters), the pilots of the Boeing 737 heard a sudden whooshing sound from the fuselage, followed by a loud, windy noise. They observed that a significant portion of the upper crown skin in section 43 had separated from the aircraft during flight. This structural failure caused an explosive decompression in the cabin. The incident tragically resulted in the death of one flight attendant, who was standing in the aisle at the time the fuselage segment detached (Czaban, 2018). Boeing 737 from Aloba Airlines is shown in Fig. 1.2 (e).

1.3.6 Sinking of the Tongan inter-island ferry ‘‘Princess Ashika’’

Before completing one month of service, this ferry tragically sank in 2009, losing 74 passengers and crew members (Fig. 1.2 (f)). Investigations revealed that severe corrosion had significantly affected structural integrity, preventing its doors and entrances from closing properly, which ultimately contributed to the disaster (C. M. Hansson, 2011).

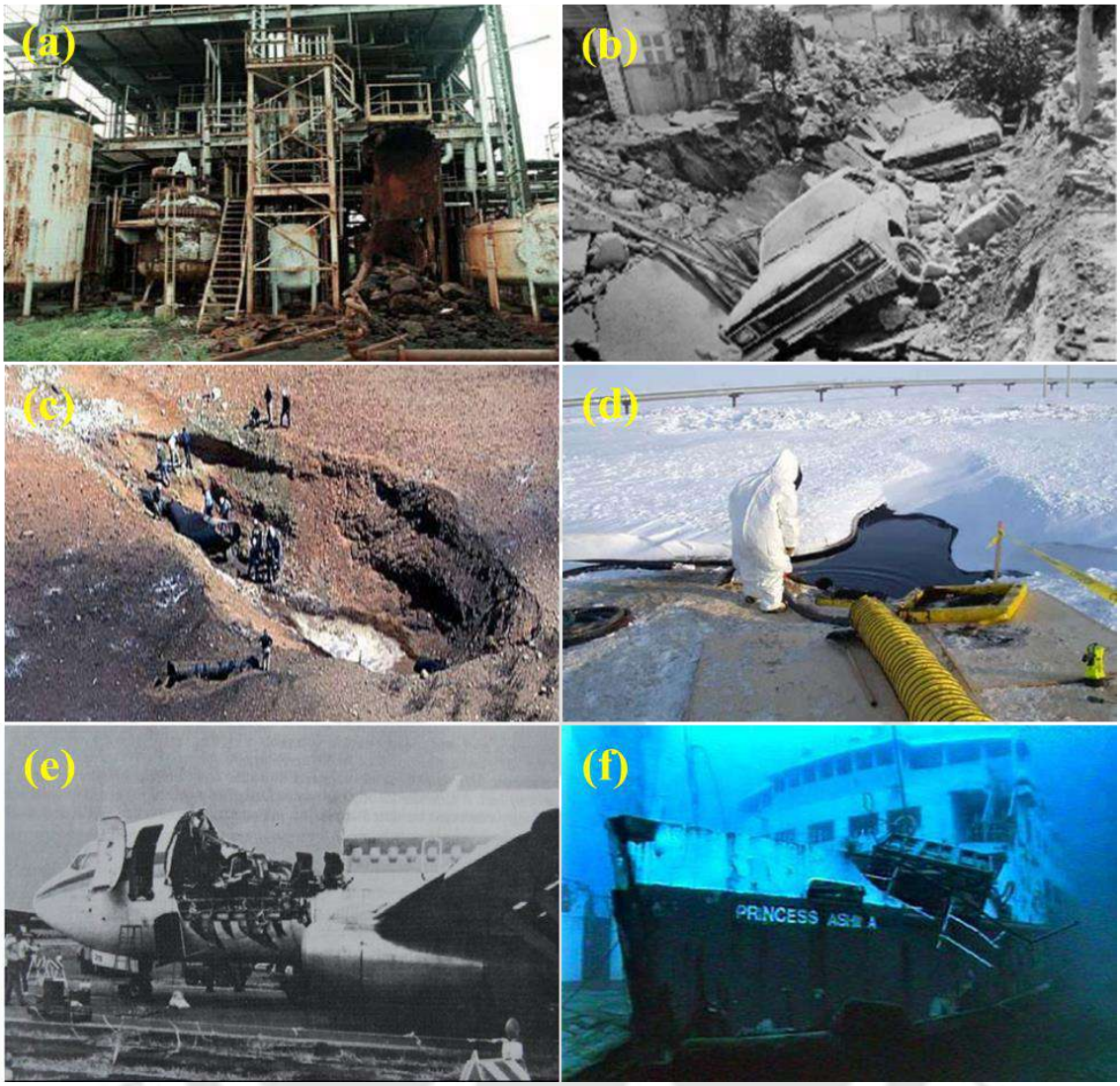

Fig. 1.2 Pictures of (a) Bhopal gas tragedy in 1984, (b) Guadalajara sewer explosions in 1992, (c) Carlsbad pipeline explosion in 2000, (d) Prudhoe Bay oil spill in 2006, (e) Accident of the aloha airlines flight Boeing 737 in 1988, and (f) Sinking of the Tongan inter-island ferry ‘‘Princess Ashika’’ in 2009.

Based on the above tragedies, the effects of corrosion can be divided into three categories, as represented by Fig. 1.3. Corrosion often originates huge failures in structures, for instance, rapid degradation of metal bodies, leading to costly repairs and a waste of time in repairing or replacing a particular system of a shutdown plant (Shehata et al., 2018). Additionally, the process of repairing corrosion is hazardous and can result in injuries or

fatalities for workers (Shehata et al., 2018). These factors compel researchers to address corrosion as a critical issue that needs aggressive attention worldwide.

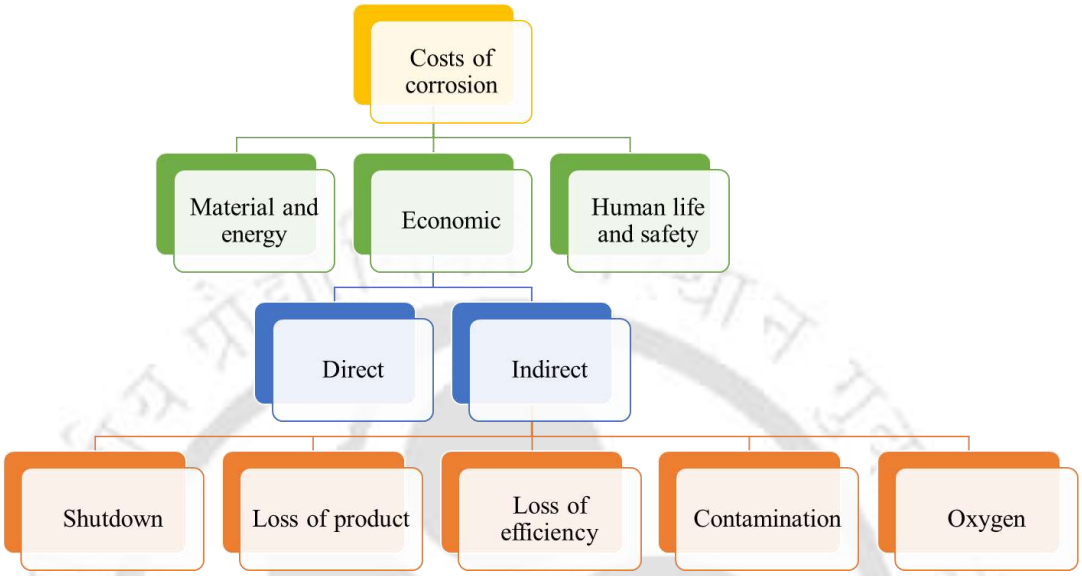

Fig. 1.3 Breakdown of corrosion cost.

Therefore, in the last few years, corrosion has become a major concern due to the abovementioned losses. Several corrosion-controlling techniques have been employed to reduce these corrosion-related losses, which will be discussed later. Few studies have reported that the implementation of the best corrosion control technique can save up to 35% of corrosion-related losses, which can be a potential savings (Solovyeva et al., 2023).

1.4 Corrosion in mild steel

Recently, mild steel (MS) has become a vital structural material due to its following properties: stronger mechanical durability, easy processing, and low cost. Therefore, MS is frequently used as a construction material in several industries, including marine, oil and gas, petrochemicals, chemical refineries, pipelines, automobile industries, and reinforced concrete structures. However, when it is exposed to processes like acid pickling, industrial washing,

acid descaling, and oil-wet cleaning, mild steel becomes highly vulnerable to corrosion, leading to material deterioration and significant economic losses (Haque et al., 2020).

In this present study, we are focusing on controlling the corrosion of mild steel metal.

1.5 Corrosion controlling techniques

Most commonly used corrosion control techniques, such as selection of material, cathodic protection, use of inhibitors, and anticorrosive coatings, are shown in Fig. 1.4. In the last few decades, these strategies have shown their outstanding corrosion mitigating nature for protecting the several metallic structures in various corrosive electrolytes.

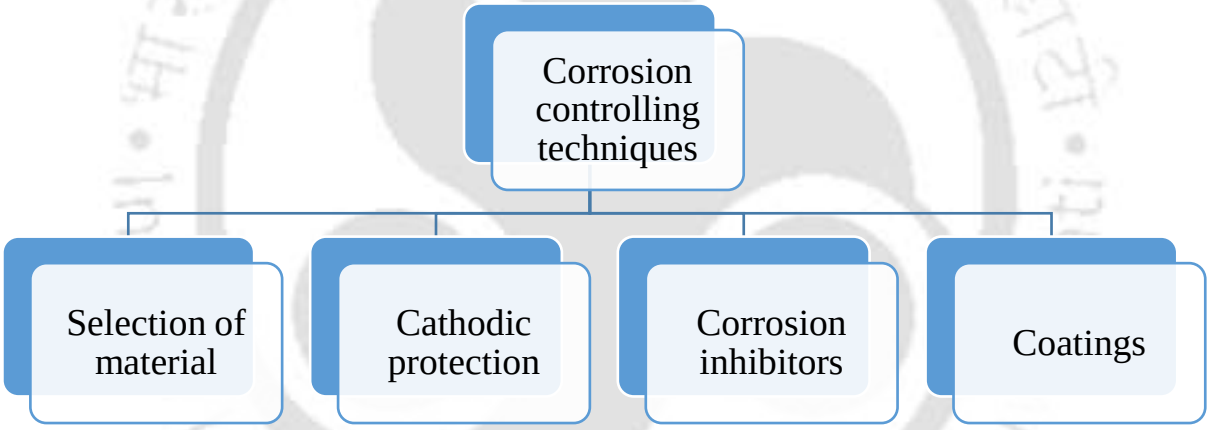

Fig. 1.4 Corrosion control strategies.

Selection of materials

Materials science and engineering play a vital role in this modern age of science and technology. Various materials are used in several sectors like industry, housing, agriculture, transportation, etc., but they are degraded mainly due to corrosion. Therefore, the primary aim to prevent corrosion is the selection of the appropriate materials and their suitable design for long service life in the specific application conditions. This involves choosing metals that are less prone to chemical reactions than steel, such as stainless steel or platinum. Additionally,

corrosion-prone areas can be strategically avoided during the design process. While no metal is completely resistant to corrosion, some exhibit greater durability over time.

However, for developing countries and industries, choosing extremely corrosion-resistant metals may not be feasible due to higher costs. Therefore, price remains a critical factor in material selection.

Advantages:

- It offers excellent metal protection against rust and other forms of corrosion, and it significantly extends the durability of used structures and objects, which reduces the frequent replacement of components.
- It enhances the capability of structures that can be used in extreme environmental conditions, such as high humidity, saltwater, chemicals, and industrial pollutants.

Disadvantages:

- It can be more expensive than traditional metals and in some cases, the higher cost may outweigh the benefits of enhanced corrosion resistance.
- Less availability may lead to potential supply chain challenges.

Cathodic protection

Cathodic protection is a widely used corrosion-controlling technique for protecting huge metallic structures from corrosion. In this technique, interesting metal (metal to be protected) is connected to highly reactive metal, which is degraded with time to protect the metal of interest. This process relies on the principles of anodic and cathodic behavior in galvanic systems. There are two types of cathodic protection: (i) impressed current cathodic protection (ICCP) and (ii) sacrificial anode cathodic protection (SACP), also known as galvanic cathodic protection (Ameh and Ikpeseni, 2018).

Impressed current cathodic protection: In this technique, metallic surface is protected by supplying the electrons from an external power source (battery). The metal (substrate) to be protected is connected to the negative terminal of the DC power source, making it the cathode. Meanwhile, an inert anode, typically a graphite rod, is connected to the positive terminal. Here, a protective current greater than the corrosion current is applied to counter the corrosion current's effects. The supplied electrons ensure the metal remains in a cathodic state, effectively preventing corrosion and safeguarding the structure (Fig. 15 (a)).

Sacrificial anode cathodic protection: The metal (substrate) to be protected is converted into a cathode using sacrificial anodes. It is accomplished by connecting the metal (substrate) to another metal with a lower electrode potential. As a result, the substrate metal acts as the cathode, while the more reactive metal serves as the anode. The anode corrodes over time, sacrificing to protect the substrate metal from corrosion (Fig. 15 (b)).

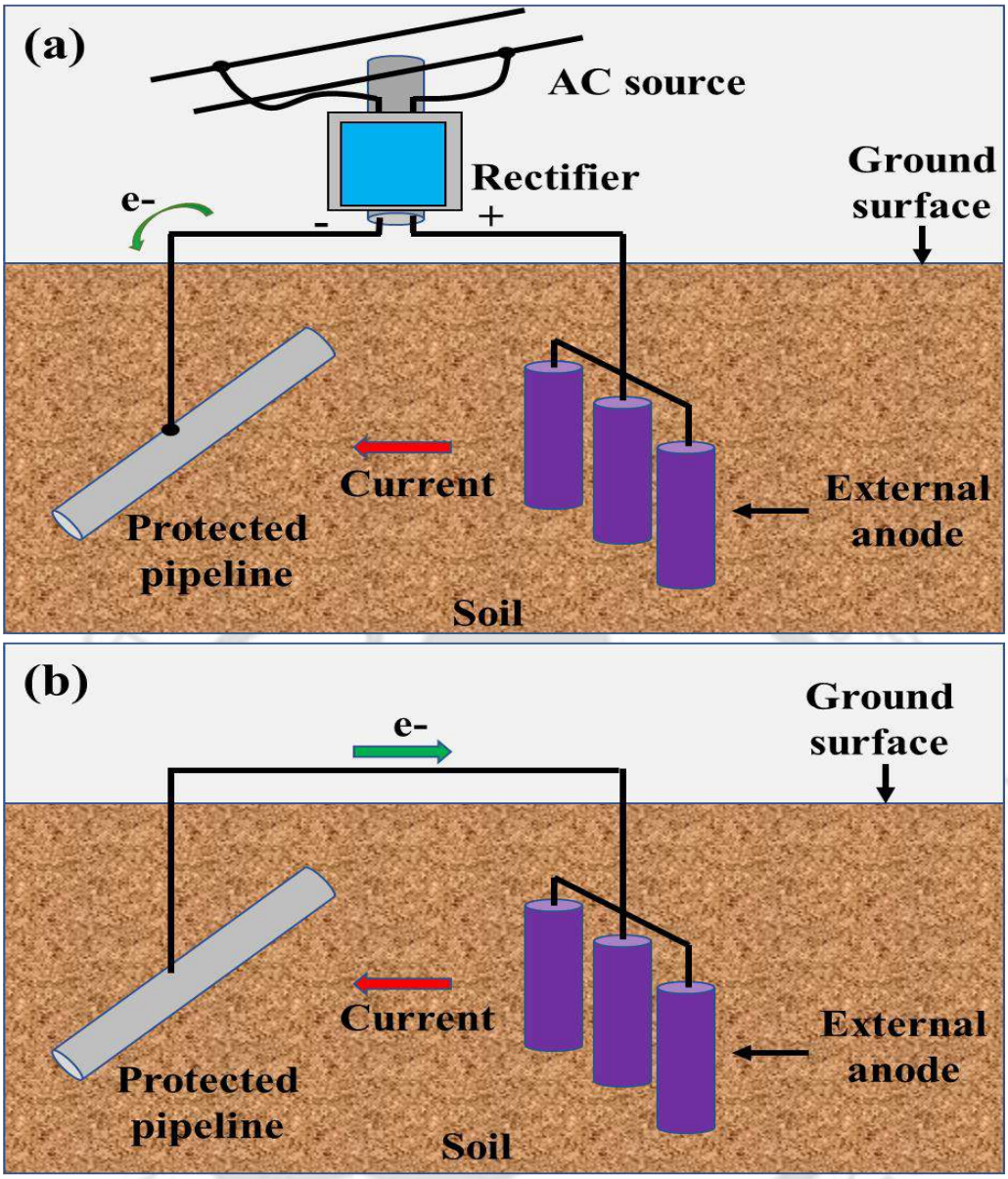

Fig. 1.5 (a) Impressed current cathodic protection and (b) sacrificial anode cathodic protection.

Advantages:

- It significantly reduces corrosion in metal structures, extending their life.
- It is effective in various environments, including soil, seawater, freshwater, and industrial corrosive conditions.

- It is very effective for pipelines, underground storage tanks, marine structures, and offshore platforms as compared to other techniques.

Disadvantages:

- It has a high initial cost because it requires power sources, anodes, and monitoring equipment.
- Impressed current cathodic protection (ICCP) requires a continuous power supply.
- It has a lower driving voltage/current.

Use of corrosion inhibitor

An inhibitor is a chemical substance or combination of substances that, when added even in very low concentrations to the corrosive environment, effectively prevents or reduces corrosion without significant reaction with the components of the environment (Shang and Zhu, 2021). The molecules of corrosion inhibitors start to adsorb on the metallic surface and hinder metal degradation in corrosive solutions by forming an inhibiting layer on the metallic surface, which isolates it from the surrounding electrolytes.

Advantages:

- Outstanding effectiveness for the protection of metals and their alloys
- Simple to use and cost-effective technique
- It can be used in a wide range of conditions, including acidic, neutral, and alkaline environments
- It can be easily applicable in irregular shapes and small diameters pipes

Disadvantages:

- Few of them can be harmful to the aquatic life.

Coating

The anti-corrosive coating is another commonly used corrosion-controlling technique that protects metallic bodies from dry and wet environments. The coating is a protective layer applied on metallic surface to reduce corrosion. It acts as a physical barrier that separates the metal surface from the corrosive environment (Udoh et al., 2024). Applying an organic coating on the surface of a reactive metal is an effective way to prevent corrosion while also providing additional surface properties without affecting its mechanical characteristics. This method is widely used to protect metal surfaces in transportation, pipelines, marine, and infrastructure industries.

Advantages:

- It is economically feasible and inert to the environment
- It can support the strength and stability of metal components by preventing deterioration
- It can be effective for lower temperature application

Disadvantages:

- Not all coatings adhere well to every type of metal, requiring specific formulations or additional treatments to ensure proper bonding.
- It does not work properly at higher temperatures.

Among all the existing corrosion-controlling methods, this research mainly focuses on corrosion inhibitors and anticorrosive coatings for the mitigation of mild steel corrosion.

1.5.1 Corrosion inhibitors

Corrosion inhibitors can be categorized either as anodic, cathodic, or mixed type depending on whether their influence (mechanism of action) is mainly retarding the anodic or cathodic reaction of the corrosion process or both of them (Hamdani et al., 2018).

❖ **Anodic inhibitor**

An anodic inhibitor increases anodic polarization and shifts the corrosion potential of inhibited systems towards the more positive side as compared to uninhibited systems, as illustrated in Fig. 1.6 (a) (Finšgar and Jackson, 2014). It is also known as a passivating inhibitor. These inhibitors significantly hinder corrosion reactions occurring at the anode by forming a complex compound with a newly produced metal ion. They adsorb onto the metal surface, creating a protective film or barrier that significantly decreases the corrosion rate. Anodic inhibitors must be present in sufficiently high concentrations for adequate metal protection. If the concentration is too low, the inhibitor molecules will not fully cover the metal surface, leaving exposed areas vulnerable to localized corrosion. Due to this risk, anodic inhibitors are sometimes considered dangerous when used in inadequate amounts. There are two types of passivating inhibitors: (i) **Oxidizing anions** (for example, chromates, nitrites, and nitrates) that can passivate steel even in the absence of oxygen. (ii) **Non-oxidizing ions** (for example, phosphates, tungstates, and molybdates) that require oxygen to effectively passivate steel (Lee et al., 2018).

❖ **Cathodic inhibitor**

Cathodic inhibitors induce cathodic polarization and shift the corrosion potential towards the more negative side in inhibited systems compared to uninhibited ones, as illustrated in Fig. 1.6 (b). These inhibitors are also known as precipitation inhibitors because they mitigate corrosion by slowing the reduction reaction of the cathodic area through the formation of precipitates that block the cathodic areas. These inhibitors significantly reduce hydrogen gas evaluation in acid environments and oxygen reduction in near-neutral conditions, decreasing the overall corrosion rate. Cathodic inhibitors are classified into three categories based on their mechanism of action: **(i) Cathodic poisons:** A compound (for example, arsenic, antimony,

selenium, and tellurium) that reduces the recombination and hydrogen evolutions is known as cathodic poison. **(ii) Cathodic precipitates:** A compound (for example, calcium, magnesium, and zinc ions) that favorably precipitates as oxides on the cathodic area and produces a shielding film on the metal's surface that behaves as a barrier for metal protection. **(ii) Oxygen scavenger:** A compound (for example, hydrazine and sodium sulphite) that reacts with existing oxygen in the system and forms a product to make oxygen-free systems which results in lesser corrosion (Buckner et al., 2016).

❖ Mix-type inhibitor

A mix-type inhibitor is a chemical compound that reduces anodic and cathodic reactions in the corrosion process. This type of inhibitor forms a protective layer on the metallic surface, which blocks both anodic and cathodic reactive sites, resulting in strong hindering of corrosion. In the presence of a mix-type inhibitor, corrosion potentials' values do not show a huge shift compared to uninhibited systems (Fig. 1.6 (c)). Organic corrosion inhibitors generally offer mix-type inhibiting behavior.

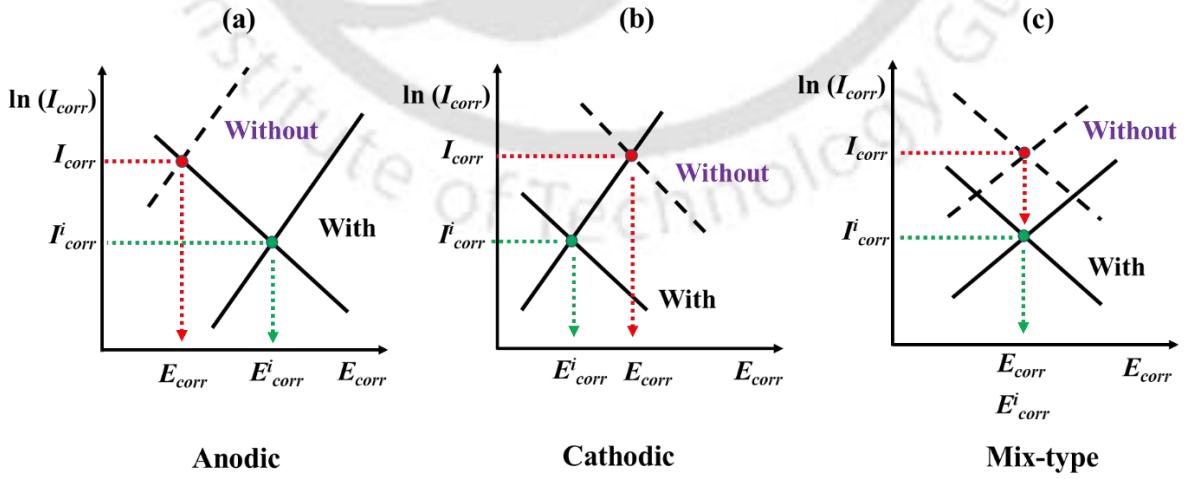

Fig. 1.6 Shifting in corrosion potential due to the presence of a corrosion inhibitor.

Based on the chemical nature, corrosion inhibitors are further classified in two categories ((i) inorganic and (ii) organic).

I. Inorganic corrosion inhibitor

Inorganic corrosion inhibitors play a crucial role in protecting metal surfaces by forming a barrier that minimizes metal exposure to corrosive environments. A huge number of inorganic compounds, including chromates, phosphates, molybdates, silicates, oxides, nitrites, dichromate, cadmium arsenic salts, nitrite, alkaline, and metal sulphides, have been widely utilized in acidic conditions. In this case, the protection is due to the reduction of electropositive ions and their deposition on the metal surface, lowering the overvoltage of the main cathodic depolarization reaction. Recent studies have shown that the addition of heavy metal ions such as Pb^{2+}, Ti^{+}, $Mn^{2+,}$ and Cd^{2+} inhibits iron corrosion in the acids medium (A. Al-Amiery et al., 2023).

II. Organic corrosion inhibitor

A wide range of organic compounds have been used as corrosion inhibitors, including amines, imines, thiourea, mercaptans, guanidine, amino acids, alcohols, and aldehydes. These inhibitors protect metal surfaces by adhering to them and forming a strong protective layer that shields the metal from corrosive environments. The use of organic compounds as inhibitors is one of the most effective methods for preventing metal corrosion in acidic environments. Organic compounds containing sulphur, nitrogen, and oxygen exhibit lower corrosion rates due to their high ability to adsorb onto the metal surface, forming a protective barrier. The adsorption of corrosion inhibitors is primarily influenced by the molecule's physical and chemical characteristics, including functional groups, molecular weight, steric factors, structure, aromaticity, the electron density of donor atoms, and the p-orbital nature of donating

electrons. The electronic structure of the molecule also plays a crucial role. Organic inhibitors can act as anodic, cathodic, or mixed-type inhibitors, either individually or in combination. Their effectiveness depends on several factors, such as molecular size, carbon chain length, aromaticity, conjugation, and the nature of bonding atoms.

In addition, recently numerous synthetic organic (amino acids, alcohols, amines, phenols, azole, and phosphate esters) and inorganic compounds (phosphate, chromate, dichromate, cadmium, arsenic salts, nitrite, alkaline, and metal sulfides) have been used as corrosion inhibitors in several harsh electrolytes for protecting the various metals and alloys from their degradation (Al-Amiery et al., 2023; Bijapur et al., 2023; Zhang et al., 2021). These synthetic inhibitors showed outstanding inhibiting effects, but unfortunately, they are expensive, and few of them are toxic to human and their environments, especially the aquatic environment fauna and flora (Ikeuba et al., 2024; Njoku et al., 2023). Nowadays, the discovery and preparation of green inhibitors have captivated the attention of both researchers and industrial professionals, and this high attention is due to their outstanding effectiveness, environmentally friendly, biodegradable behavior, and low cost. This current research is about developing a novel green corrosion inhibitor.

1.5.2 Green Corrosion inhibitors

Green corrosion inhibitors are most commonly used in corrosion mitigation applications in acidic conditions due to their simple implementation, excellent anti-corrosion properties, and eco-friendly behavior. These green corrosion inhibitors are further classified into two categories: (i) chemically synthesized and (ii) extracted from natural products and plant materials.

1.5.2.1 Chemically synthesized

In recent years, several chemically synthesized inhibitors have been used for metal protection. Considering the concept of green chemistry and the vision of human sustainability, a new corrosion inhibitor named N1-(2-aminoethyl)-N2-(2-(2-(furan-2-yl)-4,5-dihydro-1H-imidazol-1-yl) ethyl) ethane-1,2-diamine (NNED) is synthesized from biomass platform molecules. Both weight loss and electrochemical measurements demonstrated that the corrosion inhibitor had a good anti-corrosion performance for carbon steel in 1 M HCl medium, with inhibition efficiency higher than 90% at the lower level of inhibitor concentration (5 ppm) (Chen et al., 2021). Munis et al., have synthesized a green corrosion inhibitor; 2-(2-heptadecyl-4, 5-dihydro-1H-imidazole-1-yl) ethanol (HDIE), with the help of microwave radiations in solvent-free conditions. Its anti-corrosive behavior was studied by using several corrosion measuring techniques (electrochemical as well as weight loss analysis). The results showed that inhibition efficiency above 90% is achievable at 298 K with 0.5 m mL^{-1} inhibitor concentration (Munis et al., 2020). Fakir et al., have synthesized silica nanomaterials (nanosilicate) using rice husk, which was used to protect carbon steel in NaCl environment. The effects of various concentrations of inhibitor, temperature, and immersion time on the inhibition efficiency of nanosilicate corrosion inhibitor were studied using weight loss studies, electrochemical impedance spectroscopy, and potentiodynamic polarization studies. It has been found that with the increase in the concentration of inhibitors, corrosion efficiency increases. A maximum of 82 % inhibition efficiency was exhibited at 700 ppm of nanosilicate. Polarization results confirmed that nanosilicate is a mixed-type corrosion inhibitor (Fakir et al., 2023). Furthermore, Two acrylate derivatives such as, 3-((3-ethoxy-2-(ethoxycarbonyl)-3-oxoprop-1-en-1-yl)amino) benzoic acid (EOAB) and diethyl 2-((benzylamino)methylene)malonate (DBMM) were synthesized via a solvent- and heating-free procedure. Weight Loss Study demonstrated that both molecules mitigate corrosion with 85

and 90 % efficiencies. Electrochemical experiments proved that the corrosion mechanism is charge transfer and that the presence of EOAB and DBMM at any tested concentration in the electrolyte significantly increases the polarization resistance and lowers the corrosion density current. This is due to the formation of the inhibiting layer by their adsorption on the metallic surface (Machado Fernandes et al., 2024).

1.5.2.2 Extracted from natural products and plant materials

Natural (green) corrosion inhibitors are mainly derived from natural products and plant materials, which are widely used for the corrosion protection of metals due to their following advantages: easily available, nontoxic, affordable, eco-friendly procedures, environmentally acceptable, and renewable. The diversity of green corrosion inhibitors is indeed high, and many of them have the potential to be considered as efficient and practical corrosion inhibitors in the field. They can prevent metal corrosion in both acidic and alkaline environments. They are a mixture of several organic corrosion inhibitors. Therefore, green inhibitors have similar electronic structures to the traditional organic corrosion inhibitors (Wang et al., 2022) that are mainly composed of oxygen, nitrogen, sulfur atoms, aromatic rings, and unsaturated bonds, which participate in its bonding with metals (Abd El-Lateef et al., 2023; Guo et al., 2020; Jeeja et al., 2022; Wang et al., 2022). The interaction between inhibitors and the metal-electrolyte interface significantly influences the mechanism of electrochemical reactions. During these reactions, a polar functional group serves as a reaction center for stabilizing inhibitor adsorption on metal (Goyal et al., 2018; Verma et al., 2017). An effective inhibitor must replace the water molecule from the metallic surface to establish the electrostatic interaction with the charged surface. For an ideal inhibitor, this interaction should be stronger than the interaction between the water molecule and the metal surface (Ali and Mahrous, 2017). The strength of the interaction depends on the structure of inhibitor molecules, the charge of the surface, and

the type of corrosive electrolyte. This current research is about developing a novel green corrosion inhibitor.

1.5.3 Anticorrosive coatings

Covering metallic surfaces by coating is the most common and convenient technique to prevent metal corrosion. The traditional corrosion protection coating works as a physical barrier, which could isolate the metal products from the external medium to avoid the reaction condition of the corrosion process. Anticorrosive coatings consist of a coat that can be classified, as often generally, into four types: (i) metallic coatings, (ii) conversion coatings, (iii) inorganic coatings, and (iv) organic coating.

1.5.3.1 Metallic Coatings

It is usually named according to the metal used, for example, copper, zinc, nickel, and gold coatings (Pedeferri, 2018). Relatively thin coatings of metallic material can provide a satisfactory barrier between the metal and its environment (Revie and Uhlig, 2008).

1.5.3.2 Conversion Coatings

These types of coatings are formed on the surface of various metals as the result of chemical or electrochemical reactions after immersion in suitable solutions. The most popular processes for obtaining conversion coatings are phosphatizing, chromatin, and anodic oxidation.

1.5.3.3 Inorganic Coatings

These coatings are created through chemical action that changes the surface layer of metal into metallic oxide film or compound to reduce corrosion.

Hot enamels: Enamels are obtained from a mixture of silica, titanium oxides, feldspars, clay, and melting additives such as borax, fluorosilicates, nitrates, and carbonates of lithium and potassium, melted at a temperature between 1000 and 1400 °C to obtain alkaline aluminium borosilicate compounds, then rapidly cooled in water and successively ground. This powder, added with colored pigments, is sprayed on the metal surface and heated in an oven at 750–850 °C for some tens of minutes.

Thick corrosion-resistant coatings: To resist very high aggressive corrosion conditions, such as those found inside chemical reactors, thick layers of corrosion-resistant materials are used: glassy materials, cured inorganic silicates, ceramics, sulfur, graphite, and carbon, often applied in the form of tiles or bricks stuck with suitable adhesives. To absorb the inevitable differential expansion strains, membranes made of resins, asphalt, or synthetic elastomers are often interposed. Glassy and ceramic materials are resistant in all environments except hydrofluoric and caustic ones (Pedeferri, 2018).

1.5.3.4 Organic Coatings

It is an organic corrosion barrier between the metal and the corrosive environment. It maintains the durability of structures and provides resistance to weather, humidity, abrasion, chemical resistance, toughness, and aesthetic appearance. Organic coating efficiency depends on the mechanical properties of the coating system, type and concentration of suspended inhibitors, pretreatment of the metal surface, adhesion of the coating to the underlying metal base, and other additives that inhibit substrate corrosion. Coating formulation usually contains solvent, resin (binder), pigment, filler, and additives.

Organic coatings are classified according to the resin's chemical structure, and the following resins are frequently used in the paint industry.

The vinyl resin: It contains the vinyl linkage group. Vinyl coatings are copolymers of vinyl chloride and vinyl acetate. Vinyl copolymers require a large amount of solvent to dissolve. The vinyl copolymer has excellent protection against acids, alkalis, and water and good protection against the weather.

Urethane resins: It is synthesized from isocyanates and chemical compounds with hydroxyl or urethane groups, including water, polyesters, epoxies, and acrylics. Polyester and epoxy have better barrier resistance to moisture and chemical attack than acrylic polyol. Aliphatic isocyanate-based coatings are resistant to UV light and have excellent gloss and color retention.

Polyester resin: It is synthesized with components that introduce unsaturation into the polymer chain. The paint is manufactured by mixing a dissolved polyester resin in a styrene monomer with pigment and a reaction inhibitor**.**

Epoxy resins: It forms a durable protective coating only when polymerized with amine, polyamide, or esterified fatty acids. Coal-tar epoxies are modified with coal-tar filler to improve moisture resistance. Coatings are highly resistant to solvents, acids, and alkalis and are based on phenolic cross-linked epoxies. These coatings are used to protect process equipment. When the phenol-formaldehyde constituent of phenol is used to cross-link epoxy resin instead of amine, the coating has improved resistance to alkalis.

In addition, among all the above resins-based coating, Epoxy resins (EP) are widely used in several industries as a heavy-duty anticorrosion coating because of their excellent properties, such as chemical resistance, toughness, low shrinkage on cure, mechanical, corrosion resistance, high tensile strength, durability against physical damage, and excellent adhesion on various substrates.

1.6 Literature review

In this section, a literature survey was carried out on green corrosion inhibitors and nanofillers-based epoxy coatings for controlling steel corrosion.

1.6.1 Green corrosion inhibitors derived from plants

Numerous green corrosion inhibitors have been developed from various organs of plants such as, flowers (Rajendran and Karthikeyan, 2012), fruit (Bhan and Golder, 2023; Golafshani et al., 2023; Pourzarghan and Fazeli-Nasab, 2021), fruit peel (N. Bhardwaj et al., 2022; Elazabawy et al., 2023; Lin et al., 2021; Rocha et al., 2014), seed (Abbout et al., 2021; Bhardwaj et al., 2021; Fernine et al., 2022; Odewunmi et al., 2015), leaf (Qiang et al., 2018; Ramezanzadeh et al., 2019; Tan et al., 2021; Zehra et al., 2022), stem (Arora et al., 2007), and root (Singh et al., 2014) to protect the different metals from corrosive solutions (Fig. 1.7), these green corrosion inhibitor exhibited excellent corrosion inhibiting properties due to the presence of a huge range of active phytochemical like amino acids, carbohydrates, proteins, polyphenolic compounds, etc. The existence of these phytochemicals was identified using the LC-MS and FTIR analysis.

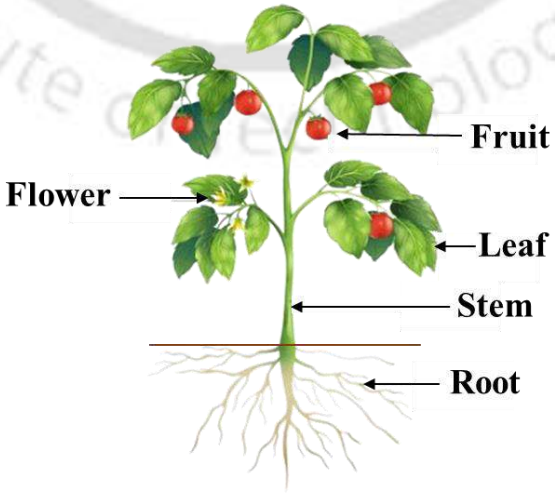

Fig. 1.7 Different plant organs.

Furthermore, yew (*Taxus baccata*) extracts were prepared and used to inhibit the carbon steel dissolution in 1 M HCl. Their anticorrosive behavior was scrutinized through weight loss and electrochemical measurements. They reached the maximum inhibitory effect (83.28 %) of yew extract at 700 mg L^{-1} compared to blank (Hanini et al., 2019). Furthermore, *Dysphania ambrosioides* (DA) was also used as a corrosion inhibitor, which showed an inhibitory efficiency of about 84% at 1.5 g L^{-1} concentration (Daoudi et al., 2022). Saeed et al. (2019) have prepared sweet melon peel extract (SMPE), which was utilized as a green corrosion inhibitor. The outcomes of electrochemical measurements displayed that the metal dissolution rate was 5 times lower in the presence of SMPE (0.5 g L^{-1}) as compared to the blank system at 333 K (Saeed et al., 2019). Onukwulia and Omotioma (2019) used bitter leaves (*Vernonia amygdalina*) extract as a corrosion-inhibiting agent for hindering the MS degradation in HCl, and its corrosion-inhibiting properties were studied by weight loss method. During the weight loss investigations, it was observed that the corrosion rate decreased with the addition of an inhibitor, and 85.40% inhibition efficiency was achieved at 1000 mg L^{-1} (Onukwulia and Omotioma, 2019). Additionally, (Mbamalu and Chinedu, 2023) used the leaf of *chromolaena odorata* for preparing a green inhibitor to protect the MS in an acidic solution, and this extract provided a good inhibitory effect with 83.33 % percentage inhibitory efficiency for 700 mg L^{-1} dose of the inhibitor (Mbamalu and Chinedu, 2023). Sanaei et al., (2019) developed *Rosa cannin* fruit extract as a corrosion inhibitor for mild steel protection from 1 M HCl, and inhibitory efficiency was investigated by electrochemical impedance spectroscopy and potentiodynamic polarization techniques. Results reveal that *Rosa cannin* fruit extract behaved as a mix-type of inhibitor, and the corrosion rate decreased with the addition of inhibitor. The maximum corrosion inhibition efficiency was achieved 86% at 800 ppm concentration of inhibitor (Sanaei et al., 2019). Umoren et al., (2015) used weight loss and electrochemical methods to study the anticorrosive and adsorption behavior of strawberry fruit extract at the

interface of steel and acids. Outcomes showed that corrosion inhibiting tendency increased with the increase the amount of strawberry fruit extract but decreased with increasing the temperature (Umoren et al., 2015). El-Katori and Al-Mhyawi, (2019) prepared Bassia muricata extract (green inhibitor) for corrosion inhibition of aluminum immersed in 1 M H_2HO_4. Anticorrosive behavior was determined by electrochemical and weight loss methods. The inhibition efficiency increases with the addition of an inhibitor and reaches 90% at 300 ppm. Tafel results showed that the inhibitor acts as a mixed type of inhibitor. The inhibitor molecules were adsorbed on metal by Temkin adsorption and formed a protective layer, which was confirmed by FESEM and AFM analysis (El-Katori and Al-Mhyawi, 2019).

1.6.2 Epoxy based coatings

Recently, epoxy coatings have been most commonly used to protect several metals and their alloys in various corrosive environments due to their following advantages: highly compressible substances with exceptional resistance to corrosion, high tensile strength, durability against physical damage, superior fatigue resistance, and excellent adhesion properties to the various substrates. Unfortunately, organic coatings generally become defective, and micropores develop during long exposure to a corrosive environment. These defects and micropores work as a passage that transfers the corrosive ions to the coating/metal interface, and corrosion starts (Xavier, 2021).

In the last few years, serious attempts have been made to improve the corrosion-resistive properties and durability of epoxy coatings by incorporating various carbon-based nanofillers. But two-dimensional graphene and its derivatives exhibited outstanding reinforcing properties in epoxy resin-based coatings among the other reported nanofillers due to its large specific surface area and exceptional permeability, which were most commonly used as nanofillers to enhance the anti-corrosive properties of epoxy coatings, and they also

enhance the physicochemical, structural, and other features. Furthermore, graphene improves the above properties of coatings because of its highly active surface with several functional groups, such as carbonyl, epoxy, and hydroxyl groups, on the GO surface (Khatoon et al., 2021). Rajabi et al. (2015) prepared the GO/epoxy coating and reported that GO nanofillers containing composite coatings showed better anti-corrosive and mechanical properties at a lower amount of nanofillers. However, on higher loading, composite coatings showed opposite results due to the aggregation of nanofillers (Rajabi et al., 2015). GO nanosheets tend to aggregate due to their high surface energy, making it challenging to achieve a uniform distribution in a polymer epoxy matrix. Therefore, the decoration of inorganic nanoparticles on GO sheets improves their surface properties, reducing their aggregation(Gu et al., 2015; Jiang et al., 2019; Li et al., 2012; Zhao et al., 2022).

Moreover, these decorated inorganic nanoparticles increase the steric hindrance and alter the interfacial interactions, resulting in a more homogeneous dispersion of the GO nanosheets within the epoxy matrix. In the literature, Pourhashem et al. (2017) decorated SiO_2 on the GO nanosheet's surface and obtained enhanced SiO_2-GO dispersion in epoxy than that of GO nanosheets. They also observed that this binary composite (SiO_2-GO) based coating showed outstanding corrosion-resisting properties among all coatings (Pourhashem et al., 2017). In the last few years, RGO has been most commonly utilized in coating preparation due to its following advantages: More reactive surface area and better compatibility with several organic solvents and matrix resins compared to pristine graphene. Its functionalization can further enhance its dispersibility in various media and provide additional features such as improved mechanical, electrical, or thermal properties. These characteristics of RGO enable its uniform distribution within the polymer matrices, leading to the formation of more durable and compact coatings due to the strong interactions between the RGO and the polymer matrix (Wang et al., 2021; Zhu et al., 2021). However, RGO tends to aggregate at higher loadings,

which negatively impacts the coating's performance. To overcome this limitation, RGO has been functionalized or decorated with other nanoparticles or polymers to enhance its dispersion and stability.

Rajitha et al. (2020) decorated the ZnO particles on RGO sheets to prepare the RGO-ZnO composite, and they found that RGO-ZnO nanocomposite in PU resin-based coatings exhibited enhanced anti-corrosive properties as compared to the individual RGO and ZnO coatings (Rajitha et al., 2020). Furthermore, RGO surface was modified by anchoring the ZrO_2 nanoparticles through single-step hydrothermal reaction, prepared ZrO2@RGO hybrid composite in EP coatings could effectively prevent electrolyte penetration, and ZrO2 nanoparticles played a synergistic role with RGO nanosheets in alleviating corrosion (Zhou et al., 2022). Few studies reported that RGO was also factionalized with MoS_2 and this binary composite was added to epoxy coating. The electrochemical test results revealed that anticorrosion property and permeability resistance of the MoS_2-RGO/epoxy composites coating was enhanced significantly due to excellent barrier property of MoS_2-RGO hybrid (Chen et al., 2018).

Few studies have reported that electrically conductive polymers play a key role in anti-corrosive coatings due to their ability to provide anodic protection and metal passivation through their own oxidation processes (Nguyen et al., 2003; Reut et al., 1999). Among all the available conducting polymers, polyaniline (PANI) is the most suitable aspirant for coating reinforcement because of its following properties: environmentally stable, simple synthesis process, better processability, and economical. PANI displays outstanding corrosion-resisting properties for metal degradation (Ahmadinia and Farshi Azhar, 2022). In the last few years, several researchers have used PANI for protecting the metal from corrosion (Kraljić et al., 2003). Guo et al. (2019) prepared a nanocomposite by doping PANI in alkyd resin and found that the prepared nanocomposite showed enhanced anti-corrosive properties (Guo et al., 2019).

Furthermore, Xiao et al. (2018) have added binary composite (PANI-GO) to epoxy resin and achieved significantly improved corrosion inhibiting behavior than that of pure epoxy coating (Xiao et al., 2018) and Goswami et al., (2024) have investigated the anticorrosive behavior of PANI wrapped nitrogen-doped graphene nanocomposites coating and found that The NGr-PANI-ES-8 nanocomposite having a maximum content of NGr (8 %) showed the highest R_c, R_{ct}, and total impedance. The total impedance of the NGr-PANI-ES-8 coated mild steel sample exhibited a huge decrease from 1.7×10^{15} to 2.17×10^{4} Ω cm^2 only in 7 days of immersion (Goswami et al., 2024). The summary of recent studies on GO or RGO based composites used for an anticorrosive application in 3.5 wt% NaCl solution is shown in Table 1.1.

Table 1.1 Summary of recent studies on GO or RGO based coatings used for an anticorrosive application in 3.5 wt% NaCl solution.

Metal	Coating matrix	nanofillers	References
Carbon steel	Epoxy	GO	(Rajabi et al., 2015)
Mild steel	Epoxy	SiO_2-GO	(Pourhashem et al., 2017)
N80 tubing	Epoxy	RGO	(Zhu et al., 2019)
Mild steel	Polyurethane	RGO-ZnO	(Rajitha et al., 2020)
Steel	Epoxy	ZrO2@RGO	(Zhou et al., 2022)
Steel	Epoxy	MoS_2-RGO	(Chen et al., 2018)
Carbon steel	Epoxy	CNNS@rGO	(Liu et al., 2022)
Mild steel	Epoxy	EP-rGO/APOD-WS2	(Xavier et al., 2024)
Mild steel	Epoxy	rmGO-PANI-ES	(Mourya et al., 2024)

1.7 Motivation of the work

This report documented the focus on green corrosion inhibitors and epoxy-based coatings to mitigate mild steel corrosion in corrosive mediums. Therefore, the motivation of the work is divided into two parts as follows:

1.7.1 Green corrosion inhibitors

Metal corrosion has become an emerging concern at local and industrial scales, which hampers their conventional production unit. In recently reported studies, several synthetic organic (amino acids, alcohols, amines, phenols, azole, and phosphate esters) and inorganic compounds (phosphate, chromate, dichromate, cadmium, arsenic salts, nitrite, alkaline, and metal sulfides) have been utilized as corrosion inhibitors in various corrosive electrolytes to mitigate the corrosion of metal and their alloys. These inhibitors are effective but costly, and some are toxic to human and their environments, especially the aquatic environment fauna and flora. Nowadays, the development of green corrosion inhibitors is gaining huge popularity as a sustainable and eco-friendly alternative to synthetic corrosion inhibitors due to their following advantages such as renewable, biodegradable, inexpensive, eco-friendly, and safe for human exposure, which makes them appropriate for metal protection in various industries namely, oil and gas, petrochemical, marine applications. The green inhibitors have similar electronic structures to the traditional organic corrosion inhibitors that are mainly composed of oxygen, nitrogen, sulfur atoms, aromatic rings, and unsaturated bonds, which participate in its interactions with metals (Wang et al., 2022)(Abd El-Lateef et al., 2023; Ikeuba et al., 2023). This interaction between inhibitors and the metal-electrolyte interface significantly influences the mechanism of electrochemical reactions. During these reactions, a polar functional group serves as the reaction's center for stabilizing the inhibitor's adsorption on metal.

In the last few decades, several bio-extracts have been used for metal protection in the acidic environment. These extracts showed good inhibition due to the presence of a wide range

of phytochemicals, such as phenolics, saponins, tannins, flavonoids, terpenoids, alkaloids, vitamins, amino acids, fatty acids, and many others. Recently, several bio-extracts have been prepared from different plants, like strawberry, *Prunusdulcis,* chayote, tinda, *Phaseolus lunatus, and Duranta erecta,* and have been used in several applications like medical purposes, nanoparticle synthesis, sensor preparation, and many others.

Umoren et al., (2015) developed a strawberry (Fragaria ananassa) fruit-based corrosion inhibitor for mild steel protection in 1 M HCl. The phytochemicals reported in the strawberry fruit were vitamin C, flavonoids, phenolic acids, lignans, and tannins. Strawberry fruit extract has been used for several medical purposes due to its good antioxidant properties. Additionally, it acts as a mix-type inhibitor, and its corrosion inhibiting tendency increased with the inhibitor concentration but declined with temperature (Umoren et al., 2015).

Oshomogho et al., (2020) reported *Prunusdulcis* (almond) seed extracts as a green corrosion inhibitor. *Prunusdulcis* plants are known to contain various phytochemicals such as phenolics, saponins, tannins, and flavonoids with organically active components like proanthocyanidins monomers, isorhamnetin-3-O-rutinoside and chlorogenic acid. These compounds contain heteroatomic components that help adsorb the metal surface, thereby causing corrosion inhibiton in corroding environments (Oshomogho et al., 2020).

Chayote, scientifically known as *Sechium edule*, is a vegetable crop that belongs to the Cucurbitaceae family. This plant produces a distinctive food crop that comprises a pear-shaped fleshy fruit with a single soft seed. Chayote is widely cultivated across tropical and subtropical regions worldwide. One of the nutritional benefits of chayote is that it contains various vitamins, including vitamins A, B, and C (ascorbic acid). Additionally, chayote is a source of several bioactive compounds, such as alkaloids, flavonoids, saponins, and terpenoids (Daulay et al., 2021; Veigas et al., 2020). The presence of ascorbic acid in chayote extract has made it

useful as a reducing and capping agent for nanoparticle synthesis (Bhan and Golder, 2023). Chayote extract has not been explored as a corrosion inhibitor.

Tinda (*Praecitrullus fistulosus*) is a vegetable crop that belongs to the Cucurbitaceae family. It is cultivated in Asia since ancient times. It is one of the excellent plants gifted by nature, having the composition of essential constituents that are required for normal and good human health (Senger et al., 2024; Tyagi et al., 2017). *Praecitrullus fistulosus* reportedly possesses a range of bioactive compounds, including polyphenols, flavonoids, ascorbic acid, tannin, alkaloid, saponin, phytosterol, diterpenes, thiamsin, carotene, proteins, carbohydrates, and cardiac glycosides (Tiwari et al., 2020). Additionally, few studies reported that tinda fruits are rich in secondary metabolites, exhibiting the following medicinal properties: anti-inflammatory, antioxidant, antihelminthic, antidiabetic activity, and antimicrobial (Madhu et al., 2019). The presence of antioxidant compounds in tinda extracts (Madhu et al., 2019) makes it useful as a reducing and stabilizing agent for synthesizing metal ions (K. Bhardwaj et al., 2022). Madhu et al., 2022 have utilized tinda extracts to synthesize silver nanoparticles (Madhu et al., 2022), but tinda extract has not been used as a corrosion inhibitor till now.

Phaseolus lunatus is an edible legume that belongs to the Fabaceae family, spreads and adapts well to dry land, and is easily cultivated. These beans and their seeds are considered as the best source of dietary proteins and essential nutrients derived from plants, exhibiting the most abundance in amino acids like lysine (Adebo, 2023) and leucine (Seidu et al., 2015), as well as high in following fatty acids, linoleic acid (Ogunji et al., 2003), oleic acid (Ezeagu and Ibegbu, 2010), 9-Octadecenoic acid (Z)-, methyl ester (Marimuthu et al., 2014) and also contain lower amount of ascorbic acid (Ogechukwu and Ikechukwu, 2021). Recently, several studies have reported that these compounds have excellent corrosion-inhibiting ability against acidic mediums (Ameh, 2018; Hermoso-Diaz et al., 2019; Jano et al., 2014; Tran et al., 2024). However, *Phaseolus lunatus* has not been explored as a corrosion inhibitor.

Duranta erecta is a widely cultivated ornamental plant, and it has attracted people's attention due to its vibrant flowers and golden berries. It is most commonly used for landscaping, hedges, decorative, and medical purposes in several countries such as India, Bangladesh, South Africa, Indonesia, Brazil, and many others. It belongs to the Verbenaceae family. Few studies have reported that ethyl acetate and aqueous extracts of *Duranta erecta* leaves exhibited significant antimalarial activity (Patil and Hooli, 2014). Furthermore, some researchers have also found that *Duranta erecta* plant organs possess several biological activities, such as antimicrobial, antiviral, antioxidant, and antimalarial properties. The plant has been found to contain diverse classes of phytoconstituents, including flavonoids, flavonoid glycosides, iridoid glycosides, steroids, alkaloids, phenolics, terpenoids, saponins, and tannins (Subsongsang and Jiraungkoorskul, 2016). Moreover, *Duranta ereacta* leaves extracts have also been utilized to prepare AgNPs (Patel and Patel, 2022), but they are not used as corrosion inhibitors.

In the above discussion, bio-extracts of chayote, tinda, *Phaseolus lunatus, and Duranta erecta* are reported to be very rich in beneficial phytochemicals and utilized for nanomaterial synthesis and medical applications, but these bio-extracts have not been explored as corrosion inhibitor for mild steel protection against HCl.

1.7.2 Epoxy based coatings

One of the most effective industrial practices for mitigating corrosion is the application of protective coatings on metallic substrates. Epoxy coatings are widely used to protect metals and their alloys from corrosion in various industries due to their excellent corrosion resistance, mechanical strength, chemical resistance, and adhesion properties. However, these epoxy coatings become defective during prolonged exposure, resulting in the failure of desired protection (Xavier, 2021). To address this issue, extensive research has been conducted by

incorporating various nanofillers into the epoxy matrix. Among the reported nanofillers, two-dimensional graphene and its derivatives have demonstrated exceptional reinforcing properties in epoxy resin-based coatings due to their large specific surface area and exceptional impermeability. These nanofillers significantly enhance the anticorrosive, physicochemical, structural, and mechanical properties of epoxy coatings, making them far superior to pure epoxy coatings in terms of durability and performance.

In recent years, reduced graphene oxide (RGO) has been widely used in coating formulations due to its several advantages, including a higher reactive surface area and better compatibility with various organic solvents and polymer matrices compared to pristine graphene. However, RGO tends to aggregate at higher loadings, which negatively impacts the coating's performance. To overcome this limitation, RGO has been functionalized or decorated with other nanoparticles (ZnO, ZrO_2, and MoS_2) or polymers to enhance its dispersion and stability (Chen et al., 2018; Rajitha et al., 2020; Zhou et al., 2022). Among the reported nanoparticles, ZnO incorporation into epoxy coatings enhances corrosion resistance, UV resistance, antibacterial properties, and mechanical strength. It also improves anti-fouling and self-healing effects, making epoxy coatings more effective for protective applications. Binary composites of RGO facilitate its uniform distribution within polymer matrices, resulting in more durable and compact coatings with strong interfacial interactions between RGO and the polymer (Wang et al., 2021; Zhu et al., 2021). Rajitha et al. (2020) decorated the ZnO particles on RGO sheets to prepare the RGO-ZnO composite, and they found that RGO-ZnO nanocomposite in PU resin-based coatings exhibited enhanced anti-corrosive properties as compared to the individual RGO and ZnO coatings (Rajitha et al., 2020). Recently, polyaniline (PANI) has been frequently used for metal protection due to its excellent anticorrosive properties. It plays a crucial role in anti-corrosive coatings because it provides anodic protection and metal passivation through its oxidation processes (Nguyen et al., 2003; Reut et

al., 1999). Among the conducting polymers, PANI is the most suitable candidate for coating reinforcement due to its following properties: environmentally stable, simple synthesizing process, better processability, and economical. Xiao et al. (2018) have tested the anticorrosive properties of epoxy coating reinforced with binary composite (PANI-GO) and achieved significantly improved corrosion-inhibiting behavior than that of pure epoxy coating (Xiao et al., 2018). Goswami et al., (2024) have investigated the anticorrosive behavior of PANI-wrapped nitrogen-doped graphene nanocomposites coating and found that NGr-PANI-ES-8 showed the highest total impedance, but its value was decreased from 1.7×10^{15} to 2.17×10^{4} Ω cm^2 only in 7 days of immersion (Goswami et al., 2024).

There is an urgent need to develop new composite materials to enhance the anticorrosive properties of protective coatings. Previous studies have demonstrated that incorporating polyaniline (PANI) with reduced graphene oxide (RGO) or zinc oxide (ZnO) as nanofillers in an epoxy matrix significantly improves corrosion resistance (Kraljić et al., 2003; Mostafaei and Nasirpouri, 2014). However, to the best of our knowledge, ternary RGO-ZnO-PANI nanocomposite has not been explored as a filler in epoxy coatings for corrosion protection in marine environments.

1.8 Knowledge gaps

Based on the above literature review, the knowledge gap is given below.

- Bio-extracts of *Sechium edule* (chayote), *Praecitrullus fistulosus* (tinda), *Phaseolus lunatus*, and *Duranta erecta* are reported to be very rich in beneficial phytochemicals and utilized for nanomaterial synthesis and medical applications.
- However, the corrosion inhibition efficiency of these bio-extracts has not been explored for the protection of mild steel against HCl.

- ❖ PANI wrapped RGO-ZnO ternary nanocomposites can be used in organic coatings, which can significantly improve the corrosion-inhibiting properties of coatings. The ZnO decorated RGO nanosheets can effectively furnish impermeability and physical barriers, whereas uniformly grown PANI on the RGO-ZnO surface increases the path distance for corrosive species towards the steel substrate.
- ❖ However, PANI wrapped RGO-ZnO ternary composite has not been used to enhance the anticorrosive properties of epoxy coating for protecting mild steel in 3.5% NaCl.

1.9 Objectives of the work

Objective 1: A novel eco-friendly inhibitor of chayote fruit extract for mild steel corrosion in 1 M HCl: Electrochemical, weight loss studies, and the effect of temperature

Objective 2: Corrosion inhibition of mild steel by tinda (*Praecitrullus fistulosus*) fruit and peel extracts

Objective 3: Investigations on corrosion inhibition of mild steel in acid medium using *Phaseolus lunatus* peel and seed extracts

Objective 4: *Duranta erecta* fruit and leaves extracts as green corrosion inhibitors for mild steel protection in hydrochloric acid

Objective 5: Anti-corrosive behavior of a novel ternary RGO-ZnO-PANI nanocomposite reinforced epoxy coating on mild steel in the marine environment

1.10 References

Al-Amiery, A.A., Yousif, E., Isahak, W.N.R.W., Al-Azzawi, W.K., 2023. A review of inorganic corrosion inhibitors: Types, mechanisms, and applications. Tribol. Ind. 45, 313–339. https://doi.org/10.24874/ti.1456.03.23.06

Abbout, S., Chebabe, D., Zouarhi, M., Rehioui, M., Lakbaibi, Z., Hajjaji, N., 2021. Ceratonia Siliqua L seeds extract as eco-friendly corrosion inhibitor for carbon steel in 1 M HCl:

Characterization, electrochemical, surface analysis, and theoretical studies. J. Mol. Struct. 1240, 130611. https://doi.org/10.1016/j.molstruc.2021.130611

Abd El-Lateef, H.M., AAA El-Remaily, M., Khodairy, A., Sayed, M.M., Yehia, N., Khalaf, M.M., Aly, K.I., 2023. Synthesis and structure design of novel unsaturated copolyesters based on indazole moiety in the main chain with good thermal stability for catalytic activity and anti-corrosion applications. J. Mol. Struct. 1273, 134345. https://doi.org/10.1016/j.molstruc.2022.134345

Adebo, J.A., 2023. A review on the potential food application of lima beans (Phaseolus lunatus L.), an Underutilized Crop. Appl. Sci. 13, 1996. https://doi.org/10.3390/app13031996

Ahmadinia, A., Azhar, F.F., 2022. Fabrication of bi-functionalized nanocomposite coating for simultaneous improved thermal stability and corrosion protection performance based on polyaniline-reduced graphene oxide/organo-modified montmorillonite. Compos. Interfaces 29, 1161–1185. https://doi.org/10.1080/09276440.2021.2007719

Al-Amiery, A.A., Isahak, W.N.R.W., Al-Azzawi, W.K., 2023. Corrosion inhibitors: Natural and synthetic organic inhibitors. Lubricants 11, 174. https://doi.org/10.3390/lubricants11040174

Ali, A.I., Mahrous, Y.S., 2017. Corrosion inhibition of C-steel in acidic media from fruiting bodies of Melia azedarach L extract and a synergistic Ni^{2+} additive. RSC Adv. 7, 23687–23698. https://doi.org/10.1039/C7RA00111H

Ameh, E.S., Ikpeseni, S.C., 2018. Pipelines cathodic protection design methodologies for impressed current and sacrificial anode systems. Niger. J. Technol. 36, 1072. https://doi.org/10.4314/njt.v36i4.12

Ameh, P.O., 2018. Electrochemical and computational study of gum exudates from Canarium schweinfurthii as green corrosion inhibitor for mild steel in HCl solution. J. Taibah Univ. Sci. 12, 783–795. https://doi.org/10.1080/16583655.2018.1514147

Arora, P., Kumar, S., Sharma, M.K., Mathur, S.P., 2007. Corrosion inhibition of aluminium by Capparis decidua in acidic media. J. Chem. 4, 450–456. https://doi.org/10.1155/2007/487820

Bhan, C., Golder, A.K., 2023. Utilizing bioinspired AgNPs as an antibacterial agent to enhance ceramic membrane performance. J. Environ. Chem. Eng. 11, 110283. https://doi.org/10.1016/j.jece.2023.110283

Bhardwaj, K., Chopra, C., Bhardwaj, P., Dhanjal, D.S., Singh, R., Najda, A., Cruz-Martins, N., Singh, S., Sharma, R., Kuča, K., Manickam, S., 2022. Biogenic Metallic Nanoparticles

from Seed Extracts: Characteristics, Properties, and Applications. J. Nanomater. 2022, 1–22. https://doi.org/10.1155/2022/2271278

Bhardwaj, N., Sharma, P., Guo, L., Dagdag, O., Kumar, V., 2022. Molecular dynamic simulation, quantum chemical calculation and electrochemical behaviour of Punica granatum peel extract as eco-friendly corrosion inhibitor for stainless steel (SS-410) in acidic medium. J. Mol. Liq. 346, 118237. https://doi.org/10.1016/j.molliq.2021.118237

Bhardwaj, N., Sharma, P., Singh, K., Rana, D., Kumar, V., 2021. Phyllanthus emblica seed extract as corrosion inhibitor for stainless steel used in petroleum industry (SS-410) in acidic medium. Chem. Phys. Impact 3, 100038. https://doi.org/10.1016/j.chphi.2021.100038

Bijapur, K., Molahalli, V., Shetty, A., Toghan, A., De Padova, P., Hegde, G., 2023. Recent trends and progress in corrosion inhibitors and electrochemical evaluation. Appl. Sci. 13, 10107. https://doi.org/10.3390/app131810107

Buckner, C.A., Lafrenie, R.M., Dénommée, J.A., Caswell, J.M., Want, D.A., Gan, G.G., Leong, Y.C., Bee, P.C., Chin, E., Teh, A.K.H., Picco, S., Villegas, L., Tonelli, F., Merlo, M., Rigau, J., Diaz, D., Masuelli, M., Korrapati, S., Kurra, P., Puttugunta, S., Picco, S., Villegas, L., Tonelli, F., Merlo, M., Rigau, J., Diaz, D., Masuelli, M., Tascilar, M., de Jong, F.A., Verweij, J., Mathijssen, R.H.J., 2016. We are IntechOpen , the world's leading publisher of Open Access books Built by scientists , for scientists TOP 1 %. Intech 11, 13.

Chen, C., He, Y., Xiao, G., Xia, Y., Li, H., He, Z., 2018. Two-dimensional hybrid materials: MoS_2-RGO nanocomposites enhanced the barrier properties of epoxy coating. Appl. Surf. Sci. 444, 511–521. https://doi.org/10.1016/j.apsusc.2018.03.013

Chen, Z., Fadhil, A.A., Chen, T., Khadom, A.A., Fu, C., Fadhil, N.A., 2021. Green synthesis of corrosion inhibitor with biomass platform molecule: Gravimetrical, electrochemical, morphological, and theoretical investigations. J. Mol. Liq. 332, 115852. https://doi.org/10.1016/j.molliq.2021.115852

Czaban, M., 2018. Aircraft corrosion – review of corrosion processes and its effects in selected cases. Fatigue Aircr. Struct. 2018, 5–20. https://doi.org/10.2478/fas-2018-0001

Daoudi, W., El Aatiaoui, A., Falil, N., Azzouzi, M., Berisha, A., Olasunkanmi, L.O., Dagdag, O., Ebenso, E.E., Koudad, M., Aouinti, A., Loutou, M., Oussaid, A., 2022. Essential oil of Dysphania ambrosioides as a green corrosion inhibitor for mild steel in HCl solution. J. Mol. Liq. 363, 119839. https://doi.org/10.1016/j.molliq.2022.119839

Daulay, A.S., Ridwanto, Syahputra, R.A., Nafitri, A., 2021. Antioxidant activity test of chayote (Sechium edule (Jacq.) Swartz) ethanol extract using DPPH method. J. Phys. Conf. Ser. 1819, 012035. https://doi.org/10.1088/1742-6596/1819/1/012035

Perez, N. ed., 2004. Electrochemistry and corrosion science, Boston Boston, MA: Springer Us. https://doi.org/10.1007/b118420

El-Katori, E.E., Al-Mhyawi, S., 2019. Assessment of the Bassia muricata extract as a green corrosion inhibitor for aluminum in acidic solution. Green Chem. Lett. Rev. 12, 31–48. https://doi.org/10.1080/17518253.2019.1569728

Elazabawy, O.E., Attia, E.M., Shawky, N.H., Hyba, A.M., 2023. Eco-friendly orange peel extract as corrosion resistant for carbon steel's deterioration in petroleum formation water. Sci. Rep. 13, 21943. https://doi.org/10.1038/s41598-023-47916-w

Ezeagu, I.E., Ibegbu, M.D., 2010. Biochemical composition and nutritional potential of ukpa: A variety of tropical lima beans (Phaseolus lunatus) from Nigeria - A short report. Pol. J. Food Nutr. Sci. 60, 231–235.

Fakir, S.H., Kumar, K.C., Ali, H., Rawat, J., Haq Farooqi, I., 2023. Synthesis and evaluation of green corrosion inhibitor from rice husk to mitigate corrosion of carbon steel in NaCl environment. Mater. Today Proc. 82, 29–37. https://doi.org/10.1016/j.matpr.2022.11.147

Fernine, Y., Salim, R., Arrousse, N., Haldhar, R., El Hajjaji, F., Kim, S.C., Ebn Touhami, M., Taleb, M., 2022. Anti-corrosion performance of Ocimum basilicum seed extract as environmental friendly inhibitors for mild steel in HCl solution: Evaluations of electrochemical, EDX, DFT and Monte Carlo. J. Mol. Liq. 355, 118867. https://doi.org/10.1016/j.molliq.2022.118867

Finšgar, M., Jackson, J., 2014. Application of corrosion inhibitors for steels in acidic media for the oil and gas industry: A review. Corros. Sci. 86, 17–41. https://doi.org/10.1016/j.corsci.2014.04.044

Fontana, M.G., Greene, N.D., Mcdonald, D.D., 1979. Corrosion Engineering. J. Electrochem. Soc. 126, 232C-232C. https://doi.org/10.1149/1.2129187

Koch, G., Varney, J., Thompson, N., Moghissi, O., Gould, M., Payer, J., 2016. International measures of prevention, application, and economics of corrosion technologies study. Challenges Corros. NACE2016.

Golafshani, M.G., Tavakoli, H., Hosseini, S.A., Akbari, M., 2023. MD and DFT computational simulations of Caffeoylquinic derivatives as a bio-corrosion inhibitor from quince extract with experimental investigation of corrosion protection on mild steel in 1 M H_2SO_4. J.

Mol. Struct. 1275, 134701. https://doi.org/10.1016/j.molstruc.2022.134701

Goswami, R.N., Mourya, P., Saini, R., Khatri, O.P., Ray, A., 2024. Polyaniline-wrapped nitrogen-doped graphene nanocomposites as protective functional fillers in epoxy coatings for remarkable enhancement of corrosion inhibition performance. Prog. Org. Coatings 189, 108335. https://doi.org/10.1016/j.porgcoat.2024.108335

Goyal, M., Kumar, S., Bahadur, I., Verma, C., Ebenso, E.E., 2018. Organic corrosion inhibitors for industrial cleaning of ferrous and non-ferrous metals in acidic solutions: A review. J. Mol. Liq. 256, 565–573. https://doi.org/10.1016/j.molliq.2018.02.045

Gu, L., Liu, S., Zhao, H., Yu, H., 2015. Facile Preparation of water-dispersible graphene sheets stabilized by carboxylated oligoanilines and their anticorrosion coatings. ACS Appl. Mater. Interfaces 7, 17641–17648. https://doi.org/10.1021/acsami.5b05531

Guo, L., Bakri, Y. El, Yu, R., Tan, J., Essassi, E.M., 2020. Newly synthesized triazolopyrimidine derivative as an inhibitor for mild steel corrosion in HCl medium: an experimental and in silico study. J. Mater. Res. Technol. 9, 6568–6578. https://doi.org/10.1016/j.jmrt.2020.04.044

Guo, R., Wang, J., Wang, H., Fei, G., Wang, C., Sun, L., Wallace, G.G., 2019. Engineering the poly(vinyl alcohol)-polyaniline colloids for high-performance waterborne alkyd anticorrosion coating. Appl. Surf. Sci. 481, 960–971. https://doi.org/10.1016/j.apsusc.2019.03.078

Hamdani, I., Mokhtari, O., Lamri, L., Zaoui, S., Bouknana, D., Aouniti, A., Berrabah, M., Bouyanzer, A., Hammouti, B., 2018. Bibliographic review on the problem of corrosion and their protection by green inhibitors. Arab. J. Chem. Environ. Res. 05, 101–123.

Hanini, K., Merzoug, B., Boudiba, S., Selatnia, I., Laouer, H., Akkal, S., 2019. Influence of different polyphenol extracts of Taxus baccata on the corrosion process and their effect as additives in electrodeposition. Sustain. Chem. Pharm. 14, 100189. https://doi.org/10.1016/j.scp.2019.100189

Hansson, C. M., 2011. The Impact of Corrosion on Society. Metall. Mater. Trans. A 42, 2952–2962. https://doi.org/10.1007/s11661-011-0703-2

Haque, J., Srivastava, V., Quraishi, M.A., Singh Chauhan, D., Lgaz, H., Chung, I.-M., 2020. Polar group substituted imidazolium zwitterions as eco-friendly corrosion inhibitors for mild steel in acid solution. Corros. Sci. 172, 108665. https://doi.org/10.1016/j.corsci.2020.108665

Hart, E., 2023. Corrosion inhibitors—principles, mechanisms, and applications, in: Corrosion

Inhibitors: Key topics in materials science and engineering. ASM International, 1–27. https://doi.org/10.31399/asm.tb.ciktmse.t56080001

Hermoso-Diaz, I.A., Foroozan, A.E., Flores-De los Rios, J.P., Landeros-Martinez, L.L., Porcayo-Calderon, J., Gonzalez-Rodriguez, J.G., 2019. Electrochemical and quantum chemical assessment of linoleic acid as a corrosion inhibitor for carbon steel in sulfuric acid solution. J. Mol. Struct. 1197, 535–546. https://doi.org/10.1016/j.molstruc.2019.07.085

Ikeuba, A.I., Faithpraise, F.O., Nwokolo, K.I., Umo, F.E., Echem, O.C., Ibrahim, A.T., Edet, H.O., Ita, B.I., Okafor, P.C., Asogwa, F.C., Amajama, J., Iwuji, P.C., 2024. A combined electrochemical and DFT investigation of ornidazole as a benign anti-corrosion agent for carbon steel materials in acidizing environments. Results Mater. 21, 100542. https://doi.org/10.1016/j.rinma.2024.100542

Ikeuba, A.I., Ntibi, J.E., Okafor, P.C., Ita, B.I., Agobi, A.U., Asogwa, F.C., Omang, B.J., Eno, E.A., Loius, H., Adalikwu, S.A., Abiola, B.A., Abeng, F.E., Abang, N.A., 2023. Kinetic and thermodynamic evaluation of azithromycin as a green corrosion inhibitor during acid cleaning process of mild steel using an experimental and theoretical approach. Results Chem. 5, 100909. https://doi.org/10.1016/j.rechem.2023.100909

Jano, A., Lame, A., Kokalari, E., 2014. Lysine as corrosion inhibitor for low alloy carbon steel in acidic media. Analele Univ. “Ovidius” Constanta - Ser. Chim. 25, 11–14. https://doi.org/10.2478/auoc-2014-0002

Jiang, F., Zhao, W., Wu, Yangmin, Wu, Yinghao, Liu, G., Dong, J., Zhou, K., 2019. A polyethyleneimine-grafted graphene oxide hybrid nanomaterial: Synthesis and anti-corrosion applications. Appl. Surf. Sci. 479, 963–973. https://doi.org/10.1016/j.apsusc.2019.02.193

K O, S., Prasad, A.R., Garvasis, J., Basheer, S.M., Joseph, A., 2019. Stearic acid grafted chitosan/epoxy blend surface coating for prolonged protection of mild steel in saline environment. J. Adhes. Sci. Technol. 33, 2250–2264. https://doi.org/10.1080/01694243.2019.1637170

Khatoon, H., Iqbal, S., Ahmad, S., 2021. Progress in organic coatings covalently functionalized ethylene diamine modified graphene oxide poly-paraphenylene diamine dispersed polyurethane anticorrosive nanocomposite coatings. Prog. Org. Coatings 150, 105966. https://doi.org/10.1016/j.porgcoat.2020.105966

Kraljić, M., Mandić, Z., Duić, L., 2003. Inhibition of steel corrosion by polyaniline coatings.

Corros. Sci. 45, 181–198. https://doi.org/10.1016/S0010-938X(02)00083-5

Landolt, D., 2007. Corrosion and surface chemistry of metals. Choice Rev. Online 45, 45–0897. https://doi.org/10.1201/9781439807880

Lee, H.S., Saraswathy, V., Kwon, S.J., Karthick, S., 2018. Corrosion inhibitors for reinforced concrete: a review, in: Corrosion inhibitors, principles and recent applications. InTech. 95-120, https://doi.org/10.5772/intechopen.72572

Li, W., Tian, H., Hou, B., 2012. Corrosion performance of epoxy coatings modified by nanoparticulate SiO_2. Mater. Corros. 63, 44–53. https://doi.org/10.1002/maco.200905620

Lin, B., Shao, J., Xu, Y., Lai, Y., Zhao, Z., 2021. Adsorption and corrosion of renewable inhibitor of Pomelo peel extract for mild steel in phosphoric acid solution. Arab. J. Chem. 14, 103114. https://doi.org/10.1016/j.arabjc.2021.103114

Liu, Z., Zhu, R., Zhang, X., Zhu, H., 2022. Improving anticorrosion performance of epoxy coating by hybrids of rGO and g-C_3N_4 nanosheets. J. Coatings Technol. Res. 19, 1219–1232. https://doi.org/10.1007/s11998-021-00603-9

Machado Fernandes, C., Coutinho, M.S., Leite, M.C., Martins, V., Batista, M.P., Faro, L. V., Al-Rashdi, A.A., Silva, J.C.M., Batalha, P.N., Lgaz, H., Ponzio, E.A., 2024. Green-synthetized β-amino-α-carbethoxy ethyl acrylates as corrosion inhibitors for mild steel in acid media: Experimental performance evaluation and atomic/molecular-level modeling. Inorg. Chem. Commun. 159, 111722. https://doi.org/10.1016/j.inoche.2023.111722

Madhu, C.S., Balaji, K.S., Shankar, J., Sunil Gowda, S.N., Sharada, A.C., 2022. Biofabrication of silver nanoparticles using Praecitrullus fistulosus fruit extract exhibits in vitro antibacterial and anticancer activity. J. Drug Deliv. Sci. Technol. 72, 103329. https://doi.org/10.1016/j.jddst.2022.103329

Madhu, C.S., Balaji, K.S., Sharada, A.C., 2019. GC/MS profile, DNA protectant and hepatoprotective effects of Praecitrullus fistulosus fruit methanol extract. Biocatal. Agric. Biotechnol. 21, 101272. https://doi.org/10.1016/j.bcab.2019.101272

Mahmoud, W.M., Elfiky, D., Robaa, S.M., Elnawawy, M.S., Yousef, S.M., 2021. Effect of atomic oxygen on LEO CubeSat. Int. J. Aeronaut. Sp. Sci. 22, 726–733. https://doi.org/10.1007/s42405-020-00336-w

Marimuthu, K., Nagaraj, N., Ravi, D., 2014. GC-MS analysis of phytochemicals, fatty acids and antimicrobial potency of dry christmas lima beans. Int. J. Pharm. Sci. Rev. Res. 27, 63–66.

Mbamalu, E.E., Chinedu, A.P., 2023. Assessment of the Corrosion inhibitory potentials of

Chromolaena odorata leaf extract on mild steel in hydrogen chloride acid environment. Moroccan J. Chem. 11, 188–204. https://doi.org/10.48317/IMIST.PRSM/morjchem-v10i3.30521

Mostafaei, A., Nasirpouri, F., 2014. Epoxy/polyaniline–ZnO nanorods hybrid nanocomposite coatings: Synthesis, characterization and corrosion protection performance of conducting paints. Prog. Org. Coatings 77, 146–159. https://doi.org/10.1016/j.porgcoat.2013.08.015

Mourya, P., Goswami, R.N., Saini, R., Ray, A., Khatri, O.P., 2024. Epoxy coating reinforced with graphene-PANI nanocomposites for enhancement of corrosion-resistance performance of mild steel in saline water. Colloids Surfaces A Physicochem. Eng. Asp. 687, 133500. https://doi.org/10.1016/j.colsurfa.2024.133500

Munis, A., Zhao, T., Zheng, M., Rehman, A.U., Wang, F., 2020. A newly synthesized green corrosion inhibitor imidazoline derivative for carbon steel in 7.5% NH_4Cl solution. Sustain. Chem. Pharm. 16, 100258. https://doi.org/10.1016/j.scp.2020.100258

News, C., 2019. Corrosion News. Mater. Corros. 70, 1917–1924. https://doi.org/10.1002/maco.201970104

Nguyen, T.D., Keddam, M., Takenouti, H., 2003. Device to study electrochemistry of iron at a defect of protective coating of electronic conducting polymer. Electrochem. Solid-State Lett. 6, B25. https://doi.org/10.1149/1.1582252

Njoku, C.N., Enendu, B.N., Okechukwu, S.J., Igboko, N., Anyikwa, S.O., Ikeuba, A.I., Onyeachu, I.B., Etim, I.-I.N., Njoku, D.I., 2023. Review on anti-corrosion properties of expired antihypertensive drugs as benign corrosion inhibitors for metallic materials in various environments. Results Eng. 18, 101183. https://doi.org/10.1016/j.rineng.2023.101183

Odewunmi, N.A., Umoren, S.A., Gasem, Z.M., 2015. Watermelon waste products as green corrosion inhibitors for mild steel in HCl solution. J. Environ. Chem. Eng. 3, 286–296. https://doi.org/10.1016/j.jece.2014.10.014

Ogechukwu, C.O., Ikechukwu, J.O., 2021. Effect of heat processing treatments on the chemical composition and functional properties of lima bean (Phaseolus lunatus) flour. Am. J. Food Sci. Nutr. 1, 14–24. https://doi.org/10.47672/ajfsn.261

Ogunji, J.O., Wirth, M., Osuigwe, D.I., 2003. Nutrient composition of some tropical legumes capable of substituting fish meal in fish diets. J. Agric. Rural Dev. Trop. Subtrop. 104, 143–148.

Onukwulia, O.D., Omotioma, M., 2019. Study of bitter leaves extract as inhibitive agent in

HCL medium for the treatment of mild steel through pickling. Port. Electrochim. Acta 37, 115–121. https://doi.org/10.4152/pea.201902115

Oshomogho, F.O., Akhihiero, T.E., Edokpayi, O., Ossai, J.E., 2020. Green corrosion inhibition of mild steel using Prunus Dulcis seeds extract in an acidic medium. Glob. J. Pure Appl. Sci. 26, 171–178. https://doi.org/10.4314/gjpas.v26i2.9

Patel, S., Patel, N.K., 2022. Biogenic synthesis of silver nanoparticles and investigation of antibacterial activity from leaves of duranta erecta. Egypt. J. Agric. Res. 101,4-12. https://doi.org/10.21608/ejar.2022.151716.1252

Patil, B.M., Hooli, A.A., 2014. Green synthesis of silver nanoparticles by duranta repens leaves and their antimicrobial efficacy. J. Nano Technology & Its Applications. 14, 13–18.

Pedeferri, P., 2018. Statistical analysis of corrosion data, in: Corrosion science and engineering. Engineering Materials. Springer, Cham. 679–696. https://doi.org/10.1007/978-3-319-97625-9_30

Petrovic, Z., 2016. Catastrophes caused by corrosion. Vojnoteh. Glas. 64, 1048–1064. https://doi.org/10.5937/vojtehg64-10388

Pourhashem, S., Vaezi, M.R., Rashidi, A., 2017. Investigating the effect of SiO_2-graphene oxide hybrid as inorganic nanofiller on corrosion protection properties of epoxy coatings. Surf. Coatings Technol. 311, 282–294. https://doi.org/10.1016/j.surfcoat.2017.01.013

Pourzarghan, V., Fazeli-Nasab, B., 2021. The use of Robinia pseudoacacia L fruit extract as a green corrosion inhibitor in the protection of copper-based objects. Herit. Sci. 9, 75. https://doi.org/10.1186/s40494-021-00545-w

Qiang, Y., Zhang, S., Tan, B., Chen, S., 2018. Evaluation of Ginkgo leaf extract as an eco-friendly corrosion inhibitor of X70 steel in HCl solution. Corros. Sci. 133, 6–16. https://doi.org/10.1016/j.corsci.2018.01.008

Rajabi, M., Rashed, G.R., Zaarei, D., 2015. Assessment of graphene oxide/epoxy nanocomposite as corrosion resistance coating on carbon steel. Corros. Eng. Sci. Technol. 50, 509–516. https://doi.org/10.1179/1743278214Y.0000000232

Rajendran, A., Karthikeyan, C., 2012. The inhibitive effect of extract of flowers of Cassia auriculata in 2 m hcl on the corrosion of aluminium and mild steel. Int. J. Plant Res. 2, 9–14. https://doi.org/10.5923/j.plant.20120201.02

Rajitha, K., Mohana, K.N.S., Hegde, M.B., Nayak, S.R., Swamy, N.K., 2020. Fabrication of ZnO/rGO and ZnO/MWCNT nanohybrids to reinforce the anticorrosion performance of polyurethane coating. FlatChem 24, 100208. https://doi.org/10.1016/j.flatc.2020.100208

Ramezanzadeh, M., Bahlakeh, G., Sanaei, Z., Ramezanzadeh, B., 2019. Corrosion inhibition of mild steel in 1 M HCl solution by ethanolic extract of eco-friendly Mangifera indica (mango) leaves: Electrochemical, molecular dynamics, Monte Carlo and ab initio study. Appl. Surf. Sci. 463, 1058–1077. https://doi.org/10.1016/j.apsusc.2018.09.029

Rani, A.T.J., Thomas, A., Arshad, M., Joseph, A., 2022. The influence of aqueous and alcoholic extracts of Garcinia cambogia fruit rind in the management of mild steel corrosion in hydrochloric acid: Theoretical and electroanalytical studies. J. Mol. Liq. 346, 117873. https://doi.org/10.1016/j.molliq.2021.117873

Reut, J., Öpik, A., Idla, K., 1999. Corrosion behavior of polypyrrole coated mild steel. Synth. Met. 102, 1392–1393. https://doi.org/10.1016/S0379-6779(98)01036-4

Revie, R.W., Uhlig, H.H., 2008. Corrosion and corrosion control: An introduction to corrosion science and engineering: Fourth edition. Wiley.1-431, https://doi.org/10.1002/9780470277270

Roberge, P.R., 2000. Handbook of corrosion engineering. Choice Rev. Online 37, 37-5122-37–5122. https://doi.org/10.5860/choice.37-5122

Rocha, J.C. da, Gomes, J.A. da C.P., D'Elia, E., 2014. Aqueous extracts of mango and orange peel as green inhibitors for carbon steel in hydrochloric acid solution. Mater. Res. 17, 1581–1587. https://doi.org/10.1590/1516-1439.285014

Saeed, M.T., Saleem, M., Usmani, S., Malik, I.A., Al-Shammari, F.A., Deen, K.M., 2019. Corrosion inhibition of mild steel in 1 M HCl by sweet melon peel extract. J. King Saud Univ. - Sci. 31, 1344–1351. https://doi.org/10.1016/j.jksus.2019.01.013

Sanaei, Z., Ramezanzadeh, M., Bahlakeh, G., Ramezanzadeh, B., 2019. Use of Rosa canina fruit extract as a green corrosion inhibitor for mild steel in 1 M HCl solution: A complementary experimental, molecular dynamics and quantum mechanics investigation. J. Ind. Eng. Chem. 69, 18–31. https://doi.org/10.1016/j.jiec.2018.09.013

Seidu, K.T., Osundahunsi, O.F., Olaleye, M.T., Oluwalana, I.B., 2015. Amino acid composition, mineral contents and protein solubility of some lima bean (Phaseolus lunatus l. Walp) seeds coat. Food Res. Int. 73, 130–134. https://doi.org/10.1016/j.foodres.2015.03.034

Senger, S.S., Singh, A., Jha, M., Jain, D.K., 2024. Phytochemical investigation and evaluation of antihyperglycemic activity of Praecitrullus fistulosus fruits. J. Drug Deliv. Ther. 14, 66–76. https://doi.org/10.22270/jddt.v14i2.6332

Shang, Z., Zhu, J., 2021. Overview on plant extracts as green corrosion inhibitors in the oil and

gas fields. J. Mater. Res. Technol. 15, 5078–5094. https://doi.org/10.1016/j.jmrt.2021.10.095

Shehata, O.S., Korshed, L.A., Attia, A., 2018. Green corrosion inhibitors, past, present, and future, in: Corrosion inhibitors, principles and recent applications. InTech, pp. 121-142. https://doi.org/10.5772/intechopen.72753

Singh, A., Lin, Y., Liu, W., Yu, S., Pan, J., Ren, C., Kuanhai, D., 2014. Plant derived cationic dye as an effective corrosion inhibitor for 7075 aluminum alloy in 3.5% NaCl solution. J. Ind. Eng. Chem. 20, 4276–4285. https://doi.org/10.1016/j.jiec.2014.01.033

Solovyeva, V.A., Almuhammadi, K.H., Badeghaish, W.O., 2023. Current downhole corrosion control solutions and trends in the oil and gas industry: A Review. Materials (Basel). 16, 1795. https://doi.org/10.3390/ma16051795

Subsongsang, R., Jiraungkoorskul, W., 2016. An updated review on phytochemical properties of "Golden Dewdrop" Duranta erecta. Pharmacogn. Rev. 10, 115. https://doi.org/10.4103/0973-7847.194042

Tan, B., Xiang, B., Zhang, S., Qiang, Y., Xu, L., Chen, S., He, J., 2021. Papaya leaves extract as a novel eco-friendly corrosion inhibitor for Cu in H_2SO_4 medium. J. Colloid Interface Sci. 582, 918–931. https://doi.org/10.1016/j.jcis.2020.08.093

Tiwari, A., Tyagi, C.., Pandey, H., Shah, S.K., 2020. Pharmacological modeling and study for antidiabetic activity of praecitrullus fistulosus leaves extracts. J. Drug Deliv. Ther. 10, 13–16. https://doi.org/10.22270/jddt.v10i4-s.4276

Tran, T.T.H., Gichovi, J., Commane, J., Podlaha, E.J., Seo, J., 2024. Examining amino acids as environmentally friendly corrosion inhibitors for Cu and Co chemical mechanical planarization. J. Environ. Chem. Eng. 12, 113669. https://doi.org/10.1016/j.jece.2024.113669

Tyagi, N., Sharma, G.N., Shrivastava, B., 2017. Phytochemical and pharmacological profile of praecitrullus fistulosus: An Overview. Bimon. Publ. Sci. J. 2, 29–35.

Udoh, I.I., Ekerenam, O.O., Daniel, E.F., Ikeuba, A.I., Njoku, D.I., Kolawole, S.K., Etim, I.-I.N., Emori, W., Njoku, C.N., Etim, I.P., Uzoma, P.C., 2024. Developments in anticorrosive organic coatings modulated by nano/microcontainers with porous matrices. Adv. Colloid Interface Sci. 330, 103209. https://doi.org/10.1016/j.cis.2024.103209

Umoren, S.A., Obot, I.B., Gasem, Z.M., 2015. Adsorption and corrosion inhibition characteristics of strawberry fruit extract at steel/acids interfaces: experimental and theoretical approaches. Ionics (Kiel). 21, 1171–1186. https://doi.org/10.1007/s11581-

014-1280-3

Veigas, G.J., Bhattacharjee, A., Hegde, K., Shabaraya, A.R., 2020. A brief review on sechium edule. Int. J. Pharm. Sci. Rev. Res. 65, 165–168. https://doi.org/10.47583/ijpsrr.2020.v65i02.026

Verma, C., Al-Moubaraki, A.H., Alfantazi, A., Rhee, K.Y., 2024. Heterocyclic amino acids-based green and sustainable corrosion inhibitors: Adsorption, bonding and corrosion control. J. Clean. Prod. 446, 141186. https://doi.org/10.1016/j.jclepro.2024.141186

Verma, C., Ebenso, E.E., Quraishi, M.A., 2017. Ionic liquids as green and sustainable corrosion inhibitors for metals and alloys: An overview. J. Mol. Liq. 233, 403–414. https://doi.org/10.1016/j.molliq.2017.02.111

Wang, H., Duan, Y., Ma, X., Wang, C., Fei, G., Ma, Y., He, Y., Sun, L., Wallace, G.G., 2021. Polyisocyanate bridged environmental graphene/epoxy nanocomposite coatings with excellent anticorrosion performance. Prog. Org. Coatings 153. https://doi.org/10.1016/j.porgcoat.2021.106167

Wang, Q., Liu, L., Zhang, Q., Wu, X., Zheng, H., Gao, P., Zeng, G., Yan, Z., Sun, Y., Li, Z., Li, X., 2022. Insight into the anti–corrosion performance of Artemisia argyi leaves extract as eco–friendly corrosion inhibitor for carbon steel in HCl medium. Sustain. Chem. Pharm. 27, 100710. https://doi.org/10.1016/j.scp.2022.100710

Xavier, J.R., 2021. Electrochemical and dynamic mechanical studies of newly synthesized polyurethane/SiO_2-Al_2O_3 mixed oxide nanocomposite coated steel immersed in 3.5% NaCl solution. Surfaces and Interfaces 22, 100848. https://doi.org/10.1016/j.surfin.2020.100848

Xavier, J.R., Vinodhini, S.P., Raja Beryl, J., 2024. Anti-corrosion and flame-retardant properties of environmentally benign smart functionalized WS_2/rGO in epoxy coatings for enhanced steel structural protection in natural seawater. Mater. Today Commun. 38, 107842. https://doi.org/10.1016/j.mtcomm.2023.107842

Xiao, F., Qian, C., Guo, M., Wang, J., Yan, X., Li, H., Yue, L., 2018. Anticorrosive durability of zinc-based waterborne coatings enhanced by highly dispersed and conductive polyaniline/graphene oxide composite. Prog. Org. Coatings 125, 79–88. https://doi.org/10.1016/j.porgcoat.2018.08.027

Zehra, B.F., Said, A., Eddine, H.M., Hamid, E., Najat, H., Rachid, N., Toumert, L.I., 2022. Crataegus oxyacantha leaves extract for carbon steel protection against corrosion in 1M HCl: Characterization, electrochemical, theoretical research, and surface analysis. J. Mol.

Struct. 1259, 132737. https://doi.org/10.1016/j.molstruc.2022.132737

Zhang, Q.H., Hou, B.S., Li, Y.Y., Zhu, G.Y., Lei, Y., Wang, X., Liu, H.F., Zhang, G.A., 2021. Dextran derivatives as highly efficient green corrosion inhibitors for carbon steel in CO_2-saturated oilfield produced water: Experimental and theoretical approaches. Chem. Eng. J. 424, 130519. https://doi.org/10.1016/j.cej.2021.130519

Zhao, Y., Liu, F., Zhao, Z., Bai, P., Ma, Y., Alhadhrami, A., Mersal, G.A.M., Lin, Z., Ibrahim, M.M., El-Bahy, Z.M., 2022. Direct ink printing reduced graphene oxide/KCu_7S_4 electrodes for high-performance supercapacitors. Adv. Compos. Hybrid Mater. 5, 1516–1526. https://doi.org/10.1007/s42114-022-00488-1

Zhou, S., Yan, J., Yan, H., Zhang, Y., Huang, J., Zhao, G., Liu, Y., 2022. ZrO_2-anchored rGO nanohybrid for simultaneously enhancing the wear resistance and anticorrosion performance of multifunctional epoxy coatings. Prog. Org. Coatings 166, 106795. https://doi.org/10.1016/j.porgcoat.2022.106795

Zhu, L., Feng, C., Cao, Y., 2019. Corrosion behavior of epoxy composite coatings reinforced with reduced graphene oxide nanosheets in the high salinity environments. Appl. Surf. Sci. 493, 889–896. https://doi.org/10.1016/j.apsusc.2019.06.271

Zhu, X., Zhao, H., Wang, L., Xue, Q., 2021. Bioinspired ultrathin graphene nanosheets sandwiched between epoxy layers for high performance of anticorrosion coatings. Chem. Eng. J. 410, 128301. https://doi.org/10.1016/j.cej.2020.128301

Chapter 2:

Materials and methods

Materials and methods

This chapter presents all the reagents and experimental methods used to synthesize, characterize, and determine the inhibition efficiency of bio-extracts (green corrosion inhibitors) and epoxy-based coatings. To complete this work, the experimental section is systematically arranged in following steps: (i) Preparation and characterization of green corrosion inhibitors, (ii) preparation and characterization of nanocomposite materials and their coatings, (iii) preparation of working electrode, (iv) fabrication of electrochemical cell and setup, (v) performing the weight loss and electrochemical analysis to study the corrosion inhibiting behavior of green corrosion inhibitors, and (vi) performing the electrochemical and salt spray analysis to study the anticorrosive behavior of nanocomposite coating.

2.1 Materials

2,6 Dichlorophenol indophenol sodium salt indicator ($C_{12}H_6C_{l2}NNaO_2.2H_2O$, 98%, CAS: 620-45-1) was purchased from Ms. Sisco Research Laboratories Pvt. Ltd., India. Hydrochloric acid (HCl, 37%, CAS: 7647-01-0), ascorbic acid ($C_6H_8O_6$, 99%, CAS: 50-81-7), sodium hydroxide (NaOH, 99%, CAS: 1310-73-2), methanol (CH_3OH, 99.8 %, CAS: 67-56-1), acetone (CH_3COCH_3, 99.0%, CAS: 67-64-1), potassium chloride (KCl, 99.5%, CAS: 7447-40-7), aniline ($C_6H_5NH_2$, ≥ 99%, CAS: 62-53-3), ethanol (C_2H_5OH, 98%, CAS no. 64-17-5), , sulphuric acid (H_2SO_4, 98%, CAS: 7664-93-9) were purchased from Ms. Merck India. 4,4′-Diaminodiphenyl sulfone ($C_{12}H_{12}N_2O_2S$, ≥97.0%, CAS: 80-08-0), 1-butyl-3-methylimidazolium acetate, bisphenol A diglycidyl ether ($C_{21}H_{24}O_4$, CAS: 1675-54-3), graphite power with particle size < 20 µm (CAS: 7782-42-5), were purchased from Mr. Sigma Aldrich, India. Hydrogen peroxide (H_2O_2, 30%, CAS: 7722-84-1), potassium permanganate ($KMnO_4$, 99%, CAS: 7722-64-7), hydrazine hydrate (N_2H_4, 80%, CAS: 10217-52-4) were purchased from Ms. Loba Chemie Pvt. Ltd, India. Zinc acetate dihydrate ($Zn(CH_3COO)_2.2H_2O$, 97%, CAS: 5970-45-6) was purchased from Ms. Hi Media Laboratories Pvt. Ltd, India. Ammonium peroxydisulfate ($(NH_4)_2S_2O_8$, 98%, CAS: 7727-54-0) was purchased from Ms. Thermo Fisher Scientific India Pvt. Ltd, India. Ag/AgCl reference and platinum wire counter electrodes were purchased from M/s. Metrohm, India. Mild steel plate (120 × 120 × 5 mm^3) was purchased from Ms. Aries Engineers, Mumbai, India. Emery papers (grade from 220 to 2000), nylon cloth, and lavigated alumina paste (Grade-I) were purchased from Ms. Metalart Graphy Ghaziabad, India. Deionized (DI) water (Millipore unit, conductivity: 0.055 µS, Elix-3, USA) was used to prepare reagent solutions.

2.2 Methods

To complete this research, the experimentation section was systematically discussed in the following steps:

- Preparation and characterization of green corrosion inhibitors
- Preparation and characterization of nanocomposite materials and their coatings
- Preparation of working electrodes
- Fabrication of electrochemical cells and setup
- Performing the weight loss and electrochemical analysis to study the corrosion-inhibiting behavior of green corrosion inhibitors
- Performing the electrochemical and salt spray analysis to study the anticorrosive behavior of nanocomposite coating.

2.2.1 Preparation of green corrosion inhibitor

2.2.1.1 *Sechium edule* (chayote) extracts

Sechium edule (chayote) fruits were bought from the Amingaon market near the Indian Institute of Technology Guwahati (Latitude: 26.190 and Longitude: 91.693), Assam, India. The fruits were first washed with tap water and then with distilled water. After that, the peel was removed, the fruits were cut into small pieces (10 mm × 10 mm × 10 mm), and 75 g of fruit pieces were added to 100 mL distilled water in four conical flasks of 250 mL (Chowdhury et al., 2021). Then pH of the mixtures was carefully adjusted to 3, 5, 7, and 9 by slowly adding HCl and NaOH stock solutions, and they were heated at 90 ± 2 °C for 12 h. The mixtures were set to cool down to room temperature and then filtered using Prefilter AP25, Ms. Millipore, India. The chayote extracts were stored in an airtight container at – 4 °C. The same procedure was used to prepare chayote extract (CE, original pH 5.2) in distilled water. The schematic preparation of the chayote extracts is illustrated in Fig. 2.1.

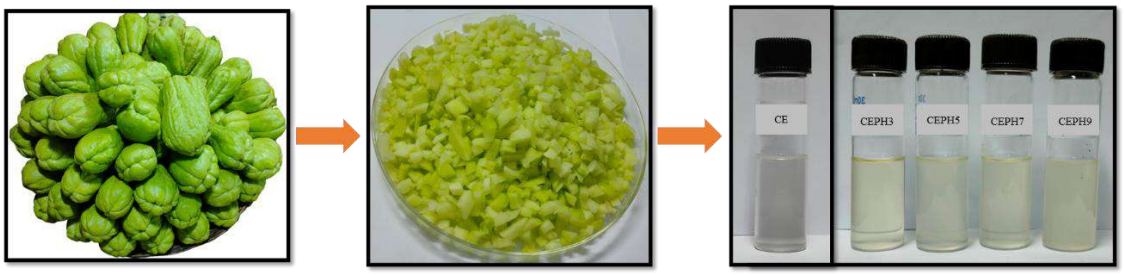

Fig. 2.1 Block diagram of chayote extract preparation.

2.2.1.2 *Praecitrullus fistulosus* (tinda) fruit and peel extracts

Praecitrullus fistulosus (tinda) fruits were purchased from the vegetable shop in Guwahati (26.1925 Latitude and 91.7317 Longitude) in Assam, India. These fruits were cleaned several times with tap water, followed by distilled water, the peel was removed and collected in a petri dish, and the fruits were sliced and dried under the shade for 3 days. After that, dried fruit pieces were ground into powder. 7.5 g of powder of tinda fruit was kept in a thimble, and glass pot was filled with methanol (150 mL). The solvent (methanol) was heated to its boiling point to reflux. Methanol vapor reaches the distillation section and then condenses in the condenser. These condensed vapors were collected in the Soxhlet chamber, and their amount increased with time. This chamber was automatically emptied by a sidearm, and the methanol was returned to the distillation pot. These cycles were repeated for a period of 2 h. After that, methanol was removed by using a rotary vacuum evaporator. The residue was collected in a petri plate and dried in a vacuum oven to further evaporate the methanol. After evaporation, dried material was collected and stored at -4 ℃ (Ishnava and Patel, 2020). The schematic diagram for tinda fruit extract (TFE) preparation is shown in Fig. 2.2. Similar process was used to prepare tinda peel extract (TPE). These extracts (TPE and TFE) were separately used to prepare the stock solutions of 500 mg L^{-1} concentration in 1 M HCl, which were further diluted by adding 1 M HCl to make several solutions of 50, 100, 150, 200, and 250 mg L^{-1}

concentrations. These extracts (TPE and TFE) were used as green corrosion inhibitors to protect the immersed mild steel in 1 M HCl.

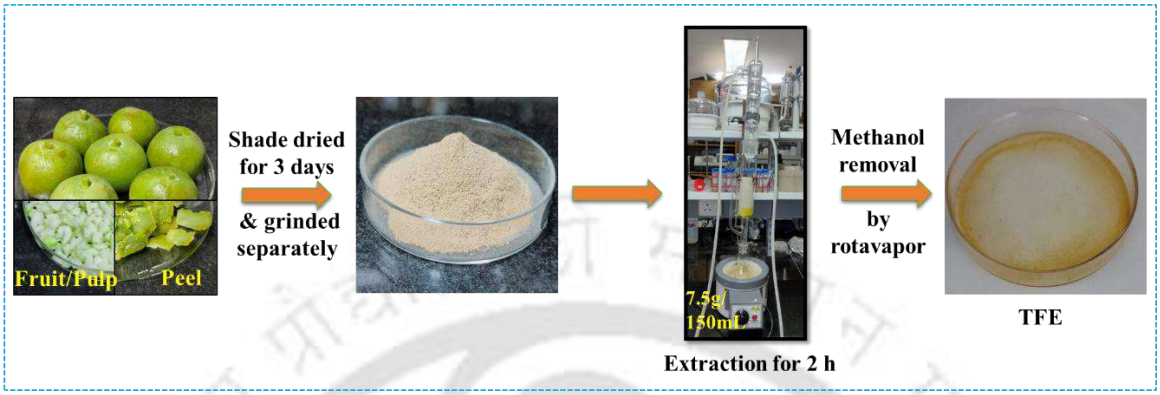

Fig. 2.2 Block diagram of TFE preparation.

2.2.1.3 *Phaseolus lunatus* (lima bean) peel and seed extracts

Phaseolus lunatus were purchased from the local market of IIT Guwahati (Latitude: 26.190 and Longitude: 91.693), Assam, India. *Phaseolus lunatus* were cleaned several times with tap water, followed by DI water to remove the dirt. *Phaseolus lunatus* peel was separated from the seeds, and both were dried at 50 ℃ for 48 h and ground separately. A 10 g of powdered *Phaseolus lunatus* peel was extracted with 30 mL of ethanol overnight in a shaker at room temperature, and the extract was filtered using Prefilter AP25 (Ms. Millipore, India). The extract was concentrated by a rotary evaporator, and the final material was taken over a petri dish and kept in a vacuum oven for further evaporation of ethanol. After evaporation, dried material (*Phaseolus lunatus* peel extract, PLPE) was collected and stored at -4 ℃. The same procedure was utilized to prepare the *Phaseolus lunatus* seed extract (PLSE). The extraction yields of PLPE and PLSE were around 17.25 % and 20.33 % respectively. A typical schematic diagram for the preparation of PLPE is shown in Fig. 2.3. A required amount of these extracts (PLPE and PLSE) was separately added to 1 M HCl solution for the preparation of the stock

solution with a concentration of 500 mg L^{-1}. Furthermore, this stock solution was diluted by adding a sufficient amount of 1 M HCl to prepare several solutions with different doses (0, 50, 100, 150, 200, 250 mgL^{-1}) of PLPE and PLSE.

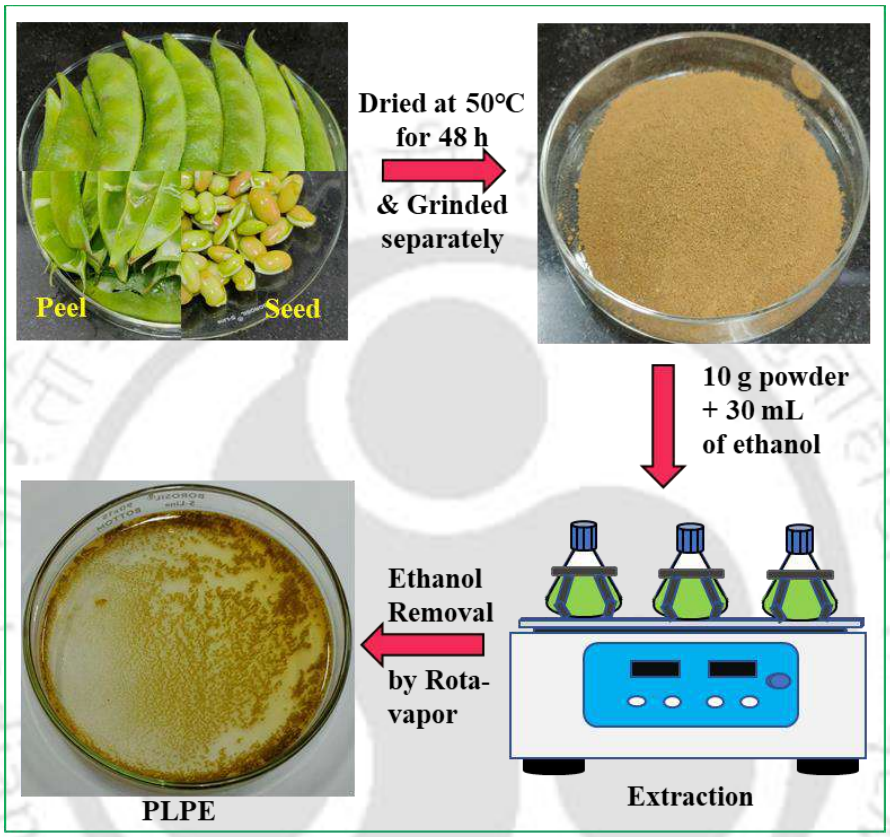

Fig. 2.3 Schematic diagram for the preparation of PLPE and the same procedure is used for PLSE.

2.2.1.4 *Duranta erecta* fruit and leaves extracts

Duranta erecta plant organs, namely fruits and leaves, were collected from the IIT Guwahati campus and washed several times with tap water. These fruits and leaves were separately dried in the shade for 4 weeks. The dried plant materials were roughly ground into powder with the help of a grinder. 15 g of the powder was extracted with 50% ethanol at room temperature for 48 h on an orbital shaker. The above mixtures were separated using a

centrifuge, and each supernatant was evaporated under vacuum in a rotary evaporator. Final materials were taken over a petri dish separately, and they were vacuum-dried for further ethanol evaporation. Dried materials (*Duranta erecta* fruit extract (DEFE) and *Duranta erecta* leaves extract (DELE)) were stored in airtight containers at -4 ℃. Fig. 2.4 shows the schematic diagram for the preparation of DEFE, and a similar processor was used for the preparation of DELE.

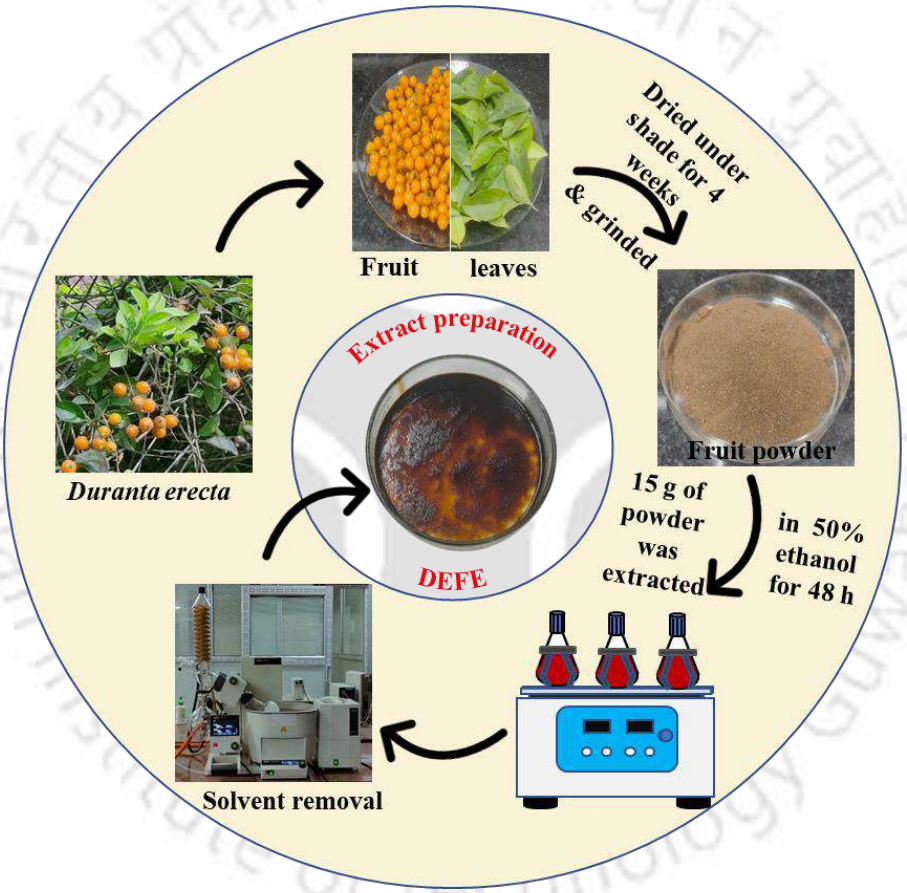

Fig. 2.4 Schematic diagram for the preparation of DEFE.

2.2.2 Characterizations of inhibitors

Prepared tinda, *Phaseolus lunatus,* and *Duranta erecta* extracts were analyzed by liquid chromatography-mass spectrometry (6410 Triple Quadrupole LC-MS, Agilent Technologies, California, USA) to identify the main compounds in these extracts. Mass spectrums were

recorded in the m/z range from 50 to 350. Available functional groups of several compounds in chayote, tinda, *Phaseolus lunatus*, and *Duranta erecta* extracts were analyzed and confirmed by Fourier transform infrared spectroscopy (FTIR) analysis. FTIR spectra were captured within the wavenumber range of 500 to 4000 cm^{-1} using the IR affinity-1; (Shimadzu, Japan).

2.2.3 Preparation of nanocomposite materials and their coatings

2.2.3.1 Preparation of GO nanosheets

Graphene oxide nanosheets (GO) were prepared by the chemical oxidation of graphite powder. 1 g of graphite powder was added to 100 mL of 98% concentrated H_2SO_4 and stirred for 12 h at room temperature. Then, the mixture was cooled below 10℃, and $KMnO_4$ was added slowly under continuous stirring. The mixture was stirred for 2.5 h. Then, 50 ml of distilled water was added dropwise and stirred at room temperature for 30 min. The oxidation reaction was terminated by adding 150 mL of distilled water, followed by 10 mL of hydrogen peroxide (30% H_2O_2). The solid product was separated and washed by centrifugation, once with 5% HCl and several times with distilled water up to pH 7. It was then dried at 60℃ in a vacuum oven for 12 h (Xue et al., 2020).

2.2.3.2 Preparation of RGO nanosheets

1200 mg of graphene oxide was added to 400 mL of distilled water and then sonicated for 2 h to obtain a colloidal suspension of graphene oxide (3 mg mL^{-1}). Suspended graphene oxide was reduced by 3 mL of hydrazine hydrate for 8 h in an oil bath at 85℃. The reaction mixture's color became darker during the reaction progression. Black reduced graphene oxide was filtered, first washed with 0.1 M HCl solution, and several times with distilled water until pH 7 was obtained (Choudhury et al., 2021).

2.2.3.3 Preparation of ZnO nanorods

A simple approach for the preparation of ZnO nanorods is given as follows: 0.439 g of Zinc acetate dihydrate was added to 25 mL of ethanol and sonicated for 30 min to obtain 0.1 M Zinc acetate dihydrate solution. Similarly, 8 g of NaOH was added to 40 mL of ethanol, and then this mixture was sonicated for 0.5 h separately to get 0.5 M NaOH solution. Zinc acetate dihydrate solution was mixed with 0.5 NaOH solution after a few minutes of stirring, transferred to a Teflon lined stainless steel autoclave, and heated in a muffle furnace at 150℃ for 24 h. A white precipitate was collected and washed with ethanol and water (Cheng and Samulski, 2004).

2.2.3.4 Preparation of binary and ternary nanocomposites

The RGO-ZnO nanocomposite was prepared through a simple ultrasonic technique. 500 mg of reduced graphene oxide (RGO) was suspended in 75 mL of distilled water by 0.5 h of sonication to obtain a colloidal suspension of reduced graphene oxide. Similarly, ZnO suspension was prepared as follows: 125 mg of ZnO was mixed in 25 mL of distilled water by 0.5 h of sonication. ZnO solution was poured into RGO solution, and the final mixture was sonicated for 45 min, then stirred for 1 h. RGO-ZnO product was centrifuged and dried at 50℃ for 12 h. The final RGO-ZnO powder was obtained after grinding by motor, a similar process was used to prepare the RGO-ZnO composite by varying the mixing ratio of RGO:ZnO (4:0.5 and 4:2) (Jayachandiran et al., 2018a) (Fig. 2.5 (a)).

PANI was wrapped on the surface of RGO-ZnO composite through the following procedure: 0.25 g of RGO-ZnO powder was added to 50 mL of distilled water and sonicated to achieve a homogeneous suspension. The HCl solution was used to set the pH =1 of the above suspension. After that, 0.25 mL of aniline monomer was poured into the above RGO-ZnO suspension under the ice bath (0–5 °C). Then, the aqueous solution of $NH_4S_2O_8$ (0.98 g/25 mL)

was added dropwise to the above mixture and stirred for 4 h on the ice bath (0–5 °C). The prepared material (RGO-ZnO-PANI nanocomposite) was collected and washed using the centrifugation technique (Zhong et al., 2020). A similar procedure was used to prepare the PANI without the addition of the RGO-ZnO composite. A schematic diagram for preparing RGO-ZnO and RGO-ZnO-PANI composites is shown in Fig. 2.5 (a). In this study, ZnO was anchored on the RGO surface to form a binary composite RGO-ZnO, which contains primarily π-π interaction. After the formation of a composite between RGO and ZnO, the stability of ZnO in acidic and marine environments was significantly enhanced compared to that of pristine ZnO. Few studies have reported that RGO-ZnO composite exhibited enhanced thermal and cyclic stability in photocatalyst and supercapacitor applications due to the synergistic effect of RGO and ZnO (Jayachandiran et al., 2018b; Tatykayev et al., 2017). Furthermore, the presence of ZnO on the RGO surface effectively prevented the aggregation of RGO sheets in the coating matrix. During the formation of the ternary composite, the RGO-ZnO composite interacts with PANI through π–π interactions, both between ZnO rods and the aromatic rings of PANI and between the rings of RGO and PANI, contributing to structural stability. Furthermore, the RGO-ZnO composite interacts with PANI also via electrostatic interactions (originating from protonated N and lone pairs on the OH group of RGO) and via hydrogen bonding (encouraged between H of the amine group and lone pair of OH group of RGO). These interactions make the huge structure of ternary composite stable (S. ul Haque et al., 2020; Kumar, 2012; Xie et al., 2020).

2.2.3.5 Preparation of EP and EP/RGO-ZnO-PANI nanocomposite coating

Firstly, 2.5 mg of RGO was suspended in 10 mL of distilled water using a magnetic stirrer for 15 min, followed by 60 min of sonication at ambient temperature. 300 mg of DDS (hardener) was added to the RGO suspension and further sonicated for 60 min. Afterward, to

prepare the 0.5 wt% RGO (Lin et al., 2019), 200 mg of epoxy resin was mixed into the above-sonicated solution and then continuously stirred for 90 min to ensure appropriate mixing. RGO reinforced epoxy resin was vacuum-dried for 15 minutes to avoid bubble formation during coating application. This coating was applied on polished MS using four-sided thin film applicator to achieve a thickness of 50 ± 2 μm. Then, coatings were cured for 96 h (Dhongde et al., 2023). A similar process was used to prepare pure epoxy (without RGO addition) and epoxy-based coating with RGO-ZnO, and EP/RGO-ZnO-PANI. For better understanding, MS coupons coated with pure epoxy or with 0.5 wt% of RGO, RGO-ZnO, and RGO-ZnO-PANI separately were represented as EP, EP/RGO, EP/RGO-ZnO, and EP/RGO-ZnO-PANI, respectively. The schematic diagram for coating preparation and its application on MS is shown in Fig. 2.5 (b).

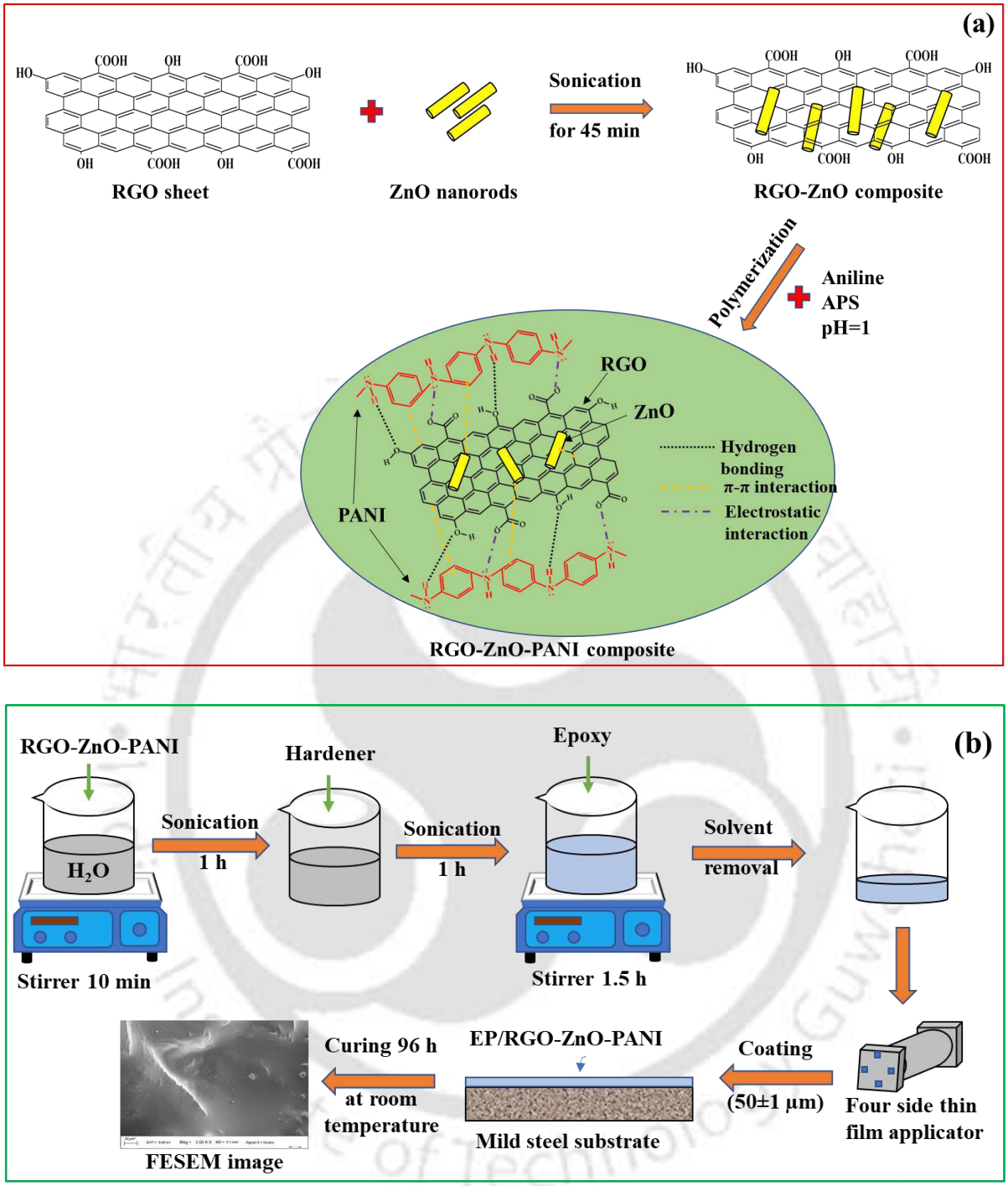

Fig. 2.5 Schematic representation of (a) synthesis of RGO-ZnO and RGO-ZnO-PANI, (b) preparation of EP/RGO-ZnO-PANI coating on the mild steel.

2.2.4. Characterizations of prepared materials and coatings

2.2.4.1 Raman analysis

The structural characteristics of all prepared nanocomposites was studied using Raman analysis. In this technique, Raman spectra were recorded in the wavenumber range of 400-2800 cm^{-1}, using a Horiba Jobin Vyon Raman system (model LabRam HR) with a 488 nm laser.

2.2.4.2 Fourier transform infrared spectroscopy (FTIR) analysis

FTIR analysis was used to investigate the interactions of nanofillers with epoxy matrix, FTIR spectra were recorded within the wavenumber range of 450 to 4000 cm^{-1} using the IR affinity-1; (Shimadzu, Japan).

2.2.4.3 Thermogravimetric analysis (TGA)

TGA analysis was utilized to investigate the improvement in thermal stability of epoxy coating due to the incorporation of several nanocomposites. These analyses were performed by using (TGA, TG 209 F1 Libra, Netzsch, Selb, Germany) in the temperature range of 28 to 800 ℃ with a heating rate of 10℃/min.

2.2.4.4 Contact angle

The prepared coatings were characterized by contact angle analysis to study the changes in contact angle due to the reinforcement of several nanocomposites in the epoxy matrix. All contact angles were captured by a goniometer (Holmarc Opto-Mechatronics, model: HOI AD-CAM-01B) with a distilled water droplet of 3 µL at a humidity of 67 % and 28 ± 2℃.

2.2.5. Preparation of working electrodes

All corrosion tests were performed with MS of the following composition: C: 0.15–0.23 %; Mn: 0.98–1.50 %; S: 0.01–0.04 %; P: 0.02–0.04 %; Cr: 0.01 %; Si: 0.17–0.40 %; and the rest iron. To prepare the working electrode for electrochemical experiments, MS was cut into a disc (diameter: ø 9 mm; thickness: 5 mm) and fixed inside the hollow Teflon in such a way that it has a free surface of 0.64 cm^2 (Fig. 2.6 (a)). MS coupons of 12 × 12 × 5 mm^3 dimensions (Fig. 2.6 (b)) were used as a working electrode in the weight loss analysis of corrosion inhibitor studies. Furthermore, the working electrode with a diameters of ø 20 mm (Fig. 2.6 (c)) was used in the electrochemical measurement of coating applications. Before conducting each experiment, electrodes were polished by using emery papers of different grit sizes (from 220 to 2000) and then polished on a disc polisher (Make: Ms. Chennai Metco Pvt Ltd., India; Model: Bainpol-VT) with the help of alumina paste. Electrodes were washed with distilled water, followed by acetone, and oven-dried before storing in a desiccator (ASTM G1) (Kumar and Das, 2023).

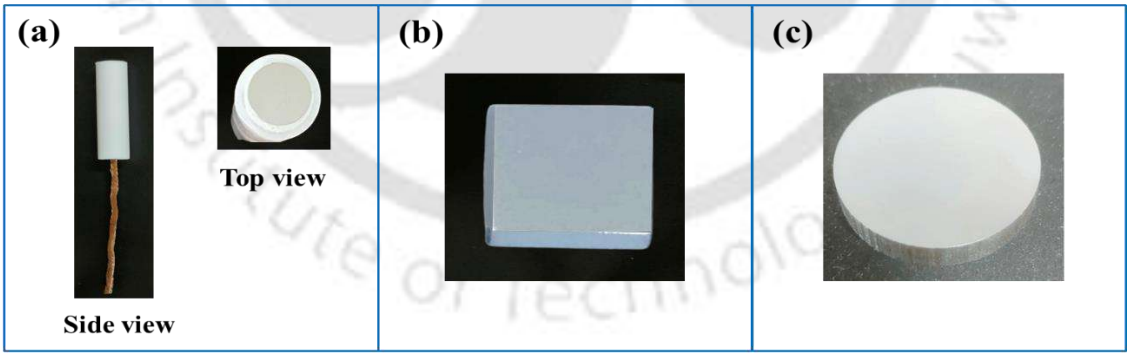

Fig. 2.6 Working electrodes for (a) electrochemical and (b) weight loss experiments of corrosion inhibitors and (c) electrochemical studies of coatings.

2.2.6. Fabrication of electrochemical cells and setups

The corrosion cell (Ms. Metrohm India Ltd.) of 100 mL capacity was used for inhibitors experiments, and a flat corrosion cell (It's design was indigenous) of 500 mL capacity was used for coating experiments; these electrochemical cells are shown in Fig. 2.7 (a) and 2.7 (b), respectively. Therefore, two different electrochemical setups were used in inhibitor and coating experiments which are presented in Figs. 2.8 (a) and 2.8 (b), respectively. All electrochemical experiments, including OCP, Potentiodynamic polarization, and EIS, were conducted using the same corrosion cell for corrosion inhibitor or coating experiments.

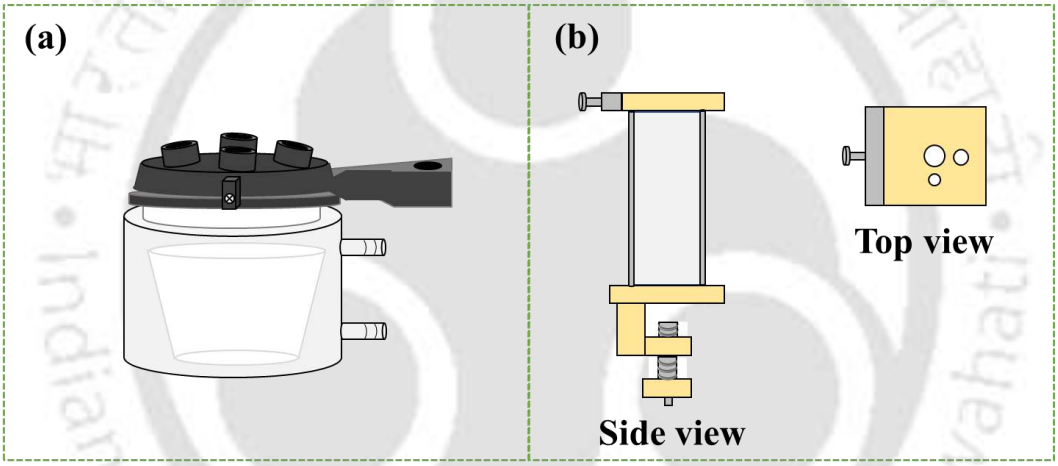

Fig. 2.7 Electrochemical cell for (a) inhibitor experiments and (b) coating experiments.

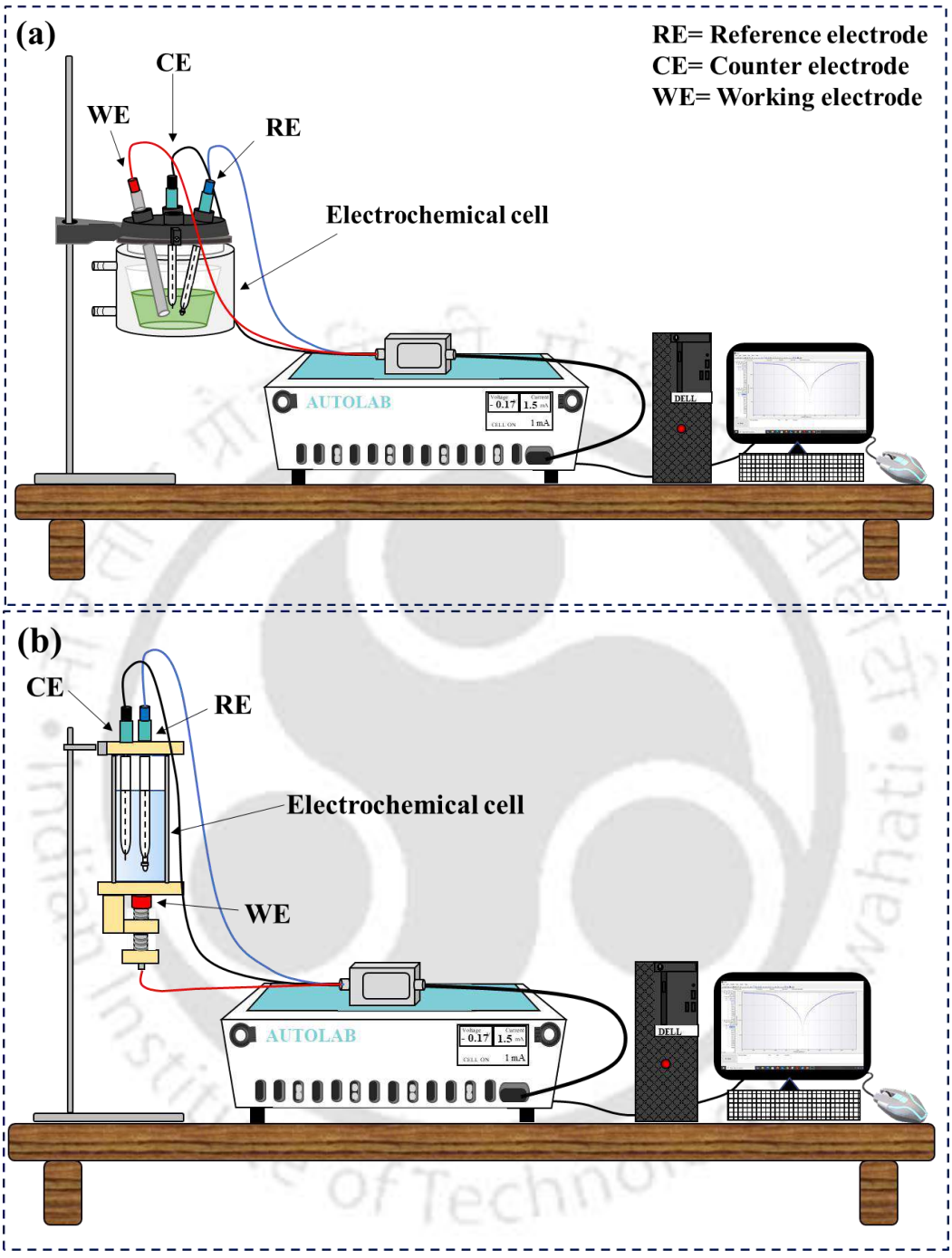

Fig. 2.8 Electrochemical setup for (a) inhibitor experiments and (b) coatings experiments.

2.2.7 Corrosion test

Corrosion-mitigating properties of developed inhibitors were studied using weight loss and electrochemical methods. Furthermore, the anticorrosive behavior of prepared coatings was investigated by electrochemical and salt spray analysis.

2.2.7.1 Weight loss method

For weight loss experiments, polished MS specimens (12 × 12 × 5 mm^3) were weighed and immersed in 50 mL of 1 M HCl solution with and without chayote, tinda *Phaseolus lunatus*, and *Duranta erecta* extracts at room temperature (28 ± 2ºC) for 4 to 48 h (Haldhar et al., 2021). Herein, to examine the effect of inhibitor concentration, MS coupons were separately immersed in 50 mL of 1 M HCl containing varying inhibitor doses in a 100 mL beaker for 24 h. After the immersion, specimens were washed gently with distilled water and acetone, dried to remove the moisture, and weighed again (ASTM G1). During these experiments, mild steel samples were suspended vertically in the corrosive solution using a fine, chemically inert thread. All surfaces of samples including front, back, and edges were fully immersed and uniformly exposed to the corrosive medium. The small area covered by the thread was excluded from the total exposed surface area during corrosion rate calculations. The weight of the specimens was determined by using a digital balance with a precision of 0.0001 ± 0.1 mg (ASTM G1). The schematic diagram is shown in Fig. 2.9. Corrosion rate (*CR*) and inhibiting efficiency (μ_{CR} %) were calculated using the following equations: Eqs. (2.1), and (2.2), respectively.

$$CR = \frac{87600\,W}{At\rho} \tag{2.1}$$

$$\mu_{CR}\,\% = \frac{CR^{\circ} - CR^{i}}{CR^{\circ}} \times 100 \tag{2.2}$$

where W is the weight loss during exposure (g), *CR* is the corrosion rate (mm $year^{-1}$), A is the exposed area of the MS coupon (cm^2), t and ρ are the exposure period (h) and density of MS (g cm^{-3}), respectively. The value of ρ was assumed to be 7.86 g cm^{-3}, CR° and CR^{i} (mm

year^{-1}) are corrosion rates in the absence and presence of inhibitors, respectively (Chu et al., 2020; Daoudi et al., 2022; Fidrusli et al., 2018; Haldhar et al., 2021). Furthermore, to investigate the stability of the inhibitors for a long immersion (0 - 48 h), several weight loss experiments were also performed using a 100 mL beaker with inhibitors for various immersion times, such as 4, 8, 12, 24, and 48 h.

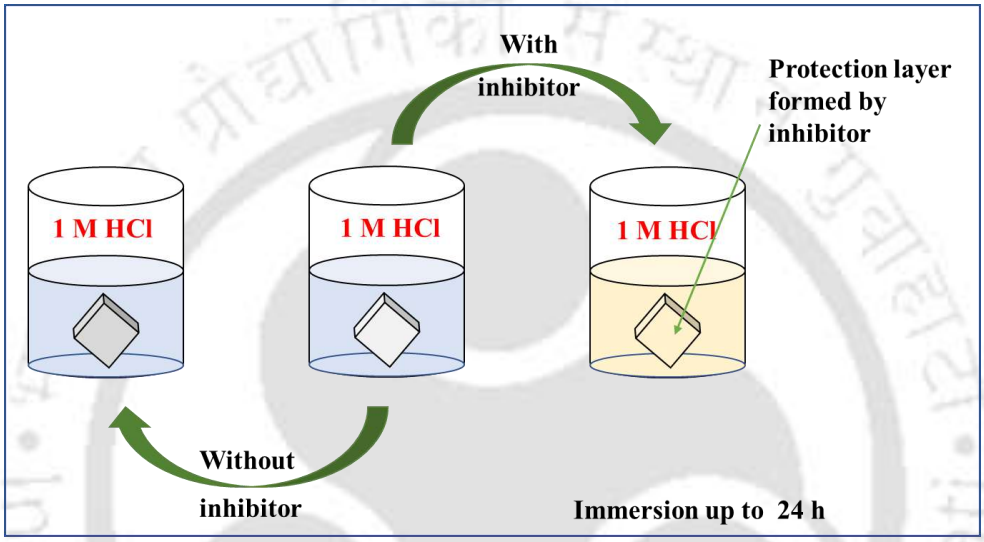

Fig. 2.9 Schematic diagram for weight loss analysis.

2.2.7.2 Electrochemical studies

All electrochemical experiments were conducted using three three-electrode setup, which was linked to potentiostat/galvanostat (Autolab, PGSTAT302N). This setup consisted following three electrodes: (a) reference electrode (Ag/AgCl, saturated with 3 M KCl), (b) counter electrode (Pt- wire), and (c) working electrode (MS embedded in Teflon rod with an exposed area of 0.64 cm^2) (El Nemr et al., 2024) for inhibitor experiments or MS disc with exposed area of 1 cm^2 (Cui et al., 2021) for coating experiments). To make a complete circuit, these electrodes were assembled in their respective electrochemical cells. A fixed amount of 70 mL of 1 M HCl solution (with and without inhibitors) and 200 mL of 3.5% NaCl solution was poured into these electrochemical cells for corrosion inhibitor and coatings experiments,

respectively. This cell has a provision that the reference electrode can be assembled very close to the exposed surface of the working electrode to detect the precise responses of the electrochemical process. Several electrochemical experiments were conducted in the presence or absence of 500, 1000, 1500, and 2000 mg L^{-1} of chayote extracts and 50, 100, 150, and 200 mg L^{-1} of tinda, *Phaseolus lunatus,* and *Duranta erecta* extracts in 1 M HCl and for uncoated and coated sample in 3.5% NaCl solution. Before every experiment, the electrodes were washed and polished with sandpaper, as mentioned in section 2.2.1.

2.2.7.2.1 Open circuit potential measurements

Before performing each electrochemical (Tafel polarization and EIS) test, MS electrodes were exposed to 1 M HCl for the period of 1 h without any external current supply to achieve a steady-state condition and stable open circuit potential (OCP) (Lin et al., 2020; Xu et al., 2021). The average OCP values were measured in the presence and the absence of chayote, tinda, *Phaseolus lunatus,* and *Duranta erecta* extracts and applied to their respective tests (Lin et al., 2020). Similarly, the average OCP values for coatings experiments were also measured by exposing uncoated and coated working electrodes to 3.5% NaCl solution for a period of 0.5 h.

2.2.7.2.2 Potentiodynamic polarization measurements

PDP experiments were conducted at a scan rate of 1 mVs^{-1} with a range of applied potential from -250 mV to + 250 mV with respect to OCP in 1 M HCl in the presence and absence of an inhibitor (Dhongde et al., 2024; Parthipan et al., 2023). The several electrokinetic parameters, such as corrosion current density (i_{corr}), corrosion potential (E_{corr}), anodic Tafel slope (b_a), and cathodic Tafel slope (b_c)) were determined by the extrapolation of the Tafel curves.

Before performing the PDP test, electrodes were immersed in the corrosive solution for a sufficient time to achieve a stable potential value, which indicates that the system has reached the study state. PDP measurement is a technique that involves the gradual change of the potential of a working electrode, either in a positive or negative direction with respect to OCP. As corrosion is an anodic and cathodic reaction process, the rate of corrosion is controlled by the kinetics of electron transfer (Kakaei et al., 2019; Mansfeld, 2005). A reaction controlled by electron transfer kinetics follows the Tafel equation (Eq. (2.3)), which is as follows:

$$i = i_0 e^{\frac{2.303\,(E - E_{corr})}{b}} \tag{2.3}$$

Where, i represents the current density, i_0 represents the exchange current density, which is also known as a reaction-dependent constant, b depicts the Tafel constant (*V/decade*), E and E_{corr} represent applied and corrosion potential, respectively. The Tafel equation stands for the individual reaction, either anodic or cathodic. But corrosion is the combination of both reactions. Therefore, Tafel equations are combined to obtain the Butler-Volmer equation. Under a charge transfer condition, the potential of anodic and cathodic reactions on the working electrode is related to the current density (Zhang et al., 2009). This relationship is given by the Butler-Volmer equation (Eq. (2.4))

$$i = i_a + i_c = i_{corr}\,(e^{\frac{2.303\,\eta}{b_a}} - e^{\frac{-2.303\,\eta}{b_c}}) \tag{2.4}$$

Where, i_a and i_c are the anodic and cathodic current densities, respectively. Here, the difference between the applied potential E, when a net current flows through the corrosion cell, and the corrosion potential, E_{corr}, is called the electrode polarization, overpotential, or overvoltage, η. The η term represents the extent to which the electrode-solution interface departs from the corrosion potential value. Overvoltage depends on the current density.

The values of E_{corr} and i_{corr} were obtained at the point of intersection resulting from the extrapolation of the linear section of the cathodic and anodic curve of the polarization curve, as shown in Fig. 2.10. The values of i_{corr} are indicative of a corrosion rate. This figure displays

the relation between applied potential (V) and the logarithm of the absolute current (A cm^{-2}). In this figure, the curved line denotes the cumulative sum of both cathodic and anodic currents for the applied potential range.

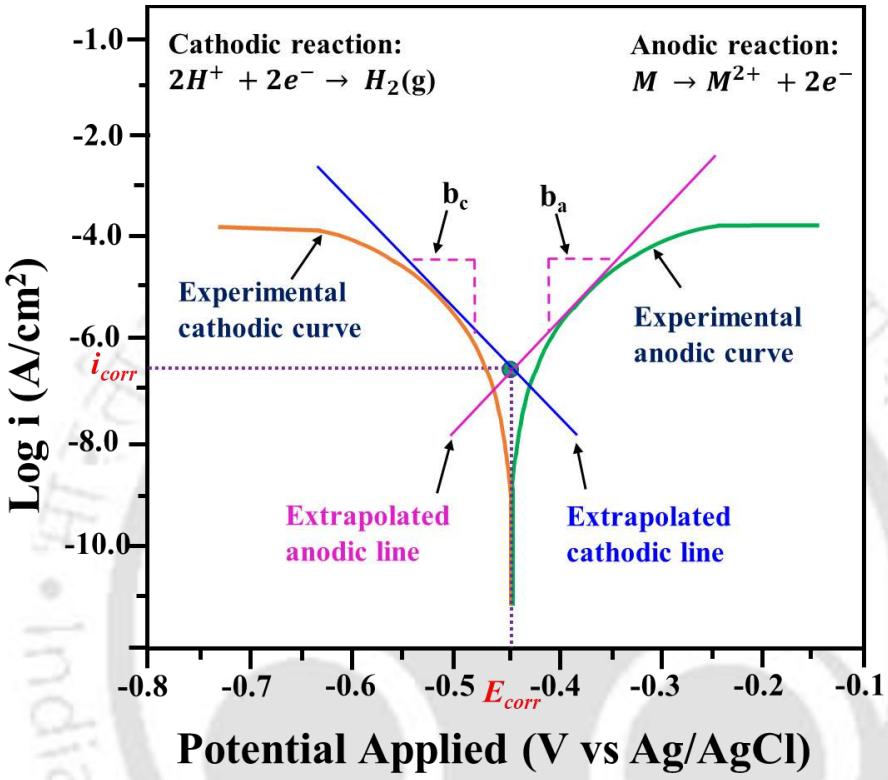

Note: i_{corr} = *corrosion current,* E_{corr} = *corrosion potential, ba = anodic slope, bc = cathodic slope*

Fig. 2.10 Pictorial representation of extrapolation of Potentiodynamic Polarization curve (Tafel plot).

The inhibition efficiencies (μ_p %) of chayote, tinda, *Phaseolus lunatus,* and *Duranta erecta* extracts were calculated from corrosion current density values (i_{corr}) by the following Eq. (2.5) (Al-Moubaraki et al., 2022; Khayatkashani et al., 2022):

$$\mu_P\% = \left(1 - \frac{i_{corr}^{in}}{i_{corr}^{\circ}}\right) \times 100 \quad (2.5)$$

where corrosion current densities (µA cm^{-2}) in the presence and absence of inhibitors are depicted by i_{corr}^{in} and i_{corr}°, respectively (Batah et al., 2022; Dhongde et al., 2023; Pal and

Das, 2022). Furthermore, the above equation (Eq. (2.5)) was also used to calculate the corrosion-inhibiting efficiencies of coatings, just by replacing the i_{corr}^{in} with i_{corr}^{c} (corrosion current densities of coated samples).

2.2.7.2.3 Electrochemical impedance spectroscopy measurements

In the electrochemical impedance spectroscopy test, a small amplitude AC signal of 10 mV and a frequency range from 0.01 Hz to 10000 Hz was applied at the steady-state open circuit potential (OCP) value. The responses of applied frequencies to MS deterioration in 1 M HCl with and without the inhibitors are illustrated by Nyquist and Bode plots.

Theoretical Consideration

In EIS analysis, several circuit elements, namely, resistance (R), capacitance (C), and inductance (L) are obtained by applying AC voltage in an electrochemical cell. When a DC voltage is employed in the electrochemical cell, then Ohm's law is followed by the values of voltage (V), resistance (R), and current (I). Similarly, If an AC voltage is applied, then impedance interrupts the current flow. This impedance can be expressed as (Eq. (2.6)):

$$Z(w) = \frac{V(w)}{I(w)} \quad (2.6)$$

Where, $\omega = 2\pi f$; it is the angular frequency of the applied AC voltage

These interruptions can be denoted by several circuit elements, for instance, R, C, and L, which constitute the overall impedance in the existing circuit. In an actual system, the electrochemical cell contains various circuit elements with numerous combinations. Thus, it is more accurate to use the concept of impedance than a circuit model consisting solely of a resistor to represent an electrochemical system. Additionally, when V is applied with the angular frequency ω, V and I have a phase difference of ø. Therefore, the above V and I values

in the AC circuit can be expressed by the following equations (Eqs 2.7 and 2.8). In these equations, V_m and I_m signify the maximum values of V and I, respectively.

$$V = V_m \sin(wt) \tag{2.7}$$

$$I = I_m \sin(wt - ø) \tag{2.8}$$

The above equation for V and I can be modified by using the complex function $j = \sqrt{-1} = e^{(\frac{j\pi}{2})}$ as follows (Eqs. (2.9 and 2.10)):

$$V = V_m e^{(jwt)} \tag{2.9}$$

$$I = I_m e^{[j(wt-ø)]} \tag{2.10}$$

As discussed above, V and I follow Ohm's law for the AC circuit model, and impedance Z(ω) is expressed as follows (Eq. (2.11)):

$$Z(w) = \frac{V(w)}{I(w)} = \frac{V_m e^{(jwt)}}{I_m e^{[j(wt-ø)]}} = \frac{V_m}{I_m} e^{(jø)} \tag{2.11}$$

This above equation can be simplified using Euler's equation, $exp(j\phi) = \cos(\phi) + j\sin(\phi)$, as follows (Eq. (2.12));

$$Z(w) = V_m I_m e^{(jø)} = V_m I_m[\cos(ø) + j\sin(ø)] = Z_0[\cos(ø) + j\sin(ø)] \tag{2.12}$$

By dividing the above equation into real and imaginary parts, the following equation can be written as follows (Eq. (2.13)):

$$Z(w) = Z_0[\cos(ø)] + j Z_0[\sin(ø)] \tag{2.13}$$

On the basis of Eq. (2.13), this EIS data can be presented by two plots such as (i) Nyquist plot (Fig. 2.11 (a)) that represents the real and imaginary parts of Z(ω) using cartesian coordinates in Eq. (2.13) $Z_{real} = Z_0 \cos\phi$, that signifies R (resistance) and $Z_{img} = Z_0 j\sin(\phi)$, which signifies C(capacitance) + L (inductance) and (ii) Bode plot that shows the phase shift and magnitude changes in the applied frequency range are shown in Fig. 2.11 (b) and (Fig. 2.11 (c)), respectively.

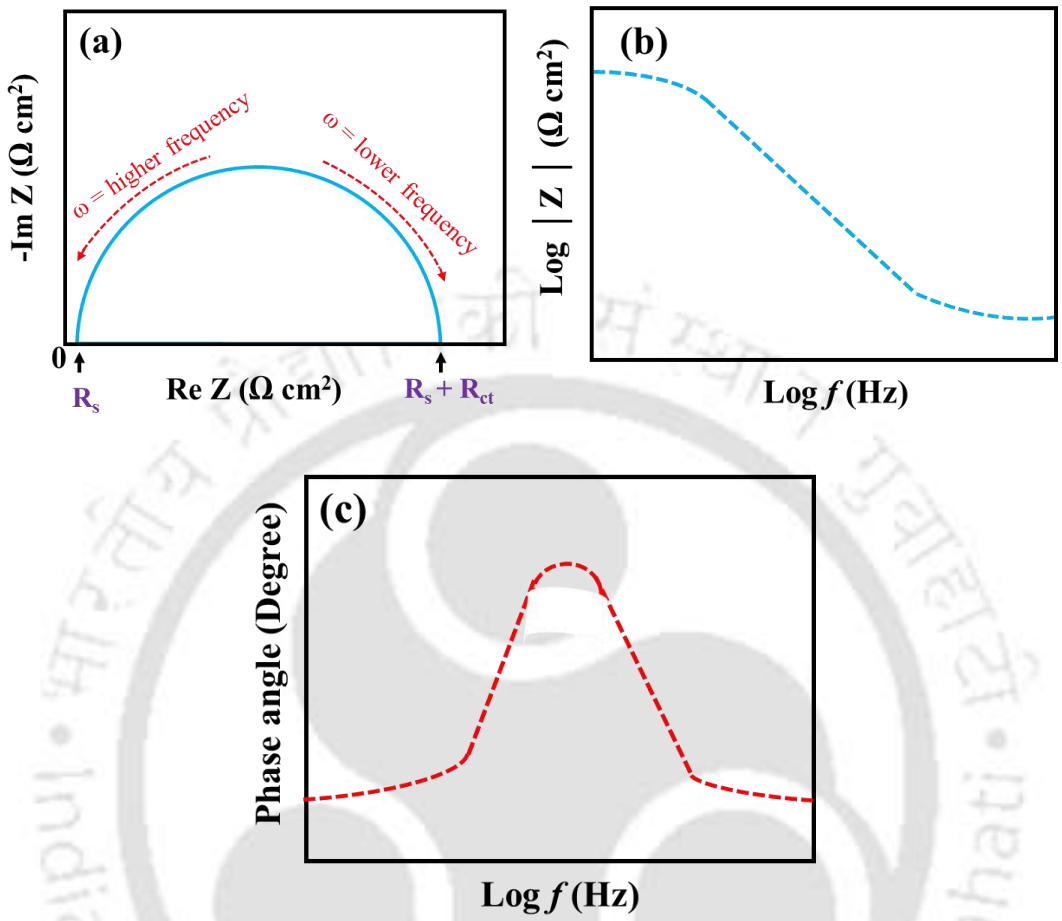

Fig. 2.11 A standard EIS plot (a) Nyquist, (b) Bode modulus, and (c) Bode phase.

These Nyquist plots were fitted to a simple equivalent circuit to obtain the EIS parameters. This circuit contains several elements, such as resistors, capacitors, and inductors, which are key components for studying the physical electrochemistry of the system. However, in cases of a system's inhomogeneity, the capacitor of the circuit does not work perfectly. To remove this inhomogeneity from the system, the capacitor was replaced by the constant phase element *CPE*, expressed as follows Eq. (2.14) (Haque et al., 2020; Tan et al., 2021):

$$Z_{CPE} = \frac{1}{Y_o(jW)^n} \tag{2.14}$$

where Z_{CPE} is the impedance of CPE, Y_o and n are numerical value and deviation parameters of CPE, respectively, *w* is the angular frequency (rad s^{-1}), j is the imaginary number. The characteristics of CPE depend on *n*.

If $n = 0, then\ Y_0 = R$ (CPE acts as resistor)

If $n = 1,\ then\ Y_0 = C\ or\ Y_0 = L$ (CPE acts either as inductor or capacitor)

If $n = 0.5,\ then\ Y_0 = W$ (CPE acts as Warburg).

The values of Y_0, n, and ω_{max} were utilized to calculate the value of double layer capacity (C_{dl}) of *CPE* (Eq. 2.15) (Mobin et al., 2022).

$$C_{dl} = \frac{Y_0}{(\omega_{max})^{n-1}} \tag{2.15}$$

where ω_{max} (rad s^{-1}) denotes the value of the angular frequency, which corresponds to the maximum imaginary impedance of the Nyquist patterns (Fadhil et al., 2020). Double layer capacity (C_{dl}) and charge transfer resistance (R_{ct}) are two crucial parameters of Nyquist patterns. The inhibition efficiency (μ_{Rct} %) of chayote, tinda, *Phaseolus lunatus*, and *Duranta erecta* extracts was calculated by the following equation (Eq. (2.16))

$$\mu_{Rct}\% = \left(1 - \frac{R_{ct}^{\circ}}{R_{ct}^{in}}\right) \times 100 \tag{2.16}$$

Where charge transfer resistances for MS immersed in 1 M HCl in the presence and absence of inhibitors are depicted by R_{ct}^{in} and R_{ct}°, respectively (Al-Moubaraki et al., 2022)(Pais and Rao, 2023; Pal and Das, 2020).

2.2.7.3 Salt spray test

The anticorrosive behavior of prepared coatings was also studied by the salt spray technique. For this analysis, MS coupons of 9 cm × 9 cm ×5 cm were coated with an average coating thickness of about 50 ± 2 μm. Then, an artificial scratch was created on each coated

sample, and these samples were placed inside the salt spray chamber, and 5 wt% NaCl solution was continuously sprayed as per ASTM B117.

2.2.8 Effect of temperature on the inhibitor's performance

To investigate the effect of temperature on inhibition efficiencies of inhibitors, a few electrochemical measurements were also performed at 313 and 323 K. The interactions between the MS surface and inhibitor molecules can be altered by the temperature.

2.2.8.1 Effect of activation energy

Herein, Tafel data was used to study the influence of activation energy on metal dissolution. The degradation of metal can be considered an Arrhenius-type phenomenon, and i_{corr} values can be expressed by the following equation (Eq. (2.17)) (Boudalia et al., 2023):

$$i_{corr} = Ae^{\frac{-E_a}{RT}} \tag{2.17}$$

where, gas constant and temperature are depicted by R (8.314 $JK^{-1}mol^{-1}$), and T (K), respectively. E_a epitomizes the activation energy of metal's dissolution, and the Arrhenius pre-exponential parameter is represented by A.

The variation in i_{corr} values with temperature elevation was used to evaluate a few kinematic parameters, such as ΔS and ΔH for metal corrosion. The transition state is another way to express the Arrhenius equation (Eq. (2.18)) (Kumar and Das, 2024).

$$i_{corr} = \frac{k_B T}{h} e^{\frac{\Delta S}{R}} e^{\frac{-\Delta H}{RT}} \tag{2.18}$$

where enthalpy, the entropy, Planck's constant, and Boltzmann's constant are represented by ΔH, ΔS, h (6.6252×10^{-34} J), and k_B (1.38066×10^{-23} JK^{-1}), respectively. Additionally, the corrosion of metal follows an unimolecular-type process only if the values for the subtraction of change in enthalpy from activation energy are equal to the values of RT, as shown in Eq. (2.19) (Eddahhaoui et al., 2024).

$$E_a - \Delta H = RT \tag{2.19}$$

where E_a designates the activation energy of MS degradation in an acidic solution, and enthalpy is depicted by ΔH.

2.2.9 Adsorption studies of inhibitors

The adsorption isotherms play a crucial role in corrosion research, which offers valuable insights into the interaction between inhibitors (adsorbate) and metal surfaces (adsorbent). To understand the basic principle of the adsorption process and the type of adsorption, a few of the most commonly used adsorption isotherms (Langmuir (Eq. (2.20)), Temkin (Eq. (2.21)), and Frumkin (Eq. (2.22))) were tested. The values of the adsorption equilibrium constant (K_{ads}) were determined using the following equations of the isotherms (Al-Moubaraki, 2018; Al-Moubaraki et al., 2022; Chen et al., 2022; Ma et al., 2021; Ravi and Pandey, 2019):

Langmuir isotherm: $\frac{C_{inh}}{\theta} = \frac{1}{K_{ads}} + C_{inh}$ (2.20)

Temkin isotherm: $\theta = f^{-1} \ln K_{ads} + f^{-1} \ln C_{inh}$ (2.21)

Frumkin isotherm: $log \frac{\theta}{(1-\theta)C_{inh}} = logK_{ads} + g\theta$ (2.22)

Where, C_{inh} is the inhibitor concentration, θ is the surface coverage, and f is the heterogeneity factor, that is, the inverse of the slope. The surface coverage (θ) was calculated from μ_P % by the following expression (Eq. (2.23)) (Zhang et al., 2021):

Surface coverage: $\theta = \frac{\mu_P\,\%}{100}$ (2.23)

where, μ_P % represents the corrosion inhibiting efficiencies in the PDP test, which are calculated from corrosion current densities [i_{corr}° (uninhibited system) and i_{corr}^{in} (inhibited system)].

2.2.10 Surface characterization

In inhibitor studies, Surface characterization was performed to investigate the changes on the surface of mild steel during corrosion in the presence or absence of inhibitors.

2.2.10.1 Field emission scanning electron microscopy (FESEM) and Energy dispersive X-ray (EDX) analyses

Polished metal samples were dipped in 1 M HCl solution in the presence or absence of optimum inhibitor concentration (2000 mg L^{-1} of chayote, and 200 mg L^{-1} of tinda, *Phaseolus lunatus,* and *Duranta erecta*) for 2 h duration. After that, the surface of these coupons was investigated by field emission scanning electron microscopy (FESEM, Sigma, Zeiss) to observe the difference in their surface morphology due to the acid immersion (Muthukrishnan et al., 2019). Furthermore, to identify the morphology of all prepared materials (GO, RGO, ZnO, RGO-ZnO, PANI, and RGO-ZnO-PANI), FESEM images were captured at a magnification of 50.0 KX. This FESEM analysis was also utilized to study the morphology of prepared coatings, and FESEM images were recorded at 2 KX magnification. Energy dispersive X-ray analysis (EDX, Sigma, Zeiss) was used to determine the changes in the element composition of immersed MS in 1 M HCl with and without inhibitor. Before each EDX measurement, MS samples were immersed in acid for 4 h (Mandour et al., 2021; Parekh et al., 2016). Furthermore, Energy-dispersive X-ray spectroscopy (EDX, Sigma, Zeiss) was used to investigate the element distribution in RGO-ZnO and RGO-ZnO-PANI nanocomposites.

2.2.10.2 Atomic force microscopy (AFM)

The topology of the MS surface was studied by AFM Bruker Dimension Icon SPM to observe the effect of the inhibitors on the surface morphology in terms of surface roughness variations. The AFM scans were conducted at a rate of 0.95 Hz, covering a 5 μm × 5 μm scan

area. Before AFM analysis, MS coupons were immersed in 1 M HCl solution containing optimum inhibitor concentration (2000 mg L^{-1} of chayote, and 200 mg L^{-1} of tinda, *Phaseolus lunatus*, and *Duranta erecta* extracts) separately or in their absence for a duration of 3 h (Ali Asaad et al., 2018; Singh et al., 2016).

2.2.10.3 X-ray diffraction (XRD)

Metallic samples were immersed in 1 M HCl solution in the presence or absence of optimum inhibitor concentration (2000 mg L^{-1} of CEPH3, and 200 mg L^{-1} of TFE, PLSE, DELE) for a 2 h duration. Subsequently, the coupons were subjected to drying in an oven, followed by an examination of the composition and characteristics of the layer corrosion product over the metal surface. This analysis was conducted by X-ray diffractometer (Rigaku, Smart Lab) using Cu Kα, and λ = 1.54178 Å) (Bhan and Golder, 2023; Muthukrishnan et al., 2019; Ravi and Golder, 2023). Furthermore, XRD analysis was also used to characterize all prepared materials, such as Graphite, GO, RGO, ZnO, RGO-ZnO, PANI, and RGO-ZnO-PANI.

2.3 References

Adhikari, S., Dhongde, N.R., Talukdar, M.K., Khan, S., Rajaraman, P.V., 2024. Investigation of carbon steels (API 5L X52 and API 5L X60) dissolution CO_2–H_2S solutions in the presence of acetic acid: Mechanistic reaction pathway and kinetics. Arab. J. Sci. Eng. 49, 8363–8381. https://doi.org/10.1007/s13369-024-08812-1

Al-Moubaraki, A.H., 2018. Potential of borage flowers aqueous extract, Borago officinalis L., against the corrosion of mild steel in phosphoric acid. Anti-Corrosion Methods Mater. 65, 53–65. https://doi.org/10.1108/ACMM-04-2017-1788

Al-Moubaraki, A.H., Chaouiki, A., Alahmari, J.M., Al-hammadi, W.A., Noor, E.A., Al-Ghamdi, A.A., Ko, Y.G., 2022. Development of natural plant extracts as sustainable inhibitors for efficient protection of mild steel: Experimental and first-principles multi-level computational methods. Materials (Basel). 15, 8688.

https://doi.org/10.3390/ma15238688

Ali Asaad, M., Sarbini, N.N., Sulaiman, A., Ismail, M., Huseien, G.F., Abdul Majid, Z., Bothi Raja, P., 2018. Improved corrosion resistance of mild steel against acid activation: Impact of novel Elaeis guineensis and silver nanoparticles. J. Ind. Eng. Chem. 63, 139–148. https://doi.org/10.1016/j.jiec.2018.02.010

Batah, A., Chaouiki, A., El Mouden, O.I., Belkhaouda, M., Bammou, L., Salghi, R., 2022. Almond waste extract as an efficient organic compound for corrosion inhibition of carbon steel (C38) in HCl solution. Sustain. Chem. Pharm. 27, 100677. https://doi.org/10.1016/j.scp.2022.100677

Bhan, C., Golder, A.K., 2023. Utilizing bioinspired AgNPs as an antibacterial agent to enhance ceramic membrane performance. J. Environ. Chem. Eng. 11, 110283. https://doi.org/10.1016/j.jece.2023.110283

Boudalia, M., Laourayed, M., El Moudane, M., Sekkat, Z., Campos, O.S., Bellaouchou, A., Guenbour, A., José Garcia, A., Amin, H.M.A., 2023. Phosphate glass doped with niobium and bismuth oxides as an eco-friendly corrosion protection matrix of iron steel in HCl medium: Experimental and theoretical insights. J. Alloys Compd. 938, 168570. https://doi.org/10.1016/j.jallcom.2022.168570

Chen, L., Lu, D., Zhang, Y., 2022. Organic compounds as corrosion inhibitors for carbon steel in HCl solution: A comprehensive review. Materials (Basel). 15, 2023. https://doi.org/10.3390/ma15062023

Cheng, B., Samulski, E.T., 2004. Hydrothermal synthesis of one-dimensional ZnO nanostructures with different aspect ratios. Chem. Commun. 4, 986–987. https://doi.org/10.1039/b316435g

Choudhury, B.J., Roy, K., Moholkar, V.S., 2021. Improvement of supercapacitor performance through enhanced interfacial interactions induced by sonication. Ind. Eng. Chem. Res. 60, 7611–7623. https://doi.org/10.1021/acs.iecr.1c00279

Chowdhury, A., Peela, N.R., Golder, A.K., 2021. Synthesis of Cu_2O NPs using bioanalytes present in Sechium edule: Mechanistic insights and application in electrocatalytic CO_2 reduction to formate. J. CO_2 Util. 51, 101622. https://doi.org/10.1016/j.jcou.2021.101622

Chu, Y., Xu, P., Ou, Y., Bai, P., Wei, Z., 2020. Corrosion behavior and interaction of mixed bacteria on carbon steel in reclaimed water. Sci. Total Environ. 718, 136679. https://doi.org/10.1016/j.scitotenv.2020.136679

Cui, J., Xiong, Z., Qiu, H., LI, J., Yang, J., 2021. Functionalized graphene oxide: Carrier for

corrosion inhibitor and barrier in waterborne epoxy coatings. Compos. Part A Appl. Sci. Manuf. 144, 106354. https://doi.org/10.1016/j.compositesa.2021.106354

Daoudi, W., El Aatiaoui, A., Falil, N., Azzouzi, M., Berisha, A., Olasunkanmi, L.O., Dagdag, O., Ebenso, E.E., Koudad, M., Aouinti, A., Loutou, M., Oussaid, A., 2022. Essential oil of Dysphania ambrosioides as a green corrosion inhibitor for mild steel in HCl solution. J. Mol. Liq. 363, 119839. https://doi.org/10.1016/j.molliq.2022.119839

Dhongde, N.R., Baranwal, P.K., Rajaraman, P.V., 2023. Functionalization of graphene oxide with an ionic liquid (1-butyl-3-methylimidazolium acetate): Preparation of epoxy-based coating on carbon steel for anticorrosive applications. J. Appl. Polym. Sci. 140, 1–17. https://doi.org/10.1002/app.54026

Dhongde, N.R., Das, N.K., Banerjee, T., Rajaraman, P.V., 2024. Synthesis of carbon quantum dots from rice husk for anti-corrosive coating applications: Experimental and theoretical investigations. Ind. Crops Prod. 212, 118329. https://doi.org/10.1016/j.indcrop.2024.118329

Eddahhaoui, F.-Z., Najem, A., Elhawary, M., Boudalia, M., Campos, O.S., Tabyaoui, M., José Garcia, A., Bellaouchou, A., Amin, H.M.A., 2024. Experimental and computational aspects of green corrosion inhibition for low carbon steel in HCl environment using extract of Chamaerops humilis fruit waste. J. Alloys Compd. 977, 173307. https://doi.org/10.1016/j.jallcom.2023.173307

El Nemr, A., Elhebshi, A., Ashour, I., El-Deab, M.S., Barghout, N.A., Eddy, N.O., Ragab, S., 2024. Camphor tree bark extract as green corrosion inhibitor of LCS in 0.5 M H_2SO_4 with and without salt effect. J. Chinese Chem. Soc. 71, 174–196. https://doi.org/10.1002/jccs.202300327

Fadhil, A.A., Khadom, A.A., Ahmed, S.K., Liu, H., Fu, C., Mahood, H.B., 2020. Portulaca grandiflora as new green corrosion inhibitor for mild steel protection in hydrochloric acid: Quantitative, electrochemical, surface and spectroscopic investigations. Surfaces and Interfaces 20, 100595. https://doi.org/10.1016/j.surfin.2020.100595

Fidrusli, A., Suryanto, Mahmood, M., 2018. Ginger extract as green corrosion inhibitor of mild steel in hydrochloric acid solution. IOP Conf. Ser. Mater. Sci. Eng. 290, 012087. https://doi.org/10.1088/1757-899X/290/1/012087

Haldhar, R., Prasad, D., Kamboj, D., Kaya, S., Dagdag, O., Guo, L., 2021. Corrosion inhibition, surface adsorption and computational studies of Momordica charantia extract: a sustainable and green approach. SN Appl. Sci. 3, 25. https://doi.org/10.1007/s42452-020-

04079-x

Haque, J., Srivastava, V., Chauhan, D.S., Quraishi, M.A., Madhan Kumar, A., Lgaz, H., 2020. Electrochemical and surface studies on chemically modified glucose derivatives as environmentally benign corrosion inhibitors. Sustain. Chem. Pharm. 16, 100260. https://doi.org/10.1016/j.scp.2020.100260

Haque, S. ul, Nasar, A., Inamuddin, Rahman, M.M., 2020. Applications of chitosan (CHI)-reduced graphene oxide (rGO)-polyaniline (PAni) conducting composite electrode for energy generation in glucose biofuel cell. Sci. Rep. 10, 10428. https://doi.org/10.1038/s41598-020-67253-6

Ishnava, K.B., Patel, K.S., 2020. In vitro study of Praecitrulus fistulosus (Stocks) Pangalo (Cucurbitaceae) fruit – A potential candidate of Anthelmintic activity. Bull. Natl. Res. Cent. 44, 130. https://doi.org/10.1186/s42269-020-00365-1

Jayachandiran, J., Yesuraj, J., Arivanandhan, M., Raja, A., Suthanthiraraj, S.A., Jayavel, R., Nedumaran, D., 2018. Synthesis and electrochemical studies of rGO/ZnO nanocomposite for supercapacitor application. J. Inorg. Organomet. Polym. Mater. 28, 2046–2055. https://doi.org/10.1007/s10904-018-0873-0

Kakaei, K., Esrafili, M.D., Ehsani, A., 2019. Graphene and Anticorrosive properties, in: Interface science and technology. 27, 303–337. https://doi.org/10.1016/B978-0-12-814523-4.00008-3

Khayatkashani, M., Soltani, N., Tavakkoli, N., Nejatian, A., Ebrahimian, J., Mahdi, M.A., Salavati-Niasari, M., 2022. Insight into the corrosion inhibition of Biebersteinia multifida root extract for carbon steel in acidic medium. Sci. Total Environ. 836, 155527. https://doi.org/10.1016/j.scitotenv.2022.155527

Kumar, A., Das, C., 2024. Corrosion inhibition of mild steel by Praecitrullus fistulosus (tinda fruit and peel) extracts. Sci. Total Environ. 929, 172569. https://doi.org/10.1016/j.scitotenv.2024.172569.

Kumar, N.A., 2012. Polyaniline-grafted reduced graphene oxide for Efficient Electrochemical Supercapacitors. ACS Nano 25, 1715–1723.

Lin, B., Zheng, S., Liu, J., Xu, Y., 2020. Corrosion inhibition effect of cefotaxime sodium on mild steel in acidic and neutral media. Int. J. Electrochem. Sci. 15, 2335–2353. https://doi.org/10.20964/2020.03.73

Lin, Y.-T., Don, T.-M., Wong, C.-J., Meng, F.-C., Lin, Y.-J., Lee, S.-Y., Lee, C.-F., Chiu, W.-Y., 2019. Improvement of mechanical properties and anticorrosion performance of epoxy

coatings by the introduction of polyaniline/graphene composite. Surf. Coatings Technol. 374, 1128–1138. https://doi.org/10.1016/j.surfcoat.2018.01.050

Ma, L., Lu, W., Yang, D., Shen, J., Gao, Z., Zhang, S., Liao, Q., 2021. Dithiocarbamate modified glucose as a novel eco-friendly corrosion inhibitor for copper in sodium chloride media. Sustain. Chem. Pharm. 22, 100488. https://doi.org/10.1016/j.scp.2021.100488

Mandour, H.S., Abdel-Karim, A.M., Fathi, A.M., 2021. Inhibition efficiency of copper corrosion in a neutral chloride solution by barbituric and thiobarbituric acids. Port. Electrochim. Acta 39, 85–103. https://doi.org/10.4152/pea.202102085

Mansfeld, F., 2005. Tafel slopes and corrosion rates obtained in the pre-Tafel region of polarization curves. Corros. Sci. 47, 3178–3186. https://doi.org/10.1016/j.corsci.2005.04.012

Mobin, M., Aslam, R., Salim, R., Kaya, S., 2022. An investigation on the synthesis, characterization and anti-corrosion properties of choline based ionic liquids as novel and environmentally friendly inhibitors for mild steel corrosion in 5% HCl. J. Colloid Interface Sci. 620, 293–312. https://doi.org/10.1016/j.jcis.2022.04.036

Muthukrishnan, P., Prakash, P., Jeyaprabha, B., Shankar, K., 2019. Stigmasterol extracted from Ficus hispida leaves as a green inhibitor for the mild steel corrosion in 1 M HCl solution. Arab. J. Chem. 12, 3345–3356. https://doi.org/10.1016/j.arabjc.2015.09.005

Pais, M., Rao, P., 2023. Green nanoparticles as a sustainable inhibitor to attenuate acid corrosion of zinc. J. Mol. Struct. 1286, 135634. https://doi.org/10.1016/j.molstruc.2023.135634

Pal, A., Das, C., 2022. New eco-friendly anti-corrosion inhibitor of purple rice bran extract for boiler quality steel: Experimental and theoretical investigations. J. Mol. Struct. 1251, 131988. https://doi.org/10.1016/j.molstruc.2021.131988

Pal, A., Das, C., 2020. A novel use of solid waste extract from tea factory as corrosion inhibitor in acidic media on boiler quality steel. Ind. Crops Prod. 151, 112468. https://doi.org/10.1016/j.indcrop.2020.112468

Parekh, K., Jauhari, S., Upadhyay, R. V., 2016. Mechanism of acid corrosion inhibition using magnetic nanofluid. Adv. Nat. Sci. Nanosci. Nanotechnol. 7, 045007. https://doi.org/10.1088/2043-6262/7/4/045007

Parthipan, P., Cheng, L., Dhandapani, P., Rajasekar, A., 2023. Metagenomics diversity analysis of sulfate-reducing bacteria and their impact on biocorrosion and mitigation approach using an organometallic inhibitor. Sci. Total Environ. 856, 159203.

https://doi.org/10.1016/j.scitotenv.2022.159203

Ravi, Pandey, L.M., 2019. Enhanced adsorption capacity of designed bentonite and alginate beads for the effective removal of methylene blue. Appl. Clay Sci. 169, 102–111. https://doi.org/10.1016/j.clay.2018.12.019

Ravi, R., Golder, A.K., 2023. Bio-based Au Doping with dominant oxygen vacancies and Ti^{3+} defects on photocatalytic functionalities of TiO_2. Ind. Eng. Chem. Res. 62, 20702–20715. https://doi.org/10.1021/acs.iecr.3c02850

Ravi, R., Kumar Golder, A., 2024. Efficient recovery of TiO_2 and Pt-doped TiO_2 photocatalysts in wastewater treatment using a pilot-scale cross-flow ultrafiltration membrane system. Sep. Purif. Technol. 339, 126710. https://doi.org/10.1016/j.seppur.2024.126710

Singh, A.K., Mohapatra, S., Pani, B., 2016. Corrosion inhibition effect of Aloe vera gel: Gravimetric and electrochemical study. J. Ind. Eng. Chem. 33, 288–297. https://doi.org/10.1016/j.jiec.2015.10.014

Tan, B., Xiang, B., Zhang, S., Qiang, Y., Xu, L., Chen, S., He, J., 2021. Papaya leaves extract as a novel eco-friendly corrosion inhibitor for Cu in H_2SO_4 medium. J. Colloid Interface Sci. 582, 918–931. https://doi.org/10.1016/j.jcis.2020.08.093

Tatykayev, B., Donat, F., Alem, H., Balan, L., Medjahdi, G., Uralbekov, B., Schneider, R., 2017. Synthesis of core/shell ZnO/rGO nanoparticles by calcination of ZIF-8/rGO composites and their photocatalytic activity. ACS Omega 2, 4946–4954. https://doi.org/10.1021/acsomega.7b00673

Xie, M., Zhang, D., Wang, Y., Zhao, Y., 2020. Facile fabrication of ZnO nanorods modified with RGO for enhanced photodecomposition of dyes. Colloids Surfaces A Physicochem. Eng. Asp. 603, 125247. https://doi.org/10.1016/j.colsurfa.2020.125247

Xu, S., Wang, Q., Wang, N., Qu, L., Song, Q., 2021. Study of corrosion property and mechanical strength of eco-friendly fabricated superhydrophobic concrete. J. Clean. Prod. 323, 129267. https://doi.org/10.1016/j.jclepro.2021.129267

Xue, D., Meng, Q.B., Lu, Y.X., Liang, L., Wei, Y.H., Liu, X. Bin, 2020. Achieving high performance anticorrosive coating via in situ polymerization of polyurethane and poly(propylene oxide) grafted graphene oxide composites. Corros. Sci. 176, 109055. https://doi.org/10.1016/j.corsci.2020.109055

Zhang, X.L., Jiang, Z.H., Yao, Z.P., Song, Y., Wu, Z.D., 2009. Effects of scan rate on the potentiodynamic polarization curve obtained to determine the Tafel slopes and corrosion current density. Corros. Sci. 51, 581–587. https://doi.org/10.1016/j.corsci.2008.12.005

Zhang, Y., Zhang, S., Tan, B., Guo, L., Li, H., 2021. Solvothermal synthesis of functionalized carbon dots from amino acid as an eco-friendly corrosion inhibitor for copper in sulfuric acid solution. J. Colloid Interface Sci. 604, 1–14. https://doi.org/10.1016/j.jcis.2021.07.034

Zhong, F., He, Y., Wang, P., Chen, C., Yu, H., Li, H., Chen, J., 2020. Graphene/V_2O_5@polyaniline ternary composites enable waterborne epoxy coating with robust corrosion resistance. React. Funct. Polym. 151, 104567. https://doi.org/10.1016/j.reactfunctpolym.2020.104567

Chapter 3:

A novel eco-friendly inhibitor of chayote fruit extract for mild steel corrosion in 1 M HCl: Electrochemical, weight loss studies, and the effect of temperature

A novel eco-friendly inhibitor of chayote fruit extract for mild steel corrosion in 1 M HCl: Electrochemical, weight loss studies, and the effect of temperature

This chapter discusses the development and efficacy of chayote (Sechium edule) fruit extract as an eco-friendly corrosion inhibitor. The extract was characterized using FTIR and UV-Vis spectroscopy, while its anticorrosive properties were assessed through weight loss measurements and electrochemical techniques. Potentiodynamic polarization studies demonstrated high protection efficiencies of 85.72% and 76.82% at a concentration of 2000 mg L^{-1} for CEPH3 and CE, respectively. The adsorption behavior of these extracts followed the Langmuir isotherm and thermodynamic analysis, confirming a spontaneous and endothermic adsorption process. Additionally, surface characterization techniques (FESEM, AFM, EDX, and XRD) revealed the formation of a protective layer on mild steel, which further reinforced the extract's effectiveness as a corrosion inhibitor.

Published Article: Kumar, A., Das, C., 2023. A novel eco-friendly inhibitor of chayote fruit extract for mild steel corrosion in 1 M HCl: Electrochemical, weight loss studies, and the effect of temperature. ***Sustain. Chem. Pharm.*** 36, 101261. https://doi.org/10.1016/j.scp.2023.101261.

3.1 Characterization of chayote extract and quantification of ascorbic acid

3.1.1 FTIR analysis of chayote extract

The presence of ascorbic acid in chayote extract was analyzed by the Fourier transform infrared spectroscopy (FTIR) technique. Fig. 3.1 shows the FTIR pattern of chayote extract, with strong absorption bands at 1763 and 1642 cm^{-1} corresponding to C=O double bond stretching in a five-membered lactone ring and C=C stretching vibrations. Other 1457 and 1320 cm^{-1} bands correspond to -CH_2 stretching and the enol-hydroxyl group. The Presence of -C-O-C- was confirmed by two bands at 1277 (weak band) and 1046 cm^{-1} (strong band). FTIR spectra also have a bigger band at 3320 cm^{-1}, related to available water in the extract. The presence of ascorbic acid in chayote extract was confirmed by the following founded functional groups: C=C, C=O, -C-O-C-, -CH_2, and -OH, which were corresponding to the bands at 1763, 1642, 1320, and 1277 cm^{-1} (Farias et al., 2018; Umer et al., 2014; Panicker et al., 2006).

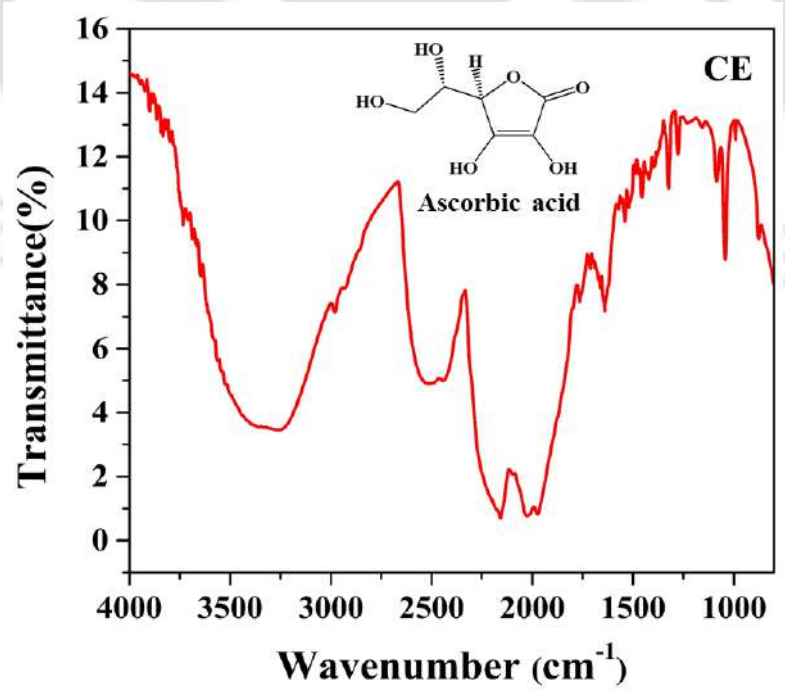

Fig. 3.1 FTIR spectra of chayote extract.

3.1.2 UV-Vis spectroscopy

UV-Vis spectroscopy was used to determine the ascorbic acid content in chayote extracts prepared at pH 3, 5, 7, and 9. A series of standard L-ascorbic acid solutions in the concentration range of 10 to 50 mg L^{-1} were prepared for the calibration studies. Then, these solutions were separately added to a DPS (2,6 Dichlorophenol indophenol sodium salt indicator) solution of 50 µM in the ratio of 1:9 (v/v; L-ascorbic acid solution/DPS solution) for UV-Vis spectroscopy analysis. In UV-Vis spectroscopy analysis, each solution contains an intense peak at the wavelength of 603 nm, corresponding to the ascorbic acid (Appendix 3A, Fig. 3A.1). The concentration vs. absorbance graph was plotted to obtain the calibration curve. For this calibration plot, good linearity was obtained with regression equation y = -0.00717x + 0.6775 and regression coefficient R^2 = 0.998. Furthermore, 23.08, 7.88, 7.04, 19.32, and 7.46 mg L^{-1} of ascorbic acid were found in chayote extracts at pH 3, 5, 7, 9, and 5.2. The highest ascorbic acid content of 23.08 mg L^{-1}, was found in chayote extract prepared in water at pH 3 (CEPH3). CE and CEPH3 were then selected for corrosion studies. The anticorrosive behavior of chayote extracts (CE and CEPH3) in HCl medium was investigated at several doses. To prepare the solutions of chayote extracts (CE and CEPH3) of 500, 1000, 1500, and 2000 mg L^{-1}, pure chayote extracts (Concentration of chayote fruit in distilled water: 7,50,000 mg L^{-1}) of 46.67, 93.33, 140.00, and 186.67 µL were carefully poured into four beakers, respectively. Then, 64.205, 64.159, 64.112, and 64.065 mL of distilled water were added into these beakers separately, and 5.748 mL of 37% HCl (12.178 M) was mixed in each beaker to prepare 70 mL of 1 M HCl. Therefore, the final concentration of 1 M HCl is maintained in each solution, as mentioned in Table 3A.1 of Appendix 3A.

3.2 Corrosion test

3.2.1 Weight loss method

3.2.1.1 Impact of inhibitor concentration

The impact of inhibitor concentration on inhibition efficiency was studied using the various concentrations from 500 mg L^{-1} to 2000 mg L^{-1} of both chayote extracts (CE and CEPH3) in 1 M HCl. Each experiment was repeated three times. The mean values of corrosion rate and protection efficiency on adding chayote extracts are shown in Table 3.1. It reveals that inhibition efficiency increases with the addition of chayote extracts, as shown in (Fig. 3.2), and maximum efficiency was achieved at 2000 mg L^{-1} concentration of chayote extracts for 24 h immersion (Haldhar et al., 2021). This increment in corrosion efficiency was due to significant metal surface coverage by the formed layer of adsorbed inhibitor molecules.

Table 3.1 Weight loss data after 24 h exposure of inhibited or uninhibited MS specimens in 1 M HCl.

Inhibitor	Concentration (mg L^{-1})	*CR* (mm $year^{-1}$)	μ_{CR} %
Blank	0	7.93 ± 0.50	-
CE	500	4.81 ± 0.51	39.34 ± 0.93
	1000	3.61 ± 0.43	54.48 ± 0.94
	1500	2.52 ± 0.28	68.22 ± 0.58
	2000	1.88 ± 0.10	76.29 ± 0.50
CEPH3	500	4.44 ± 0.33	44.01 ± 0.39
	1000	2.89 ± 0.34	63.56 ± 0.72
	1500	2.12 ± 0.14	73.27 ± 0.94
	2000	1.26 ± 0.04	84.11 ± 0.58

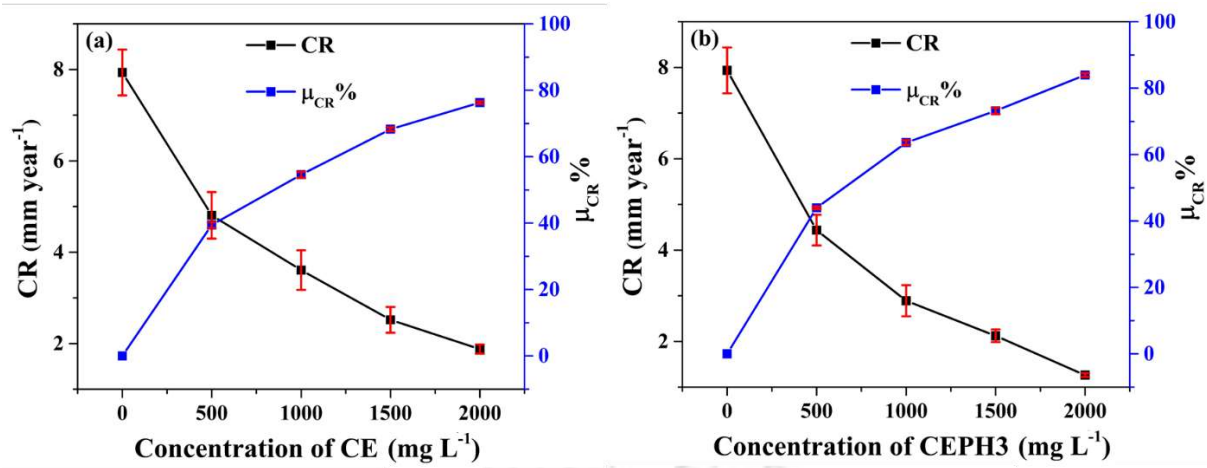

Fig. 3.2 Effect of inhibitor concentration on corrosion rate and inhibition efficiency (a CE, and (b CEPH3.

3.2.1.2 Effect of immersion time

In order to investigate the inhibiting stability of chayote extracts for long exposure, weight loss experiments were conducted in 1 M HCl in the presence and absence of chayote extracts at 2000 mg L^{-1} concentration for 4 to 48 h. The obtained inhibition efficiencies at different immersion times were plotted in Fig. 3.3. It was observed that the inhibition efficiency of both extracts increased up to 24 h (Rocha et al., 2010; Daoudi et al., 2022). On further increasing the immersion time from 24 to 48 h, the inhibition efficiency of chayote extracts remains almost invariant, which could be due to the formation of a compact strong layer of adsorbed inhibitor on the metal surface and the thickness of adsorbed inhibitor layer on the metal surface is almost constant after 24 h of immersion time (Faustin et al., 2015). Previous studies also reported immersion time of 24 h for the investigation of the concentration effect of inhibitor by weight loss measurements (Haldhar et al., 2021).

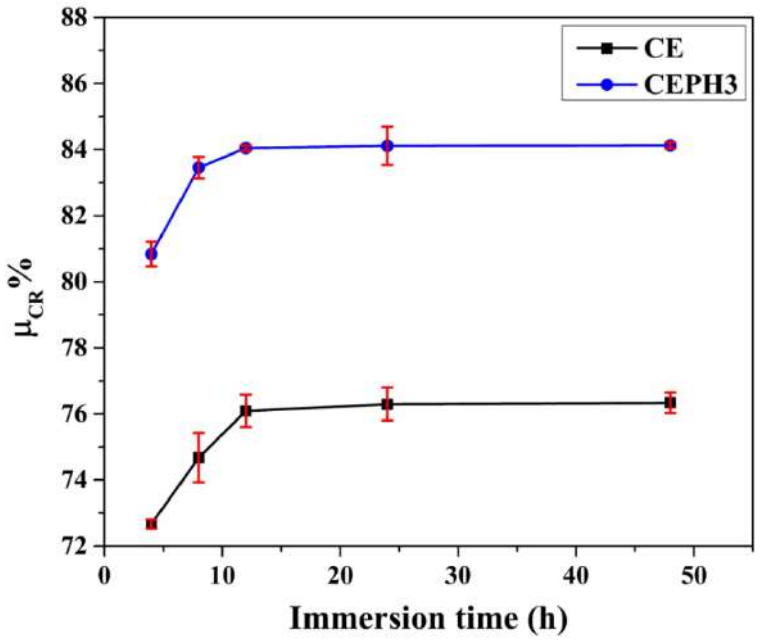

Fig. 3.3 Effect of immersion time on inhibition efficiency of both extracts.

3.2.2 Electrochemical measurements

Electrochemical studies are used to understand the inhibiting behavior of chayote extracts to protect the MS specimens against corrosion in terms of i_{corr}, E_{corr}, R_{ct}, and inhibition efficiency. Herein, each electrochemical test was performed thrice using several amounts (500-2000 mg L^{-1}) of both chayote extracts (CE & CEPH3) at 30 ºC.

3.2.2.1 OCP measurements

It is a steady-state or equilibrium value of developed potential for the working electrode with respect to the reference electrode at zero current supply. In this work, OCP was measured for 1 h at various concentrations of both chayote extracts, such as 0, 500, 1000, 1500, and 2000 mg L^{-1}. The value of OCP was shifted to the positive direction in the presence of chayote extracts as compared to the uninhibited system, which is shown in Figs. 3.4 (a) and 3.4 (b) for CE and CEPH3, respectively.

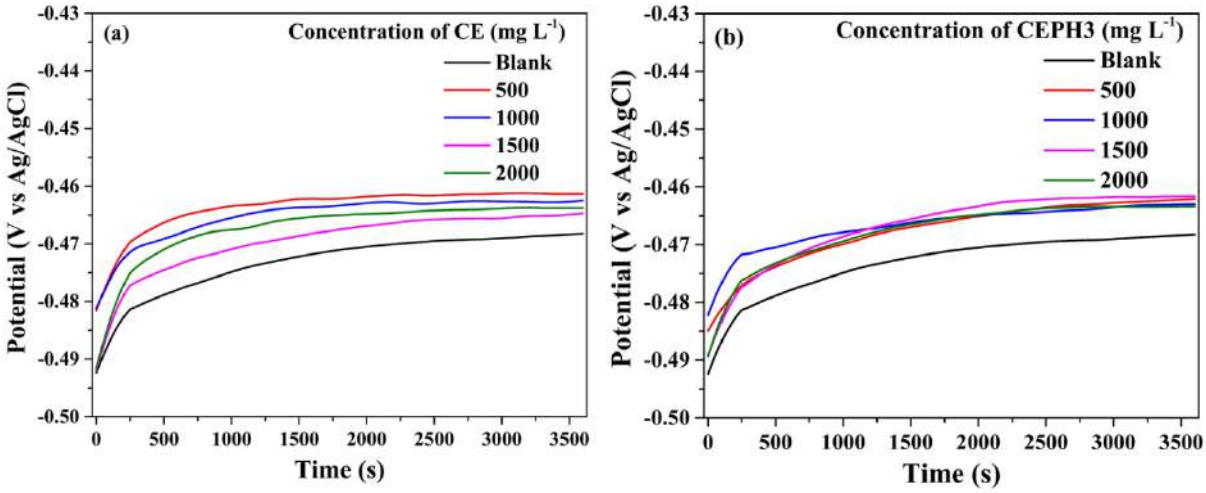

Fig. 3.4 OCP plots MS immersed in 1 M HCl in the presence and absence of CE a) and CEPH3 b).

3.2.2.2 PDP measurements

Polarization curves help to understand the corrosion inhibition effect of inhibitors in the form of anodic, cathodic, and mixed-type inhibitors. Tafel graphs for the immersion of uninhibited or inhibited MS specimens in 1 M HCl are demonstrated in Fig. 3.5 (a) and Fig. 3.5 (b) for CE and CEPH3, respectively. In these plots, it was found that E_{corr} (average corrosion potential) shifted positively on adding both chayote extracts compared to the absence of chayote extracts, which signifies that both chayote extracts behave predominantly as an anodic inhibitor. The anodic polarization of MS in 1 M HCl in the presence of both chayote extracts is dependent on electrode potential. Inhibited systems exhibit a minute effect on the anodic reaction when the corrosion potential shifts in the positive direction due to the presence of chayote extracts (Al-Moubaraki and Awaji, 2020). Few studies reported that if the corrosion potential shift is less than 85 mV relative to an uninhibited system, the inhibitor might be considered a mixed type of inhibitor. If the corrosion potential shifted more than 85 mV, then the inhibitor can be considered a cathodic or anodic inhibitor (Wang et al., 2019). In the present study, both chayote extracts work as a mixed type of inhibitor because the shift of E_{corr} is less than 85 mV.

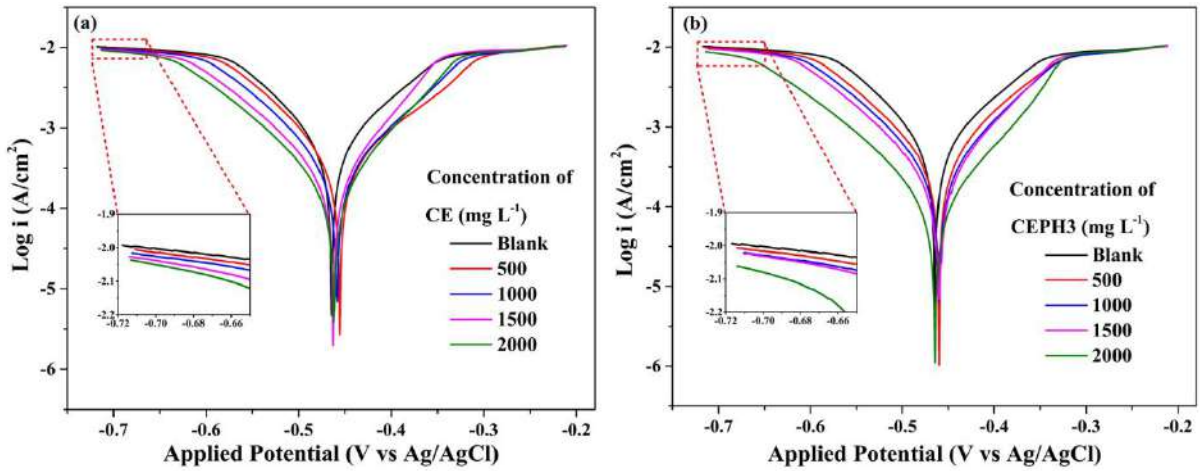

Fig. 3.5 Tafel plot for MS immersed in 1 M HCl in the presence and absence of CE a), CEPH3 b).

Furthermore, Tafel plots were fitted by using Nova 1.1.0 software to obtain Tafel parameters, including anodic Tafel slope b_a (V dec^{-1}), cathodic Tafel slope b_c (V dec^{-1}), corrosion current density (i_{corr}), polarization resistance (R_p), corrosion potential (E_{corr}), and Corrosion rate (CR), as shown in Fig. 3.6. This figure shows the fitted Tafel plot for mild steel corrosion in the absence of inhibitors. During this fitting, only the linear regions of cathodic and anodic branches were considered to avoid the error in the calculating Tafel slopes and corrosion current densities arising from non-linear regions. The obtained Tafel parameters are shown in Table 3.2. From this table, it was observed that corrosion potential values obtained from the Tafel plot are close to those of open-circuit potential (Canales et al., 2021), which were measured before each electrochemical test in the 3.2.2.1 section. Fig. 3.5 depicts that anodic and cathodic currents were decreased with the addition of chayote extracts as hydrogen evolution and metal dissolution both the reaction were hindered. Additionally, corrosion current density (i_{corr}) decreased, and polarization resistance increased with the addition of chayote extracts in the 1 M HCl solution. These two events indicate that chayote extracts (CEPH3 and CE) form a strong protective layer on immersed MS surface in 1 M HCl.

Furthermore, the corrosion rate decreased with increasing inhibitor concentration. These values were compared with those obtained from the weight loss analysis, as shown in Table 3A.2 of Appendix 3A. This comparison revealed that both electrochemical and weight loss methods yielded almost similar corrosion rate values. Table 3.2 reveals that the optimum concentration for both chayote extracts is 2000 mg L^{-1}. The highest protection efficiency (85.72 %) was found for immersed MS 1 M HCl solution in the presence of CEPH3 (Asaad et al., 2018; Ji et al., 2011; Saxena et al., 2018).

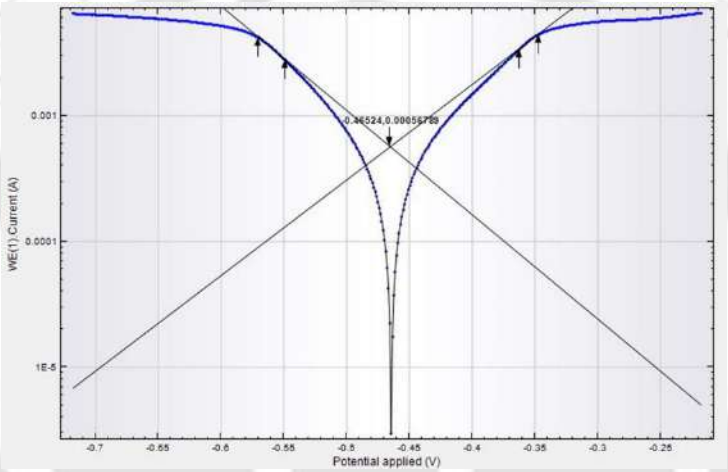

Fig. 3.6 Pictorial representation of fitting in Tafel plots of MS corrosion in 1 M HCl in the absence of inhibitors.

Table 3.2 Tafel parameters for MS immersed in 1 M HCl in the presence and absence of CE and CEPH3.

Inhibitor	Conc. (mg L^{-1})	b_a (mV dec^{-1})	$-b_c$ (mV dec^{-1})	*OCP* (mV vs. Ag/AgCl)	E_{corr} (mV vs. Ag/AgCl)	i_{corr} (µA cm^{-2})	R_p (Ω cm^2)	*CR* (mm $Year^{-1}$)	μ_P (%)
Blank	0	110.59 ± 0.52	120.25 ± 1.04	-468.15 ± 5.68	-465.25 ± 5.56	734.98 ± 5.23	34.04 ± 0.12	8.54 ± 0.45	-
CE	500	94.51 ± 0.55	133.14 ± 2.10	-461.34 ± 4.45	-457.82 ± 4.32	410.99 ± 4.16	58.41 ± 0.03	4.77 ± 0.50	44.08 ± 0.27
	1000	92.65 ± 0.91	99.69 ± 1.23	-462.56 ± 1.95	-459.10 ± 2.00	305.67 ± 3.58	68.23 ± 0.05	3.55 ± 0.44	58.41 ± 0.73
	1500	93.35 ± 0.78	73.38 ± 0.66	-464.82 ± 3.48	-462.78 ± 3.26	224.30 ± 2.18	79.55 ± 0.18	2.60 ± 0.31	69.48 ± 0.76
	2000	95.39 ± 0.75	78.45 ± 0.67	-463.79 ± 2.26	-461.58 ± 2.49	170.35 ± 1.53	109.74 ± 0.08	1.98 ± 0.12	76.82 ± 0.54
Blank	0	110.59 ± 0.52	120.25 ± 1.04	-468.15 ± 5.68	-465.25 ± 5.56	734.98 ± 5.23	34.04 ± 0.12	8.54 ± 0.45	-
CEPH3	500	102.67 ± 0.39	91.16 ± 0.51	-462.16 ± 3.66	-459.73 ± 3.50	381.70 ± 1.98	54.94 ± 0.13	4.43 ± 0.35	48.07 ± 0.49
	1000	97.59 ± 0.33	90.81 ± 0.32	-462.93 ± 2.86	-460.99 ± 2.61	282.39 ± 1.05	72.34 ± 0.02	3.28 ± 0.38	61.58 ± 0.44
	1500	78.95 ± 0.34	66.33 ± 1.34	-461.59 ± 2.47	-460.76 ± 2.55	169.77 ± 2.15	92.21 ± 0.13	1.97 ± 0.12	76.90 ± 0.07
	2000	87.17 ± 1.20	84.39 ± 1.33	-463.57 ± 3.23	-463.54 ± 3.74	104.92 ± 1.66	177.48 ± 0.18	1.21 ± 0.03	85.72 ± 0.40

3.2.2.3 EIS measurements

EIS experiments were performed to analyze the kinetics and nature of the electrochemical process occurring at the interface of MS and 1 M HCl and how it changes in the presence of chayote extracts (CEPH3 and CE). Nyquist patterns for MS in the presence of CE and CEPH3 are shown in Figs. 3.7 (a) and 3.7 (b), respectively. Fig. 3.7 shows that Nyquist plots of all experiments have the same depressed semicircle, which directs heterogeneity of the MS surface. This same pattern of Nyquist plots in the absence and presence of chayote extracts revealed that the addition of inhibitor (CEPH3 or CE) into 1 M HCl did not affect the mechanism of the corrosion process (Umoren et al., 2015). Each semicircle contains a large capacitive loop at higher frequencies, corresponding to charge transfer through the double layer. At low frequencies, one inductive loop was observed in the absence of chayote extracts, but it was not noticeable for inhibited systems. This inductive loop generally occurs due to the relaxation of adsorbed intermediate species, such as H^{+}_{ads}, Cl^{-}_{ads}, etc., from the metallic surface and depicts unstable corrosion products at the metal surface (Haque et al., 2021). For the inhibited systems, the disappearance of the inductive loop is usually regarded as a phenomenon of "degradation" for EIS (Haldhar et al., 2018; Pal and Das, 2022). These Nyquist plots for inhibited or uninhibited systems depict that reactions on the interface of metal-electrolytes are charge transfer controlled, and the semicircle diameter represents the charge transfer resistance (R_{ct}). Figs. 3.7 (a) and 3.7 (b) show that the diameter of the semicircles increases on increasing the amount of the chayote extracts from 500 to 2000 mg L^{-1}, on further increase of concentration of chayote extracts, the diameter of the semicircle decreases, which implies that the optimum concentration for both chayote extracts is 2000 mg L^{-1}. Corresponding Bode magnitude and Bode phase plots for both chayote extracts are shown in Fig. 3.8. In Nyquist plots and Bode plots, a semicircle and a single narrow peak, respectively, show a one-time constant in the electrochemical process.

The metal-electrolyte interface's capacitive or resistive properties are indicated by the Bode graphs' different values of phase angles (90° or 0°). Although the phase angles in all figures were less than 90°, no pure capacitive behavior was seen. Peak height rise as inhibitor (CE and CEPH3) concentration was increased, indicating a robust capacitive response at the metal-electrolyte interface (Pal and Das, 2023).

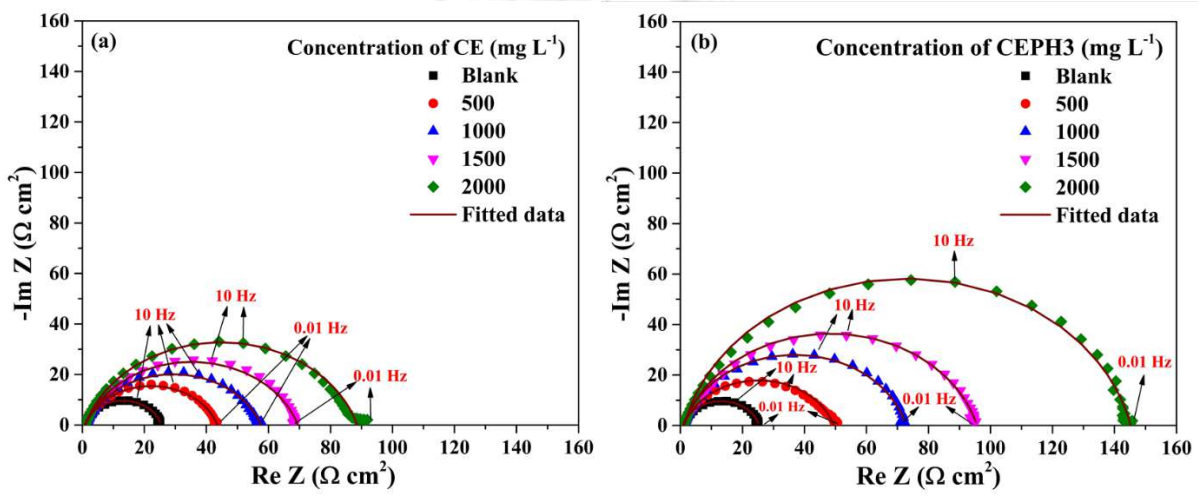

Fig. 3.7 Nyquist graphs for MS immersed in 1 M HCl in the presence and absence of CE a), CEPH3 b).

To understand the corrosion process on the metal-electrolyte interface, the above Nyquist plots were fitted to equivalent circuit models such as $R_s(Q_{dl}\ R_{ct})$ (Chidiebere et al., 2015). Simple Randles circuits have R_s (solution resistance) in series with R_{ct} (charge transfer resistance) and constant phase element (*CPE)*, but R_{ct} and *CPE* are in parallel with each other (M'hiri et al., 2016; Srivastava et al., 2018; Verma et al., 2018). The equivalent circuit is shown in Fig. 3.9. The obtained values of Nyquist parameters such as R_s, R_{ct}, *CPE*, n, goodness of fit (χ^2), μ_{Rct} (%), and C_{dl} calculated are shown in Table 3.3. From this table, it was observed that the values of χ^2 lie in the range from 1.12×10^{-3} to 4.36×10^{-3}, which depicts the good fitting of

Nyquist plots to the proposed equivalent circuit (Mourya et al., 2014; Tang et al., 2021). The R_{ct} values significantly increased with the addition of both chayote extracts (Table 3.3).

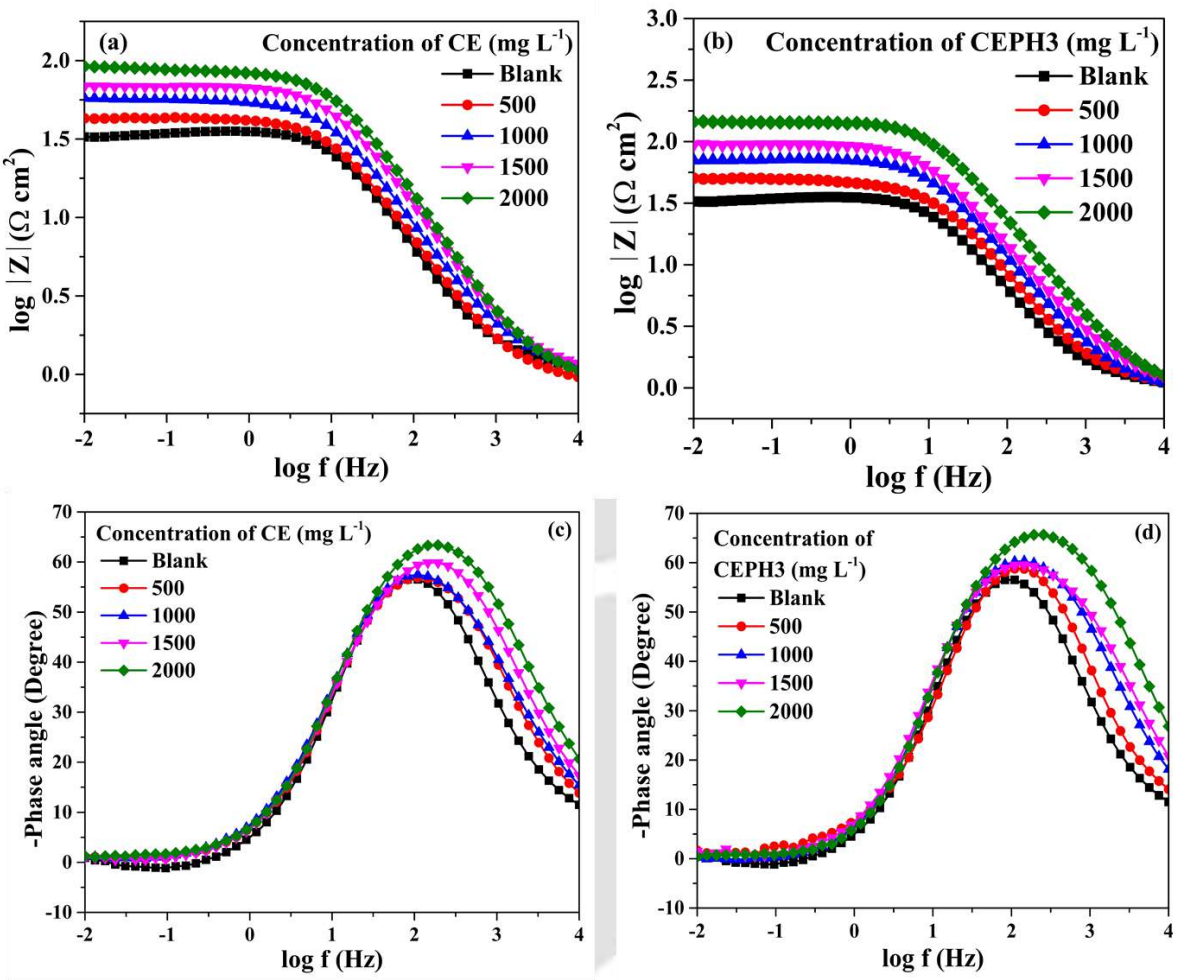

Fig. 3.8 Bode plots and phase plots for MS immersed in 1 M HCl in the presence or absence of CE and CEPH3.

This increment was due to the strong chayote extract's adsorption on the metal surface, forming a shielding layer on a metal surface that hindered the transfer of ions through the metal-electronic interface. Higher protection efficiency for MS immersed in 1 M HCl was obtained in the presence of CEPH3 as compared to CE (Table 3.3). Furthermore, R_p values were compared with those obtained from PDP measurements as presented in Table 3A.2 of

Appendix 3A, this table shows that these values are different but close to each other for inhibited or uninhibited systems. These findings suggest that results from EIS analysis have well aligned with outcomes of PDP test. The obtained inhibition efficiencies of EIS test were compared with inhibition efficiencies of PDP and weight loss analysis, and these values were higher in PDP test and their reliability were investigated by calculating p-values which confirm that electrochemical data are highly statistically significant ($p < 0.0001$) (Table 3A.3 of the Appendix 3A).

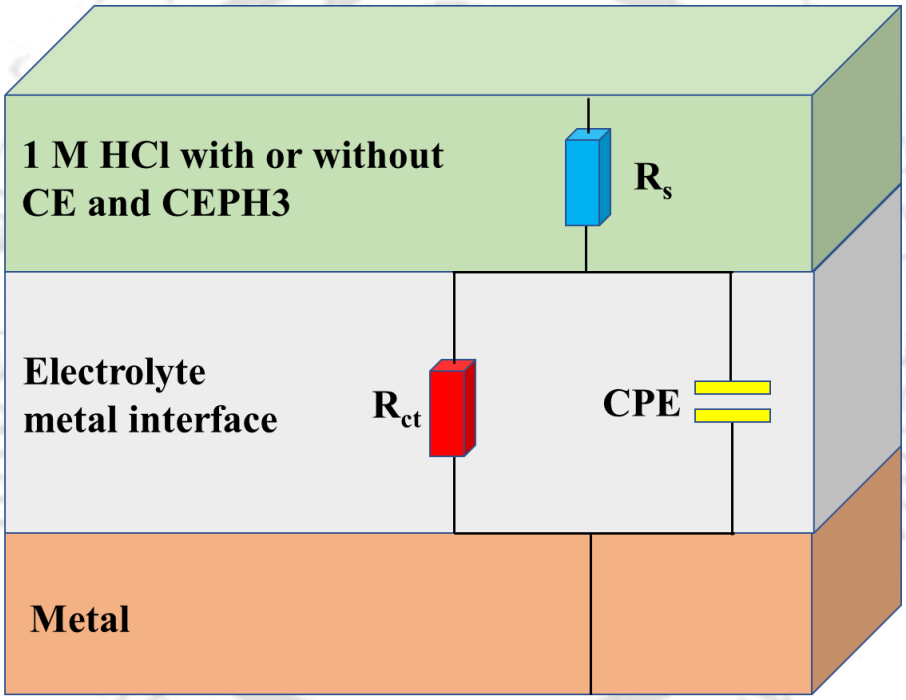

Fig. 3.9 Equivalent circuit for blank and inhibited systems with CE and CEPH3.

Table 3.3 Nyquist parameters for MS immersed in 1 M HCl in the presence and absence of CE and CEPH3.

Inhibitor	Conc. (mg L^{-1})	R_s (Ω cm^2)	R_{ct} (Ω cm^2)	CPE parameters		C_{dl} (μF cm^{-2})	Goodness of fit	μ_{Rct} (%)
				n	Y_0 (μMho cm^{-2})		(χ^2) $\times 10^{-3}$	
Blank	0	0.84 ± 0.001	25.89 ± 0.14	0.81 ± 0.001	875.67 ± 6.29	348.06 ± 0.46	1.12	-
CE	500	0.90 ± 0.001	42.80 ± 0.12	0.80 ± 0.001	780.39 ± 2.78	330.17 ± 0.61	2.11	39.50 ± 0.17
	1000	1.04 ± 0.001	56.66 ± 0.15	0.79 ± 0.001	665.93± 2.18	268.61 ± 0.34	3.23	54.30 ± 0.12
	1500	1.05 ± 0.001	68.60 ± 0.21	0.80 ± 0.001	453.23 ± 1.65	195.67 ± 0.29	2.15	62.25 ± 0.11
	2000	0.92 ± 0.001	87.48 ± 0.29	0.82 ± 0.001	354.40 ± 1.45	162.58 ± 0.28	4.36	70.40 ± 0.10
Blank	0	0.84 ± 0.001	25.89 ± 0.14	0.81 ± 0.001	875.67 ± 6.29	348.06 ± 0.46	1.12	-
CEPH3	500	1.07 ± 0.001	48.25 ± 0.14	0.81 ± 0.001	612.84 ± 2.87	260.41 ± 0.43	3.19	46.34 ± 0.16
	1000	1.00 ± 0.001	72.43 ± 0.28	0.81 ± 0.001	453.99 ± 1.99	199.47 ± 0.35	1.54	64.25 ± 0.14
	1500	1.04 ± 0.002	96.29 ± 0.54	0.79 ± 0.001	408.55 ± 2.40	164.33 ± 0.39	1.71	73.11 ± 0.15
	2000	1.01 ± 0.002	145.87 ± 0.81	0.83 ± 0.001	195.22 ± 1.01	93.93 ± 0.21	2.48	82.25 ± 0.10

3.3 Inhibition effect of ascorbic acid

Electrochemical experiments were conducted with ascorbic acid using the same ascorbic acid equivalent (0.061 mg L^{-1}) present in CEPH3 (with 2000 mg L^{-1}) at 30 ºC. Experiment data were compared with pre-obtained results for CEPH3 (with 2000 mg L^{-1}) in section 3.2. In electrochemical measurement, it was observed that values of OCP shifted in the positive direction in the presence of ascorbic acid and CEPH3 compared to the uninhibited system, as illustrated in Fig. 3.10 and Table 3.4. The obtained Tafel and Nyquist parameters for ascorbic acid and CEPH3 are listed in Tables 3.4 and 3.5, respectively. i_{corr} (in Tafel polarization) of the inhibited system significantly reduced (Fig. 3.11 (a)), and charge transfer resistance (Nyquist pattern) increased (Fig. 3.11 (b)), as compared to the uninhibited system, which indicates that ascorbic acid behaved as a good inhibitor (Ferreira et al., 2004). From Tables 3.4 and 3.5, it was observed that ascorbic acid and CEPH3 both have almost similar inhibiting behavior.

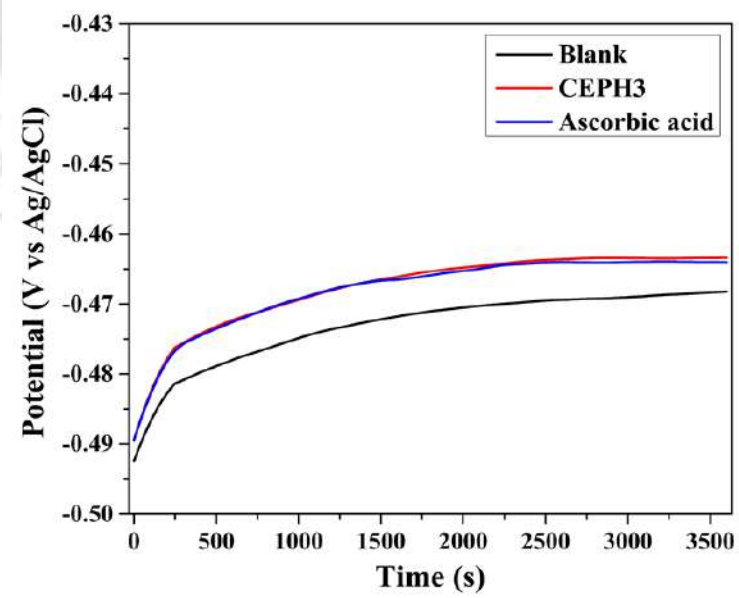

Fig. 3.10 OCP plots MS immersed in 1 M HCl in the presence and absence of CEPH3 and standard ascorbic acid.

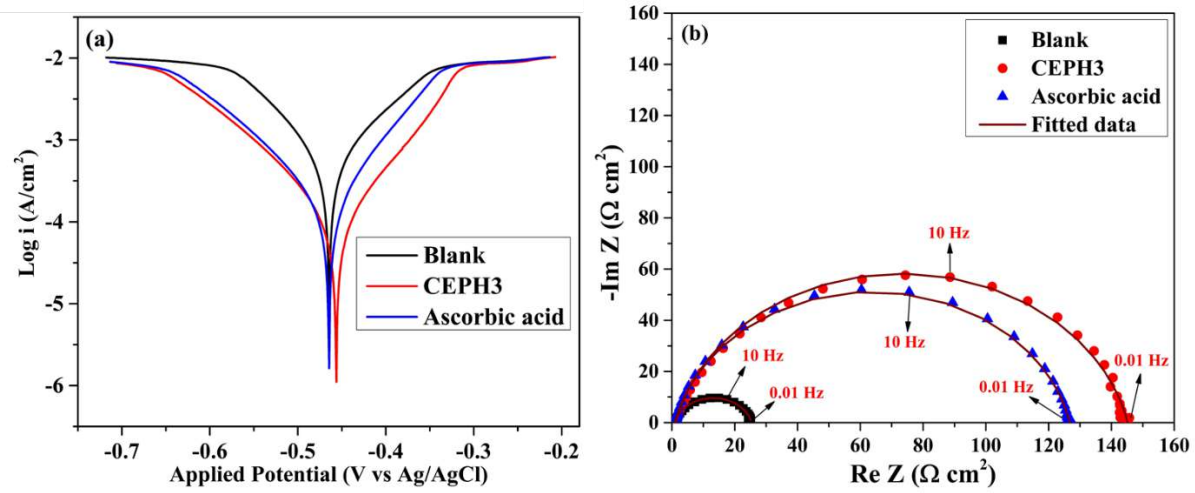

Fig. 3.11 Tafel plots a) and Nyquist plots b) of MS immersed in 1 M HCl in presence and absence of CEPH3 and standard ascorbic acid.

Table 3.4 Tafel parameters for MS immersed in 1 M HCl in the presence and absence of CEPH3 and standard ascorbic acid.

Inhibitor	Conc. (mg L^{-1})	b_a (mV dec^{-1})	$-b_c$ (mV dec^{-1})	*OCP (mV)*	E_{corr} (mV vs. Ag)	i_{corr} (µA cm^{-2})	R_p (Ω cm^2)	μ_P (%)
Blank	0	110.59 ± 0.52	120.25 ± 1.04	-468.15 ± 5.68	-465.25 ± 5.56	734.98 ± 5.23	34.04 ± 0.12	-
CEPH3	2000	87.17 ± 1.20	84.39 ± 1.33	-463.57 ± 3.23	-463.54 ± 3.74	104.92 ± 1.66	177.48 ± 0.18	85.72 ± 0.40
AA	0.061	79.21 ± 0.72	62.15 ± 0.61	-464.01 ± 3.35	-464.70 ± 2.95	132.15 ± 1.28	114.45 ± 0.06	82.02 ± 0.27

Table 3.5 Nyquist parameters for MS immersed in 1 M HCl in the presence and absence of CEPH3 and standard ascorbic acid.

Inhibitor	Conc. (mg L^{-1})	R_s (Ω cm^2)	R_{ct} (Ω cm^2)	CPE parameters		C_{dl} (µF cm^{-2})	Goodness of fit	μ_{Rct} (%)
				n	Y_0 (µMho cm^{-2})		(χ^2) ×10^{-3}	
Blank	0	0.84 ± 0.001	25.89 ± 0.14	0.81 ± 0.001	875.67 ± 6.29	348.06 ± 0.46	1.12	-
CEPH3	2000	1.01 ± 0.002	145.87 ± 0.81	0.83 ± 0.001	195.22 ± 1.01	93.93 ± 0.21	2.48	82.25 ± 0.10
AA	0.061	1.01 ± 0.001	126.09 ± 0.32	0.87 ± 0.001	180.50 ± 0.43	102.90 ± 0.10	2.61	79.46 ± 0.11

3.4 Effect of temperature

To study the thermal stability of chayote extracts, few electrochemical tests were also performed for uninhibited or inhibited MS with optimum concentration (2000 mg L^{-1}) of both chayote extracts (CE and CEPH3) at the temperature of 313 and 323 K. Here, all experiments were also performed under the same conditions as used in (section 3.2). Before each electrochemical test, 1 h OCP was measured at 303, 313, and 323 K, as shown in Figs. 3.12 (a), 3.12 (b), and 3.12 (c).

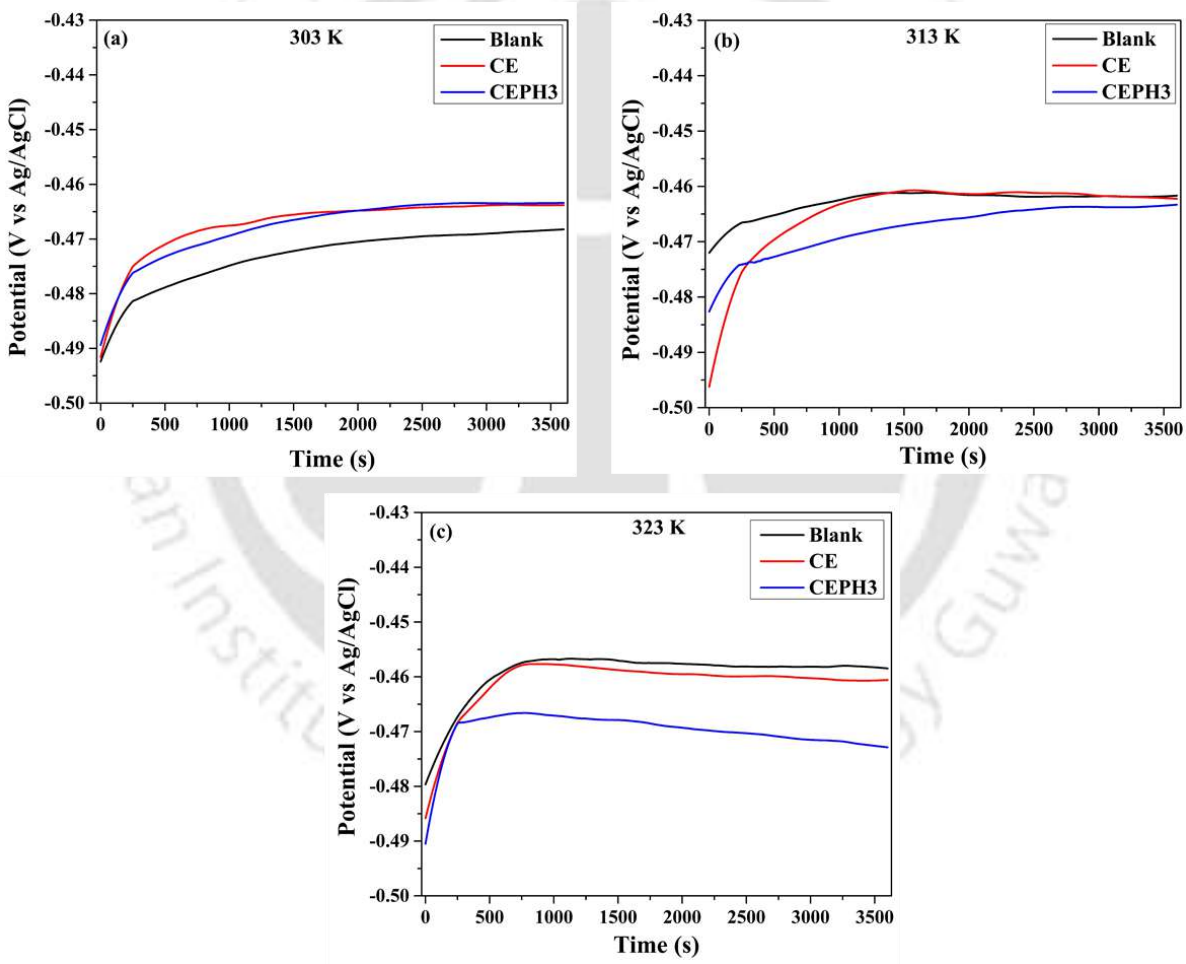

Fig. 3.12 OCP plots MS immersed in 1 M HCl in presence and absence of CE and CEPH3 at 303, 313, 323 K.

The Figs. 3.13(b), 3.13(d), and 3.13(f) show the Tafel plots of uninhibited and inhibited MS with optimum concentrations of both chayote extracts in 1 M HCl at 303, 313, and 323 K.

From Table 3.6, it was observed that i_{corr} increased and protection efficiency decreased with increasing the temperature from 303 K to 323 K. This decrease in protection efficiency caused due to the replacement of a few adsorbed inhibitor molecules from the surface of MS by water molecules, so charge transfer resistance decreased. Still, this phenomenon does not affect the protective layer much.

Figs. 3.13(a), 3.13(c), and 3.13(e) show the Nyquist plots of uninhibited and inhibited MS with optimum concentrations of both chayote extracts in 1 M HCl at 303, 313, 323 K. Nyquist plots exhibit similar depressed semicircles, which indicate the heterogeneous nature of the metal surface. In each semicircle, a large capacitive loop was observed at higher frequencies, signifying the transfer of charges through the double layer. One inductive loop was found to appear for uninhibited systems at low frequency. The inductive loop showed the relaxation of species (H^{+}_{ads}, Cl^{-}_{ads}) and corrosion products from the MS surface. This inductive loop disappeared in the presence of an inhibitor, and only one capacitive loop remained. It signifies that MS dissolution in acid is mainly charge transfer controlled. These Nyquist plots for inhibited or uninhibited systems depict that reactions on the interface of metal-electrolytes are charge transfer controlled, and the semicircle diameter represents the charge transfer resistance (R_{ct}). To obtain the EIS parameters, Nyquist plots were fitted to an equivalent circuit model, as mentioned in section 3.2. Nyquist parameters are shown in Table 3.7. From Table 3.6, it was observed that polarization resistance and protection efficiency both decreased with increasing temperature. 71.88% protection efficiency was obtained in inhibited MS by CEPH3 in 1 M HCl at 323 K.

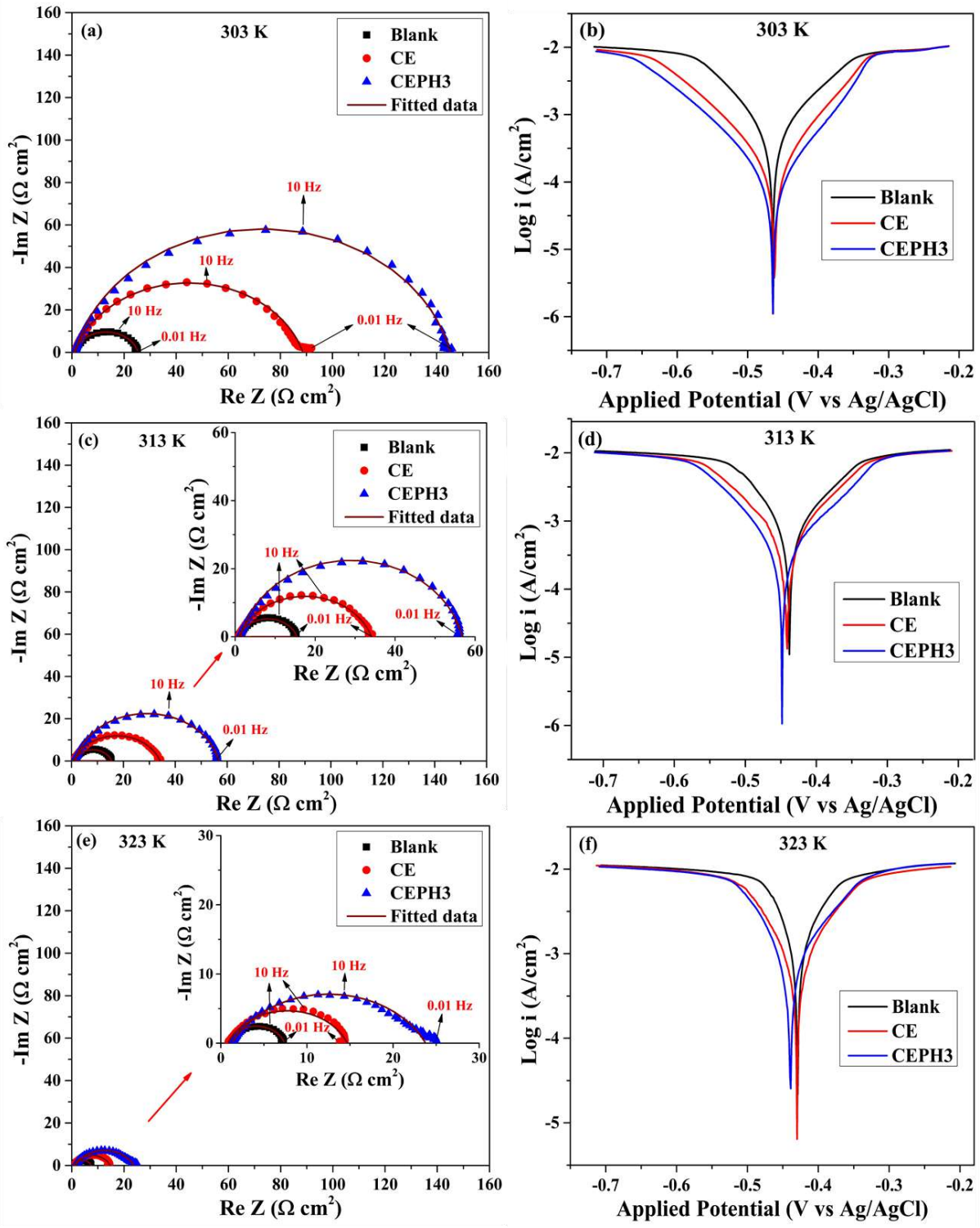

Fig. 3.13 Nyquist and Tafel plots for both chayote extracts (CE and CEPH3) at 303, 313, and 323.

Table 3.6 Tafel parameters for both chayote extracts (CE and CEPH3) at 303 K, 313 K, and 323 K.

Temperature (K)	Inhibitor	Conc. (mg L^{-1})	b_a (mV dec^{-1})	$-b_c$ (mV dec^{-1})	*OCP (mV)*	E_{corr} (mV vs. Ag)	i_{corr} (µA cm^{-2})	R_p (Ω cm^2)	*CR* (mm $Year^{-1}$)	μ_P (%)
303	Blank	0	110.59 ± 0.52	120.25 ± 1.04	-468.15 ± 5.68	-465.25 ± 5.56	734.98 ± 5.23	34.04 ± 0.12	8.54 ± 0.45	–
	CE	2000	95.39 ± 0.75	78.45 ± 0.67	-463.79 ± 2.26	-461.58 ± 2.49	170.35 ± 1.53	109.74 ± 0.08	1.98 ± 0.12	76.82 ± 0.54
	CEPH3	2000	87.17 ± 1.20	84.39 ± 1.33	-463.57 ± 3.23	-463.54 ± 3.74	104.92 ± 1.66	177.48 ± 0.18	1.22 ± 0.03	85.72 ± 0.40
313	Blank	0	105.06 ± 1.08	165.79 ± 2.35	-461.76 ± 6.93	-437.85 ± 6.52	1302.48 ± 11.03	21.44 ± 0.04	15.13 ± 0.94	–
	CE	2000	69.43 ± 0.30	69.81 ± 0.97	-462.25 ± 5.10	-441.90 ± 2.27	410.56 ± 3.39	36.82 ± 0.03	4.77 ± 0.15	68.48 ± 0.10
	CEPH3	2000	70.18 ± 1.30	92.65 ± 2.53	-463.35 ± 4.12	-448.28 ± 3.84	336.30 ± 3.17	51.55 ± 0.13	3.91 ± 0.10	74.18 ± 0.44
323	Blank	0	146.54 ± 1.38	285.84 ± 1.51	-458.16 ± 5.43	-429.41 ± 6.35	4429.22 ± 36.40	9.50 ± 0.01	51.45 ± 2.96	–
	CE	2000	135.80 ± 6.59	164.93 ± 2.36	-460.72 ± 3.45	-431.94 ± 2.34	1692.34 ± 22.56	19.10 ± 0.34	19.66 ± 1.03	61.79 ± 0.22
	CEPH3	2000	96.73 ± 0.28	134.21 ± 1.84	-472.63 ± 4.47	-439.48 ± 3.57	1245.30 ± 9.53	19.60 ± 0.01	14.46 ± 0.92	71.88 ± 0.13

Table 3.7 EIS parameters for both chayote extracts (CE and CEPH3) at 303 K, 313 K, and 323 K.

Temperature (K)	Inhibitor	Conc. (mg L^{-1})	R_s (Ω cm^2)	R_{ct} (Ω cm^2)	*CPE* parameters		C_{dl} (μF cm^{-2})	Goodness of fit (χ^2) $\times 10^{-3}$	μ_{Rct} (%)
					n	Y_0 (μMho cm^{-2})			
303	Blank	0	0.84 ± 0.001	25.89 ± 0.14	0.81 ± 0.001	875.67 ± 6.29	348.06 ± 0.46	1.12	-
	CE	2000	0.92 ± 0.001	87.48 ± 0.29	0.82 ± 0.001	354.40 ± 1.45	162.58 ± 0.28	4.36	70.40 ± 0.10
	CEPH3	2000	1.01 ± 0.002	145.87 ± 0.81	0.83 ± 0.001	195.22 ± 1.01	93.93 ± 0.21	2.48	82.25 ± 0.10
313	Blank	0	0.85 ± 0.002	16.51 ± 0.07	0.77 ± 0.001	1492.67 ± 16.43	446.72 ± 1.74	1.68	-
	CE	2000	0.87 ± 0.001	33.31 ± 0.13	0.80 ± 0.001	561.07 ± 3.23	192.79 ± 0.39	2.87	50.44 ± 0.29
	CEPH3	2000	1.08 ± 0.002	56.17 ± 0.34	0.81 ± 0.001	489.40 ± 3.60	188.11 ± 0.39	1.45	70.61 ± 0.09
323	Blank	0	0.88 ± 0.003	7.67 ± 0.04	0.71 ± 0.002	3744.063 ± 28.06	865.87 ± 2.57	2.23	-
	CE	2000	0.82 ± 0.001	13.79 ± 0.07	0.76 ± 0.001	1273.41± 12.57	347.77 ± 0.92	3.17	44.36 ± 0.07
	CEPH3	2000	1.28 ± 0.001	22.66 ± 0.05	0.71± 0.001	1169.40.22 ± 6.59	248.80 ± 0.37	4.29	66.14 ± 0.00

3.4.1 Effect of activation energy

Tafel data was utilized to determine the effect of activation energy on the corrosion rate of uninhibited and inhibited MS immersed in 1 M HCl. To calculate the activation energy of uninhibited and inhibited systems, ln (i_{corr}) (μA cm^{-2}) was plotted with 1/T (K^{-1}), which is presented in Fig. 3.14(a). This Figure shows a linear straight line for the slope of (-E_a/R) with an intercept of (ln A). The calculated activation energies for all systems are shown in (Table 3.8). The influence of temperature can be used to assess kinetic parameters, such as enthalpy and entropy of the corrosion process. Furthermore, to calculate the values of enthalpy and entropy, ln (i_{corr}/T) (μA cm^{-2} K^{-1}) were plotted against 1/T, which is shown in Fig. 3.14 (b). This Figure shows a linear straight line for the slope of (-ΔH /R) with the intercept of ($\ln\frac{k_B}{h} + \frac{\Delta S}{R}$). Calculated ΔH and ΔS are shown in Table 3.8.

From Table 3.8, it is observed that E_a increases with the addition of chayote extracts, which means more energy is required to corrode the metal surface compared to uninhibited MS. Few studies reported a decrease in inhibition efficiency with a rise in temperature, with a corresponding increase in corrosion activation energy (E_a) of inhibited system as compared to uninhibited, this change signifies the development of an adsorption film by physical (electrostatic) interactions. Conversely, inhibition efficiency increases with an increase in temperature, and the activation energy decreases in the presence of the inhibitor as compared to uninhibited systems, suggesting a chemisorption mechanism (Popova et al., 2003; Satapathy et al., 2009). In this work, chayote extracts inhibit the MS corrosion by physical interaction with the MS surface. The computed value of enthalpy of activation for an uninhibited system is positive, and it also increases in the presence of chayote extracts, which means that corrosion of MS is an endothermic process.

The obtained values of (E_a - ΔH) were nearly the same and equal to the value of RT for each system, implying that the corrosion process is an unimolecular reaction. Additionally, the

change in entropy shifted to more positive values for inhibited systems. This increase in entropy is attributed to the assumption of an activated complex forming in the rate-determining step of the corrosion process. The overall entropy rises because the conversion of reactants into activated complexes involves replacing pre-adsorbed water molecules on the surface of MS. Consequently, the inhibited system anticipates a more orderly arrangement of inhibitor molecules on the MS surface due to their association.

If the values of entropy decreased for the inhibited system as compared to blank, it indicates that in the rate-determining phase, activation of chayote extracts represents a dissociation rather than an association step and that the transition from reactants to the activated complex results in an increase in disordering (Al-Moubaraki and Awaji, 2020; Aloui et al., 2009; Jeeja et al., 2022).

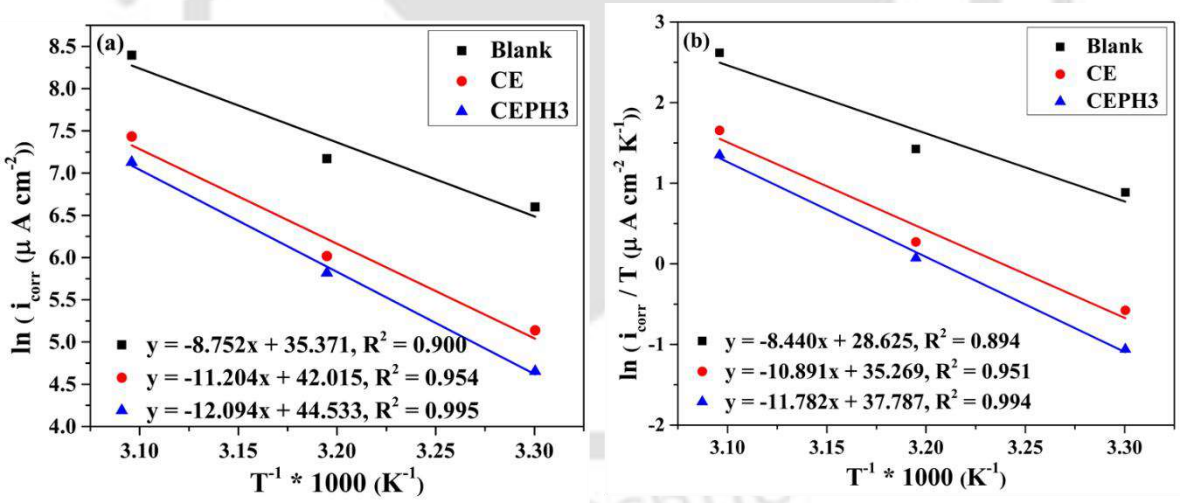

Fig. 3.14 Arrhenius (a) and Transition state plots (b) for CE and CEPH3 at 303 K, 313 K, and 323 K.

Table 3.8 Kinetic parameters for blank, CE, and CEPH3 in 1 M HCl.

Inhibitor	Conc. (mg L^{-1})	Pre-exponential factor, A (μA cm^{-2})	E_a (kJ mol^{-1})	ΔH (kJ mol^{-1})	ΔS (J mol^{-1} K^{-1})	E_a - ΔH (kJ mol^{-1})
Blank	0	$(2.30 \pm 0.21) \times 10^{15}$	72.76 ± 0.25	70.17 ± 0.27	40.45 ± 0.78	2.59
CE	2000	$(1.76 \pm 0.17) \times 10^{18}$	93.15 ± 0.75	90.55± 0.74	95.68 ± 0.75	2.60
CEPH3	2000	$(2.19 \pm 0.22) \times 10^{19}$	100.55 ± 0.84	97.95± 0.87	116.62± 0.84	2.60

3.5 Adsorption studies

In this work, Langmuir, Temkin, and Frumkin adsorption isotherms were tested at several θ (surface coverage) values for various amounts of ascorbic acid (C_{inh} (mg L^{-1})) of both chayote extracts, such as CE (0.005, 0.01, 0.015, and 0.02 mg L^{-1}) and CEPH3 (0.015, 0.031, 0.046, and 0.061 mg L^{-1}). For these adsorption isotherms, fitting plots are shown in Fig. 3.15. The most excellent fit was gained for Langmuir adsorption isotherm because its slopes are very near to 1 for both chayote extracts (Fig. 3.15 (a) and (b)). The obtained values of K_{ads} for both chayote extracts are 142.857 L mg^{-1} (CE) and 47.62 L mg^{-1} (CEPH3) (Table 3.9). The values of standard Gibbs free energy (ΔG^o_{ads}) at room temperature were calculated by the following equation (Eq. (3.1)) (Zhou and Zhou, 2014):

$$\Delta G^o_{ads} = -RTln(K_{ads} \times M_{adsorbate} \times 1000 \times C_{water}) \quad (3.1)$$

where K_{ads} represent equilibrium adsorption constant (L mg^{-1}), C_{water} represents the concentration of water in solution (55.5 mol L^{-1}), $M_{adsorbate}$ represent the molecular weight of the inhibitor (Ascorbic acid, 176.12 g mol^{-1}), R represents gas constant (R = 8.314 J K^{-1} mol^{-1}), and T represents absolute temperature (K). Few studies have reported that the value of ΔG^o_{ads} is -20 $kJmol^{-1}$ or less negative than that, corresponding to the physisorption of charged inhibitor molecules with the charged metal surface. If the value of ΔG^o_{ads} is -40 $kJmol^{-1}$ or more negative, electrons are shared by the inhibitor and charged metal, and this adsorption is known as

chemisorption. If the value of ΔG^{o}_{ads} lies between -40 kJmol^{-1} and -20 kJmol^{-1}, the adsorption is known as a mixed type of adsorption.

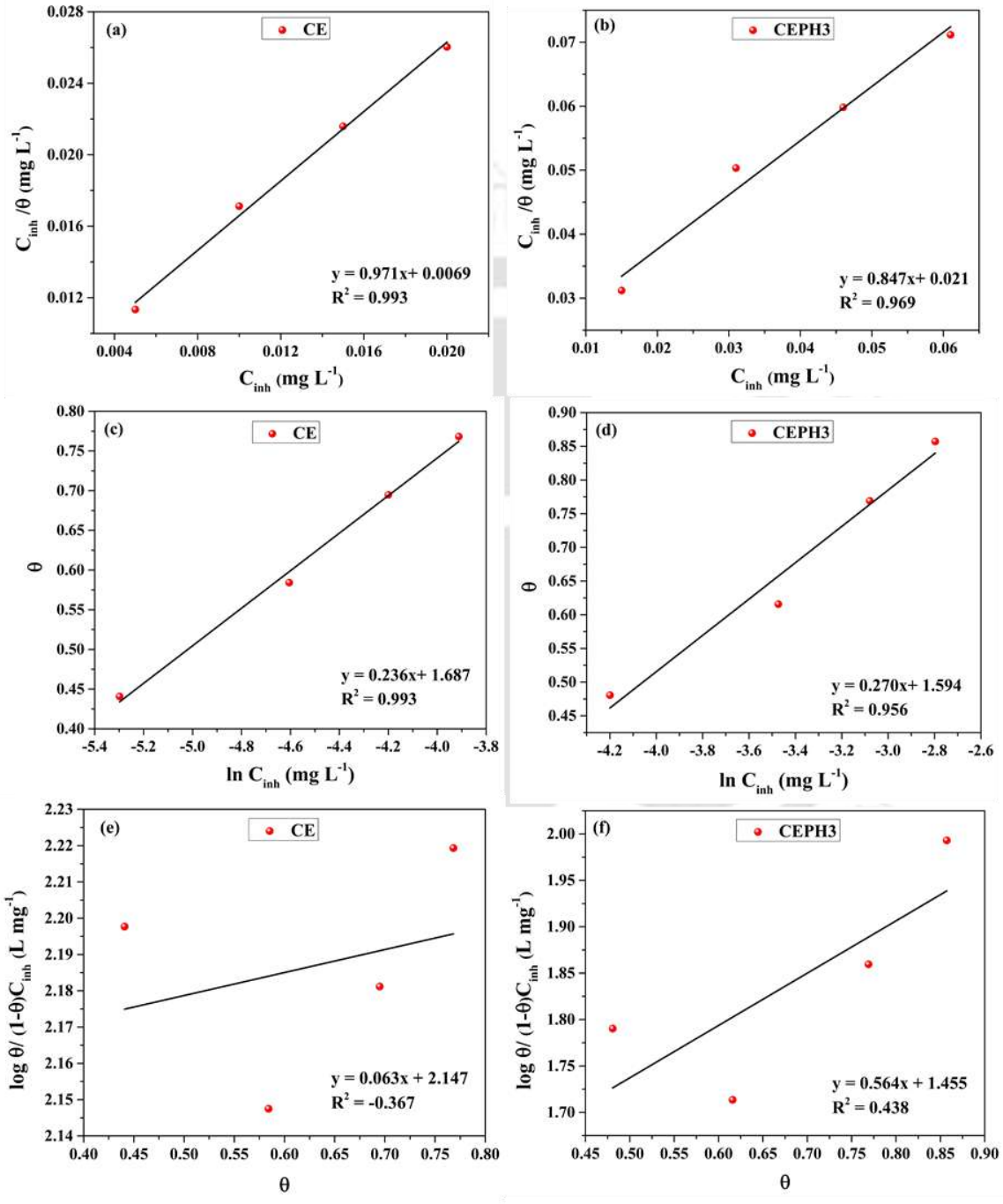

Fig. 3.15 Langmuir (a, b), Temkin (c,d), and Frumkin adsorption isotherm (e,f) for CE and CEPH3, respectively.

In the present study, the unbound lone pair of hydroxyl groups of ascorbic acid interacts with the metal surface, resulting in the strong adsorption of chayote extracts on the metal surface. Hence, the obtained values of ΔG^{o}_{ads} for both extracts are -53.046 kJmol^{-1} (CE) and -50.278 kJmol^{-1} (CEPH3). The negative value of ΔG^{o}_{ads} represents chayote extract (ascorbic acid) molecules could self-adsorb on MS surface from acid solution (1 M HCl) as expected since organic molecules are adsorbed by spontaneous adsorption process (Al-Moubaraki, 2018; Kaya et al., 2023b, 2023a) The calculated values are more negative than -40 kJmol^{-1}, which depicts that the chayote extracts are adsorbed by chemical adsorption process on the metal surface (Chidiebere et al., 2015).

Table 3.9 Adsorption isotherm parameters.

Inhibitor	$1/K_{ads}$ (mg L^{-1})	K_{ads} (L mg^{-1})	ΔG^{o}_{ads} (KJ mol^{-1})
CE	0.007 ± 0.001	142.857 ± 2.101	-53.046 ± 0.036
CEPH3	0.021 ± 0.001	47.619 ± 0.816	-50.278 ± 0.042

3.6 Surface investigation

3.6.1 FESEM analysis

FESEM images of MS before and after their immersion in 1 M HCl for the period of 2 h are depicted in Figs. 3.16 (a) and (b), respectively. The first images demonstrated a highly polished, smooth, and corrosion-free surface used in corrosion tests. Fig. 3.16 (b) displayed that exposed MS was significantly destructed and corrosion products completely covered the metal surface. A significant accumulation of corrosion products on the metal surface signifies the metal's poor performance against corrosion media. This image also contains many pits and cracks due to the HCl attack on MS. Figs. 3.16 (c) and (d) illustrate the spectra of inhibited MS after 2 h immersion in acid, showing a smoother surface compared to uninhibited MS. It implies

that the adsorption of chayote extracts forms a shielding layer on the surface of the metal, which provides sufficient resistance to transfer the corrosive ions from the electrolyte to the interface of the solution and metal surface.

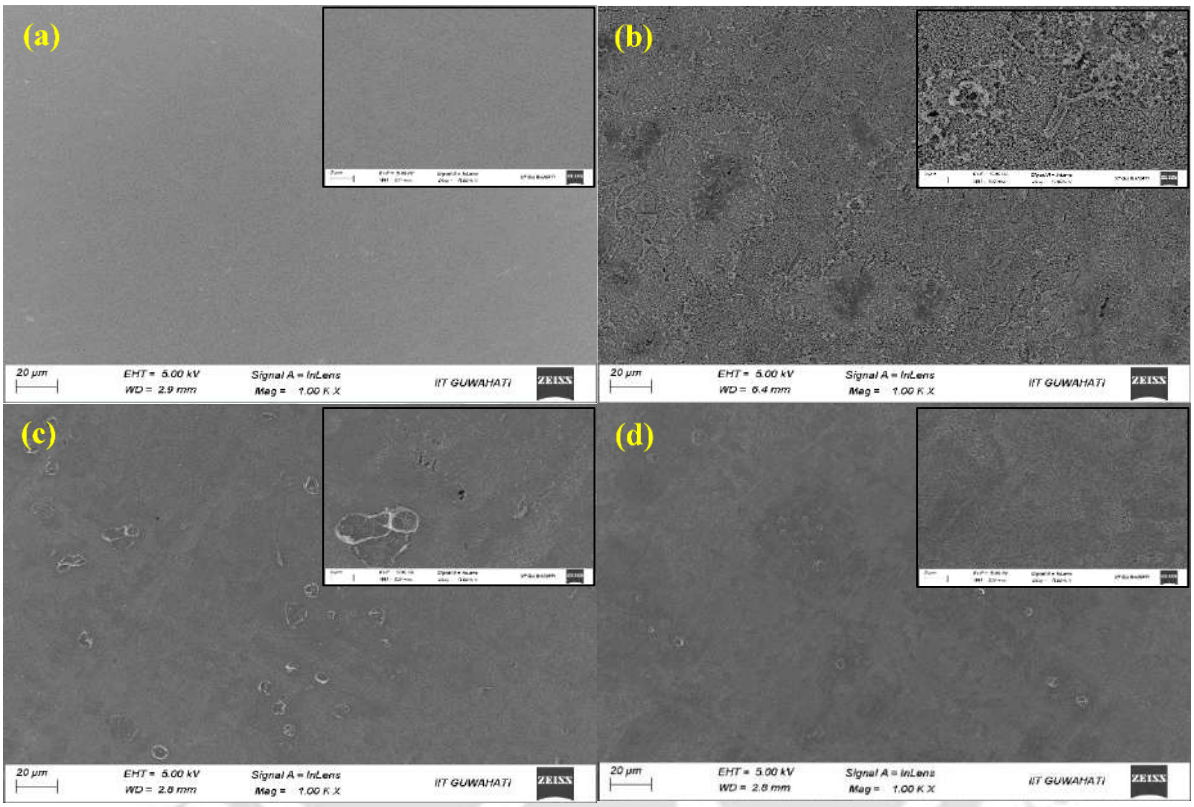

Fig. 3.16 FESEM images of a) polished MS before immersion, b) uninhibited MS after immersion, c) and d) inhibited MS immersed in 1 M HCl in the presence of CE and CEPH3.

3.6.2 EDX analysis

The surface of inhibited and uninhibited MS specimens after their immersion in 1 M HCl has been investigated by EDX analysis. The image of the uninhibited MS surface after 4 h immersion in 1 M HCl and selected pit (from uninhibited spectra) are shown in Figs. 3.17 (a) and (b), respectively. On comparing these two spectra, a higher percentage of oxygen and chloride ions were found inside the pit, which implies that pits have been corroded rapidly

compared to plane surfaces. Figs. 3.17 (c) and 3.16 (d) show EDX spectra of inhibited MS after 4 h immersion in 1 M HCl in the presence of CE and CEPH3, respectively. On comparing all the EDX spectra, it has been observed that the percentage of oxygen and chloride ions are significantly less in inhibited systems and least for CEPH3, which shows the strong adsorption of chayote extracts on the metal surface.

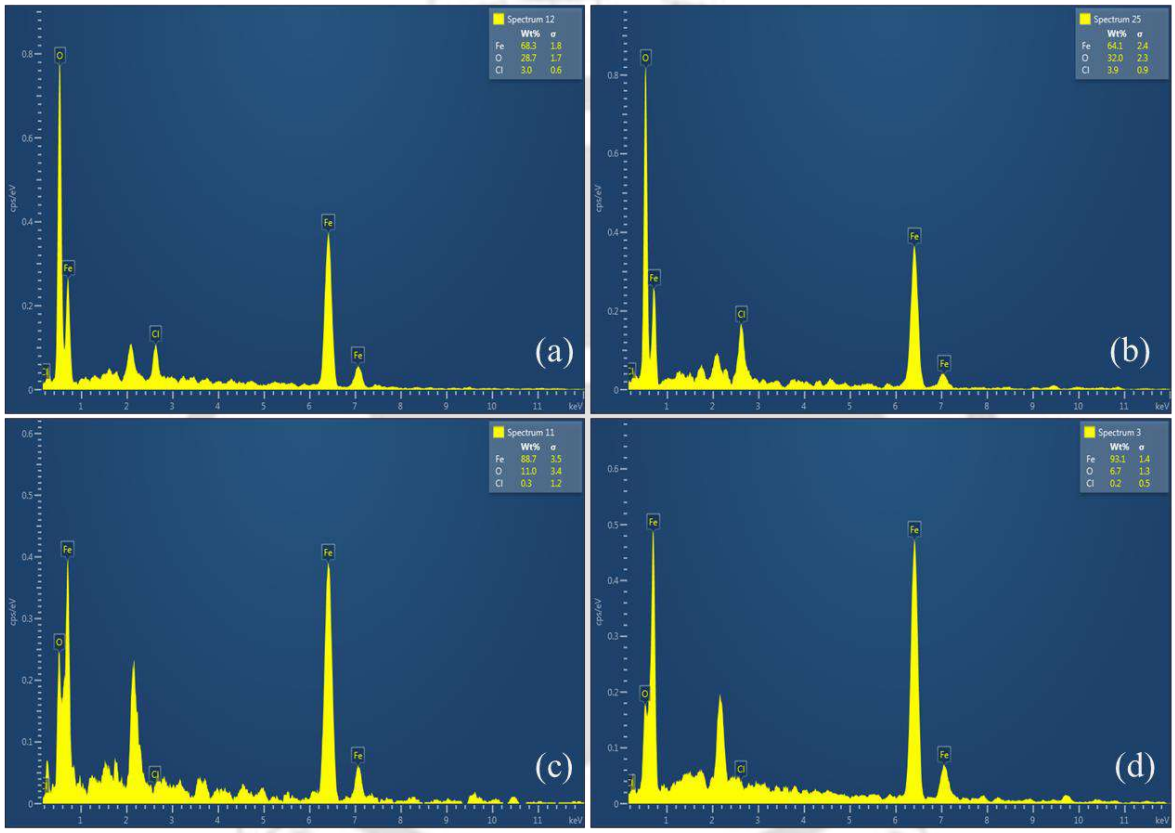

Fig. 3.17 EDX image of a) uninhibited MS, b) selected pits from uninhibited spectra, c) inhibited with CE, and d) inhibited with CEPH3 after immersion in 1 M HCl.

3.6.3 AFM analysis

AFM analysis is a tool utilized to observe the effect of the green inhibitor against the corrosion of MS in corrosive electrolytes in terms of change in roughness. The AFM images of MS after 3 h exposure to 1 M HCl, in the presence or absence of chayote extracts (Fig. 3.18). The image of uninhibited MS is shown in Fig. 3.18(a), has a highly rough and cracked surface, which means MS surface is hugely damaged by the attack of corrosive ions in the uninhibited system. In the absence of chayote extracts, MS has an average surface roughness of 486.70 nm. The roughness of the MS surface decreases from 486.70 nm to 29.40 nm and 23.18 nm in the presence of CE and CEPH3, respectively (Figs. 3.18(b)-(c)). This significant change in surface roughness in the presence of both chayote extracts suggests that inhibitor molecules form a protective layer on the metal surface, isolating the metal surface from a corrosive medium (Verma et al., 2017). From these figures, it is also observed that a higher smooth surface was obtained with CEPH3 (Fig. 3.18(c)) due to the strong adsorption of CEPH3 molecules on the metal surface.

3.6.4 XRD analysis

XRD patterns of MS samples before and after their immersion in 1 M HCl for 2 h with and without chayote extracts are shown in Fig. 3.19. XRD spectra of MS coupons before immersion show a strong peak at 44.59° with three weak peaks at 64.8°, 82.2°, and 90° (Fig. 3.19(a)). The XRD spectrum of uninhibited MS shows a series of peaks at 35.2°, 44.59°, 64.8°, 82.2°, and 90° (Fig. 3.19(b)), which are well matched with peaks of Fe and $FeCl_2$ in JCPDS: 06-0696. The peak at 35.2° corresponds to the chloride of iron, and the rest corresponds to iron (Fe). In XRD spectra of inhibited MS, the peaks appear only for iron at 44.59°, 82.2°, and 90° (Fig. 3.19(c)). From these spectrums, it has been observed that peak intensity was decreased.

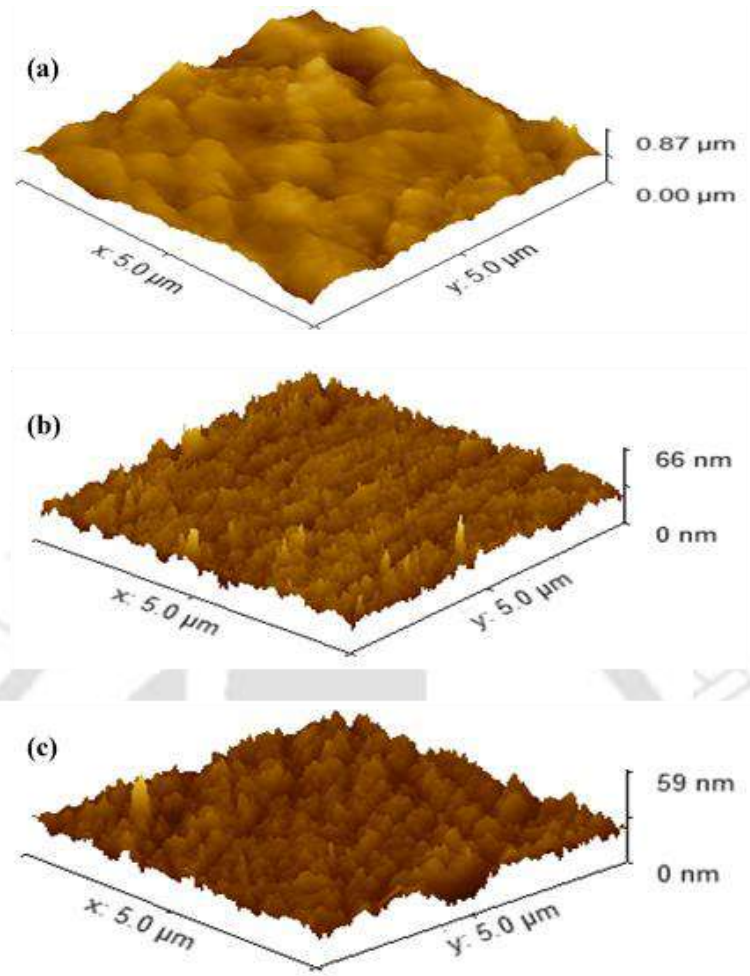

Fig. 3.18 AFM image of uninhibited MS a), inhibited with CE b), and CEPH3 c) after immersion in 1 M HCl.

The corrosion product may include substantially less metal oxide than usual, which could help prevent corrosion for inhibited systems, implying that adsorbed inhibitor molecules formed a defensive layer. This method may help complete the interaction of the inhibitor with the metallic surface. The XRD analysis is well concord with the outcomes of FESEM, EDX, and AFM analysis (Muthukrishnan et al., 2019).

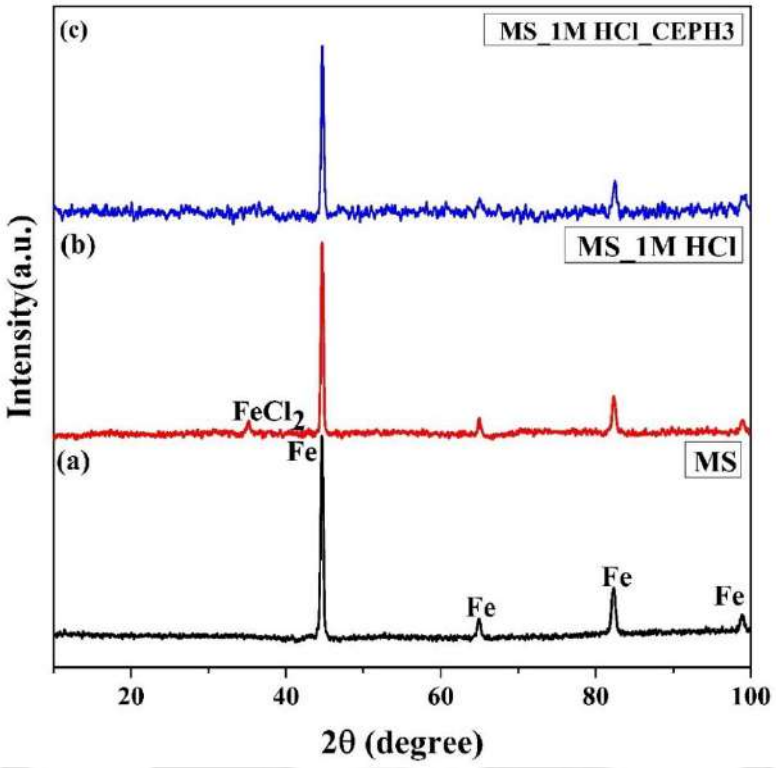

Fig. 3.19 XRD spectra of highly polished MS (a), absence of inhibitor (b), and (c) presence of inhibitor after exposed to 1 M HCl.

3.7 Mechanism of corrosion and inhibition

The mechanism for the corrosion of MS in 1 M HCl solution is proposed as follows:

The anodic dissolution mechanism of MS is given by the following reactions (Eqs. (3.2 – 3.5)):

$$Fe + Cl^- \leftrightarrow (FeCl^-)_{ads} \quad (3.2)$$

$$(FeCl^-)_{ads} \leftrightarrow (FeCl)_{ads} + e^- \quad (3.3)$$

$$(FeCl)_{ads} \rightarrow (FeCl^+)_{ads} + e^- \quad (3.4)$$

$$(FeCl^+)_{ads} \leftrightarrow Fe^{2+} + Cl^- \quad (3.5)$$

The cathodic hydrogen evolution mechanism is given by the following reactions (Eqs. (3.6 – 3.8)):

$$Fe + H^+ \leftrightarrow (FeH^+)_{ads} \quad (3.6)$$

$$(FeH^+)_{ads} + 2e^- \rightarrow (FeH)_{ads} \quad (3.7)$$

$$(FeH^+)_{ads} + H^+ + 2e^- \rightarrow Fe + H_2 \quad (3.8)$$

The anticorrosive behavior of both chayote extracts in corrosive solutions depends on their interaction with metal (Shukla and Quraishi, 2009). Electrostatic interactions with pre-adsorbed Cl^- ions on a metal surface cause protonated inhibitor molecules to be adsorbed (physical adsorption). On the metal surface, the H+ ions and the protonated inhibitor compete for electrons. Then, the cationic form of chayote extracts transforms back into neutral after absorbing electrons from the metal surface. Chemical adsorption of inhibitors is encouraged due to the presence of inhibitor molecules (ascorbic acid) with unbound lone pairs. The accumulation of electrons on the metal surface causes more negative charges over time. To relieve the excess of negative charge, the electron moves from the d-orbital of Fe to the unoccupied π antibonding orbital of the inhibitor (retro-donation), resulting in an increase in the inhibitor's adsorption on the metal surface (Srivastava et al., 2018).

Results from Tafel measurement show that chayote extracts behaved as a mixed type of inhibitor. Adsorption isotherms revealed that the chayote extracts (ascorbic acid) were adsorbed by a chemical adsorption process. The anticorrosive behavior of ascorbic acid has been investigated in few studies. Ascorbic acid forms chelate by utilizing the hydroxyl groups within the lactone ring. These chelates can strongly bind to the steel surface by forming stable bonds with coordinately unsaturated Fe-ions on the metal surface (Brixi et al., 2022).

3.8 Summary

Chayote extract was developed as a novel inhibitor to protect the immersed MS in 1 M HCl. The prepared extract showed an excellent inhibitory effect against 1 M HCl due to the presence of ascorbic acid. The presence of ascorbic acid in chayote extract was confirmed by FTIR analysis. The ascorbic acid content strongly depends upon the pH of the extracting

solvent in chayote extract. Therefore, the extract was prepared at different pH (3, 5, 7, and 9) of extracting solvent (water) to improve its inhibition efficiency. The maximum ascorbic acid content was extracted at pH 3 (CEPH3). Subsequently, CEPH3 and CE (original pH 5.2) chayote extracts were selected to investigate their anticorrosive behavior in 1 M HCl. After all studies, the following conclusion is obtained.

The corrosion current density (i_{corr}) reduction was obtained as 76.82% and 85.72% compared to blank on the addition of CE and CEPH3, respectively. The average corrosion potential shifted to the positive side by adding both chayote extracts. Furthermore, the highest inhibiting efficiency (85.72%) was obtained in the presence of 2000 mg L^{-1} of CEPH3.

The values of charged transfer resistances (R_{ct}) using CE and CEPH3 were found to be about 3.38 and 5.63 folds higher compared to blank (25.89 Ω cm^2), resulting in charge transfer resistance increased with the concentration of both chayote extracts. Moreover, charge transfer resistance increased because corrosive ions faced higher hindrances to reaching the metal surface in the inhibited system. Similar inhibition behavior of CE and CEPH3 chayote extracts was obtained in weight loss studies.

CEPH3 showed a remarkable inhibition efficiency of 71.88 % at 323 K. In the presence of chayote extracts, obtained values of E_a, ΔH, and ΔS were increased compared to uninhibited immersed MS in 1 M HCl.

The chayote extracts (CE and CEPH3) were adsorbed on the surface of the metal by the chemical adsorption process, which was confirmed by the values of ΔG°_{ads} obtained as -53.046 kJ mol^{-1} and -50.278 kJ mol^{-1} in the case of CE and CEPH3, respectively.

Surface investigations showed that CEPH3 creates a strong shielding layer over the metal-acid interface due to the presence of ascorbic acid in the extract, resulting in strong mitigation to MS dissolution in 1 M HCl.

3.9 References

Al-Moubaraki, A.H., 2018. Potential of borage flowers aqueous extract, Borago officinalis L., against the corrosion of mild steel in phosphoric acid. Anti-Corrosion Methods Mater. 65, 53–65. https://doi.org/10.1108/ACMM-04-2017-1788

Al-Moubaraki, A.H., Awaji, H., 2020. 1-X-4-[4´-(–OCH3)-Styryl] pyridinium iodides, potent inhibitors for stainless steel corrosion in 2 M HCl acid solutions. Int. J. Corros. Scale Inhib. 9, 460–501. https://doi.org/10.17675/2305-6894-2020-9-2-5

Ali Asaad, M., Sarbini, N.N., Sulaiman, A., Ismail, M., Huseien, G.F., Abdul Majid, Z., Bothi Raja, P., 2018. Improved corrosion resistance of mild steel against acid activation: Impact of novel Elaeis guineensis and silver nanoparticles. J. Ind. Eng. Chem. 63, 139–148. https://doi.org/10.1016/j.jiec.2018.02.010

Aloui, S., Forsal, I., Sfaira, M., Touhami, M.E., Taleb, M., Baba, M.F., Daoudi, M., 2009. New mechanism synthesis of 1,4-benzothiazine and its inhibition performance on mild steel in hydrochloric acid. Port. Electrochim. Acta 27, 599–613. https://doi.org/10.4152/pea.200905599

Brixi, N.K., Sail, L., Bezzar, A., 2022. Application of ascorbic acid as green corrosion inhibitor of reinforced steel in concrete pore solutions contaminated with chlorides. J. Adhes. Sci. Technol. 36, 1176–1199. https://doi.org/10.1080/01694243.2021.1962090

Canales, C., Galarce, C., Rubio, F., Pineda, F., Anguita, J., Barros, R., Parragué, M., Daille, L.K., Aguirre, J., Armijo, F., Pizarro, G.E., Walczak, M., De la Iglesia, R., Navarrete, S.A., Vargas, I.T., 2021. Testing the Test: A comparative study of marine microbial corrosion under laboratory and field conditions. ACS Omega 6, 13496–13507. https://doi.org/10.1021/acsomega.1c01762

Chidiebere, M.A., Oguzie, E.E., Liu, L., Li, Y., Wang, F., 2015. Ascorbic acid as corrosion inhibitor for Q235 mild steel in acidic environments. J. Ind. Eng. Chem. 26, 182–192. https://doi.org/10.1016/j.jiec.2014.11.029

Daoudi, W., El Aatiaoui, A., Falil, N., Azzouzi, M., Berisha, A., Olasunkanmi, L.O., Dagdag, O., Ebenso, E.E., Koudad, M., Aouinti, A., Loutou, M., Oussaid, A., 2022. Essential oil of Dysphania ambrosioides as a green corrosion inhibitor for mild steel in HCl solution. J. Mol. Liq. 363, 119839. https://doi.org/10.1016/j.molliq.2022.119839

Farias, M.D.P., Albuquerque, P.B.S., Soares, P.A.G., de Sá, D.M.A.T., Vicente, A.A., Carneiro-da-Cunha, M.G., 2018. Xyloglucan from Hymenaea courbaril var. courbaril seeds as encapsulating agent of l-ascorbic acid. Int. J. Biol. Macromol. 107, 1559–1566.

https://doi.org/10.1016/j.ijbiomac.2017.10.016

Faustin, M., Maciuk, A., Salvin, P., Roos, C., Lebrini, M., 2015. Corrosion inhibition of C38 steel by alkaloids extract of Geissospermum laeve in 1 M hydrochloric acid: Electrochemical and phytochemical studies. Corros. Sci. 92, 287–300. https://doi.org/10.1016/j.corsci.2014.12.005

Ferreira, E.., Giacomelli, C., Giacomelli, F.., Spinelli, A., 2004. Evaluation of the inhibitor effect of l-ascorbic acid on the corrosion of mild steel. Mater. Chem. Phys. 83, 129–134. https://doi.org/10.1016/j.matchemphys.2003.09.020

Haldhar, R., Prasad, D., Kamboj, D., Kaya, S., Dagdag, O., Guo, L., 2021. Corrosion inhibition, surface adsorption and computational studies of Momordica charantia extract: a sustainable and green approach. SN Appl. Sci. 3, 25. https://doi.org/10.1007/s42452-020-04079-x

Haldhar, R., Prasad, D., Saxena, A., Kumar, R., 2018. Experimental and theoretical studies of Ficus religiosa as green corrosion inhibitor for mild steel in 0.5 M H_2SO_4 solution. Sustain. Chem. Pharm. 9, 95–105. https://doi.org/10.1016/j.scp.2018.07.002

Haque, J., Verma, C., Srivastava, V., Nik, W.B.W., 2021. Corrosion inhibition of mild steel in 1 M HCl using environmentally benign Thevetia peruviana flower extracts. Sustain. Chem. Pharm. 19, 100354. https://doi.org/10.1016/j.scp.2020.100354

Jeeja, R., A., Thomas, A., Arshad, M., Joseph, A., 2022. The influence of aqueous and alcoholic extracts of Garcinia cambogia fruit rind in the management of mild steel corrosion in hydrochloric acid: Theoretical and electroanalytical studies. J. Mol. Liq. 346, 117873. https://doi.org/10.1016/j.molliq.2021.117873

Ji, G., Shukla, S.K., Dwivedi, P., Sundaram, S., Prakash, R., 2011. Inhibitive effect of argemone mexicana plant extract on acid corrosion of mild steel. Ind. Eng. Chem. Res. 50, 11954–11959. https://doi.org/10.1021/ie201450d

Kaya, F., Solmaz, R., Geçibesler, İ.H., 2023a. Investigation of adsorption, corrosion inhibition, synergistic inhibition effect and stability studies of Rheum ribes leaf extract on mild steel in 1 M HCl solution. J. Taiwan Inst. Chem. Eng. 143, 104712. https://doi.org/10.1016/j.jtice.2023.104712

Kaya, F., Solmaz, R., Halil Geçibesler, İ., 2023b. The use of methanol extract of Rheum Ribes (Işgın) flower as a natural and promising corrosion inhibitor for mild steel protection in 1 M HCl solution. J. Ind. Eng. Chem. 122, 102–117. https://doi.org/10.1016/j.jiec.2023.02.013

M'hiri, N., Veys-Renaux, D., Rocca, E., Ioannou, I., Boudhrioua, N.M., Ghoul, M., 2016. Corrosion inhibition of carbon steel in acidic medium by orange peel extract and its main antioxidant compounds. Corros. Sci. 102, 55–62. https://doi.org/10.1016/j.corsci.2015.09.017

Mourya, P., Banerjee, S., Singh, M.M., 2014. Corrosion inhibition of mild steel in acidic solution by Tagetes erecta (Marigold flower) extract as a green inhibitor. Corros. Sci. 85, 352–363. https://doi.org/10.1016/j.corsci.2014.04.036

Muthukrishnan, P., Prakash, P., Jeyaprabha, B., Shankar, K., 2019. Stigmasterol extracted from Ficus hispida leaves as a green inhibitor for the mild steel corrosion in 1 M HCl solution. Arab. J. Chem. 12, 3345–3356. https://doi.org/10.1016/j.arabjc.2015.09.005

Pal, A., Das, C., 2023. Novel use of kitchen waste: protection of boiler quality steel from corrosion in acidic media using onion waste. Chem. Pap. 77, 1107–1127. https://doi.org/10.1007/s11696-022-02549-7

Pal, A., Das, C., 2022. Investigations on corrosion inhibition in acidic media for BQ steel using banana flower bract, an eco-friendly novel agro-waste: Experimental and theoretical considerations. Inorg. Chem. Commun. 145, 110024. https://doi.org/10.1016/j.inoche.2022.110024

Popova, A., Sokolova, E., Raicheva, S., Christov, M., 2003. AC and DC study of the temperature effect on mild steel corrosion in acid media in the presence of benzimidazole derivatives. Corros. Sci. 45, 33–58. https://doi.org/10.1016/S0010-938X(02)00072-0

Rocha, J.C. D, Gomes, J.A. D C.P., D'Elia, E., 2010. Corrosion inhibition of carbon steel in hydrochloric acid solution by fruit peel aqueous extracts. Corros. Sci. 52, 2341–2348. https://doi.org/10.1016/j.corsci.2010.03.033

Satapathy, A.K., Gunasekaran, G., Sahoo, S.C., Amit, K., Rodrigues, P.V., 2009. Corrosion inhibition by Justicia gendarussa plant extract in hydrochloric acid solution. Corros. Sci. 51, 2848–2856. https://doi.org/10.1016/j.corsci.2009.08.016

Saxena, A., Prasad, D., Haldhar, R., 2018. Investigation of corrosion inhibition effect and adsorption activities of Cuscuta reflexa extract for mild steel in 0.5 M H_2SO_4. Bioelectrochemistry 124, 156–164. https://doi.org/10.1016/j.bioelechem.2018.07.006

Shukla, S.K., Quraishi, M.A., 2009. Cefotaxime sodium: A new and efficient corrosion inhibitor for mild steel in hydrochloric acid solution. Corros. Sci. 51, 1007–1011. https://doi.org/10.1016/j.corsci.2009.02.024

Srivastava, V., Chauhan, D.S., Joshi, P.G., Maruthapandian, V., Sorour, A.A., Quraishi, M.A.,

2018. PEG-functionalized chitosan: a biological macromolecule as a novel corrosion inhibitor. ChemistrySelect 3, 1990–1998. https://doi.org/10.1002/slct.201701949

Tang, M., Li, X., Deng, S., Lei, R., 2021. Synergistic inhibition effect of Mikania micrantha extract with KI on steel corrosion in H_2SO_4 solution. J. Mol. Liq. 344, 117926. https://doi.org/10.1016/j.molliq.2021.117926

Umer, A., Naveed, S., Ramzan, N., Rafique, M.S., Imran, M., 2014. A green method for the synthesis of copper nanoparticles using L-ascorbic acid. Matéria (Rio Janeiro) 19, 197–203. https://doi.org/10.1590/S1517-70762014000300002

Umoren, S.A., Obot, I.B., Gasem, Z.M., 2015. Adsorption and corrosion inhibition characteristics of strawberry fruit extract at steel/acids interfaces: Experimental and theoretical approaches. Ionics (Kiel). 21, 1171–1186. https://doi.org/10.1007/s11581-014-1280-3

Verma, C., Olasunkanmi, L.O., Ebenso, E.E., Quraishi, M.A., 2018. Adsorption characteristics of green 5-arylaminomethylene pyrimidine-2,4,6-triones on mild steel surface in acidic medium: Experimental and computational approach. Results Phys. 8, 657–670. https://doi.org/10.1016/j.rinp.2018.01.008

Verma, C., Quraishi, M.A., Kluza, K., Makowska-Janusik, M., Olasunkanmi, L.O., Ebenso, E.E., 2017. Corrosion inhibition of mild steel in 1M HCl by D-glucose derivatives of dihydropyrido [2,3-d:6,5-d′] dipyrimidine-2, 4, 6, 8(1H,3H, 5H,7H)-tetraone. Sci. Rep. 7, 44432. https://doi.org/10.1038/srep44432

Wang, C., Chen, J., Hu, B., Liu, Z., Wang, C., Han, J., Su, M., Li, Y., Li, C., 2019. Modified chitosan-oligosaccharide and sodium silicate as efficient sustainable inhibitor for carbon steel against chloride-induced corrosion. J. Clean. Prod. 238, 117823. https://doi.org/10.1016/j.jclepro.2019.117823

Yohannan Panicker, C., Tresa Varghese, H., Philip, D., 2006. FT-IR, FT-Raman and SERS spectra of vitamin C. Spectrochim. Acta Part A Mol. Biomol. Spectrosc. 65, 802–804. https://doi.org/10.1016/j.saa.2005.12.044

Zhou, Xueyong, Zhou, Xin, 2014. The unit problem in the thermodynamic calculation of adsorption using the langmuir equation. Chem. Eng. Commun. 201, 1459–1467. https://doi.org/10.1080/00986445.2013.818541

Chapter 4:

Corrosion inhibition of mild steel by tinda (*Praecitrullus fistulosus*) fruit and peel extracts

Corrosion inhibition of mild steel by tinda (*Praecitrullus fistulosus*) fruit and peel extracts

This chapter discusses the corrosion inhibition efficiency of tinda (Praecitrullus fistulosus) fruit and peel extracts for mild steel protection in 1 M HCl. These extracts were characterized by LC-MS and FTIR analyses, which revealed the presence of phenol, 3,5-bis (1,1-dimethyl ethyl)-, 9-octadecenoic acid, methyl ester, hexadecanoic acid 15-methyl-, methyl ester, 9, 12-octadecadienoic acid, methyl ester, 9, 12, 15-octadecatrienoic acid, methyl ester, (Z,Z,Z-), ascorbic acid, and phytol, contributing the corrosion resistance. Electrochemical and gravimetric studies revealed high inhibition efficiencies of 83.73% and 87.59% at 200 mg L^{-1} for tinda peel extract (TPE) and fruit extract (TFE), respectively. PDP results showed that these extracts exhibited mixed-type inhibition. During adsorption studies, the best fit was obtained for the Langmuir adsorption model. The obtained values of thermodynamic parameters suggest that MS corrosion occurs spontaneously by the endothermic process. Surface investigations (FESEM, AFM, EDX, and XRD) demonstrated the formation of a corrosion inhibiting layer by adsorbed extract molecules on the metal surface.

Published Article: Kumar, A., Das, C., 2024. Corrosion inhibition of mild steel by *Praecitrullus fistulosus* (tinda fruit and peel) extracts. ***Sci. Total Environ***. 929, 172569. https://doi.org/10.1016/j.scitotenv.2024.172569.

4.1 Characterization of tinda extracts

4.1.1 LC-MS analysis

Tinda extracts (TPE and TFE) were analyzed by liquid chromatography-mass spectroscopy to identify the available compounds. The mass spectra of these extracts are shown in Fig. 4.1, which contains several distinct peaks at various m/z values. The following major constituents were identified, such as Phenol, 3,5-bis (1,1-dimethylethyl)- (m/z: 206.17), 9-octadecenoic acid, methyl ester (m/z: 296.27), hexadecanoic acid 15-methyl-, methyl ester (m/z: 284.27), 9, 12-Octadecadienoic acid, methyl ester (m/z: 294.25), 9, 12, 15-octadecatrienoic acid, methyl ester, (Z,Z,Z-) (m/z: 292.23), ascorbic acid (m/z: 176.03), and phytol (m/z: 296.31), in the both extract. These compounds have the necessary characteristics (aromatic system, double bonds, conjugated bonds, heteroatoms, and long carbon chains) to be effective corrosion inhibitors. Thus, tinda extracts can be considered as a compound that contains several corrosion inhibitors. Furthermore, few recent studies reported that several plant extracts exhibited the anti-corrosion behavior due to the presence these compounds, phenol, 3,5-bis (1,1-dimethylethyl)- (Ameh et al., 2020), 9-octadecenoic acid, methyl ester (Ameh, 2018), hexadecanoic acid 15-methyl-, methyl ester (Itodo et al., 2018), 9, 12-octadecadienoic acid, methyl ester (Obot et al., 2022), 9, 12, 15-octadecatrienoic acid, methyl ester, (Z,Z,Z-) (Bhuvaneswari et al., 2018), ascorbic acid (Umoren et al., 2015) and phytol (Jeeja et al., 2023; Thakur et al., 2023). These compounds also have different characteristics like anti-inflammatory, cancer preventive character, and antioxidant properties (Alzurfi et al., 2019; Hagr et al., 2019; Ishnava and Patel, 2020; Shawer et al., 2022), which make TPE and TFE active for several applications.

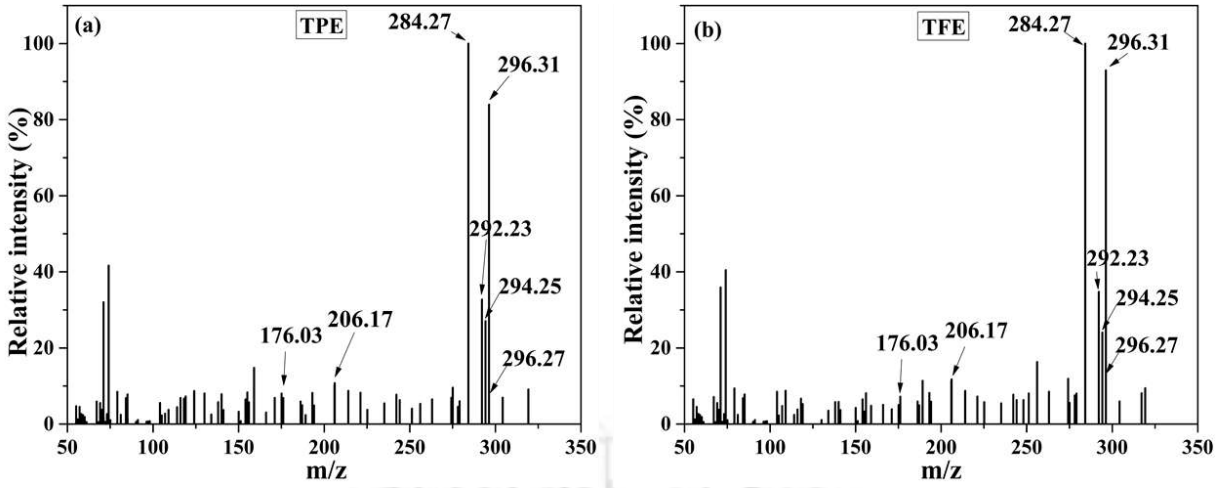

Fig. 4.1. Mass spectra of TPE and TFE.

4.1.2 FTIR analysis

Figs. 4.2 (a) and (b) depict the FTIR spectra of TPE and TFE, respectively. These spectra contain a broad peak at 3367 (TPE) and 3354 (TFE) cm^{-1}, which corresponds to -OH stretching frequency (water, alcohol, and phenol) (Itodo et al., 2018; Thummajitsakul et al., 2020). The peaks at 2926 (TPE) and 2923 (TFE) represent the asymmetric stretching of CH_2 group. Other peaks around 1645 (TPE) and 1636 cm^{-1} (TFE) correspond to the C=O stretching frequency and aromatic rings in the extracts (Jeeja et al., 2022). The bands at 1408 (TPE) and 1400 (TFE) represent the alkene bending vibrations in extracts (Ishnava and Patel, 2020). The peak at 1361 and 1373 cm^{-1} belongs to CH_3 bending vibration in TPE and TFE, respectively (Jeeja et al., 2023). These extracts also contain several functional groups, such as acids, esters, and anhydrides, which correspond to the band at 1245 (TPE) and 1238 (TFE) cm^{-1} (Itodo et al., 2018). Furthermore, C-O-C stretching vibrations in TPE and TFE are confirmed by a peak at 1022 cm^{-1} and 1032 cm^{-1}, respectively (Thomas et al., 2020). All these functional groups were tabulated in Table 4.1, which shows that similar functional groups were present in both tinda extracts (TPE and TFE). The functional groups -OH, C=O, C-O-C, C=C, and aromatic rings confirmed the presence of heteroatoms in the tinda extracts, which participate in their

bonding with metal and make them useful as a corrosion inhibitor (Haldhar et al., 2021). Furthermore, these functional groups reconfirmed the data obtained from the LC-MS analysis.

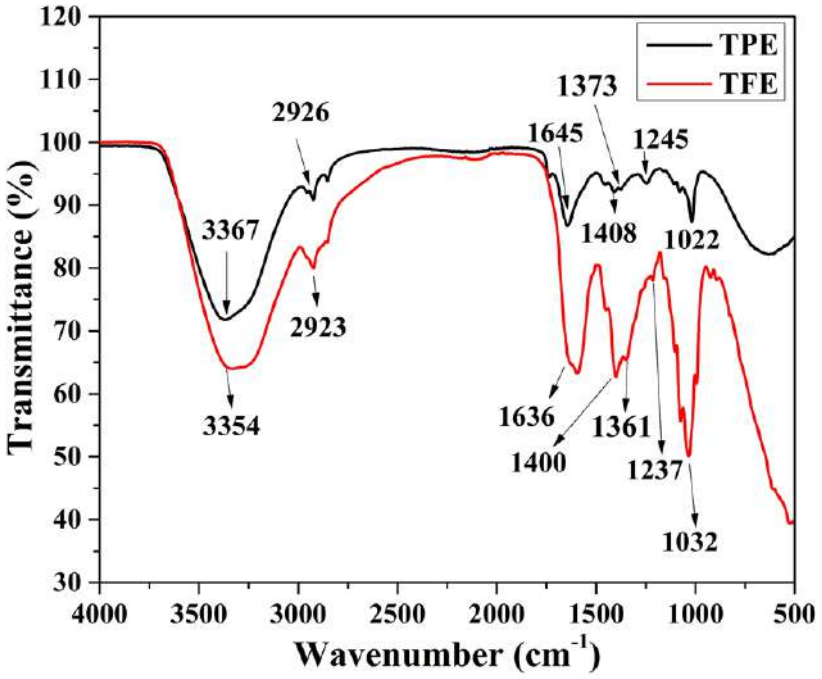

Fig. 4.2. FTIR spectra of (a) TPE and (b) TFE.

Table 4.1 FTIR peaks of TPE and TFE.

Functional group	Inhibitors Peaks from FTIR spectra (cm^{-1})	
	TPE	TFE
-OH stretching frequency of water, alcohol, phenol	3367	3354
asymmetric stretching of CH_2 group	2926	2923
C=O stretching frequency and aromatic rings	1645	1636
alkene bending vibration	1408	1400
CH_3 bending vibration	1373	1361
acids, esters and anhydrides	1245	1238
C-O-C stretching vibrations	1022	1032

4.2 Corrosion test

4.2.1 Gravimetric analysis

4.2.1.1 Effect of concentration of inhibitor

The effect of the concentration of inhibitor on inhibition efficiencies of both extracts was investigated at their various doses, such as 0, 50, 100, 150, 200, and 250 mg L^{-1}. Herein, each gravimetric experiment was repeated thrice, and mean values of corrosion rate and inhibition efficiency were plotted in Fig. 4.3. From this figure, it was observed that corrosion rate decreases and inhibition efficiency increases with increasing concentration up to 200 mg L^{-1} of both extracts (TPE and TFE). This increase in percentage inhibition efficiency signifies effective coverage of the metal surface by adsorbed inhibitor molecules. On further increasing the amount of extracts to 250 mg L^{-1}, inhibition efficiency exhibited a marginal increment (~1 %), which means extract molecules that are adsorbed on the MS surface maintain a constant inhibition efficiency beyond 200 mg L^{-1} concentration of extracts (Al-Amiery et al., 2022). These observations could be explained by the fact that, at lower doses, there are not enough inhibitor molecules that can completely cover the metal surface, which shows less inhibition efficiency. However, as the inhibitor dose increases, a large number of molecules will be available to occupy the active sites of the metallic surface, resulting in enhanced surface coverage and protection efficiency. Once the amount of inhibitor exceeds a certain threshold, all active sites on the metal surface are fully engaged with the inhibitor's molecules, resulting in maximum inhibiting efficiency that remains constant (Al-Amiery et al., 2023). In this work, the constant inhibition efficiency beyond the dose of 200 mg L^{-1} of extracts, depicting that the surface of coverage achieved equilibrium and systems exhibited maximum inhibition efficiency, which implies that 200 mg L^{-1} is the optimum concentration of extracts. Similar behavior is also reported by other researchers (Al-Amiery et al., 2023; Betti et al., 2023). The highest percentage inhibition efficiencies of about 81.59 and 86.00 % were obtained at the

optimum concentration (200 mg L^{-1}) of TPE and TFE, respectively, for 24 h immersion at room temperature (Haldhar et al., 2021). Few studies have also reported the same immersion time (24 h) for studying the effect of inhibitor concentration (Haldhar et al., 2021).

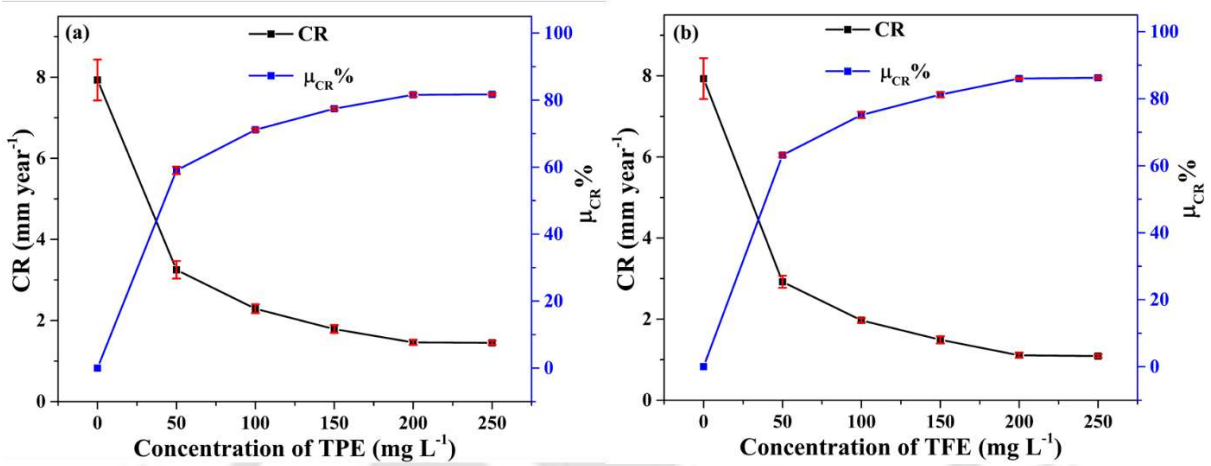

Fig. 4.3 Variations in corrosion rates and inhibition efficiency at different concentrations of TPE a) and TFE b).

4.2.1.2 Effect of immersion time

Immersion time is an important parameter that is used to investigate the stability of the inhibitors' inhibiting behavior during their long exposure. In this work, several gravimetric experiments were conducted at optimum inhibitor concentration (200 mg L^{-1}) for various immersion times, such as 4, 8, 12, 24, and 48 h. It was noticed that the values of percentage inhibition efficiencies were found to improve up to the period of 24 h (Rocha et al., 2010; Daoudi et al., 2022), and after that, these values remained unchanged up to 48 h (Fig. 4.4). These findings depicted that adsorption of tinda extracts on MS surface was completed within 24 h, after that present extracts molecule in the solution involved in repairing the inhibitive layer deteriorated by corrosive ions. The reasons could be attributed to the adsorptive film of the inhibitor that rests upon the immersion time. The adsorptive film becomes more compact

and uniform during prolonged immersion time (1-24 h), and then the adsorptive film achieves a saturated state, and its thickness maximizes before 24 - 48 h (Faustin et al., 2015).

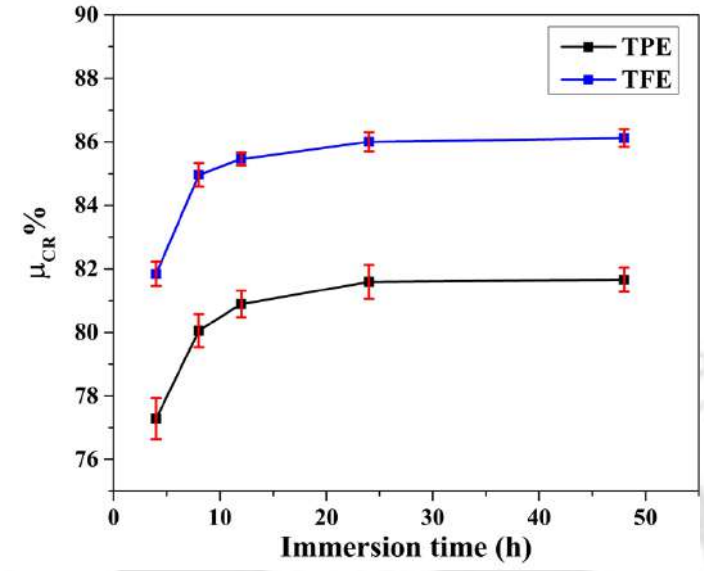

Fig. 4.4 Inhibition efficiencies of TPE and TFE at different immersion times.

4.2.2 Electrochemical measurements

Electrochemical analyses serve as a valuable tool for investigating the anti-corrosive nature of tinda extracts for MS protection from corrosion. This anticorrosive nature of extracts was evaluated in terms of few important parameters such as i_{corr}, E_{corr}, R_{ct}, and inhibition efficiency. In this study, each electrochemical experiment was carried out three times using different concentrations (0-200 mg L^{-1}) of tinda extracts (TPE and TFE) at 30 ºC.

4.2.2.1 Open circuit potential measurement

The open circuit potential (OCP) is a stable or equilibrium voltage developed on MS (working electrode) with respect to Ag/AgCl, 3 M (reference electrode), when no current is supplied. OCP measurements were conducted for a duration of 1 h at different doses of tinda extracts (TPE and TFE), ranging from 0 to 200 mg L^{-1}. The inhibited systems exhibited a

positive shift in the OCP values compared to the blank system, as illustrated in Figs. 4.5 (a) and (b) for TPE and TFE, respectively.

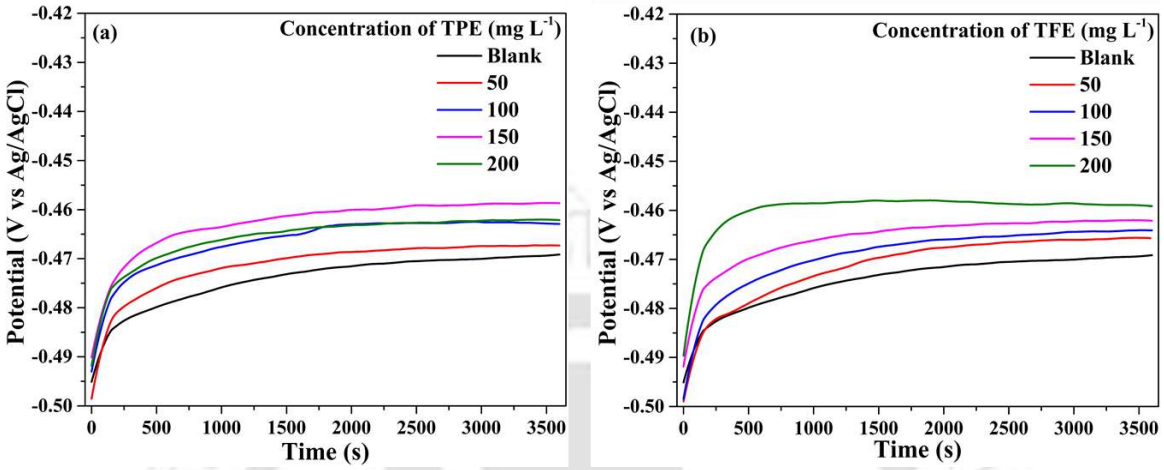

Fig. 4.5 OCP graphs for MS immersed in 1 M HCl, in the presence and absence of TPE a), and TFE b).

4.2.2.2 Potentiodynamic polarization test

PDP measurements were conducted to explore the kinetics of the electrochemical process, which occurs on the metal-electrolyte interface. The effect of polarizations is represented by Tafel plots in Figs 4.6 a and 4.6 b, with and without TPE and TFE, respectively. Several Tafel parameters were obtained by fitting the Tafel plots, which are listed in Table 4.2. This table demonstrates a noticeable positive shift in the average corrosion potential (E_{corr}) when both tinda extracts were introduced separately compared to uninhibited systems, indicating their predominant role as anodic inhibitors. Anodic polarization of MS immersed in 1 M HCl for inhibited systems is contingent upon the electrode potential. In inhibited systems, the anodic reaction is minimally affected when the values of E_{corr} shift positively due to the presence of tinda extracts (Al-Moubaraki and Awaji, 2020). Several studies have reported that an inhibitor typically worked as a mixed-type inhibitor when E_{corr} shift lies within ± 85 mV

compared to an uninhibited system. Otherwise, the inhibitor is considered as either cathodic or anodic type (Wang et al., 2019). In this work, tinda extracts (TPE and TFE) exhibited corrosion potential shift within 85 mV, which signifies that these extract beaves as mixed-type of inhibitors. Furthermore, it was also observed that the obtained values of E_{corr} from the Tafel analysis are close to their OCP values (Canales et al., 2021), which were determined prior to every electrochemical experiment in the previous section. Fig. 4.6 illustrates a decrease in both anodic and cathodic currents with increasing the amount of tinda extracts. This reduction suggests hindrance in H_2 formation and MS degradation reactions. Furthermore, the values of i_{corr} and R_p decreased and increased, respectively, with the incorporation of extracts (TPE and TFE) into 1 M HCl. These changes depict the construction of a robust protective layer on the MS by tinda extracts. Additionally, Table 4.2 shows that corrosion rate values were decreased with the addition of tinda extracts. These values are well aligned with the corrosion rate values obtained from weight loss method, as presented in Table 4A.1 of Appendix 4A. These extracts exhibited the highest inhibition efficiency of about 83.73 and 87.11 % at the optimum concentration (200 mg L^{-1}) of TPE and TFE, respectively (Ali Asaad et al., 2018; ji et al., 2011; Saxena et al., 2018).

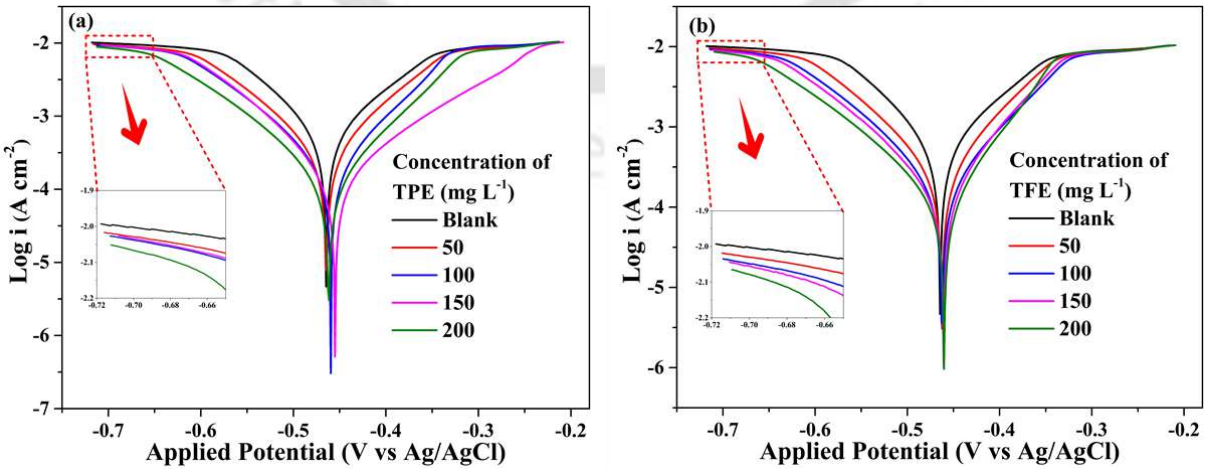

Fig. 4.6 Tafel plots for MS immersed in 1 M HCl with and without TPE a) and TFE b).

Table 4.2 Tafel parameters for MS immersed in 1 M HCl with and without TPE and TFE.

Inhibitor	Conc. (mg L^{-1})	b_a (mV dec^{-1})	$-b_c$ (mV dec^{-1})	*OCP* (mV vs. Ag/AgCl)	E_{corr} (mV vs. Ag/AgCl)	i_{corr} (μA cm^{-2})	R_p (Ω cm^2)	*CR* (mm $Year^{-1}$)	μ_P (%)
Blank	0	110.59 ± 0.52	120.25 ± 1.04	-468.15 ± 5.68	-465.25 ± 5.56	734.98 ± 5.23	34.04 ± 0.12	8.54 ± 0.45	-
TPE	50	90.27 ± 0.53	77.46 ± 1.24	-467.22 ± 4.52	-464.23 ± 4.40	292.00 ± 3.23	62.00 ± 0.05	3.39 ± 0.23	60.49 ± 0.36
	100	91.47 ± 0.88	80.83 ± 1.31	-462.29 ± 2.10	-459.76 ± 2.31	195.81 ± 2.30	95.17 ± 0.08	2.27 ± 0.09	73.51 ± 0.83
	150	87.55 ± 0.76	134.79 ± 1.10	-458.71 ± 3.31	-455.45 ± 1.97	150.15 ± 1.52	153.52 ± 0.39	1.74 ± 0.08	79.68 ± 0.97
	200	84.81 ± 0.69	79.17 ± 0.71	-462.23 ± 2.42	-461.30 ± 2.37	120.23 ± 1.09	147.92 ± 0.13	1.40 ± 0.06	83.73 ± 0.61
Blank	0	110.59 ± 0.52	120.25 ± 1.04	-468.15 ± 5.68	-465.25 ± 5.56	734.98 ± 5.23	34.04 ± 0.12	8.54 ± 0.45	-
TFE	50	90.18 ± 0.41	74.35 ± 0.43	-465.67 ± 3.70	-462.17 ± 3.72	256.08 ± 1.41	69.13 ± 0.17	2.97 ± 0.16	65.35 ± 0.68
	100	87.44 ± 0.30	79.41 ± 0.29	-464.04 ± 3.18	-462.84 ± 4.10	172.44 ± 0.78	104.81 ± 0.03	2.00 ± 0.05	76.67 ± 0.56
	150	82.84 ± 0.36	62.57 ± 1.22	-462.18 ± 2.50	-460.61 ± 2.76	123.99 ± 1.59	124.86 ± 0.23	1.44 ± 0.08	83.22 ± 0.11
	200	81.41 ± 1.08	60.69 ± 0.97	-459.14 ± 2.98	-460.48 ± 3.02	95.29 ± 1.51	158.47 ± 0.19	1.11 ± 0.05	87.11 ± 0.50

4.2.2.3 EIS measurements

The EIS technique is another way that was used to investigate the kinetics of the electrochemical process during MS immersion in 1 M HCl with and without TPE and TFE. Figs. 4.7 (a) and 4.7 (b) demonstrated the Nyquist patterns for inhibited and uninhibited systems. These Nyquist plots contain a similar semicircle of depressed nature, which signifies the heterogeneity of the surface of the metal. The Nyquist plot showed a consistent pattern for both uninhibited and inhibited systems, indicating that the incorporation of the extracts (TPE or TFE) into the acidic solution did not alter the corrosion process mechanism (Umoren et al., 2015). A significant capacitive loop appears at higher frequencies of every semicircle, representing charge transfer through the double layer. In the absence of extracts, at low frequency, an inductive loop was observed, which was not seen in their presence.

The appearance of this inductive loop is commonly associated with the relaxation of adsorbed intermediate species, such as H^{+}_{ads}, Cl^{-}_{ads}, and others, suggesting the presence of unstable corrosion products on the metal (Haque et al., 2021). In the presence of inhibitors, vanishing this inductive loop is commonly interpreted as the "degradation" process in electrochemical impedance spectroscopy studies (Haldhar et al., 2018; Pal and Das, 2022a). Nyquist graphs of tinda extracts or blank systems illustrate that the nature of the reaction occurring at the metal-electrolyte interface is mainly controlled by charge transfer. The diameter of the semicircle in the Nyquist plots depicts the charge transfer resistance (R_{ct}) (Bhan and Kumar Golder, 2023). This diameter was increased with the addition of extracts and achieved a maximum value at 200 mg L^{-1} (Figs. 4.7(a) and 4.7(b)).

Fig. 4.8 demonstrates Bode magnitude and phase graphs of uninhibited and inhibited systems. Additionally, Bode and Nyquist graphs contain only one peak and semicircle, respectively, confirming that the electrochemical process of MS dissolution has a one-time constant equivalent circuit model.

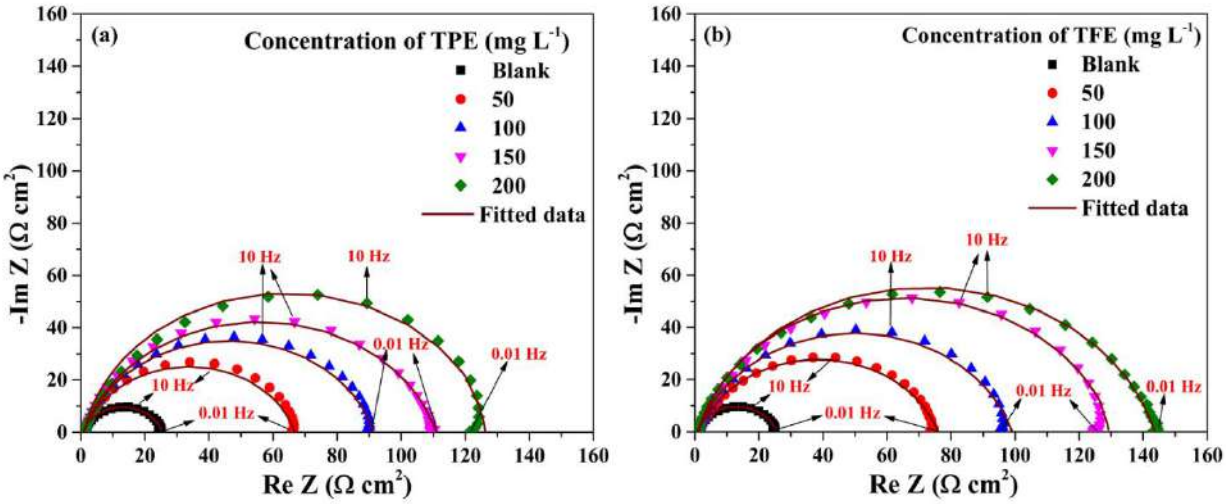

Fig. 4.7 Nyquist graphs for MS immersed in 1 M HCl with and without TPE a), TFE b).

The Bode graphs reveal distinct phase angles between 0° and 90°, reflecting the resistive or capacitive characteristics of the interface of metal and electrolyte. All the phase plots showed phase angles less than 90°, suggesting the absence of pure capacitive behavior. It was also observed that peak height notably increases with the amount of extracts, which signifies a strengthened capacitive response at the interface between the metal and electrolyte (Pal and Das, 2023). In order to briefly understand the electrochemical processes occurring at the interface of metal and electrolyte, Nyquist plots were fitted to a simple Randle circuit model ($R_s(Q_{dl}\ R_{ct})$), where R_s presents solution resistance, R_{ct} and *CPE* represent the charge transfer resistance and constant phase element, respectively (Chidiebere et al., 2015). This circuit contains R_s in series with R_{ct} and *CPE*, but R_{ct} and *CPE* are parallel (M'hiri et al., 2016; Srivastava et al., 2018; Verma et al., 2018). Fig. 4.9 shows the used equivalent circuit model.

The several Nyquist parameters, such as R_s, R_{ct}, *CPE*, n, goodness of fit (χ^2), μ_{Rct} (%), and $C_{dl,}$ calculated are listed in Table 4.3. The obtained values of χ^2 lie between 1.12×10^{-3} and 3.32×10^{-3}, representing an excellent fit of Nyquist plots to an equivalent circuit model (Mourya et al., 2014; Tang et al., 2021). The values of R_{ct} significantly increase with increasing the amount of extracts. This increase resulted from the effective adsorption of tinda extracts on the

metal surface, resulting in the preparation of a protective layer that obstructed ions' movement across the interface of metal-electrolyte. TFE exhibited a large protection efficiency as compared to TPE. Additionally, R_p values were compared with those obtained from PDP test, as shown in Table 4A.1 of the Appendix 4A. This table demonstrates that these values are distinct but close for each system, which signifies that results of the EIS study are concord with the findings of PDP test. Furthermore, the obtained inhibition efficiencies from the EIS test were compared with inhibition efficiencies of PDP and gravimetric analysis, and evaluated p-values confirms that electrochemical data are highly statistically significant ($p < 0.0001$) (Table 4A.2 of the Appendix 4A).

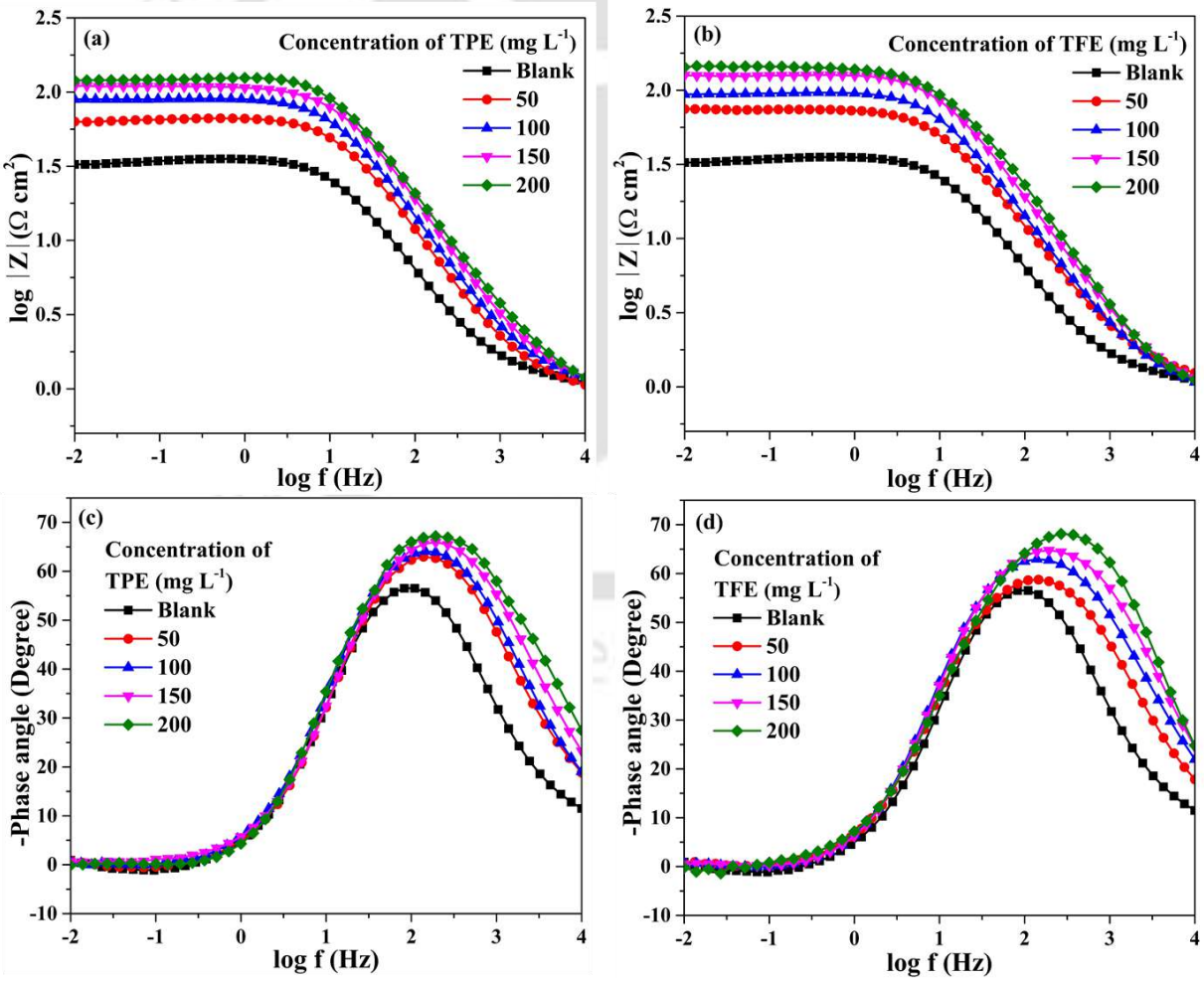

Fig. 4.8 Bode and phase graphs of MS immersed in 1 M HCl with and without TPE (a,c) and TFE (b,d).

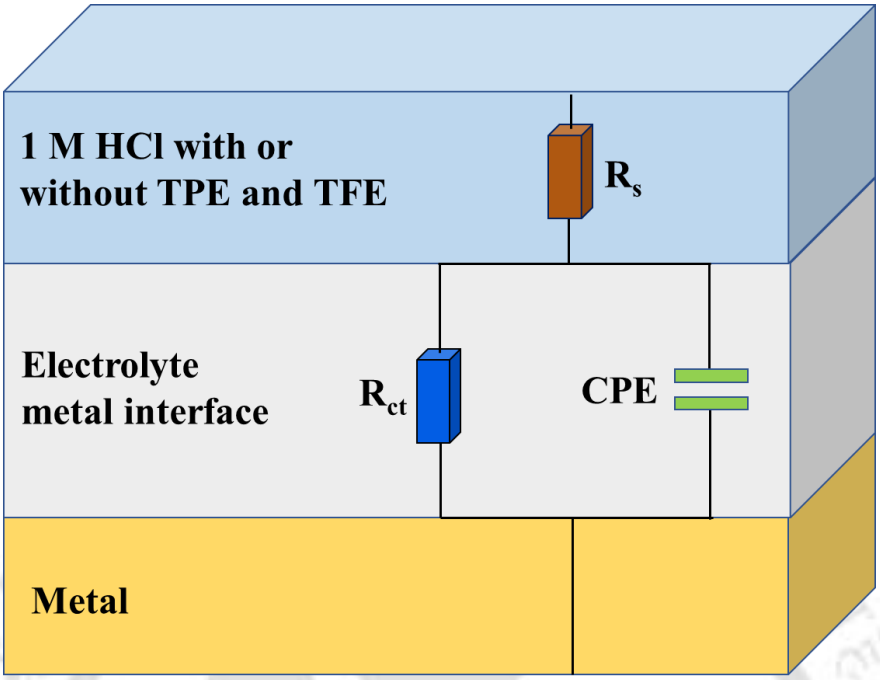

Fig. 4.9 Proposed equivalent circuit model for MS corrosion in 1 M HCl with or without TPE and TFE.

Table 4.3 Nyquist parameters for MS immersed in 1 M HCl with and without TPE and TFE.

Inhibitor	Conc. (mg L^{-1})	R_s (Ω cm^2)	R_{ct} (Ω cm^2)	*CPE* parameters		C_{dl} (μF cm^{-2})	Goodness of fit	μ_{Rct} (%)
				n	Y_0 (μMho cm^{-2})		(χ^2) $\times 10^{-3}$	
Blank	0	0.84 ± 0.001	25.89 ± 0.14	0.81 ± 0.001	875.67 ± 6.29	348.06 ± 0.46	1.12	-
TPE	50	0.94 ± 0.001	65.83 ± 0.19	0.83 ± 0.001	377.87 ± 1.56	177.47 ± 0.38	1.21	60.81 ± 0.29
	100	1.08 ± 0.002	90.30 ± 0.26	0.84 ± 0.001	294.09 ± 1.02	148.28 ± 0.21	2.23	71.43 ± 0.18
	150	1.00 ± 0.001	109.84 ± 0.37	0.83 ± 0.001	231.11 ± 0.83	110.77 ± 0.25	3.11	76.51 ± 0.13
	200	0.93 ± 0.001	125.18 ± 0.44	0.82 ± 0.001	228.06 ± 0.91	107.63 ± 0.19	3.32	79.39 ± 0.12
Blank	0	0.84 ± 0.001	25.89 ± 0.14	0.81 ± 0.001	875.67 ± 6.29	348.06 ± 0.46	1.12	-
TFE	50	1.12 ± 0.002	74.08 ± 0.20	0.80 ± 0.001	469.12 ± 2.23	195.65 ± 0.40	2.98	65.51 ± 0.25
	100	0.92 ± 0.001	97.16 ± 0.33	0.81 ± 0.001	355.03 ± 1.49	163.40 ± 0.29	1.32	73.45 ± 0.16
	150	0.94 ± 0.002	127.97 ± 0.68	0.82 ± 0.001	246.56 ± 1.46	118.48 ± 0.31	1.57	79.84 ± 0.13
	200	0.91 ± 0.001	142.69 ± 0.84	0.84 ± 0.001	191.42 ± 0.86	96.85 ± 0.17	2.31	81.92 ± 0.15

4.3 Effect of temperature

In order to investigate the thermal stability of tinda extracts, some additional electrochemical experiments were conducted for immersed MS in 1 M HCl with and without tinda extracts. These experiments were carried out by using the optimal amount (200 mg L^{-1}) of extracts at temperatures of 313 K and 323 K, under identical conditions as those detailed in section 4.2.2. Before every single experiment, open circuit potential (OCP) was recorded by exposing the working electrodes to acid for a period of 1 h at 303 K, 313 K, and 323 K (Figs. 4.10 (a), 4.10 (b), and 4.10 (c)).

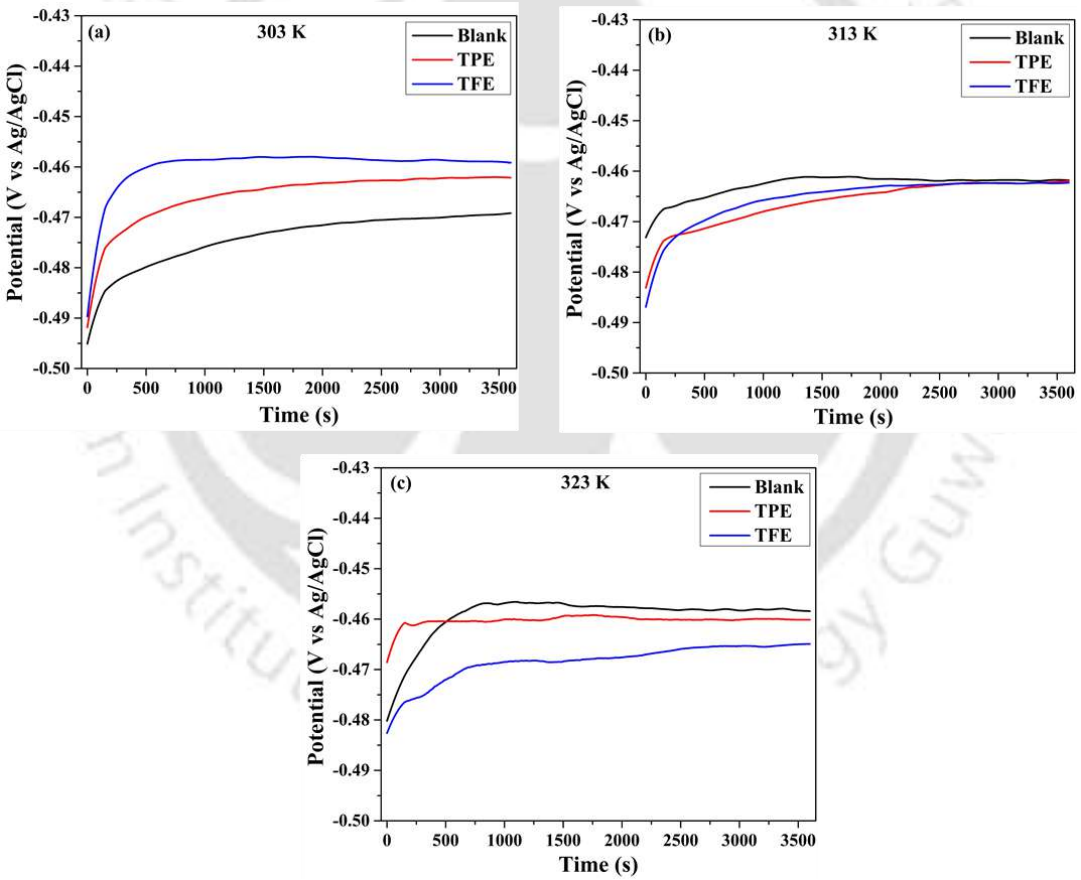

Fig. 4.10 OCP graphs for MS immersed in 1 M HCl at 303 (a), 313 (b), and 323 K (c), in the presence and absence of TPE and TFE.

The Tafel plots for MS immersed in 1 M HCl in the presence or absence of both extracts at 303, 313, and 323 K are illustrated in Figs. 4.11 (b), 4.11 (d), and 4.11 (f), respectively. All obtained Tafel parameters are listed in Table 4.4. From Table 4.4, it was observed that the values of i_{corr} (corrosion current) and protection efficiency were increased and decreased on rising temperatures from 303 to 323 K. The decline in the values of μ_p (%) resulted from the displacement of few pre-adsorbed inhibitor molecules from the metal surface by water molecules, leading to a reduction in the charge transfer resistance. However, this occurrence has a minimal impact on the protective layer. Figs 4.11 (a), 4.11 (c), and 4.11 (e) illustrate the Nyquist graphs for immersed MS in 1 M HCl with and without extracts at 303, 313, and 323 K. The Nyquist graphs display consistently depressed semicircles, suggesting the heterogeneity of the surface of MS. In every semicircle, a prominent capacitive loop exists at large frequency, indicating the movement of corrosive charges across the double layer. An inductive loop was detected in the uninhibited system at low frequencies, indicating the relaxation of few species (such as H^{+}_{ads} and Cl^{-}_{ads}), and corrosion products from the metal. In the presence of the inhibitor, this inductive loop vanished, leaving only a capacitive loop. It suggests that the dissolution of MS in acid is predominantly controlled by charge transfer. Nyquist patterns for MS degradation in the presence or absence of extracts illustrate that reactions occurring at the metal-electrolyte interface are predominantly governed by charge transfer, and the diameter of the semicircle represents the charge transfer resistance (R_{ct}). Additionally, EIS parameters were evaluated, as discussed in section 4.2.2.3. All obtained EIS parameters have been listed in Table 4.5. Furthermore, Table 4.4 showed that R_p and μ_P (%) declined as the temperature increased. The inhibited MS treated with TPE and TFE in acid at 323 K exhibited a protection efficiency of 70.71 and 72.74%, respectively.

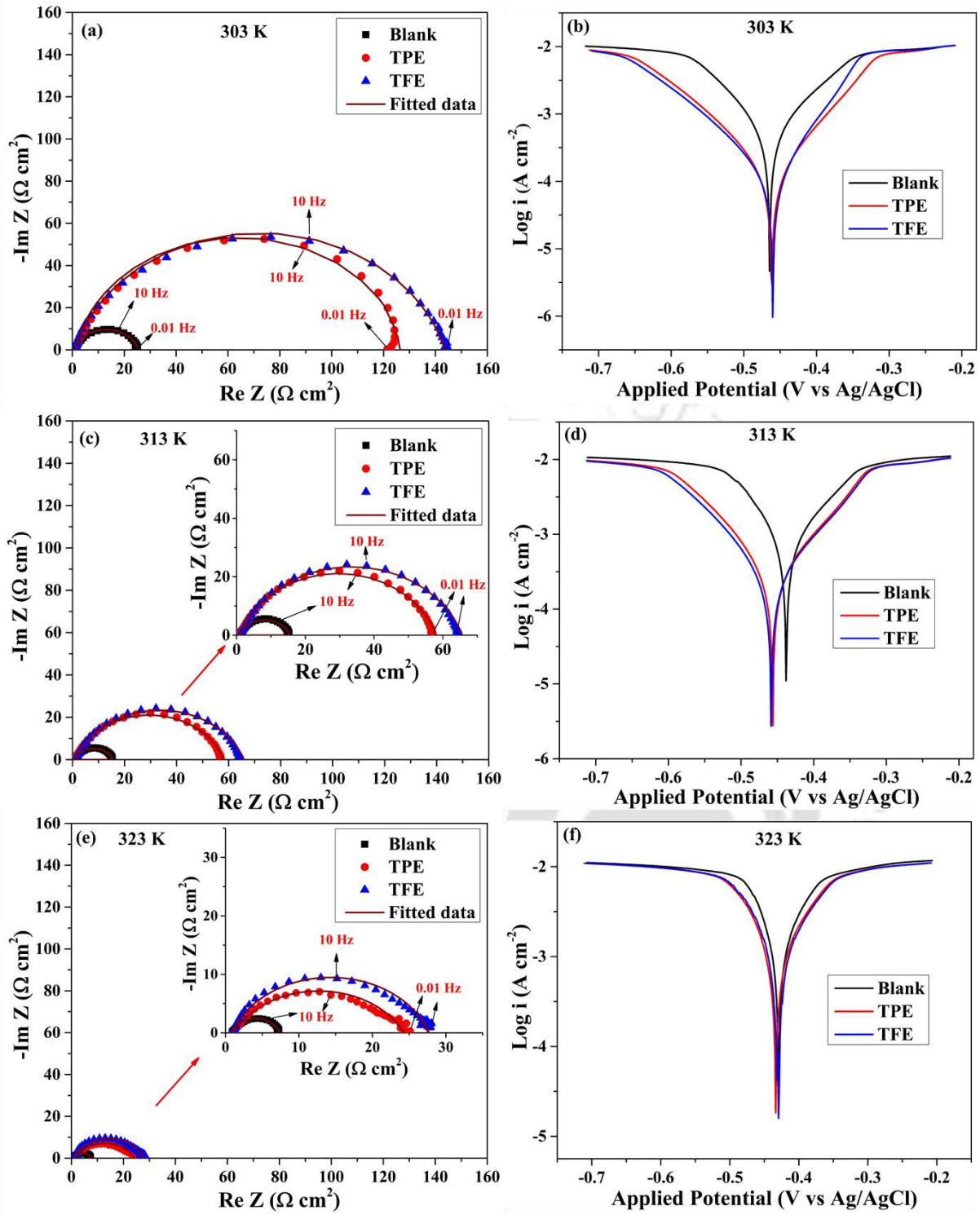

Fig. 4.11 Nyquist graphs (a, c, e) and Tafel graphs (b, d, f) for tinda extracts (TPE and TFE) at 303 K, 313 K, and 323 K.

Table 4.4 Tafel parameters for MS immersed in 1 M HCl with and without TPE and TFE at 303, 313, and 323 K.

Temperature (K)	Inhibitor	Conc. (mg L^{-1})	b_a (mV dec^{-1})	$-b_c$ (mV dec^{-1})	*OCP* (mV vs. Ag/AgCl)	E_{corr} (mV vs. Ag/AgCl)	i_{corr} (µA cm^{-2})	R_p (Ω cm^2)	*CR* (mm $Year^{-1}$)	μ_P (%)
303	Blank	0	110.59 ± 0.52	120.25 ± 1.04	-468.15 ± 5.68	-465.25 ± 5.56	734.98 ± 5.23	34.04 ± 0.12	8.54 ± 0.45	-
	TPE	200	84.81 ± 0.69	79.17 ± 0.71	-462.23 ± 2.42	-461.30 ± 2.37	120.23 ± 1.09	147.92 ± 0.13	1.40 ± 0.06	83.73 ± 0.61
	TFE	200	81.41 ± 1.08	60.69 ± 0.97	-459.14 ± 2.98	-460.48 ± 3.02	95.29 ± 1.51	158.47 ± 0.19	1.11 ± 0.05	87.11 ± 0.50
313	Blank	0	105.06 ± 1.08	165.79 ± 2.35	-461.76 ± 6.93	-437.85 ± 6.52	1302.48 ± 11.03	21.44 ± 0.04	15.13 ± 0.94	-
	TPE	200	93.75 ± 0.41	104.65 ± 1.52	-461.98 ± 4.99	-456.68 ± 3.41	318.13 ± 2.71	67.51 ± 0.06	3.70 ± 0.26	75.68 ± 0.13
	TFE	200	100.28 ± 1.91	106.66 ± 2.84	-462.35 ± 4.23	-458.58 ± 4.12	290.41 ± 2.59	77.29 ± 0.21	3.37 ± 0.21	77.80 ± 0.48
323	Blank	0	146.54 ± 1.38	285.84 ± 1.51	-458.16 ± 5.43	-429.41 ± 6.35	4429.22 ± 36.40	9.50 ± 0.01	51.45 ± 2.96	-
	TPE	200	81.68 ± 3.98	108.47 ± 162	-460.29 ± 3.51	-433.04 ± 3.36	1333.03 ± 18.72	15.18 ± 0.31	15.17 ± 1.00	70.71 ± 0.26
	TFE	200	81.46 ± 0.33	93.02 ± 1.31	-465.12 ± 4.58	-429.87 ± 3.53	1226.05 ± 10.23	15.38 ± 0.04	14.25 ± 0.84	72.74 ± 0.15

Table 4.5 EIS parameters for MS immersed in 1 M HCl with and without TPE and TFE at 303, 313, and 323 K.

Temperature (K)	Inhibitor	Conc. (mg L^{-1})	R_s (Ω cm^2)	R_{ct} (Ω cm^2)	*CPE* parameters		C_{dl} (μF cm^{-2})	Goodness of fit (χ^2) $\times 10^{-3}$	μ_{Rct} (%)
					n	Y_0 (μMho cm^{-2})			
303	Blank	0	0.84 ± 0.001	25.89 ± 0.14	0.81 ± 0.001	875.67 ± 6.29	348.06 ± 0.46	1.12	-
	TPE	200	0.93 ± 0.001	125.18 ± 0.44	0.82 ± 0.001	228.06 ± 0.91	107.63 ± 0.19	3.32	79.39 ± 0.12
	TFE	200	0.91 ± 0.001	142.69 ± 0.84	0.84 ± 0.001	191.42 ± 0.86	96.85 ± 0.17	2.31	81.92 ± 0.15
313	Blank	0	0.85 ± 0.002	16.51 ± 0.07	0.77 ± 0.001	1492.67 ± 16.43	446.72 ± 1.74	1.68	-
	TPE	200	0.96 ± 0.001	57.12 ± 0.25	0.80 ± 0.001	580.87 ± 3.36	244.66 ± 0.51	3.12	71.34 ± 0.43
	TFE	200	1.02 ± 0.001	64.68 ± 0.40	0.79 ± 0.001	573.67 ± 4.12	229.91 ± 0.47	2.03	74.69 ± 0.10
323	Blank	0	0.88 ± 0.003	7.67 ± 0.04	0.71 ± 0.002	3744.06 ± 28.06	865.87 ± 2.57	2.23	-
	TPE	200	1.07 ± 0.001	22.87 ± 0.13	0.71 ± 0.001	1687.34 ± 15.86	455.18 ± 1.23	3.32	66.59 ± 0.11
	TFE	200	0.95 ± 0.001	26.23 ± 0.06	0.74 ± 0.002	1366.58 ± 7.53	364.26 ± 0.63	4.50	70.87 ± 0.16

4.3.1 Effect of activation energy

The activation energies for both uninhibited and inhibited systems were determined by plotting ln (i_{corr}) (µA cm^{-2}) against 1/T (K^{-1}), as depicted in Fig. 4.12 (a). This figure represents a straight line, where ($-E_a/R$) and (ln A) correspond to slope and intercept, respectively. The values of E_a for blank and inhibited systems have been listed in Table 4.6. Additionally, the entropy and enthalpy of metal degradation in the presence and absence of inhibitor were evaluated by plotting the ln (i_{corr}/T) (µA cm^{-2} K^{-1}) against 1/T (K^{-1}). This graphical representation exhibits a linear trend, displaying a straight line which has a slope of (-ΔH /R) and an intercept of ($\ln\frac{k_B}{h} + \frac{\Delta S}{R}$) (Fig. 4.12 (b)). The determined values for ΔH and ΔS are listed in Table 4.6.

Upon analyzing Table 4.6, a higher value of activation energies was obtained for inhibited systems than that of uninhibited systems, which implies that a higher amount of energy is needed to induce corrosion on the surface of MS in inhibited systems compared to blank systems. Some research studies have indicated a decline in inhibition efficiency as temperature rises, leading to an increase in the corrosion activation energy (E_a) for inhibited systems compared to the blank system. These shifts depict the formation of the inhibitor layer due to its physical interaction with the metal. On the other hand, at higher temperatures, the value of inhibition efficiency tends to rise, resulting in decreased activation energy for inhibited systems compared to blank systems, suggesting a chemisorption mechanism (Aslam et al., 2022; Bangera et al., 2022; Ravi and Golder, 2024). In this study, the value of activation energy declined with increasing temperature, which implies that tinda extracts were adsorbed preferentially by the physical adsorption process.

The obtained value of enthalpy of corrosion for the blank system displays a positive value, and this value further escalates in the presence of both tinda extracts. This trend indicates that the corrosion process of MS is endothermic. The difference between (E_a - ΔH) remains

nearly identical and equal to RT across all systems. This observation suggests that the metal degradation conforms to an unimolecular-type process (Odewunmi et al., 2021; Nijarubini and Mallika, 2023). Moreover, there is a noticeable shift towards more positive values of the entropy change for MS degradation in the presence of an inhibitor. The increase in entropy is associated with the concept that an activated complex is formed during the determining step of the degradation phenomenon. The total entropy rises as reactants transform into activated complexes, displacing previously adsorbed H_2O molecules from the metal surface. Therefore, tinda extracts molecules form a packed layer over metal due to their interaction and bonding. If the system's entropy declined for inhibited systems as related to blank, depicted during the rate-determining step, the activation of tinda extracts molecules implies their dissociation in place of association. This recommends a conversion of reactant molecules to the activated complex structure, which depicts increased disorder rather than a structured arrangement (Al-Moubaraki and Awaji, 2020; Fitoz et al., 2023; Jeeja et al., 2022).

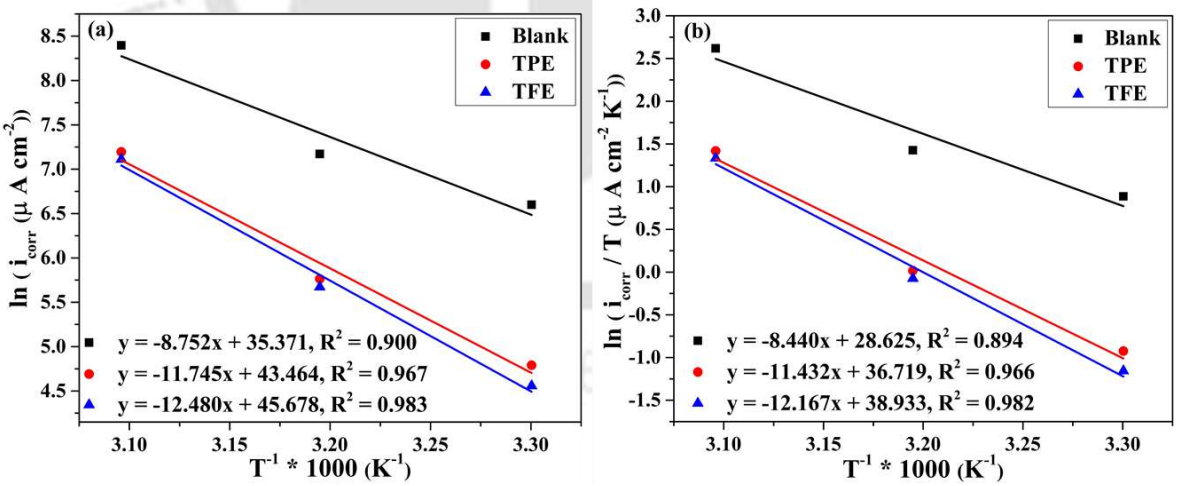

Fig. 4.12 Arrhenius plots (a) and Transition state plots (b) of inhibited or uninhibited systems.

Table 4.6 Kinetic parameters for inhibited and uninhibited systems.

Inhibitor	Conc. (mg L^{-1})	Pre-exponential factor, A (μA cm^{-2})	E_a (kJ mol^{-1})	ΔH (kJ mol^{-1})	ΔS (J mol^{-1} K^{-1})	$E_a - \Delta H$ (kJ mol^{-1})
Blank	0	$(2.30 \pm 0.21) \times 10^{15}$	72.76 ± 0.25	70.17 ± 0.27	40.45 ± 0.78	2.59
TPE	200	$(7.52 \pm 0.23) \times 10^{18}$	97.65 ± 0.81	95.05 ± 0.79	107.74 ± 0.80	2.60
TFE	200	$(6.88 \pm 0.19) \times 10^{19}$	103.76 ± 0.89	101.16 ± 0.92	126.15 ± 0.91	2.60

4.4 Adsorption studies

Numerous isotherm models play a vital role in understanding how plant extract species interact with metal. To determine the nature and intensity of adsorption, several values of θ (surface coverage) for various doses (0, 50, 100, 150, and 200 mg L^{-1}) of both tinda extracts (TPE and TFE) were tested across different adsorption isotherms (Langmuir, Temkin, and Frumkin adsorption isotherm) (Fig. 4.13). On comparing, the Langmuir adsorption isotherm model emerged as the best fit (its slope is very close to 1 for both extracts). The values obtained for the adsorption constant (K_{ads}) are 32.26 L g^{-1} (TPE) and 37.04 L g^{-1} (TFE), as listed in Table 4.7. These values were used to calculate the Standard Gibbs free energy (ΔG^o_{ads}) for inhibited systems using the following expression (Eq. (4.1)).

$$\Delta G^o_{ads} = -RTln(C_{water}\, K_{ads}) \quad (4.1)$$

where K_{ads} is the equilibrium adsorption constant (L g^{-1}), C_{water} is water concentration in solution (1000 g L^{-1}), R and T are gas constant (8.314 J K^{-1} mol^{-1}) and temperature (K), respectively. Some research stated that ΔG^o_{ads} values around or above -20 kJ mol^{-1} signify physisorption, where charged inhibitor molecules interact with a charged MS. Conversely, values below -40 kJ mol^{-1} imply chemisorption, where electrons are shared between the metal and inhibitor. When ΔG^o_{ads} falls between -40 kJ mol^{-1} and -20 kJ mol^{-1}, it's considered mixed-type adsorption. In this work, ΔG^o_{ads} values are -26.15 and -26.50 kJ mol^{-1} for TPE and TFE,

respectively. These values lie between -40 kJ mol^{-1} and -20 kJ mol^{-1}, which implies that both TPE and TFE are adsorbed by a mixed-type adsorption process. Furthermore, the negative ΔG^{o}_{ads} value signifies that tinda both extract molecules have the ability to self-adsorb onto the MS from corrosive electrolyte (Al-Moubaraki, 2018; Kaya et al., 2023b, 2023a).

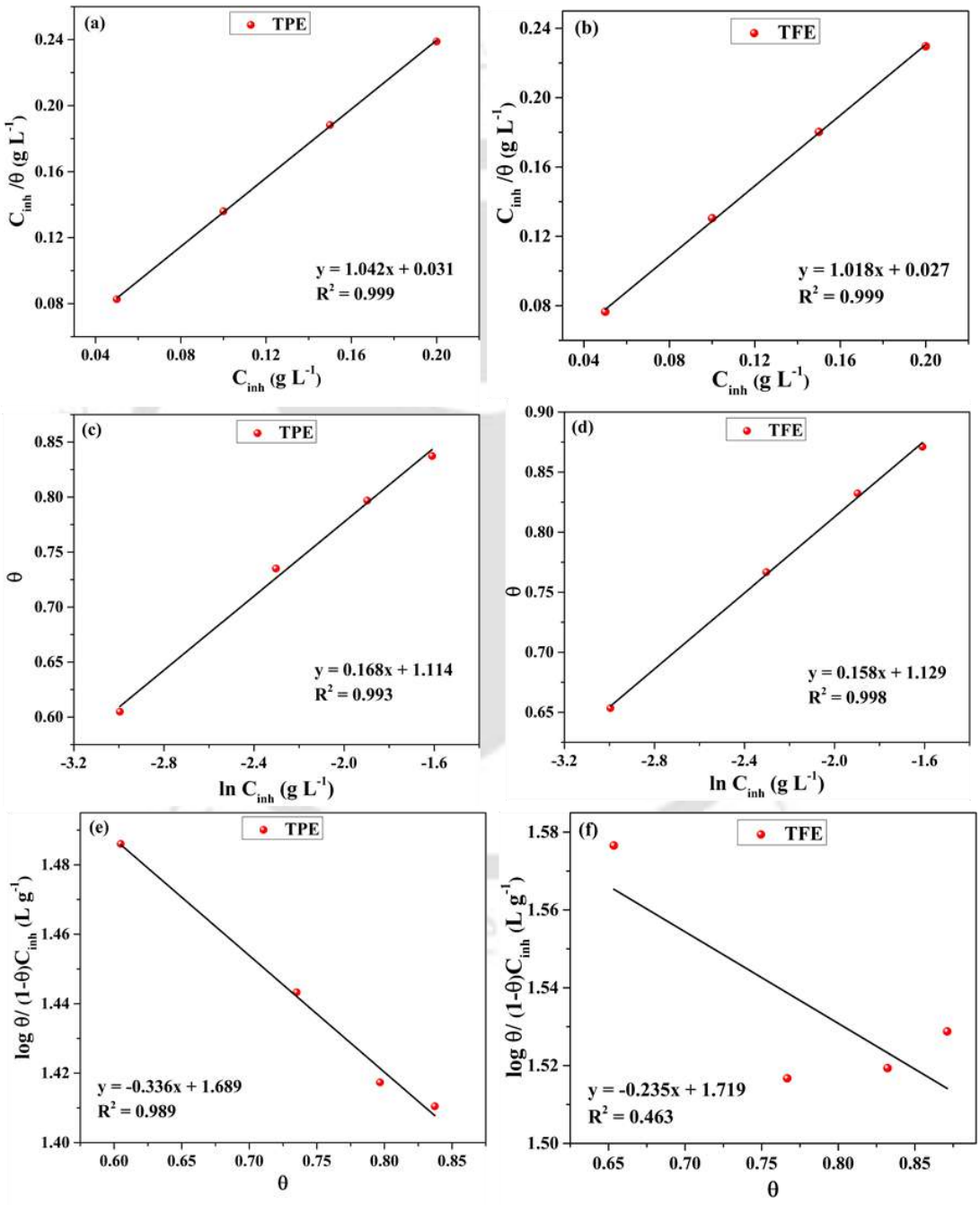

Fig. 4.13. (a, b) Langmuir, (c,d) Temkin, and (e,f) Frumkin isotherms of TPE and TFE, respectively.

Table 4.7 Adsorption isotherm parameters.

Inhibitor	$\frac{1}{K_{ads}}$ (g L^{-1})	K_{ads} (L g^{-1})	ΔG^{o}_{ads} (KJ mol^{-1})
TPE	0.031 ± 0.001	32.26 ± 1.976	-26.15 ± 0.028
TFE	0.027 ± 0.001	37.04 ± 1.012	-26.50 ± 0.035

4.5 Surface investigations

4.5.1 FESEM analysis

FESEM analysis was performed to investigate the variation in the surface morphology of metal due to acidic attack in the presence and absence of the inhibitor. Highly smooth and rough MS surfaces are depicted in Figs. 4.14 (a) and (b), which correspond to the FESEM image of polished MS before and after their 2 h exposure to 1 M HCl, respectively. From these images, it was observed that the MS surface was heavily damaged due to an acid attack in the absence of inhibitors, containing several cracks and pits. Figs. 4.14 (c) and (d) show FESEM images of inhibited systems in the presence of TPE and TFE, respectively, which contain a smoother surface than the blank system.

Furthermore, on comparing these images, it was observed that the addition of tinda extracts (TPE and TFE) provided a significant difference in the microstructures of the MS immersed in 1 M HCl. In the absence of these extracts, the acid attacked the surface severely and corroded the surface by inducing anodic and cathodic reactions on the MS surface, which is confirmed by the presence of cracks and pits in the absence of extracts, as indicated in acidic media. Whereas when the extracts (TPE and TFE) were employed on the surface, such types of strongly corroded structures were not observed in 1 M HCl (Pal and Das, 2022b). These findings imply that both extracts are adsorbed on the metal surface and form a protective layer, which significantly hinders the penetration of corrosive ions from the corrosive solution to the

surface of the metal. These findings are consistent with the outcomes of weight loss and electrochemical studies.

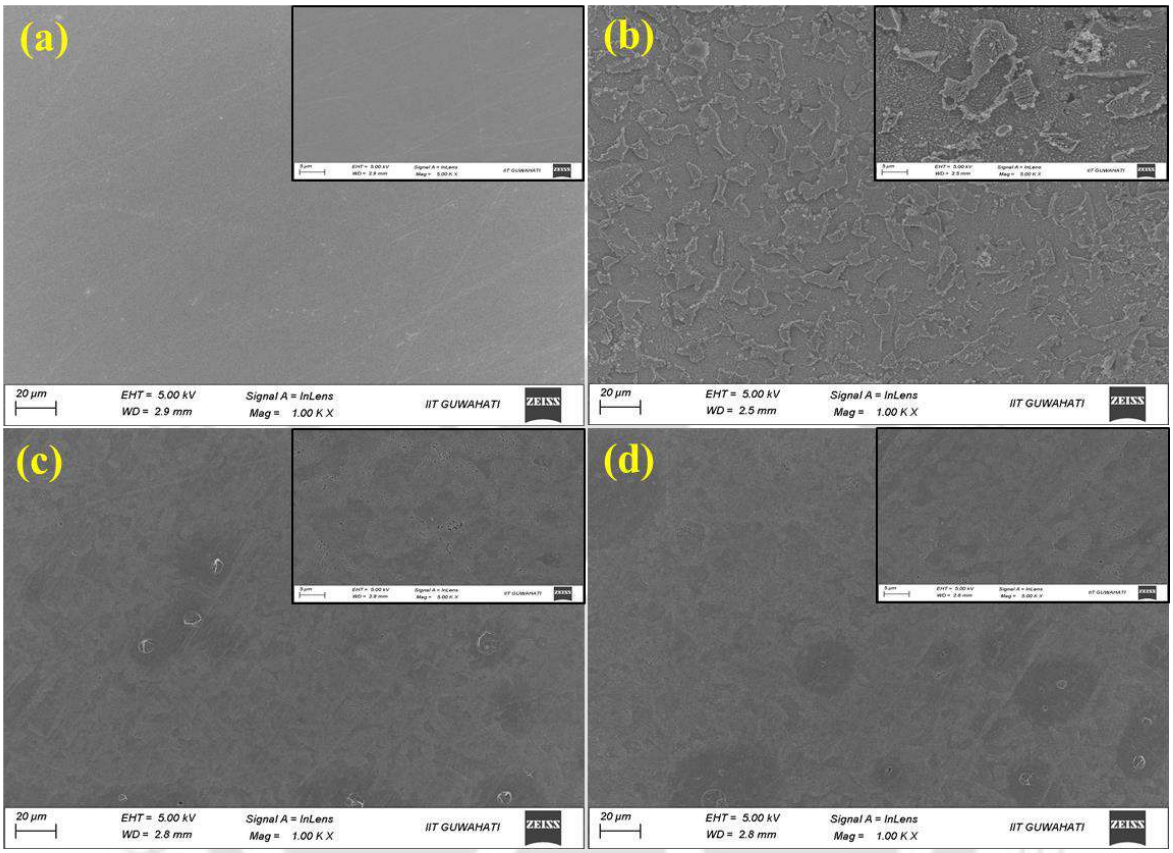

Fig. 4.14 FESEM pictures depict a) MS surface pre-immersion, b) MS without inhibitors, and c) and d) MS with inhibitors, exposed to 1 M HCl with TPE and TFE, respectively.

4.5.2 EDX analysis

EDX analysis was used to investigate elemental variation in the MS surface after their 4 h immersion in 1 M HCl with and without TPE and TFE, shown in Fig. 4.15. Figs 4.15 (a) and 4.15 (b) demonstrate the EDX image of uninhibited MS and pit (from uninhibited MS), respectively. The presence Cl^- in EDX spectra proves that the Cl^- is adsorbed on the MS surface due to its electrostatic attraction with Fe^{2+} on the MS surface in HCl medium (Pal and Das,

2020). These spectra showed a notable decrease and increase in the weight percentage of Fe (from 73.2 to 66.6%) and Cl^- ions (from 2.5 to 3.6%), respectively, within the pit. This suggests that the corrosion process has occurred aggressively within the pits when compared to the flat plane surfaces. Spectra for inhibited systems with TPE and TFE are illustrated by Figs 4.15 (c) and (d), respectively. On comparing all the spectra, it was found that the percentage of Cl^- ions significantly decreased in the presence of extracts and obtained a minimum for TFE, which implies that both extracts adsorbed on the metal surface and formed a strong protective layer that isolates the metal from the electrolyte.

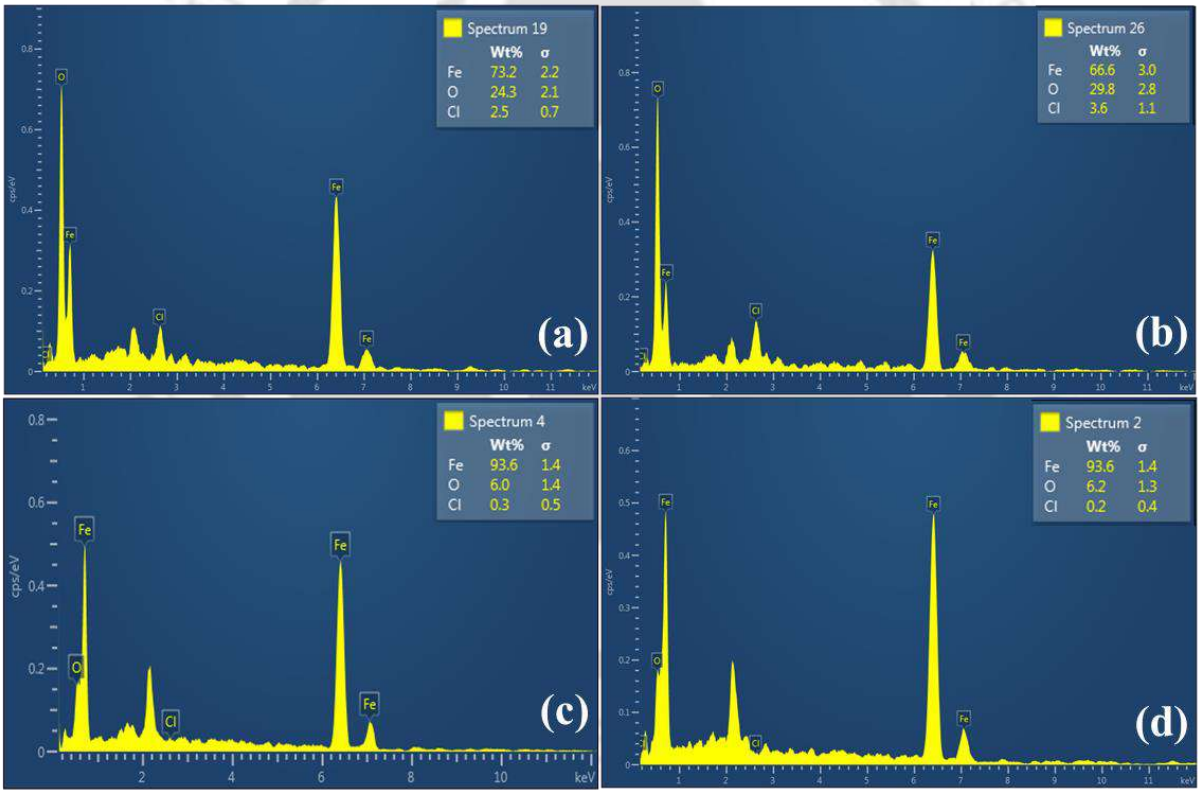

Fig. 4.15 EDX spectrum of a) MS without inhibitor, b) Pits from blank, c) and d) inhibited by TPE and TFE, respectively, after exposure to 1 M HCl.

4.5.3 AFM analysis

The AFM investigation serves as a valuable technique for examining the impact of the tinda extracts on MS dissolution in an acidic medium, specifically in terms of alterations in surface roughness. Fig. 4.16 illustrates the AFM spectra for MS after their 3 h exposure to 1 M HCl. Fig. 4.16 (a) displays the spectrum of the uninhibited MS, exhibiting a significantly rough and cracked surface. This indicates severe damage to the MS surface caused by corroding ions in the absence of inhibitors, which has 492.6 nm average surface roughness. Figs 4.16 (b) and (c) demonstrate the images of inhibited MS with TPE and TFE, respectively. On comparing these images, it has been noticed that surface roughness reduces to 24.58 and 19.33 nm in the presence of TPE and TFE, respectively. This reduction in surface roughness implies that extract molecules adsorbed on metal to form a strong protective layer, which isolates the metal from electrolytes (Verma et al., 2017). These images also indicate that TFE (Fig. 4.16 (c)) resulted in a notably smoother surface, attributed to the robust adsorption of TFE molecules onto the metal surface.

4.5.4 XRD analysis

Fig. 4.17 (a) illustrates the XRD pattern of the polished MS sample before exposure to acid, exhibiting a dominant peak at 2θ value of about 44.59°, accompanied by weaker peaks at various 2θ values of about 64.8°, 82.2°, and 90°. Furthermore, Fig. 4.17 (b) depicts the XRD pattern of MS exposed to 1 M HCl for 2 h without inhibitor, exhibits several peaks at various 2θ values of 35.2°, 44.59°, 64.8°, 82.2°, and 90° corresponding to the Fe and $FeCl_2$ peaks in JCPDS: 06-0696. A peak at 2θ values of 35.2° signifies iron chloride ($FeCl_2$), while the others indicate iron (Fe). Fig. 4.17 (c) shows the XRD spectrum of inhibited MS with TFE, displaying Fe peaks at 44.59°,64.8°, 82.2°, and 90°, with reduced intensity. Additionally, it was noticed that the intensity of the iron chloride peak has been diminished, indicating the development of

a protective layer by adsorbed molecules of TFE. This method potentially facilitates complete interaction between the inhibitor molecules and the surface of MS. Additionally, the obtained outcomes from the XRD technique align well with the findings of EDX, AFM, and FESEM techniques (Muthukrishnan et al., 2019).

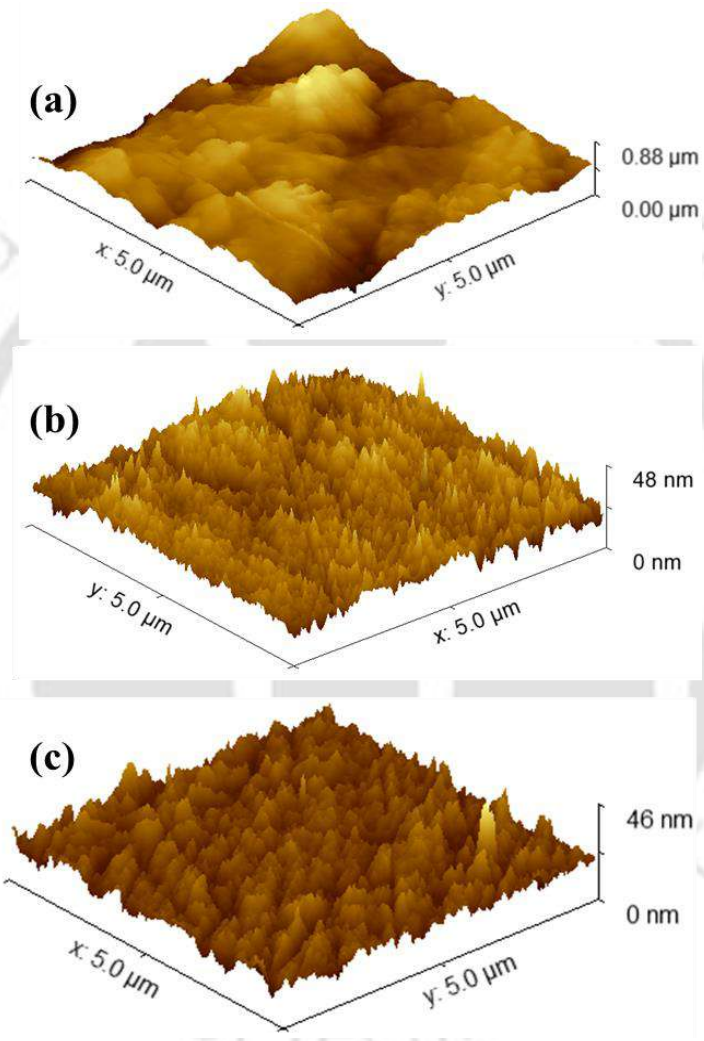

Fig. 4.16 AFM spectrum of a) MS without inhibitor, b) and c) MS with TPE and TFE, respectively, after their exposure to 1 M HCl.

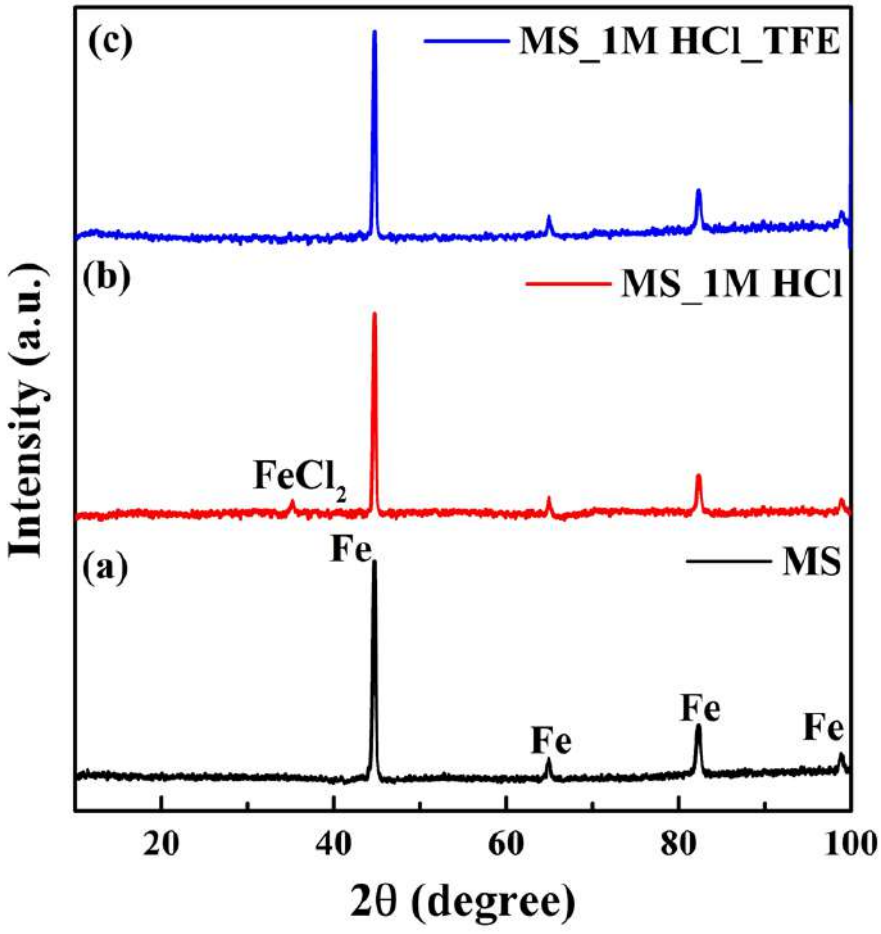

Fig. 4.17 XRD pattern of a) unused MS, (b) MS without inhibitor, and (c) MS with TFE, after exposure to 1 M HCl.

4.6 Corrosion inhibition mechanism

MS degradation mechanism in 1 M HCl is suggested by the following steps:

The mechanism for the anodic degradation of MS is given by the following reactions (Eqs. (4.2- 4.5)):

$$Fe + Cl^- \leftrightarrow (FeCl^-)_{ads} \quad (4.2)$$

$$(FeCl^-)_{ads} \leftrightarrow (FeCl)_{ads} + e^- \quad (4.3)$$

$$(FeCl)_{ads} \rightarrow (FeCl^+)_{ads} + e^- \quad (4.4)$$

$$(FeCl^+)_{ads} \leftrightarrow Fe^{2+} + Cl^- \quad (4.5)$$

The mechanism for cathodic hydrogen evolution is given by the following reactions (Eqs. (4.6- 4.8)):

$$Fe + H^+ \leftrightarrow (FeH^+)_{ads} \quad (4.6)$$

$$(FeH^+)_{ads} + e^- \rightarrow (FeH)_{ads} \quad (4.7)$$

$$(FeH^+)_{ads} + H^+ + 2e^- \rightarrow Fe + H_2 \quad (4.8)$$

The corrosion inhibition properties of both extracts (TPE and TFE) in corrosive environments rely on their interaction with metals (Alao et al., 2023; Pal and Das, 2020). The electrostatic interactions occur between the extract's molecules and pre-adsorbed Cl^- ions on the metal surface, leading to the adsorption of protonated inhibitor molecules (physical adsorption). Over this metal, competition arises between protonated inhibitor molecules and H^+ for electrons. Positively charged inhibitor returns to neutral form after absorbing the electron from MS. The presence of unbound lone pairs in the inhibitor molecule induces their chemical adsorption on the metal surface. As electrons accumulate on the metal surface over time, they become increasingly negatively charged. To mitigate this surplus of negative charge, electrons shift from Fe's d-orbital to the vacant π antibonding orbital of the inhibitor molecules (retro-donation), consequently enhancing the adsorption of inhibitor molecules onto the surface of MS (Srivastava et al., 2018). Outcomes from Tafel experiments depict that both extracts act as mixed-type inhibitors and are adsorbed on metal surfaces by a mixed-type adsorption, which was confirmed by isotherm studies. Additionally, results from surface investigations show that both extracts form a strong protective layer on the surface of MS, which isolates the MS from the electrolytes.

4.7 Literature comparison

The inhibition efficiencies of tinda extracts from electrochemical and weight loss techniques were compared with the recently published work on plant-based extracts. (Al-

Senani et al., 2015) prepared *petroselinum crispum* leaves extract to inhibit the MS corrosion in 1 M HCl. They found a maximum inhibition efficiency of about 81.39 % at a 60 % (v/v) concentration of extract (Al-Senani et al., 2015). (Daoudi et al., 2022) developed *Dysphania ambrosioides* (DA) leaves extract as a corrosion inhibitor, adsorbed by mixed-type adsorption, and gave 84 % maximum inhibition efficiency at 1500 mg L^{-1} amount of inhibitor (Daoudi et al., 2022). Furthermore, the anti-corrosive behavior of yew (*Taxus baccata*) extract was studied by electrochemical and weight methods, and the highest inhibition efficiency (83.28 %) was obtained at 700 mg L^{-1} (Hanini et al., 2019). Few studies reported that *Chromolaena odorata* leaf extract exhibited effective inhibitory efficiency of about 83.33 % at 700 mg L^{-1} for MS immersed in 1 M HCl (Mbamalu and Chinedu, 2023). All these studies were tabulated in Table 4.8, which shows that the current work demonstrated a clear superiority over several previous studies.

Table 4.8 Comparison of corrosion inhibition efficiencies of tinda extracts with the recently published plant-based extracts.

Inhibitor	Metal	*Corrosive medium*	Optimum concentration	*Experimental techniques*	*Inhibition efficiency*	References
Petroselinum crispum (Parsley) leaves extract	Carbon steel	1 M HCl	60 % (v/v)	WL	81.39	(Al-Senani et al., 2015)
Thymus Vulgari plant extract	Stainless Steel	1 M HCl	2 % (v/v)	EIS	62.15	(Ehsani et al., 2017)
Uvaria chamae leaves extract	Mild steel	2.5 M HCl	4000 mg L^{-1}	WL	84.60	(Al et al., 2018)
Bitter leaves (*Vernonia amygdalina*) extract	Mild steel	HCl	1000 mg L^{-1}	WL	85.40	(Onukwuli and Omotioma, 2019)
English yew (*Taxus baccata*) extract	Carbon steel	1 M HCl	700 mg L^{-1}	PDP	83.28	(Hanini et al., 2019)
	Carbon steel	1 M HCl	800 mg L^{-1}	EIS	74.26	
	Carbon steel	1 M HCl	700 mg L^{-1}	WL	61.78	
Ipomoea batatas extract (physically modified Starch)	Galvanized steel	1 M HCl	700 mg L^{-1}	PDP	60.44	(Anyiam et al., 2020)
	Galvanized steel	1 M HCl	700 mg L^{-1}	WL	64.26	
Prunus dulcis seeds extracts	Mild steel	1.5 M HCl	1500 mg L^{-1}	WL	69.95	(Oshomogho et al., 2020)
Dysphania ambrosioides (DA) leaves extract	Mild steel	1 M HCl	1500 mg L^{-1}	PDP	81.69	(Daoudi et al., 2022)
	Mild steel	1 M HCl	1500 mg L^{-1}	EIS	81.18	

	Mild steel	1 M HCl	1500 mg L^{-1}	WL	84.00	
Sarampa wood (*Xylocarpus Moluccensis*) extract	Mild steel	1 M HCl	500 mg L^{-1}	PDP	68.00	(Prifiharni et al., 2022)
	Mild steel	1 M HCl	500 mg L^{-1}	EIS	68.00	
Curcuma. L extract	Mild steel	0.1 M HCl	50 mg L^{-1}	EIS	81.10	(Abidli et al., 2023)
Chromolaena odorata Leaf Extract	Mild steel	1 M HCl	700 mg L^{-1}	PDP	81.60	(Mbamalu and Chinedu, 2023)
	Mild steel	1 M HCl	700 mg L^{-1}	WL	83.33	
Senna Obtusifolia/ Leaves Extract	Mild steel	0.5 M HCl	800 mg L^{-1}	PDP	75.55	
	Mild steel	0.5 M HCl	800 mg L^{-1}	EIS	76.32	(Abdulbasit et al., 2023)
	Mild steel	0.5 M HCl	800 mg L^{-1}	WL	85.67	
Tinda peal extract (TPE)	Mild steel	1 M HCl	200 mg L^{-1}	PDP	83.73	**Present study**
	Mild steel	1 M HCl	200 mg L^{-1}	EIS	79.39	
	Mild steel	1 M HCl	200 mg L^{-1}	WL	81.59	
Tinda fruit extract (TFE)	Mild steel	1 M HCl	200 mg L^{-1}	PDP	87.11	
	Mild steel	1 M HCl	200 mg L^{-1}	EIS	81.92	
	Mild steel	1 M HCl	200 mg L^{-1}	WL	86.00	

4.8 Summary

The inhibiting effectiveness of tinda extracts (TPE and TFE) on MS immersed in 1 M HCl was investigated using electrochemical and gravimetric techniques. The prepared extracts showed excellent inhibiting behavior due to the presence of several compounds, such as phenol, 3,5-bis (1,1-dimethylethyl)-, 9-octadecenoic acid, methyl ester, hexadecanoic acid 15-methyl-, methyl ester, 9, 12-octadecadienoic acid, methyl ester, 9, 12, 15-octadecatrienoic acid, methyl ester, (Z,Z,Z-), ascorbic acid, and phytol, which were identified by LC/MS analysis. The existence of these compounds was further confirmed by FTIR analysis. After all observations, the following findings were obtained.

- The average corrosion potential (E_{corr}) exhibited a positive shift for inhibited systems as compared to uninhibited systems.
- The values of i_{corr} and inhibition efficiencies were decreased and increased, respectively, with increasing inhibitor concentration.
- The maximum inhibitory efficiencies (83.73 and 87.11 %) were achieved at 200 mg L^{-1} of TPE and TFE, respectively.
- The value of R_{ct} was found as 25.89 Ω cm^2 for the uninhibited system, which was increased to 125.18 Ω cm^2 and 142.69 Ω cm^2 on the addition of TPE (200 mg L^{-1}) and TFE (200 mg L^{-1}) respectively, which implies that corrosive ions face more hindrance to reaching the metal surface for inhibited systems as compared to blank.
- The outcomes from the gravimetric analysis revealed almost the same inhibiting behavior of both tinda extract (TPE and TFE) as recorded in electrochemical studies.
- Both tinda extract (TPE and TFE) exhibited significant inhibitory effects with 70.71 and 72.74 % inhibition efficiency at 323 K. The values of E_a, ΔH, and ΔS exhibited a positive hike as compared to blank.

- The obtained values of ΔG°_{ads} for TPE and TFE lie between -20 and -40 kJ $mol^{-1,}$ but close to -20 kJ $mol^{-1\ 1,}$ which depicts preferentially physical adsorption (mixed-type adsorption) of the extract on the metal surface.
- The results from the electrochemical and gravimetric analysis showed that tinda extracts adsorbed on metal and constructed a protective layer of extract molecules, which hindered the MS corrosion, these findings were well supported by outcomes of surface characterization techniques.

4.9 References

Abdulbasit, Y., Abdullahi, B., Bishir, U., 2023. Experimental and theoretical evaluation of corrosion inhibition performance of senna obtusifolia leaves extract on mild steel in 0.5M HCl. Moroccan J. Chem. 11, 282–299. https://doi.org/10.48317/IMIST.PRSM/morjchem-v11i2.38203

Abidli, I., Souissi, N., Essalah, K., Novoa, X.R., 2023. A combined experimental and theoretical approach effect of Curcuma. L extract as a corrosion inhibitor on iron in acidic solution. Can. Metall. Q. 63, 1–19. https://doi.org/10.1080/00084433.2023.2240113

AI, O., KJ, U., MC, E., PC, O., EC, O., 2018. Thermodynamic and kinetic studies of powerful eco friendly green inhibitors; Costus afer, Uvaria chamae and Xylopia aethiopia for the control of mild steel corrosion in HCl solution. J. Phys. Chem. Biophys. 08. https://doi.org/10.4172/2161-0398.1000264

Al-Amiery, A., Isahak, W.N.R.W., Al-Azzawi, W.K., 2023. ODHI: A promising isatin-based corrosion inhibitor for mild steel in hydrochloric acid. J. Mol. Struct. 1288, 135829. https://doi.org/10.1016/j.molstruc.2023.135829

Al-Amiery, A.A., Al-Azzawi, W.K., Isahak, W.N.R.W., 2022. Isatin Schiff base is an effective corrosion inhibitor for mild steel in hydrochloric acid solution: gravimetrical, electrochemical, and computational investigation. Sci. Rep. 12, 17773. https://doi.org/10.1038/s41598-022-22611-4

Al-Amiery, A.A., Betti, N., Isahak, W.N.R.W., Al-Azzawi, W.K., Wan Nik, W.M.N., 2023. Exploring the effectiveness of Isatin–schiff base as an environmentally friendly corrosion inhibitor for mild steel in hydrochloric acid. Lubricants 11, 211.

https://doi.org/10.3390/lubricants11050211

Al-Moubaraki, A.H., 2018. Potential of borage flowers aqueous extract, Borago officinalis L., against the corrosion of mild steel in phosphoric acid. Anti-Corros. Methods Mater. 65, 53–65. https://doi.org/10.1108/ACMM-04-2017-1788

Al-Moubaraki, A.H., Awaji, H., 2020. 1-X-4-[4´-(–OCH3)-Styryl] pyridinium iodides, potent inhibitors for stainless steel corrosion in 2 M HCl acid solutions. Int. J. Corros. Scale Inhib. 9, 460–501. https://doi.org/10.17675/2305-6894-2020-9-2-5

Al-Senani, G., Al-Saeedi, S., Almufarij, R., 2015. Green corrosion inhibitors for carbon steel by green leafy vegetables extracts in 1 M HCl. Orient. J. Chem. 31, 2077–2086. https://doi.org/10.13005/ojc/310428

Alao, A.O., Popoola, A.P., Dada, M.O., Sanni, O., 2023. Utilization of green inhibitors as a sustainable corrosion control method for steel in petrochemical industries: A review. Front. Energy Res. 10, 1–21. https://doi.org/10.3389/fenrg.2022.1063315

Ali Asaad, M., Sarbini, N.N., Sulaiman, A., Ismail, M., Huseien, G.F., Abdul Majid, Z., Bothi Raja, P., 2018. Improved corrosion resistance of mild steel against acid activation: Impact of novel Elaeis guineensis and silver nanoparticles. J. Ind. Eng. Chem. 63, 139–148. https://doi.org/10.1016/j.jiec.2018.02.010

Alzurfi, S.K.L., Rabeea, M.A.A., Algburi, J.B., Ibrahimi, N.N., Al-Haidarey, M.J.S., 2019. Identification lipid compounds of aquatic plant hydrilla verticillata (Linn. F.) royal. Res. J. Pharm. Technol. 12, 5621. https://doi.org/10.5958/0974-360X.2019.00973.9

Ameh, P.O., 2018. Electrochemical and computational study of gum exudates from Canarium schweinfurthii as green corrosion inhibitor for mild steel in HCl solution. J. Taibah Univ. Sci. 12, 783–795. https://doi.org/10.1080/16583655.2018.1514147

Ameh, P.O., Eddy, N.O., 2020. Theoretical and experimental investigations of the corrosion inhibition action of piliostigma thonningii extract on mild steel in acidic medium. Commun. Phys. Sci. 2018, 27–42

Anyiam, C.K., Ogbobe, O., Oguzie, E.E., Madufor, I.C., Nwanonenyi, S.C., Onuegbu, G.C., Obasi, H.C., Chidiebere, M.A., 2020. Corrosion inhibition of galvanized steel in hydrochloric acid medium by a physically modified starch. SN Appl. Sci. 2, 520. https://doi.org/10.1007/s42452-020-2322-2

Aslam, R., Mobin, M., Shoeb, M., Aslam, J., 2022. Novel ZrO_2-glycine nanocomposite as eco-friendly high temperature corrosion inhibitor for mild steel in hydrochloric acid solution. Sci. Rep. 12, 9274. https://doi.org/10.1038/s41598-022-13359-y

Bangera, S., Alva, V.D.P., Sannaiah, P.N., 2022. Hemigraphis colorata (HC) leaves extract as effectual green inhibitor for mild steel corrosion in 1 M HCl. Biointerface Res. Appl. Chem. 13, 200. https://doi.org/10.33263/BRIAC132.200

Betti, N., Al-Amiery, A.A., Al-Azzawi, W.K., Isahak, W.N.R.W., 2023. Corrosion inhibition properties of schiff base derivative against mild steel in HCl environment complemented with DFT investigations. Sci. Rep. 13, 8979. https://doi.org/10.1038/s41598-023-36064-w

Bhan, C., Kumar Golder, A., 2023. Bio-based hierarchical vertically aligned 2D ZnO nanostructures for ultra selective electrochemical sensing of p-Chloroaniline. Chem. Eng. J. 475, 146122. https://doi.org/10.1016/j.cej.2023.146122

Bhuvaneswari, T.K., Vasantha, V.S., Jeyaprabha, C., 2018. Pongamia pinnata as a green corrosion inhibitor for mild steel in 1 N sulfuric acid medium. Silicon 10, 1793–1807. https://doi.org/10.1007/s12633-017-9673-3

Canales, C., Galarce, C., Rubio, F., Pineda, F., Anguita, J., Barros, R., Parragué, M., Daille, L.K., Aguirre, J., Armijo, F., Pizarro, G.E., Walczak, M., De la Iglesia, R., Navarrete, S.A., Vargas, I.T., 2021. Testing the Test: A comparative study of marine microbial corrosion under laboratory and field conditions. ACS Omega 6, 13496–13507. https://doi.org/10.1021/acsomega.1c01762

Chidiebere, M.A., Oguzie, E.E., Liu, L., Li, Y., Wang, F., 2015. Ascorbic acid as corrosion inhibitor for Q235 mild steel in acidic environments. J. Ind. Eng. Chem. 26, 182–192. https://doi.org/10.1016/j.jiec.2014.11.029

Daoudi, W., El Aatiaoui, A., Falil, N., Azzouzi, M., Berisha, A., Olasunkanmi, L.O., Dagdag, O., Ebenso, E.E., Koudad, M., Aouinti, A., Loutou, M., Oussaid, A., 2022. Essential oil of Dysphania ambrosioides as a green corrosion inhibitor for mild steel in HCl solution. J. Mol. Liq. 363, 119839. https://doi.org/10.1016/j.molliq.2022.119839

Ehsani, A., Mahjani, M.G., Hosseini, M., Safari, R., Moshrefi, R., Mohammad Shiri, H., 2017. Evaluation of Thymus vulgaris plant extract as an eco-friendly corrosion inhibitor for stainless steel 304 in acidic solution by means of electrochemical impedance spectroscopy, electrochemical noise analysis and density functional theory. J. Colloid Interface Sci. 490, 444–451. https://doi.org/10.1016/j.jcis.2016.11.048

Faustin, M., Maciuk, A., Salvin, P., Roos, C., Lebrini, M., 2015. Corrosion inhibition of C38 steel by alkaloids extract of Geissospermum laeve in 1 M hydrochloric acid: Electrochemical and phytochemical studies. Corros. Sci. 92, 287–300.

https://doi.org/10.1016/j.corsci.2014.12.005

Fitoz, A., Yılmaz, H., Hayvalı, M., Emregül, K.C., 2023. Evaluation of an aza dipyrromethene derivative as a green corrosion inhibitor via experimental and theoretical methods. J. Mol. Liq. 391, 123407. https://doi.org/10.1016/j.molliq.2023.123407

Hagr, T.E., Adam, I.A., Almain, A.A., Mohammed, M.M., 2019. Phytochemical screening, GC-MS Analysis, antibacterial and antioxidant activity of seeds oil of Annona squmosa L . Sudanese medicinal plant. Open Sci. J. Pharm. Pharmacol. 7, 1–6.

Haldhar, R., Prasad, D., Kamboj, D., Kaya, S., Dagdag, O., Guo, L., 2021. Corrosion inhibition, surface adsorption and computational studies of Momordica charantia extract: A sustainable and green approach. SN Appl. Sci. 3, 25. https://doi.org/10.1007/s42452-020-04079-x

Haldhar, R., Prasad, D., Saxena, A., Kumar, R., 2018. Experimental and theoretical studies of Ficus religiosa as green corrosion inhibitor for mild steel in 0.5 M H_2SO_4 solution. Sustain. Chem. Pharm. 9, 95–105. https://doi.org/10.1016/j.scp.2018.07.002

Hanini, K., Merzoug, B., Boudiba, S., Selatnia, I., Laouer, H., Akkal, S., 2019. Influence of different polyphenol extracts of Taxus baccata on the corrosion process and their effect as additives in electrodeposition. Sustain. Chem. Pharm. 14, 100189. https://doi.org/10.1016/j.scp.2019.100189

Haque, J., Verma, C., Srivastava, V., Nik, W.B.W., 2021. Corrosion inhibition of mild steel in 1 M HCl using environmentally benign Thevetia peruviana flower extracts. Sustain. Chem. Pharm. 19, 100354. https://doi.org/10.1016/j.scp.2020.100354

Ishnava, K.B., Patel, K.S., 2020. In vitro study of *Praecitrulus fistulosus* (Stocks) Pangalo (Cucurbitaceae) fruit – A potential candidate of Anthelmintic activity. Bull. Natl. Res. Cent. 44, 130. https://doi.org/10.1186/s42269-020-00365-1

Itodo, A.U., Aondofa, B.G., Iorungwa, M.S., 2018. Retarding mild steel corrosion using a blend of schiff base metal complex and neem plant extract. ChemSearch J. 9, 45–63.

Jeeja, R., A., Thomas, A., Arshad, M., Joseph, A., 2022. The influence of aqueous and alcoholic extracts of Garcinia cambogia fruit rind in the management of mild steel corrosion in hydrochloric acid: Theoretical and electroanalytical studies. J. Mol. Liq. 346, 117873. https://doi.org/10.1016/j.molliq.2021.117873

Jeeja, R.A., Arshad, M., Kuruvilla, M., Joseph, A., 2023. Computational modelling and correlation of physical parameters of 1-heptatriacotanol, phytol and 3, 7, 11, 15-tetra methyl-2-hexadecen-1-ol with the corrosion inhibition efficiency of CIW for mild steel in

HCl. Corros. Eng. Sci. Technol. 58, 243–258. https://doi.org/10.1080/1478422X.2023.2165238

Ji, G., Shukla, S.K., Dwivedi, P., Sundaram, S., Prakash, R., 2011. Inhibitive effect of argemone mexicana plant extract on acid corrosion of mild steel. Ind. Eng. Chem. Res. 50, 11954–11959. https://doi.org/10.1021/ie201450d

Kaya, F., Solmaz, R., Geçibesler, İ.H., 2023a. Investigation of adsorption, corrosion inhibition, synergistic inhibition effect and stability studies of Rheum ribes leaf extract on mild steel in 1 M HCl solution. J. Taiwan Inst. Chem. Eng. 143, 104712. https://doi.org/10.1016/j.jtice.2023.104712

Kaya, F., Solmaz, R., Halil Geçibesler, İ., 2023b. The use of methanol extract of Rheum Ribes (Işgın) flower as a natural and promising corrosion inhibitor for mild steel protection in 1 M HCl solution. J. Ind. Eng. Chem. 122, 102–117. https://doi.org/10.1016/j.jiec.2023.02.013

M'hiri, N., Veys-Renaux, D., Rocca, E., Ioannou, I., Boudhrioua, N.M., Ghoul, M., 2016. Corrosion inhibition of carbon steel in acidic medium by orange peel extract and its main antioxidant compounds. Corros. Sci. 102, 55–62. https://doi.org/10.1016/j.corsci.2015.09.017

Mbamalu, E.E., Chinedu, A.P., 2023. Assessment of the corrosion inhibitory potentials of chromolaena odorata leaf extract on mild steel in hydrogen chloride acid environment. Moroccan J. Chem. 11, 188–204. https://doi.org/doi.org/10.48317/IMIST.PRSM/morjchem-v10i3.30521

Mourya, P., Banerjee, S., Singh, M.M., 2014. Corrosion inhibition of mild steel in acidic solution by Tagetes erecta (Marigold flower) extract as a green inhibitor. Corros. Sci. 85, 352–363. https://doi.org/10.1016/j.corsci.2014.04.036

Muthukrishnan, P., Prakash, P., Jeyaprabha, B., Shankar, K., 2019. Stigmasterol extracted from Ficus hispida leaves as a green inhibitor for the mild steel corrosion in 1 M HCl solution. Arab. J. Chem. 12, 3345–3356. https://doi.org/10.1016/j.arabjc.2015.09.005

Nijarubini, V., Mallika, J., 2023. Application of silk protein hydrolysate as a potent anti-corrosive agent for mild steel in HCl solution. RASAYAN J. Chem. 16, 972–984. https://doi.org/10.31788/rjc.2023.1628367

Obot, A.S., Boekom, E.J., Ita, B.N., Utam, E.C., 2022. Kinetics consideration of ethanol leaves extract of costus lucanusianus as green corrosion inhibitor for mild steel and aluminium in HCl solution. Int. J. Res. -Granthaalayah 10.

https://doi.org/10.29121/granthaalayah.v10.i1.2022.4461

Odewunmi, N.A., Mazumder, M.A.J., Ali, S.A., Alharbi, B.G., 2021. Hydroquinone decorated with alkyne, quaternary ammonium, and hydrophobic motifs to mitigate corrosion of x-60 mild steel in 15 wt.% HCl. Chem. – An Asian J. 16, 801–821. https://doi.org/10.1002/asia.202100085

Onukwuli, O.D., Omotioma, M., 2019. Study of Bitter leaves extract as inhibitive agent in hcl medium for the treatment of mild steel through pickling. Port. Electrochim. Acta 37, 115–121. https://doi.org/10.4152/pea.201902115

Oshomogho, F.O., Akhihiero, T.E., Edokpayi, O., Ossai, J.E., 2020. Green corrosion inhibition of mild steel using Prunus Dulcis seeds extract in an acidic medium. Glob. J. Pure Appl. Sci. 26, 171–178. https://doi.org/10.4314/gjpas.v26i2.9

Pal, A., Das, C., 2023. Novel use of kitchen waste: protection of boiler quality steel from corrosion in acidic media using onion waste. Chem. Pap. 77, 1107–1127. https://doi.org/10.1007/s11696-022-02549-7

Pal, A., Das, C., 2022a. Investigations on corrosion inhibition in acidic media for BQ steel using banana flower bract, an eco-friendly novel agro-waste: Experimental and theoretical considerations. Inorg. Chem. Commun. 145, 110024. https://doi.org/10.1016/j.inoche.2022.110024

Pal, A., Das, C., 2022b. New eco-friendly anti-corrosion inhibitor of purple rice bran extract for boiler quality steel: Experimental and theoretical investigations. J. Mol. Struct. 1251, 131988. https://doi.org/10.1016/j.molstruc.2021.131988

Pal, A., Das, C., 2020. A novel use of solid waste extract from tea factory as corrosion inhibitor in acidic media on boiler quality steel. Ind. Crops Prod. 151, 112468. https://doi.org/10.1016/j.indcrop.2020.112468

Prifiharni, S., Mashanafie, G., Priyotomo, G., Royani, A., Ridhova, A., Elya, B., Soedarsono, J.W., 2022. Extract sarampa wood (Xylocarpus Moluccensis) as an eco-friendly corrosion inhibitor for mild steel in HCl 1M. J. Indian Chem. Soc. 99, 100520. https://doi.org/10.1016/j.jics.2022.100520

Rocha, J.C. D, Gomes, J.A. D C.P., D'Elia, E., 2010. Corrosion inhibition of carbon steel in hydrochloric acid solution by fruit peel aqueous extracts. Corros. Sci. 52, 2341–2348. https://doi.org/10.1016/j.corsci.2010.03.033

Saxena, A., Prasad, D., Haldhar, R., 2018. Investigation of corrosion inhibition effect and adsorption activities of Cuscuta reflexa extract for mild steel in 0.5 M H_2SO_4.

Bioelectrochemistry 124, 156–164. https://doi.org/10.1016/j.bioelechem.2018.07.006

Shawer, E., Sabae, S., El-Gamal, A., Elsaied, H., 2022. Characterization of bioactive compounds with antioxidant activity and antimicrobial activity from freshwater cyanobacteria. Egypt. J. Chem. 65, 0–0. https://doi.org/10.21608/ejchem.2022.127880.5681

Srivastava, V., Chauhan, D.S., Joshi, P.G., Maruthapandian, V., Sorour, A.A., Quraishi, M.A., 2018. PEG-functionalized chitosan: a biological macromolecule as a novel corrosion inhibitor. ChemistrySelect 3, 1990–1998. https://doi.org/10.1002/slct.201701949

Tang, M., Li, X., Deng, S., Lei, R., 2021. Synergistic inhibition effect of Mikania micrantha extract with KI on steel corrosion in H_2SO_4 solution. J. Mol. Liq. 344, 117926. https://doi.org/10.1016/j.molliq.2021.117926

Thakur, A., Kumar, A., Kaya, S., Benhiba, F., Sharma, S., Ganjoo, R., Assad, H., 2023. Electrochemical and computational investigations of the Thysanolaena latifolia leaves extract: An eco-benign solution for the corrosion mitigation of mild steel. Results Chem. 6, 101147. https://doi.org/10.1016/j.rechem.2023.101147

Thomas, A., Prajila, M., Shainy, K.M., Joseph, A., 2020. A green approach to corrosion inhibition of mild steel in hydrochloric acid using fruit rind extract of Garcinia indica (Binda). J. Mol. Liq. 312, 113369. https://doi.org/10.1016/j.molliq.2020.113369

Thummajitsakul, S., Samaikam, S., Tacha, S., Silprasit, K., 2020. Study on FTIR spectroscopy, total phenolic content, antioxidant activity and anti-amylase activity of extracts and different tea forms of Garcinia schomburgkiana leaves. LWT 134, 110005. https://doi.org/10.1016/j.lwt.2020.110005

Umoren, S.A., Obot, I.B., Gasem, Z.M., 2015. Adsorption and corrosion inhibition characteristics of strawberry fruit extract at steel/acids interfaces: experimental and theoretical approaches. Ionics (Kiel). 21, 1171–1186. https://doi.org/10.1007/s11581-014-1280-3

Verma, C., Olasunkanmi, L.O., Ebenso, E.E., Quraishi, M.A., 2018. Adsorption characteristics of green 5-arylaminomethylene pyrimidine-2,4,6-triones on mild steel surface in acidic medium: Experimental and computational approach. Results Phys. 8, 657–670. https://doi.org/10.1016/j.rinp.2018.01.008

Verma, C., Quraishi, M.A., Kluza, K., Makowska-Janusik, M., Olasunkanmi, L.O., Ebenso, E.E., 2017. Corrosion inhibition of mild steel in 1 M HCl by D-glucose derivatives of dihydropyrido [2,3-d:6,5-d′] dipyrimidine-2, 4, 6, 8(1H,3H, 5H,7H)-tetraone. Sci. Rep. 7,

44432. https://doi.org/10.1038/srep44432

Wang, C, Chen, J., Hu, B., Liu, Z., Wang, Chongbin, Han, J., Su, M., Li, Y., Li, C., 2019. Modified chitosan-oligosaccharide and sodium silicate as efficient sustainable inhibitor for carbon steel against chloride-induced corrosion. J. Clean. Prod. 238, 117823. https://doi.org/10.1016/j.jclepro.2019.117823

Chapter 5:

Investigations on corrosion inhibition of mild steel in acid medium using *Phaseolus lunatus* peel and seed extracts

Investigations on corrosion inhibition of mild steel in acid medium using *Phaseolus lunatus* peel and seed extracts

This chapter presents the corrosion inhibition potential of Phaseolus lunatus (lima bean) peel and seed extracts to mitigate mild steel corrosion in 1 M HCl. LC-MS and FTIR analyses were used to identify active compounds (lysine, leucine, oleic acid, linoleic acid, 9-Octadecenoic acid (Z)-, methyl ester, and ascorbic acid) therein, which are responsible for corrosion inhibition. Electrochemical and weight loss studies showed that maximum efficiencies of 85.69% and 90.78% were achieved at 200 mg L^{-1} of Phaseolus lunatus peel extract (PLPE) and Phaseolus lunatus seed extract (PLSE), respectively. These extracts acted as mixed-type inhibitors. During the adsorption studies, Langmuir adsorption isotherm exhibited the best fit, and extracts followed the preferentially physical adsorption process. Thermodynamic analysis confirmed the spontaneous and endothermic corrosion of MS. Surface characterization confirmed the formation of a protective layer on the MS surface, which effectively protects MS from corrosive electrolytes.

Published Article: Kumar, A., Das, C., 2025. Investigations on corrosion inhibition of mild steel in acid medium using *Phaseolus lunatus* peel and seed extracts. ***Mater. Today Commun.*** 49, 113752. https://doi.org/10.1016/j.mtcomm.2025.113752.

5.1 Characterization of PLPE and PLSE

5.1.1 LC-MS analysis

Phaseolus lunatus peel and seed extracts (PLPE and PLSE) were examined by liquid chromatography-mass spectroscopy to identify the available compounds. The mass spectra corresponding to the LC-MS analysis of PLPE and PLSE exhibited characteristic peaks of lysine, leucine, oleic acid, linoleic acid, 9-Octadecenoic acid (Z)-, methyl ester, and ascorbic acid at m/z values of 147.1, 132.10, 282.26, 281.25, 296.27, and 176.03, respectively, as shown in Fig. 5.1. Moreover, PLSE (Fig. 5.1 b) displayed higher relative intensities of leucine, linoleic acid, and ascorbic acid compared to PLPE (Fig. 5.1 a), suggesting a greater abundance of these compounds in PLSE. These compounds have all the necessary features (double bonds, conjugated bonds, heteroatoms, and long carbon chains) to be effective corrosion inhibitors. Recently, several studies have reported that these compounds have excellent corrosion-inhibiting ability against acidic media (Ameh, 2018; Hermoso-Diaz et al., 2019; Mahgoub et al., 2019; Wang et al., 2023).

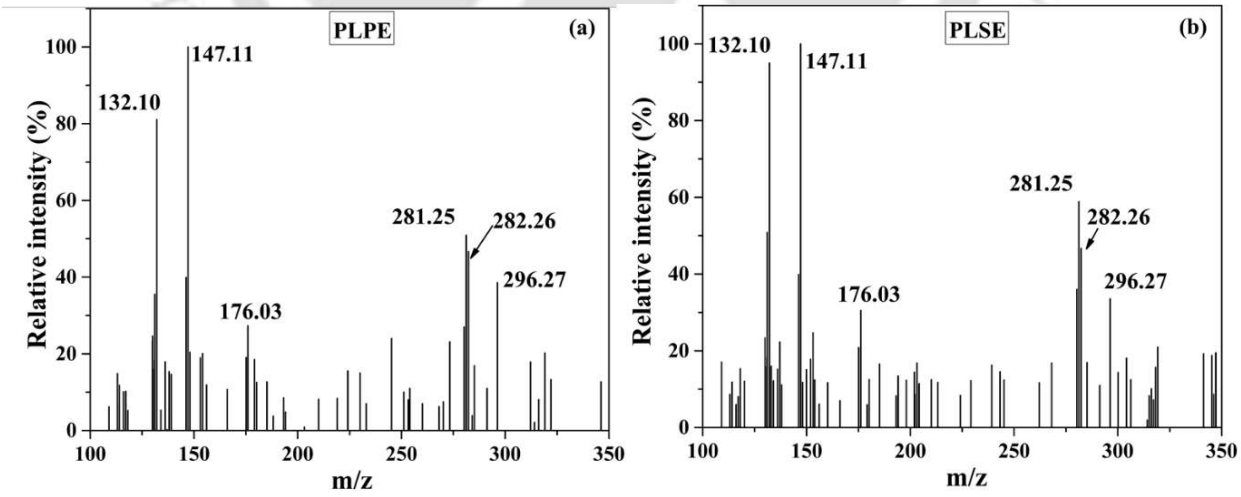

Fig. 5.1 Mass spectrums of PLPE (a) and PLSE (b).

5.1.2 FTIR analysis

The FTIR spectra of PLPE and PLSE are shown in Fig. 5.2. The bands at 3345 cm^{-1} and 3347 cm^{-1} were attributed to the O–H stretching vibration in PLPE and PLSE, respectively. Furthermore, weak bands between wavenumbers 2950−3100 cm^{-1} were attributed to N−H stretching bands (Naik et al., 2018; Shah et al., 2024). The peaks at 2903 cm^{-1} (PLPE) and 2900 cm^{-1} (PLSE) denote the asymmetric stretching of the CH_2 group. Additionally, bands at 1718, 1645 cm^{-1} for PLPE and 1717, 1647 cm^{-1} for PLSE correspond to C=O bending. The bands at 1417 cm^{-1} (PLPE) and 1418 cm^{-1} (PLSE) represent the alkene bending vibrations in extracts (Ishnava and Patel, 2020). The absorptions at 1383 cm^{-1} (PLPE) and 1384 cm^{-1} (PLSE) could be due to the CH_3 bending vibration in both extracts. Furthermore, bands in the range of 1026 – 1086 cm^{-1} correspond to C-O-C stretching vibrations in both *Phaseolus lunatus* extracts, such as PLPE (1045 and 1086 cm^{-1}) and PLSE (1047 and 1086 cm^{-1}). The bands at 878 and 879 are related to the -OH out plane bonds in PLPE and PLSE, respectively (Masuku et al., 2021). These results showed that both *Phaseolus lunatus* extracts (PLPE and PLSE) contained nitrogen and oxygen in their functional groups (O–H, C=O, C=C, C-O-C, and NH), that are well aligned with the findings of LC-MS analysis.

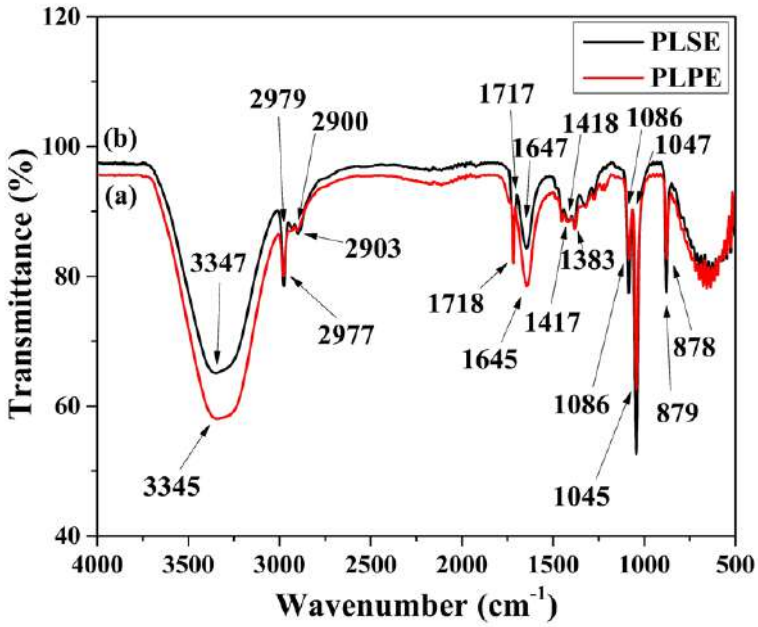

Fig. 5.2 FTIR spectra of (a) PLPE and (b) PLSE.

5.2 Corrosion test

5.2.1 Weight loss studies

5.2.1.1 Effect of concentration of *Phaseolus lunatus* extracts

The weight loss measurement technique is most commonly used to evaluate the rate of corrosion as well as to scrutinize the anticorrosive behavior of inhibitors due to their ease of use. In this work, weight loss measurements were performed thrice with the same operational conditions using several concentrations of *Phaseolus lunatus* extract. To investigate the corrosion mitigation nature of *Phaseolus lunatus* extracts, various amounts of these extracts (PLPE and PLSE) were used, such as 0, 50, 100, 150, 200, and 250 mgL^{-1}. During the experiments, it was noticed that corrosion rates decreased with the addition of PLPE and PLSE up to 200 mg L^{-1}, which signifies that molecules of PLPE and PLSE adsorbed on MS and generate an inhibiting layer that acts as a barrier between MS and corrosive solution. Furthermore, the layer's compactness was increased with the addition of PLPE and PLSE up to 200 mg L^{-1}. As the doses of PLPE and PLSE increased further to 250 mg L^{-1}, the values of

inhibiting efficiencies displayed a marginal rise (~1%), indicating the adsorption of PLPE and PLSE on MS to exhibit an unchanged inhibitory efficiency above 200 mg L^{-1} concentrations of inhibitors. These outcomes can be explained by the fact that the available inhibitor molecules are very less as compared to the active site of the metallic surface at lower doses of inhibitor, which are not capable of covering the whole surface of the metal, resulting in a low inhibitory effect but these adsorbed molecules increase on metal surface with increasing the concentration of inhibitors. After a certain dose of inhibitors, all active sites of the metallic surface were completely occupied by adsorbed inhibitor molecules, leading to the highest constant inhibitory efficiency (Kumar and Das, 2024).

The values of inhibition efficiencies for *Phaseolus lunatus* extracts were constant above their amounts of 200 mg L^{-1}, indicating that the metal's surface was covered with PLPE and PLSE, and it reached equilibrium. Hence, this system showed the highest inhibitory effect. These findings suggest that 200 mg L^{-1} is the optimal dose of PLPE and PLSE for their corrosion-inhibiting behavior (Fig. 5.3). Few studies have also reported a similar variation in inhibition efficiency (Boudalia et al., 2023). For the optimum amount of *Phaseolus lunatus* extracts, the following maximum inhibition efficiencies were obtained: 85.50 % (PLPE) and 90.54 % (PLSE) after 24 h of exposure. Similar immersion times of 24 h have been reported by few studies that have examined the impact of inhibitor concentration (Boutoumit et al., 2024).

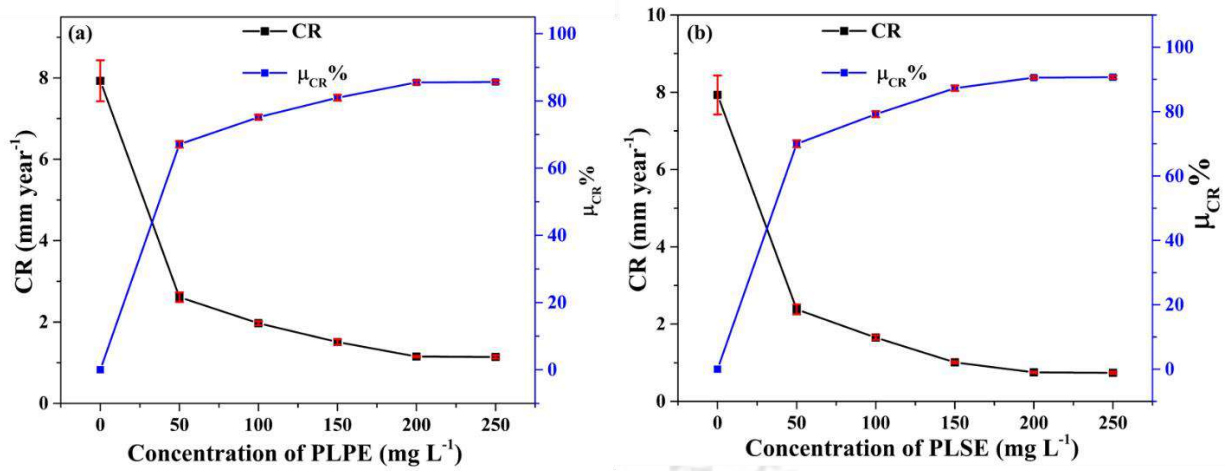

Fig. 5.3. Variations in CR and μ_{CR} % with increasing the amounts of PLPE a) and PLSE b).

5.2.1.2 Effect of immersion time

The effect of immersion time is the most commonly used technique, which provides valuable insights regarding the durability of the inhibitory nature of inhibitors. Herein, numerous weight loss measurements were performed at optimal doses (200 mg L^{-1}) of PLPE and PLSE, along with extending the immersion time from 0 to 48 h, such as 4, 8, 12, 24, and 48 h. Fig. 5.4 represents the impact of extended immersion time on the inhibition efficiency of *Phaseolus lunatus* extract at the optimum concentration (200 mg L^{-1}). The presented data shows that the percentage inhibition efficiencies increase up to 24 h of exposure time. After that, the inhibition efficiencies of both *Phaseolus lunatus* extracts remained constant for the exposure time up to 48 h. These observations signify that the adsorption of PLPE and PLSE on metal was accomplished within 24 h and reached an equilibrium stage. After 24 h, the available molecules of inhibitor in 1 M HCl participate in repairing the adsorbed layer of inhibitor molecules deteriorated due to the attack of corrosive species.

The reasons for this phenomenon are linked to the inhibitor's film, which develops with time on the metal as it is immersed in the inhibited system. This film becomes increasingly

dense and consistent during extended immersion periods from 1 to 24 h. The adsorbed protective layer becomes saturated, and its thickness reaches a steady state value before the immersion period of 24 - 48 h (Kumar and Das, 2024).

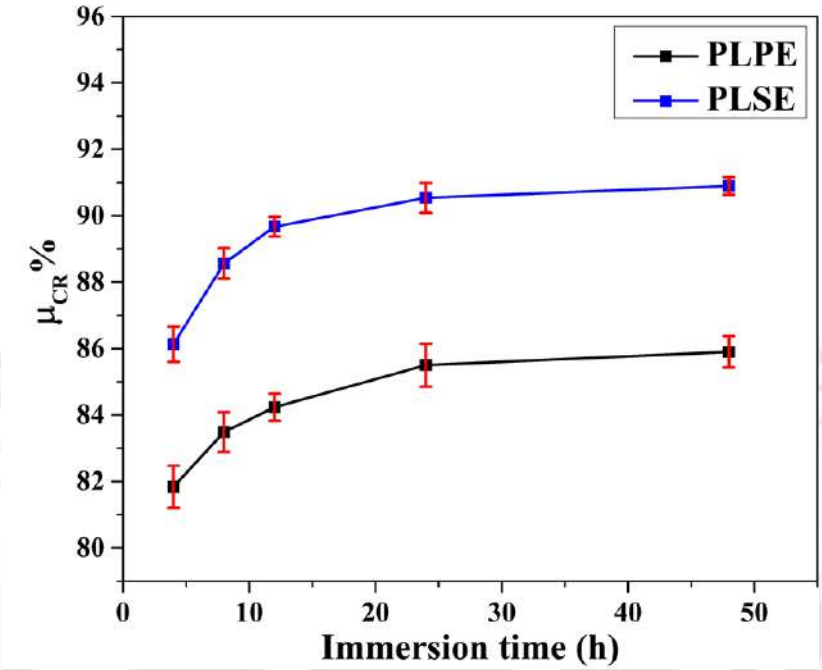

Fig. 5.4 The variation in the inhibitory efficiencies of PLPE and PLSE with the exposure time.

5.2.2 Electrochemical studies

Electrochemical analysis is another way to investigate the anticorrosive behavior of corrosion inhibitors. In this work, *Phaseolus lunatus* extracts were employed to mitigate the corrosion of MS immersed in 1 M HCl. Each experiment was repeated thrice for several doses (0-200 mg L^{-1}) of PLPE and PLSE at 30 ºC.

5.2.2.1 OCP measurements

The variation in OCP values of MS immersed in 1 M HCl with and without *Phaseolus lunatus* extracts was recorded prior to each electrochemical measurement, such as EIS and Potentiodynamic polarization measurements. The OCP curves (Figs. 5.5 (a) and (b)) depicted that the allowed time of 1 h was sufficient to reach a steady state value. However, OCP values were shifted positively in solutions containing *Phaseolus lunatus* extracts as compared to the blank system, which could be explained by the adsorption of *Phaseolus lunatus* extracts on MS (Li et al., 2019).

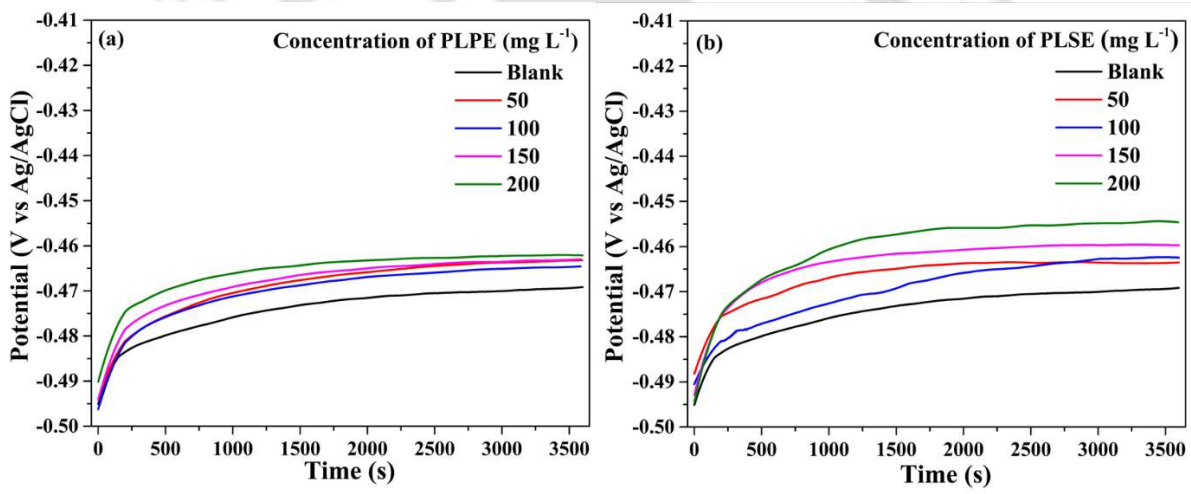

Fig. 5.5. OCP graphs for MS immersed in 1 M HCl in the presence and absence of PLPE a), and PLSE b).

5.2.2.2 Potentiodynamic polarization

The Tafel polarization technique has been employed to study the kinetics of reactions happening on the interface of MS and acid with and without Phaseolus lunatus extracts. Figs. 5.6 (a) and 5.6 (b) display the Tafel curves for MS exposure to 1 M HCl without and with PLPE and PLSE, respectively. Table 5.1 assembles the generated Tafel parameters, such as E_{corr} (corrosion potential), i_{corr} (corrosion current density), b_c (cathodic Tafel slope), and b_a (anodic

Tafel slope), by fitting the Tafel plots using Nova 1.1.0 software. Table 5.1 illustrates that E_{corr} shifted positively for *Phaseolus lunatus* extracts containing systems than that of blank, demonstrating their anodic type behavior of PLPE and PLSE. The anodic polarization of metal in the acidic medium in the presence of an inhibitor depends on the electrode potential. For inhibitor-containing systems, the anodic reactions are slightly affected when the E_{corr} exhibited a positive shift due to the presence of PLPE and PLSE (Al-Moubaraki and Awaji, 2020).

Few studies have reported that an inhibitor showed mixed-type inhibiting behavior only if E_{corr} shifts lie within ± 85 mV as compared to blank. Otherwise, the inhibitor exhibits cathodic or anodic behavior (Boutoumit et al., 2024). In this work, the variation in corrosion potential values lies within ± 85 mV, indicating that *Phaseolus lunatus* extracts (PLPE and PLSE) exhibited mix-type inhibiting behavior.

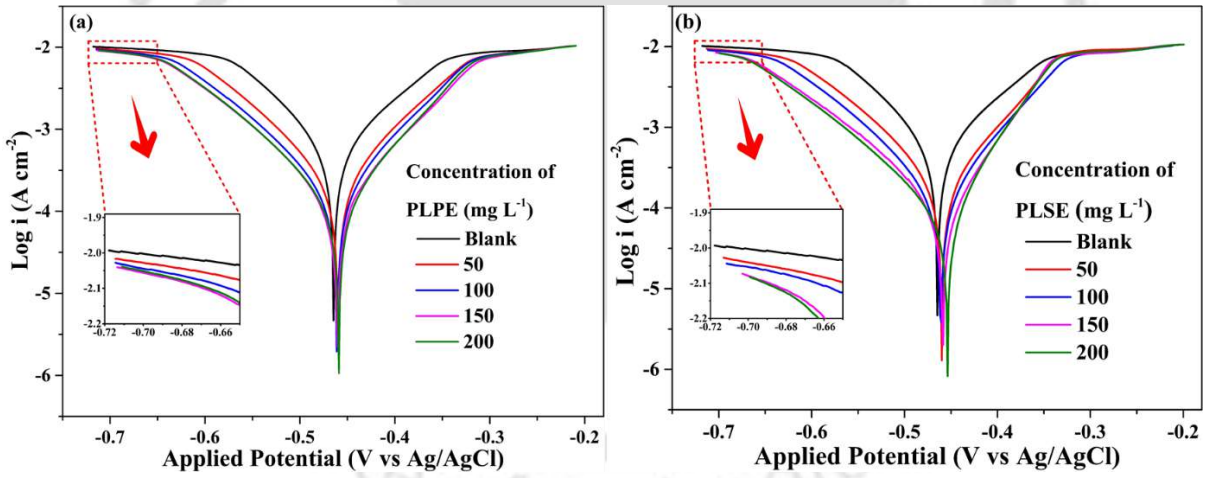

Fig. 5.6 Tafel curves for MS immersed in 1 M HCl with and without several concentrations of PLPE a) and PLSE b).

Additionally, it was noted that the E_{corr} values obtained from the Tafel curves closely align with their respective OCP values, which were recorded before each electrochemical test in the earlier section. The values of anodic and cathodic currents decreased with the

incorporation of *Phaseolus lunatus* extracts compared to blank (Table 5.1), which explains interruptions in metal corrosion and hydrogen gas formation. Fig. 5.6 illustrates that the addition of *Phaseolus lunatus* extracts (PLPE and PLSE) significantly reduces corrosion current densities (i_{corr}) values without affecting the corrosion potential (E_{corr}) values, indicating that both extracts function as pickling-type inhibitors (El Khatib et al., 2020). Two simultaneous phenomena (reduction in the values of corrosion current densities and improvement in polarization resistance) were seen with the addition of *Phaseolus lunatus* extracts (PLPE and PLSE) to MS immersed in 1 M HCl. Moreover, the corrosion rate values significantly decreased in the presence of inhibitors (PLPE and PLSE). These values were compared with those obtained from the weight loss analysis, as shown in Table 5A.1 of Appendix 5A. The comparison revealed that the results from the potentiodynamic polarization method are well supported by the weight loss analysis. These phenomena describe the formation of an inhibiting layer on the MS due to the adsorption of *Phaseolus lunatus* extract. PLPE and PLSE provide the highest inhibitory efficiencies, 85.69 and 90.78 %, respectively, at their optimum amounts (200 mg L^{-1}) (Ali Asaad et al., 2018).

Table 5.1 The obtained parameters from Tafel analysis for MS with and without several concentrations of PLPE and PLSE in 1 M HCl.

Inhibitor	Conc. (mg L^{-1})	b_a (mV dec^{-1})	$-b_c$ (mV dec^{-1})	*OCP* (mV vs. Ag/AgCl)	E_{corr} (mV vs. Ag/AgCl)	i_{corr} (µA cm^{-2})	R_p (Ω cm^2)	*CR* (mm $Year^{-1}$)	μ_P (%)
Blank	0	110.6 ± 0.5	120.2 ± 1.0	-468.1 ± 5.7	-465.2 ± 5.6	734.98 ± 5.23	34.04 ± 0.12	8.54 ± 0.45	_
PLPE	50	103.3 ± 0.5	83.3 ± 0.5	-463.2 ± 3.7	-460.4 ± 3.7	241.77 ± 1.35	82.84 ± 0.22	2.81 ± 0.15	67.11 ± 0.71
	100	108.7 ± 1.4	82.7 ± 1.3	-464.5 ± 3.0	-462.0 ± 3.1	177.98 ± 2.84	114.58 ± 0.15	2.07 ± 0.11	75.78 ± 0.44
	150	99.5 ± 0.5	83.5 ± 1.6	-463.0 ± 2.5	-460.2 ± 2.6	134.81 ± 1.74	146.30 ± 0.27	1.57 ± 0.07	81.66 ± 0.12
	200	83.0 ± 0.7	67.1 ± 0.6	-462.0 ± 3.3	-459.1 ± 2.0	105.19 ± 1.12	153.23 ± 0.42	1.22 ± 0.04	85.69 ± 0.87
Blank	0	110.6 ± 0.5	120.2 ± 1.0	-468.1 ± 5.7	-465.2 ± 5.6	734.98 ± 5.23	34.04 ± 0.12	8.54 ± 0.45	_
PLSE	50	94.3 ± 0.9	85.2 ± 1.3	-463.6 ± 2.1	-460.8 ± 2.3	215.03 ± 2.63	90.45 ± 0.19	2.50 ± 0.14	70.74 ± 0.82
	100	94.1 ± 0.3	79.3 ± 0.3	-462.3 ± 3.2	-459.9 ± 4.1	148.26 ± 0.68	126.05 ± 0.15	1.72 ± 0.06	79.83 ± 0.61
	150	85.3 ± 0.7	70.3 ± 0.6	-459.7 ± 3.4	-458.8 ± 3.2	93.10 ± 1.02	179.71 ± 0.42	1.08 ± 0.05	87.33 ± 0.91
	200	89.6 ± 0.9	49.4 ± 0.6	-454.8 ± 1.8	-453.7 ± 1.8	67.77 ± 0.85	204.08 ±0.21	0.79 ± 0.03	90.78 ± 0.44

5.2.2.3 EIS measurements

It is another method that can be utilized to inspect the kinetics of the electrochemical phenomenon happening during metal degradation in an acidic medium with and without *Phaseolus lunatus* extracts. Obtained Nyquist plots from EIS measurements at several concentrations (0, 50, 100, 150, and 200 mg L^{-1}) of PLPE and PLSE are depicted by Figs. 5.7 (a) and (b), respectively. All Nyquist curves exhibited identical depressed semicircles, which describes the heterogeneity of the metallic surface. From these figures, it can be seen that Nyquist plots showed a similar pattern for both uninhibited and inhibited systems, suggesting that the incorporation of inhibitors into the acidic solution did not alter the mechanism of the corrosion process (Pal and Das, 2022a). Additionally, in each semicircle, a prominent capacitive loop appears at higher frequencies, suggesting that charge is transferred across the double layer. For uninhibited systems, an insignificant inductive loop was detected at lower frequencies, and it completely vanished in the case of inhibited systems. The inductive loop is often linked to the relaxation of adsorbed intermediate species like H^{+}_{ads}, Cl^{-}_{ads}, and others, indicating the existence of unstable corrosion products on the surface of the MS (Haque et al., 2021). For inhibitor-containing systems, the disappearance of the inductive loop is typically interpreted as the "degradation" process in EIS studies (Kumar and Das, 2024). The Nyquist pattern of inhibited or uninhibited systems shows the nature of electrochemical reactions happening at the interface of metal and corrosive solution, which is mainly controlled by charge transfer resistance. In each Nyquist curve, the semicircle's diameter represents the value of R_{ct} (charge transfer resistance) (Bhan and Golder, 2024; Bhan and Kumar Golder, 2023). The value of this diameter was improved with the addition of *Phaseolus lunatus* extracts (PLPE and PLSE) and maximized at 200 mg L^{-1} (Figs. 5.7 (a) and 5.7 (b)).

Bode magnitude and bode phase patterns for MS degradation in acidic solution with and without PLPE and PLSE are displayed in Fig 5.8. From Bode curves, it was noticed that

each system (inhibited or blank) at several doses of extracts exhibited different values of phase angle, which lie between 0° and 90°, signifying the capacitive or resistive features of the metal electrolyte interface. All these obtained values of phase angles are less than 90°, signifying the non-pure capacitive behavior. From Figs. 5.8 (c) and (d), it was noticed that the peak height of the phase plot rises with the addition of PLPE and PLSE, which illustrates the strengthening of capacitive behavior on the metal-electrolyte interface (Pal and Das, 2023).

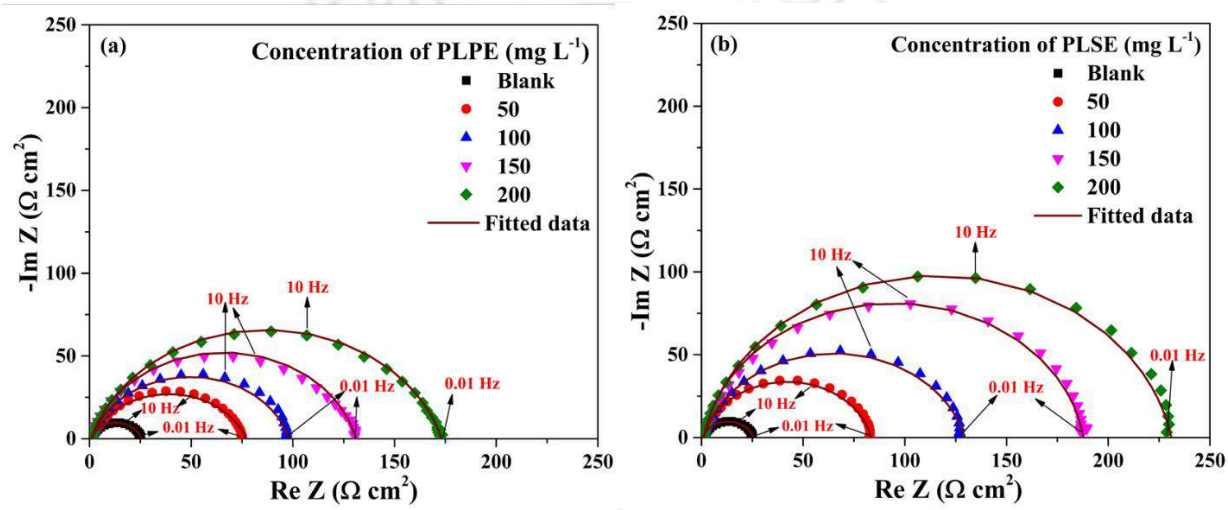

Fig. 5.7 Nyquist diagrams of MS exposed to 1 M HCl with and without the several concentrations of PLPE a) and PLSE b).

To explore the technical characteristics of the Nyquist plot, an equivalent circuit model (simple Randle circuit) was employed, as depicted in Fig. 5.9, where solution resistance, charge transfer resistance, and constant phase element are denoted by R_s, R_{ct}, and *CPE*, respectively (Bhan et al., 2025). All Nyquist parameters such as R_s, R_{ct}, Y_0, C_{dl}, n, goodness of fit (χ^2), and μ_{Rct} (%) were obtained by fitting the Nyquist plots with the proposed electrochemical circuit using Nova 1.1.0 software, and their values were tabulated Table 5.2. The obtained values of χ^2 lie in the range of 1.01×10^{-3} to 3.61×10^{-3}, depicting a good fitting of EIS data to a proposed circuit (Tang et al., 2021). From a careful examination of Table 5.2, it was noticed that R_{ct}

values were continuously improved with increasing the doses of extracts in 1 M HCl. Higher R_{ct} values for inhibited systems mean higher corrosion resistance to metal dissolution (slower corrosion rate) in the presence of inhibitors (Ma et al., 2016). It was due to the formation of a protective layer at the metal-electrolyte interface, which separates the metal from the corrosive electrolyte and significantly hinders the transfer of corrosive ions from the bulk electrolyte to the metal surface (Hidalgo et al., 2025; Pal and Das, 2022b). Furthermore, PLSE shows higher corrosion mitigation behavior than PLPE at 200 mg L^{-1}. Additionally, obtained R_p values from EIS and Tafel measurement were tabulated and compared in Table 5A.1 of the Appendix 5A, this comparison showed that these values were different by close to each other for both uninhibited and inhibited systems, which implies that outcomes of EIS are well align with the findings of PDP test. Moreover, inhibition efficiencies of EIS were compared with that of PDP and weight loss analysis. These values were higher for PDP tests and calculated p-values confirm that electrochemical data are highly statistically significant ($p< 0.0001$) (Table 5A.2 of Appendix 5A).

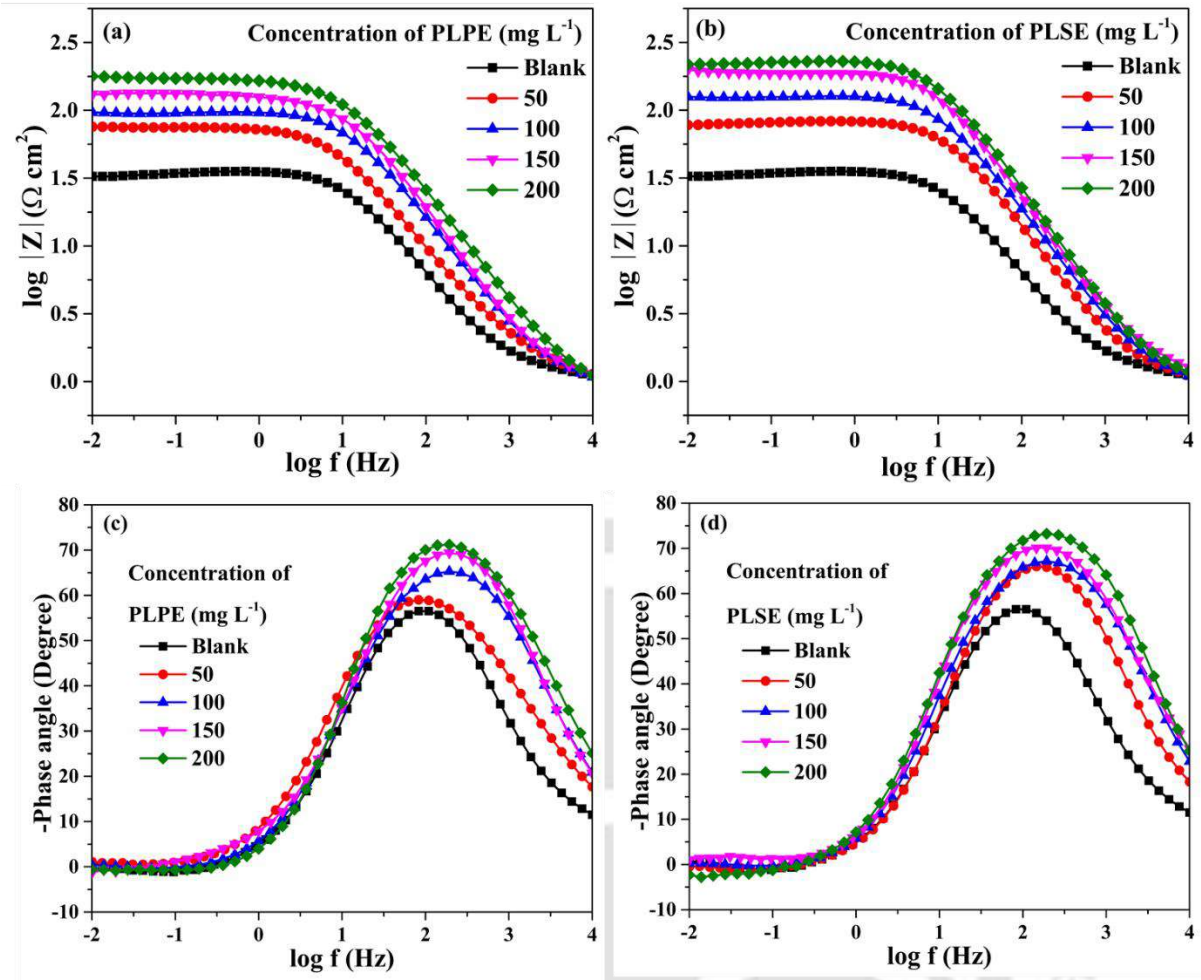

Fig. 5.8 Bode and phase patterns for MS corrosion in 1 M HCl with and without the several concentrations of PLPE (a,c) and PLSE (b,d).

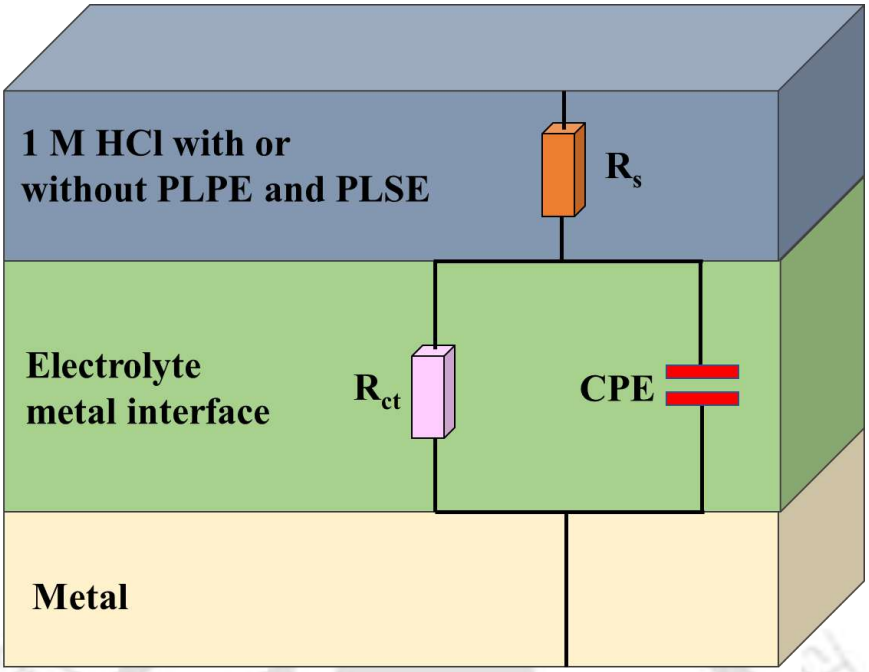

Fig. 5.9 Equivalent circuit model for MS corrosion in 1 M HCl with or without PLPE and PLSE.

Table 5.2 Nyquist parameters for MS corrosion in 1 M HCl without and with the several concentrations of PLPE and PLSE.

Inhibitor	Conc. (mg L^{-1})	R_s (Ω cm^2)	R_{ct} (Ω cm^2)	CPE parameters		C_{dl} (μF cm^{-2})	Goodness of fit	μ_{Rct} (%)
				n	Y_0 ($\mu\Omega^{-1}$ cm^{-2} s^n)		(χ^2) $\times 10^{-3}$	
Blank	0	0.84 ± 0.001	25.89 ± 0.14	0.81 ± 0.001	875.67 ± 6.29	348.06 ± 0.46	1.12	–
PLPE	50	1.05 ± 0.002	75.97± 0.45	0.79 ± 0.001	613.39 ± 3.14	261.88 ± 0.57	3.46	65.92 ± 0.23
	100	0.94 ± 0.001	97.11 ± 0.30	0.84 ± 0.001	271.28 ± 1.31	137.76 ± 0.26	2.98	73.34 ± 0.16
	150	0.99 ± 0.002	129.95 ± 0.52	0.86 ± 0.002	199.94 ± 0.98	112.43 ± 0.23	1.34	80.08 ± 0.21
	200	0.84 ± 0.001	172.31 ± 0.88	0.83 ± 0.001	178.11 ± 0.97	88.32 ± 0.20	1.01	84.97 ± 0.13
Blank	0	0.84 ± 0.001	25.89 ± 0.14	0.81 ± 0.001	875.67 ± 6.29	348.06 ± 0.46	1.12	–
PLSE	50	1.06 ± 0.002	83.87 ± 0.24	0.86 ± 0.002	264.73 ± 0.89	147.24 ± 0.21	2.26	69.13 ± 0.17
	100	0.94 ± 0.001	127.30 ± 0.38	0.85 ± 0.001	221.23 ± 1.00	116.84 ± 0.24	3.61	79.66 ± 0.37
	150	1.11 ± 0.002	190.52 ± 0.65	0.87 ± 0.001	152.86 ± 0.67	90.58 ± 0.19	1.76	86.41 ± 0.14
	200	0.99 ± 0.001	227.07 ± 1.18	0.89 ± 0.002	121.11 ± 0.70	75.78 ± 0.17	2.46	88.60 ± 0.16

5.3 Effect of temperature

The majority of scientific studies and literature reviews reported that the elevation of temperature results in the desorption of the organic compounds and degradation of metal or formation of complexes on the metallic surface, which accelerates the metal degradation (Daoudi et al., 2022). Therefore, to study the effect of temperature on MS dissolution in 1 M HCl in the absence and presence of *Phaseolus lunatus* extracts (PLPE and PLSE) at their optimum amount (200 mg L^{-1}), several OCP, PDP, and EIS measurements were performed at 313 and 323 K. Before every electrochemical measurement, 1 h OCP was recorded at the temperature of 313 and 323 K. The OCP plots corresponding to temperatures of 303, 313, and 323 K are shown in Figs. 5.10 (a), (b), and (c), respectively, and their values are tabulated in Table 5.3.

Figs. 5.11 (b), 5.11 (d), and 5.11 (f) display the Tafel graphs for MS dissolution in acid solution with and without *Phaseolus lunatus* extracts, and Tafel parameters are assembled in Table 5.3. This Table shows that i_{corr} values increased in both blank and inhibited systems with increasing temperature, which indicates that an increase in temperature often accelerates the corrosion process, leading to a higher rate of MS dissolution. However, at higher temperatures, obtained i_{corr} values in the presence of inhibitor were lower than those of blank, indicating that *Phaseolus lunatus* extracts exhibit inhibiting properties at all studied temperatures (Varvara et al., 2020). Figs. 5.11 (a), 5.11 (c), and 5.11 (e) demonstrate Nyquist plots of MS dissolution in the acidic medium with and without *Phaseolus lunatus* extracts. To evaluate the Nyquist parameters, these Nyquist plots were analyzed using Nova 1.1.0 software, as previously stated in section 5.2.2.3, and all obtained Nyquist parameters are tabulated in Table 5.4. In this Table, the values of n were between 0.71 and 0.89, which indicates the degree of deviation from the ideal capacitor. Few studies have reported that this value describes the characteristics of CPE. If n = 1, CPE behaves as an ideal capacitor; n < 1, CPE behaves as a nonideal capacitor, and n

= 0, CPE behaves as a pure resistor. The general increase in n value may be attributed to the increase in surface coverage and decrease in surface heterogeneity by the inhibitor molecules (Amegroud et al., 2024; Boudalia et al., 2023).

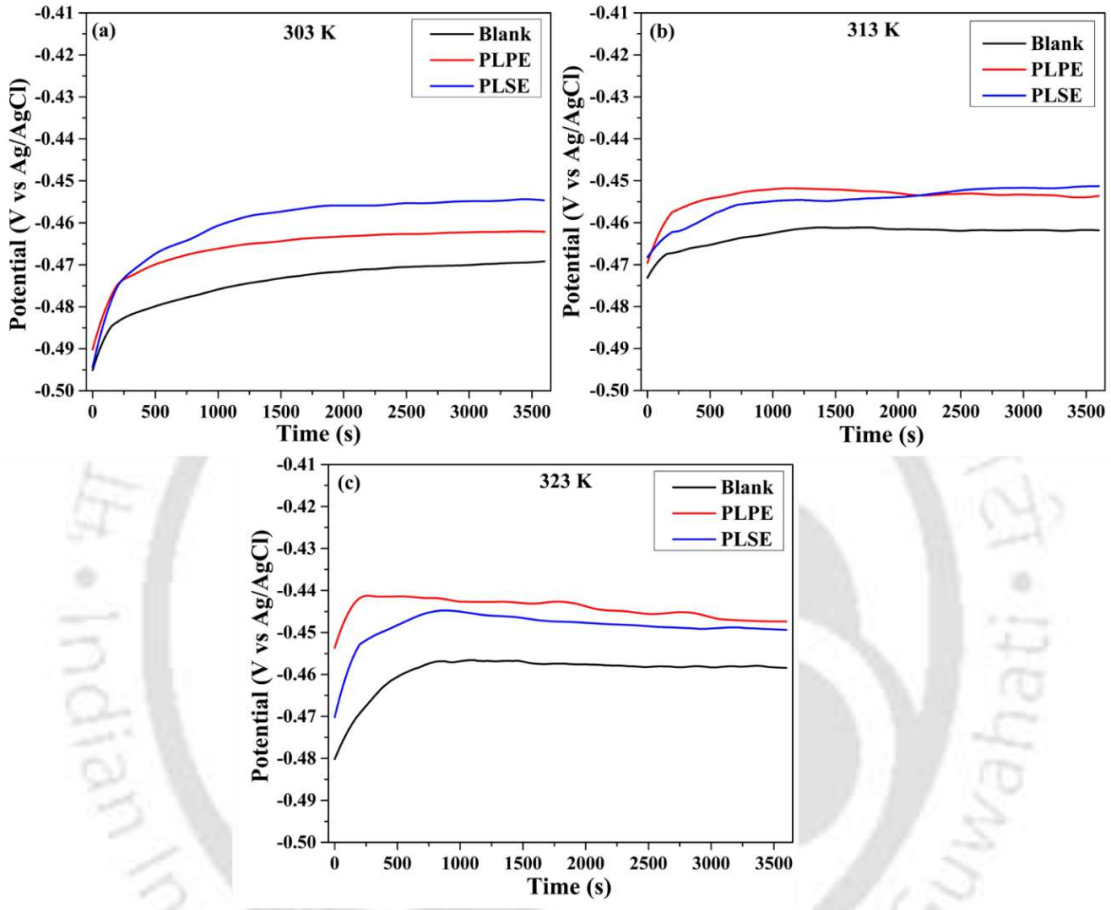

Fig. 5.10 OCP graphs for MS immersed in 1 M HCl at 303, 313, and 323 K, in the presence and absence of PLPE and PLSE.

On careful observation of Table 5.4, it was found that values of R_{ct} and μ_P (%) reduced with temperature elevation, which means temperature elevation leads to the degradation of the metal. Furthermore, Table 5.3 displayed that PLPE and PLSE containing systems showed inhibitory efficiency of 71.92 and 78.43 %, respectively, at 323 K. In this work, the inhibition efficiencies in both PDP and EIS methods were decreased with increasing temperature,

suggesting that the protective layer weakened due to partial desorption of some inhibitor molecules from the MS surface, resulting in poor protection of MS at higher temperatures (Varvara et al., 2020).

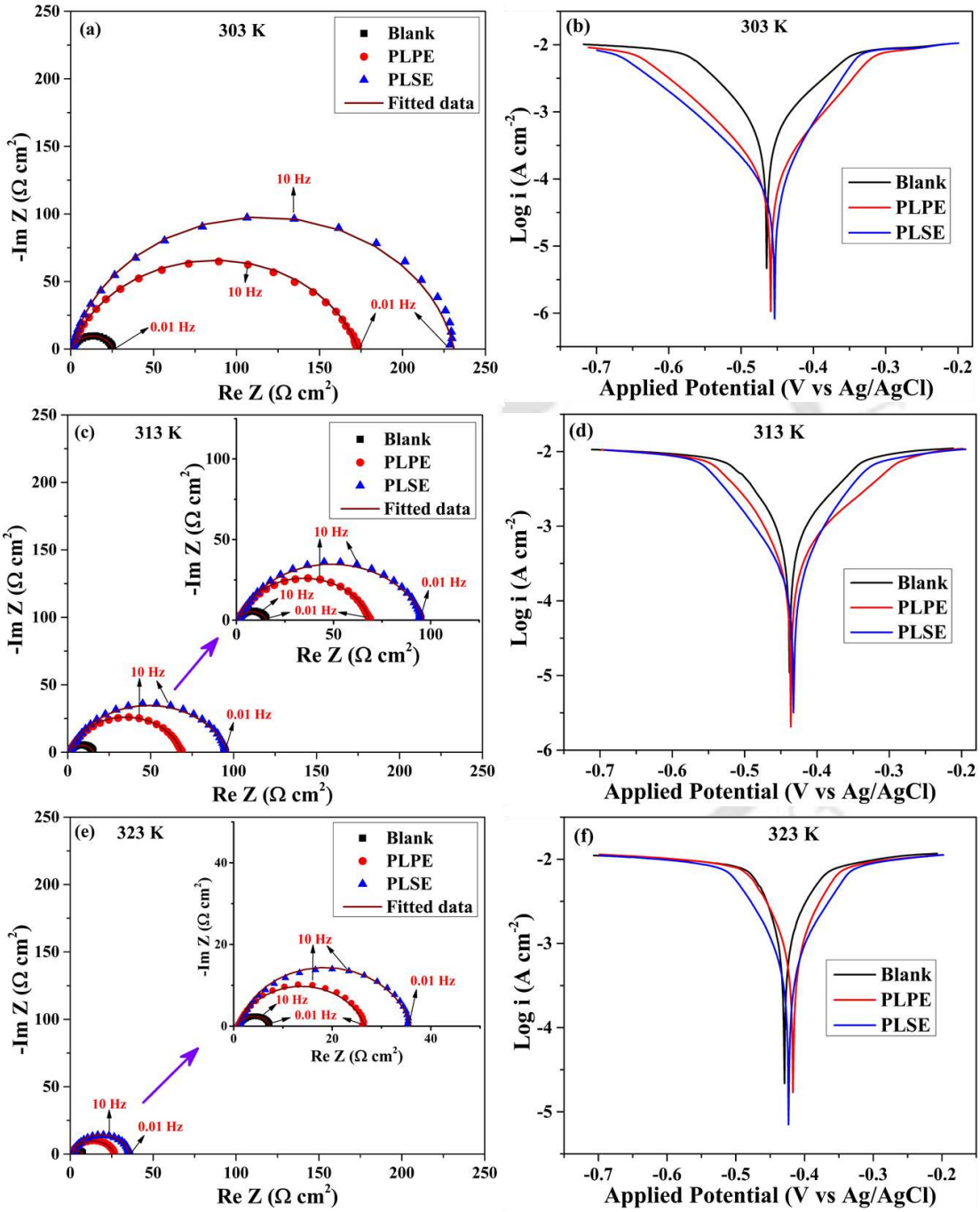

Fig. 5.11 Nyquist plots (a, c, e) and Tafel plots (b, d, f) for blank, PLPE, and PLSE at 303, 313, and 323 K.

Table 5.3 Tafel parameters for MS degradation in 1 M HCl without and with the several concentrations of PLPE and PLSE at 303, 313, and 323 K.

Temperature (K)	Inhibitor	Conc. (mg L^{-1})	b_a (mV dec^{-1})	$-b_c$ (mV dec^{-1})	*OCP* (mV vs. Ag/AgCl)	E_{corr} (mV vs. Ag/AgCl)	i_{corr} (µA cm^{-2})	R_p (Ω cm^2)	*CR* (mm $Year^{-1}$)	μ_P (%)
303	Blank	0	110.6 ± 0.5	120.2 ± 1.0	-468.1 ± 5.7	-465.2 ± 5.6	734.98 ± 5.23	34.04 ± 0.12	8.54 ± 0.45	_
	PLPE	200	83.0 ± 0.7	67.1 ± 0.6	-462.0 ± 3.3	-459.1 ± 2.0	105.19 ± 1.12	153.23 ± 0.42	1.22 ± 0.04	85.69 ± 0.87
	PLSE	200	89.6 ± 0.9	49.4 ± 0.6	-454.8 ± 1.8	-453.7 ± 1.8	67.77 ± 0.85	204.08 ±0.21	0.79 ± 0.03	90.78 ± 0.44
313	Blank	0	105.1 ± 1.1	165.8 ± 2.3	-461.8 ± 6.9	-437.8 ± 6.5	1302.48 ± 11.03	21.44 ± 0.04	15.13 ± 0.94	_
	PLPE	200	67.1 ± 1.0	84.6 ± 1.7	-453.1 ± 4.1	-436.2 ± 3.9	311.41 ± 3.10	52.22 ± 0.24	3.62 ± 0.15	76.09 ± 0.53
	PLSE	200	74.3 ± 1.2	56.6 ± 0.9	-451.2 ± 4.8	-432.7 ± 4.6	196.64 ± 1.48	70.93 ± 0.20	2.28 ± 0.08	84.90 ± 0.76
323	Blank	0	146.5 ± 1.4	285.8 ± 1.5	-458.2 ± 5.4	-429.4 ± 6.3	4429.22 ± 36.40	9.50 ± 0.01	51.45 ± 2.96	_
	PLPE	200	86.7 ± 1.6	85.4 ± 2.3	-447.7 ± 4.0	-416.9 ± 3.6	1255.67 ± 12.15	14.87 ± 0.04	14.59 ± 0.92	71.92 ± 0.46
	PLSE	200	104.8 ± 2.3	116.9 ± 1.7	-449.5 ± 3.4	-423.3 ± 2.3	964.34 ± 11.20	24.83 ± 0.46	11.21 ± 0.73	78.43 ± 0.30

Table 5.4 EIS parameters for the exposure of MS to 1 M HCl without and with several concentrations of PLPE and PLSE at temperatures of 303, 313, and 323 K.

Temperature (K)	Inhibitor	Conc. (mg L^{-1})	R_s (Ω cm^2)	R_{ct} (Ω cm^2)	*CPE* parameters		C_{dl} (μF cm^{-2})	Goodness of fit (χ^2) $\times 10^{-3}$	μ_{Rct} (%)
					n	Y_0 ($\mu\Omega^{-1}$ cm^{-2} s^n)			
303	Blank	0	0.84 ± 0.001	25.89 ± 0.14	0.81 ± 0.001	875.67 ± 6.29	348.06 ± 0.46	1.12	–
	PLPE	200	0.84 ± 0.001	172.31 ± 0.88	0.83 ± 0.001	178.11 ± 0.97	88.32 ± 0.20	1.01	84.97 ± 0.13
	PLSE	200	0.99 ± 0.001	227.07 ± 1.18	0.89 ± 0.002	121.11 ± 0.70	75.78 ± 0.17	2.46	88.60 ± 0.16
313	Blank	0	0.85 ± 0.002	16.51 ± 0.07	0.77 ± 0.001	1492.67 ± 16.43	446.72 ± 1.74	1.68	–
	PLPE	200	1.03 ± 0.002	69.29 ± 0.43	0.78 ± 0.001	645.37 ± 4.76	264.71 ± 0.57	2.79	76.37 ± 0.11
	PLSE	200	1.05 ± 0.002	95.75 ± 0.39	0.80 ± 0.001	404.69 ± 2.99	163.34 ± 0.35	1.35	82.90 ± 0.49
323	Blank	0	0.88 ± 0.003	7.67 ± 0.04	0.71 ± 0.002	3744.06 ± 28.06	865.87 ± 2.57	2.23	–
	PLPE	200	0.84 ± 0.001	26.64 ± 0.06	0.80 ± 0.001	910.39 ± 5.23	401.58 ± 0.76	3.21	71.32 ± 0.22
	PLSE	200	1.10 ± 0.002	35.78 ± 0.20	0.82 ± 0.001	773.69 ± 7.65	364.11 ± 1.01	2.06	78.65 ± 0.15

5.3.1 Effect of activation energy

The obtained values of corrosion current densities (i_{corr}) for different temperatures (303, 313, and 323 K) can be further utilized to obtain the kinetic (activation energy) and thermodynamic (entropy and enthalpy) thermodynamic parameters like activation energy, enthalpy, and entropy of metal dissolution in the acidic medium with and without of PLPE and PLSE. Furthermore, the values of ln (i_{corr}) (µA cm^{-2}) were plotted with 1/T (K^{-1}) to evaluate E_a for metal dissolution with and without PLPE and PLSE (Fig. 5.12 (a)). This plot displays a straight line, which has the following: slope (-E_a/R) and intercept (ln A). Table 5.5 assembles the generated values of E_a for uninhibited or inhibited systems.

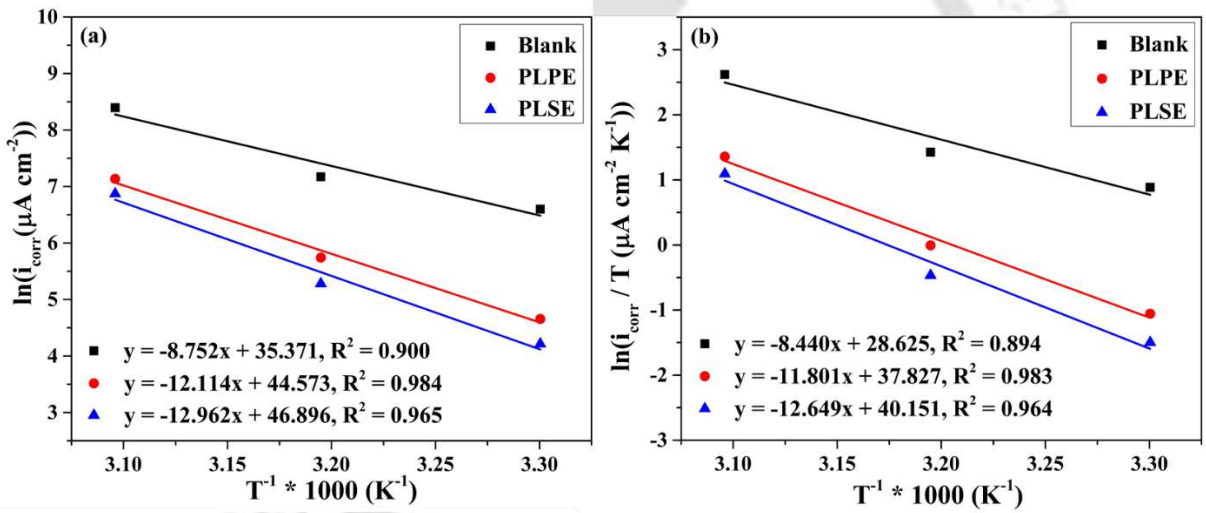

Fig. 5.12 Arrhenius plots (a) and Transition state plots (b) for MS corrosion with and without optimum concentrations of PLPE and PLSE.

Additionally, the values of ln (i_{corr}/T) (µA cm^{-2} K^{-1}) were plotted with 1/T (K^{-1}) (Fig. 5.12 (b)) to evaluate the enthalpy and entropy of MS dissolution for both uninhibited or inhibited systems. Fig. 5.12 (b) demonstrates a straight line that has the following: slope (-ΔH /R) and intercept ($\ln\frac{k_B}{h} + \frac{\Delta S}{R}$). Obtained entropy and enthalpy are tabulated in Table 5.5. On

careful observation of Table 5.5, it was found that inhibited systems exhibited higher E_a than blank, which means metal corrosion is more difficult in the presence of PLPE and PLSE (Dhongde et al., 2025). Few studies reported that inhibitors follow the physical adsorption to adsorb on metal if two events occur: a decrease in inhibition efficiency on temperature elevation along with the rise in activation energy of inhibitor-containing systems than that of blank. On the other hand, it will follow the chemisorption if the values of inhibition efficiency increase with temperature rise, coupled with a decrease in activation energy in the presence of inhibitors compared to blank (Kumar and Das, 2024). In this work, inhibition efficiencies of both extracts declined on temperature elevation, with improved activation energies for PLPE and PLSE compared to blank, illustrating the physical adsorption of *Phaseolus lunatus* extracts on the MS surface. The evaluated positive enthalpy values for inhibited and uninhibited systems depict that MS dissolution is an endothermic process, and these values were shifted to more positive on the addition of inhibitor as compared to blank, which means the addition of inhibitor leads to a strong protective layer. The calculated values of E_a - ΔH were almost equal to the product of R and T in each system, confirming that MS dissolution follows the unimolecular-type process (Eddahhaoui et al., 2024).

In the literature, a few studies have reported that values of entropy of activation shifted positively with the addition of inhibitor, indicating that there is an increment in the randomness or disorder at the metal/solution interface with some structural changes in the inhibitor species and the metal surface during the adsorption process (Al-Moubaraki et al., 2022; Lavanya and Machado, 2024; Matad et al., 2014). Since the molecular weight and size of the inhibitor are much larger than water molecules, the adsorbed water molecules, displaced by the inhibitor species, gain more translational entropy than is lost by the inhibitor ions/molecules, thus allowing for the prevalence of randomness in the system (Al-Moubaraki and Awaji, 2020). If the system's entropy decreased on the addition of inhibitors compared to blank, activation of

inhibitor molecules recommends their association rather than dissociation in the rate-determining step. Herein, the existence of *Phaseolus lunatus* extracts leads to an increased activation entropy value compared to blank. This signifies an elevated degree of disorder in the diffusion of reactants towards the activated complex (Boutoumit et al., 2024).

Table 5.5 Kinetic parameters for MS degradation in 1 M HCl without and with optimum concentration of PLPE and PLSE.

Inhibitor	Conc. (mg L^{-1})	Pre-exponential factor, A (μA cm^{-2})	E_a (kJ mol^{-1})	ΔH (kJ mol^{-1})	ΔS (J mol^{-1} K^{-1})	$(E_a - \Delta H)$ (kJ mol^{-1})
Blank	0	$(2.30 \pm 0.21) \times 10^{15}$	72.76 ± 0.25	70.17 ± 0.27	40.45 ± 0.78	2.59
PLPE	200	$(2.28 \pm 0.12) \times 10^{19}$	100.72 ± 0.94	98.11 ± 0.85	116.95 ± 1.00	2.60
PLSE	200	$(2.33 \pm 0.14) \times 10^{20}$	107.77 ± 1.01	105.16 ± 0.87	136.27 ± 0.85	2.60

5.4 Adsorption studies

Mostly, the inhibitive effect of inhibitors is dependent upon their adsorption ability. To understand the adsorption mechanism of studied *Phaseolus lunatus* extracts (PLPE and PLSE) on the interface of MS and HCl, several adsorption isotherms (Langmuir, Temkin, and Frumkin) were used by fitting the surface coverage values as a function of the amount of *Phaseolus lunatus* extracts from 50 to 200 mg L^{-1}. Fig. 5.13 illustrates the adsorption isotherm plots for both extracts. From these plots, it was found that Langmuir isotherm was the most suitable mode to fit the results of PDP measurements, with all linear regression coefficients (R^2) approximately 1 for both extracts, as adsorption follows the Langmuir model, which suggests equal surface energy to all the active sites and assumes the formation of a monolayer of the adsorbed molecules on a homogeneous surface without the interaction of individual molecules of inhibitors (Thomas et al., 2020).

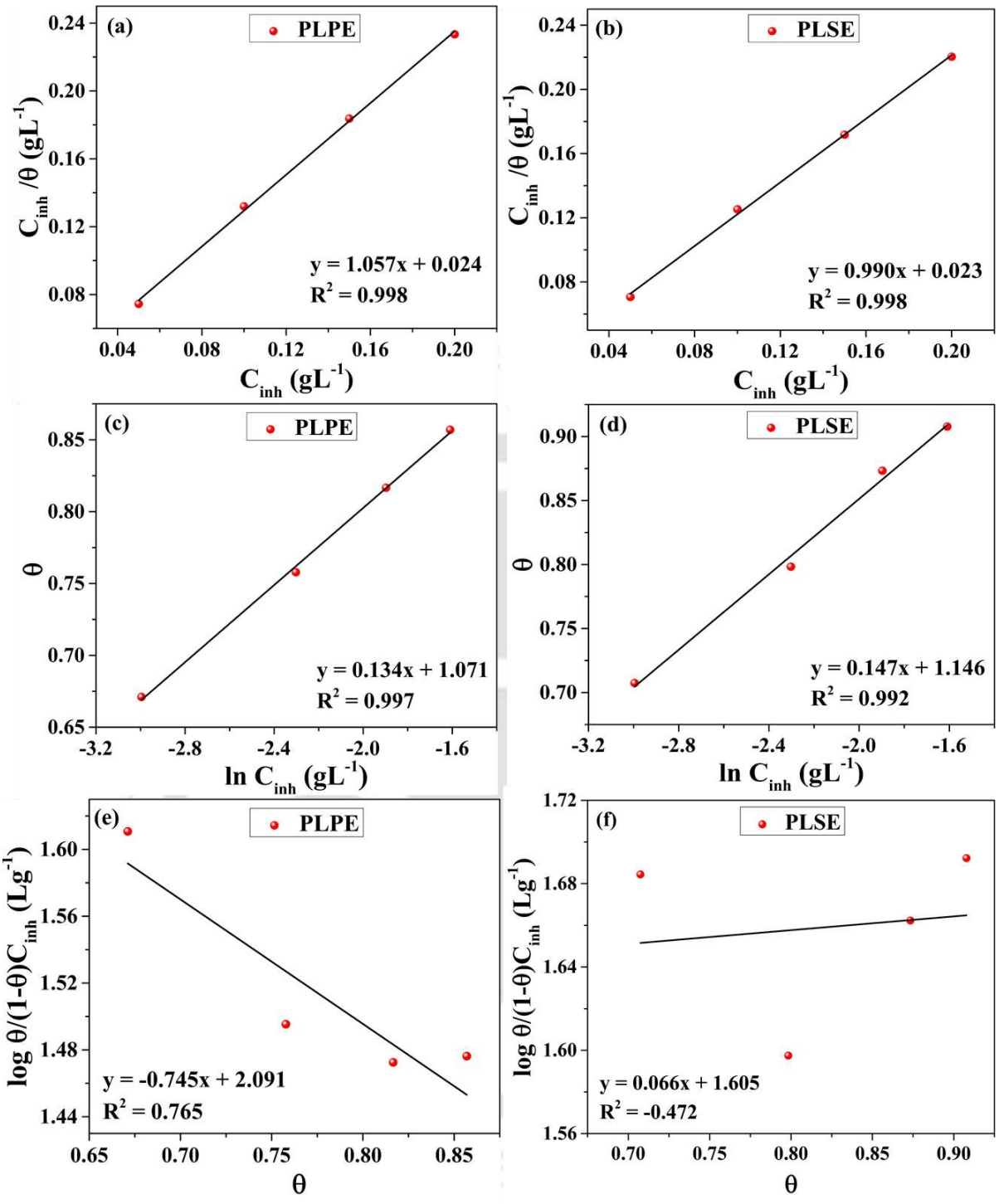

Fig. 5.13 (a, b) Langmuir, (c,d) Temkin, and (e,f) Frumkin isotherms of PLPE and PLSE, respectively.

Furthermore, Langmuir plots were utilized to calculate the equilibrium adsorption constant (Kads) values, which were obtained as 41.67 and 43.48 L g^{-1} for PLPE and PLSE,

respectively. Standard Gibbs free energy (ΔG^o_{ads}) for PLPE and PLSE were evaluated using Eq. (5.1):

$$\Delta G^o_{ads} = -RTln(C_{water}\, K_{ads}) \quad (5.1)$$

Where, K_{ads} is the equilibrium adsorption constant (L g^{-1}), C_{water} is water concentration in solution (1000 g L^{-1}), R and T are gas constant (8.314 J K^{-1} mol^{-1}) and temperature (K), respectively. Several studies have reported that the value of ΔG^o_{ads} describes the nature of the adsorption process. If $\Delta G^o_{ads} \geq$ -20 kJmol^{-1}, then the interaction between inhibitors and the surface is considered electrostatic, and the adsorption process is known as physisorption (Kumar et al., 2025). If $\Delta G^o_{ads} \leq$ -40 kJmol^{-1}, then the electrons are shared or transferred between inhibitor molecules and the metal surface to form a coordinate bond, which is also known as chemisorption. Moreover, if -40 kJmol^{-1} $\leq \Delta G^o_{ads} \leq$ -20 kJmol^{-1}, then adsorption occurred by mixed-type adsorption following both physisorption and chemisorption (Yin et al., 2025). In this work, evaluated values of ΔG^o_{ads} are -26.80 kJ mol^{-1} (PLPE) and -26.90 kJ mol^{-1} (PLSE) for inhibited systems (Table 5.6), which lie in the range of -40 to -20 kJ mol^{-1}, but closer to -20 kJ mol^{-1} signifying that PLPE and PLSE favored physical adsorption (mix-type adsorption). Additionally, the negative values of ΔG^o_{ads} indicate that both extract's (PLPE and PLSE) molecules have the ability to self-adsorb on metal from 1 M HCl solution (Kumar and Das, 2024).

Table 5.6 Adsorption isotherm parameters.

Inhibitor	$\frac{1}{K_{ads}}$ (g L^{-1})	K_{ads} (L g^{-1})	ΔG^o_{ads} (kJ mol^{-1})
PLPE	0.024 ± 0.001	41.67 ± 1.230	-26.80 ± 0.059
PLSE	0.023 ± 0.002	43.48 ± 1.964	-26.90 ± 0.024

5.5 Surface characterization

5.5.1 FESEM

In order to explore the inhibitory effect of *Phaseolus lunatus* extracts in terms of variations in the surface morphology of MS, metal-corroded specimens were analyzed using FESEM analysis. The FESEM images of the MS surface were captured earlier and after their 2 h immersion in acid in the absence and presence of 200 mg L^{-1} amount of *Phaseolus lunatus* extracts (Fig. 5.14). Figs. 5.14 (a) and 5.14 (b) illustrate FESEM images of polished MS before and after their acid immersion, respectively. On careful observation, deep ravines and several pits were found on MS for the uninhibited system, which was significantly different from the FESEM picture of the polished MS surface. MS was extremely damaged due to free acid attack in the absence of *Phaseolus lunatus* extract (Eddahhaoui et al., 2024). Furthermore, smoother surfaces were found for inhibited systems with PLPE (Fig. 5.14 (c)) and PLSE (Fig. 5.14 (d)) as compared to uninhibited systems. Findings from these pictures illustrate that the incorporation of PLPE and PLSE gives noticeable variations in the metal microstructures during acidic immersion. In blank systems, the acid aggressively attacked the metal, promoting both cathodic and anodic reactions. This degradation was confirmed by the formation of multiple cracks and pits on mild steel (MS) in 1 M HCl in the absence of *Phaseolus lunatus* extracts. However, with the addition of *Phaseolus lunatus* extracts to MS exposed to acid, harshly degraded structures were not found in this case as obtained in uninhibited systems (Dhongde et al., 2025). These outcomes depict that PLPE and PLSE adsorbed MS surfaces to create a protective layer that isolates the metallic surface from the corrosive solution. It acts as a barrier to hinder the transfer of corrosive ions from electrolytes to MS (Hidalgo et al., 2025).

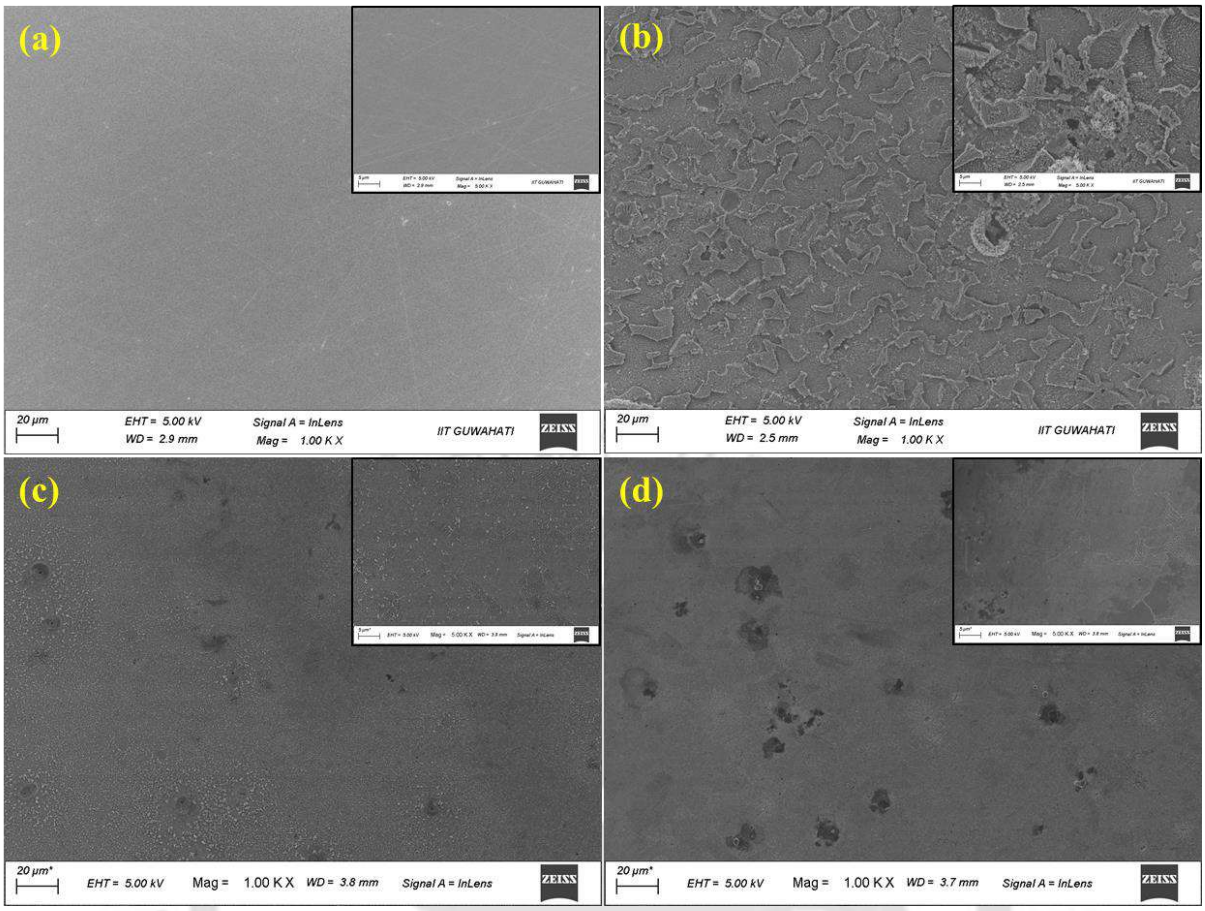

Fig. 5.14 FESEM pictures for a) polished MS, b) uninhibited MS after immersion, c) and d) inhibited MS with PLPE and PLSE, respectively, after 2 h immersion in 1 M HCl.

5.5.2 EDX

EDX analysis was utilized to study the effect of *Phaseolus lunatus* extracts on the elemental composition (wt%) of the MS surface after their 4 h exposure to 1 M HCl as compared to blank. Figs 5.15 (a) and 5.15 (b) illustrated the EDX spectra of MS degraded in the acidic medium without *Phaseolus lunatus* extracts and that of selected pit from blank systems, respectively. Detection of Cl in these spectra verifies the adsorption of Cl^- on metal, which was influenced by its electrostatic attraction with Fe^{2+} on metallic surface in acid (Kumar and Das, 2024). Furthermore, these spectra show that the weight percentage of Cl and Fe

increased and decreased in the pit compared to the plane surface, which displays that rapid and severe corrosion occurred inside the pit compared to the flat surface.

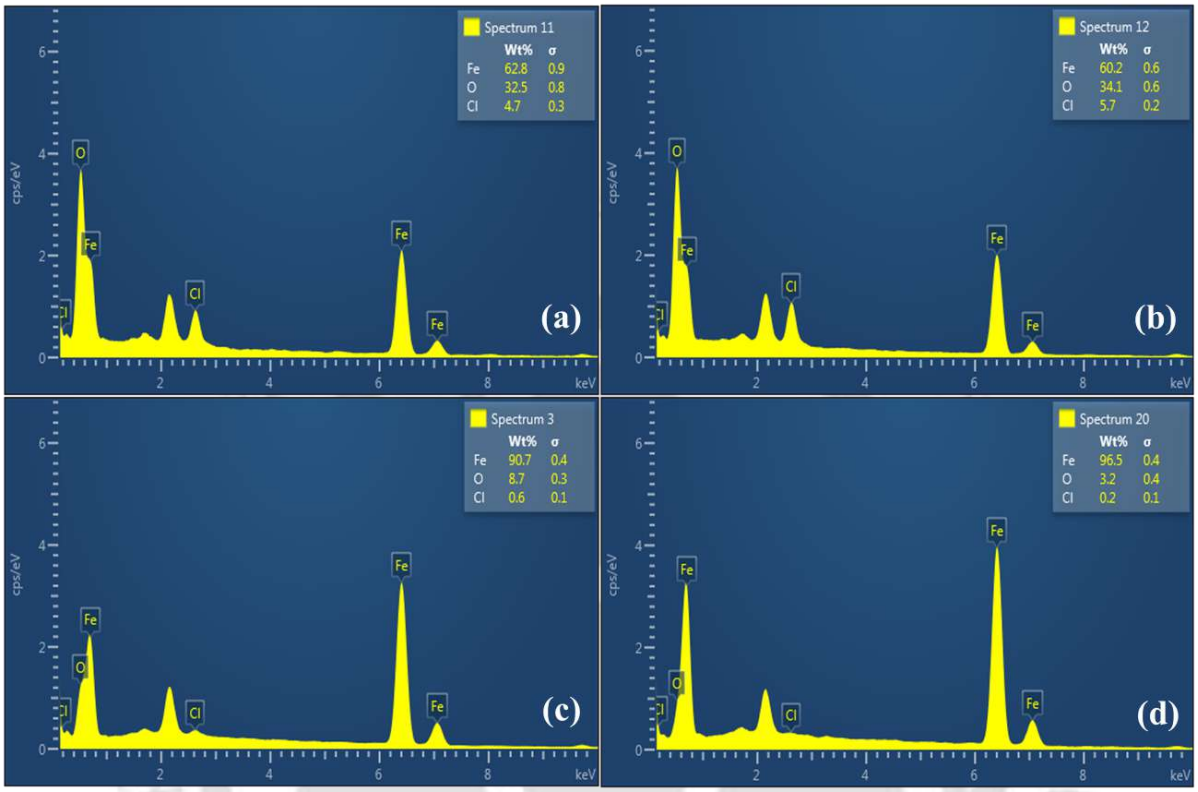

Fig. 5.15 EDX spectra for a) uninhibited MS, b) selected pits from the uninhibited spectrum, c) and d) MS inhibited with PLPE and PLSE, respectively, after 4 h immersion in acid.

Figs. 5.15 (c) and (d) represent EDX spectra of inhibited systems for PLPE and PLSE, respectively. From these spectra, it was observed that the amount of Cl and Fe decreased and increased in the presence of both PLPE and PLSE as compared to the blank system, and the highest improvement was noticed for PLSE. These figures show an unknown peak at around 2.2 keV, corresponding to Au, which is used to make coating during sample analysis (Bhan and Golder, 2024). These observations indicate that *Phaseolus lunatus* extract adsorbed on MS and forms a defensive layer, which significantly mitigates metal corrosion.

5.5.3 AFM

Surface roughness of the MS surface was investigated using the AFM technique after their 3 h exposure to 1 M HCl without and with *Phaseolus lunatus* extracts. 3-D AFM images are shown in Fig. 5.16. The values of average roughness of the investigated area (5.0 µm × 5.0 µm) were evaluated using the Gwyddion software. Fig. 5.16 (a) shows the AFM image of MS after 3 h immersion in the acidic medium without *Phaseolus lunatus* extract, which exhibited an average surface roughness of about 375.40 nm. This higher roughness is obtained due to the presence of several hills and valleys on the metal surface, which were formed during the free acid attack, indicating that the surface is severely damaged by the dissolution of the MS (Amegroud et al., 2024; Boudalia et al., 2023). Figs 5.16 (b) and 5.16 (c) illustrate the AFM images of inhibited MS with PLPE and PLSE, respectively, which have an average surface roughness of about 17.48 nm and 15.83 nm. From these observations, it was found that the MS surface was smooth in the presence of inhibitors as compared to the blank system, and a smoother surface was seen for the addition of PLSE, which signifies that the adsorption of *Phaseolus lunatus* extracts on MS in the acidic medium significantly mitigates its dissolution by generating a protective layer between metal and electrolyte.

5.5.4 XRD

XRD plot of polished MS before the corrosion test is demonstrated by Fig. 5.17 (a), which contains a large peak at 2θ value of 44.59°, along with several small peaks at different 2θ values of about 64.8°, 82.2°, and 98.84°. Additionally, the XRD plot of MS after 2 h immersion in 1 M HCl without *Phaseolus lunatus* extract is represented by Fig. 5.17 (b); this spectrum contained peaks at different 2θ values of about 35.2°, 44.59°, 64.8°, 82.2°, and 98.84° related to the Fe and $FeCl_2$ peaks in JCPDS: 06-0696. Among these peaks, $FeCl_2$ peaks were found at 35.2°, and others corresponded to Fe.

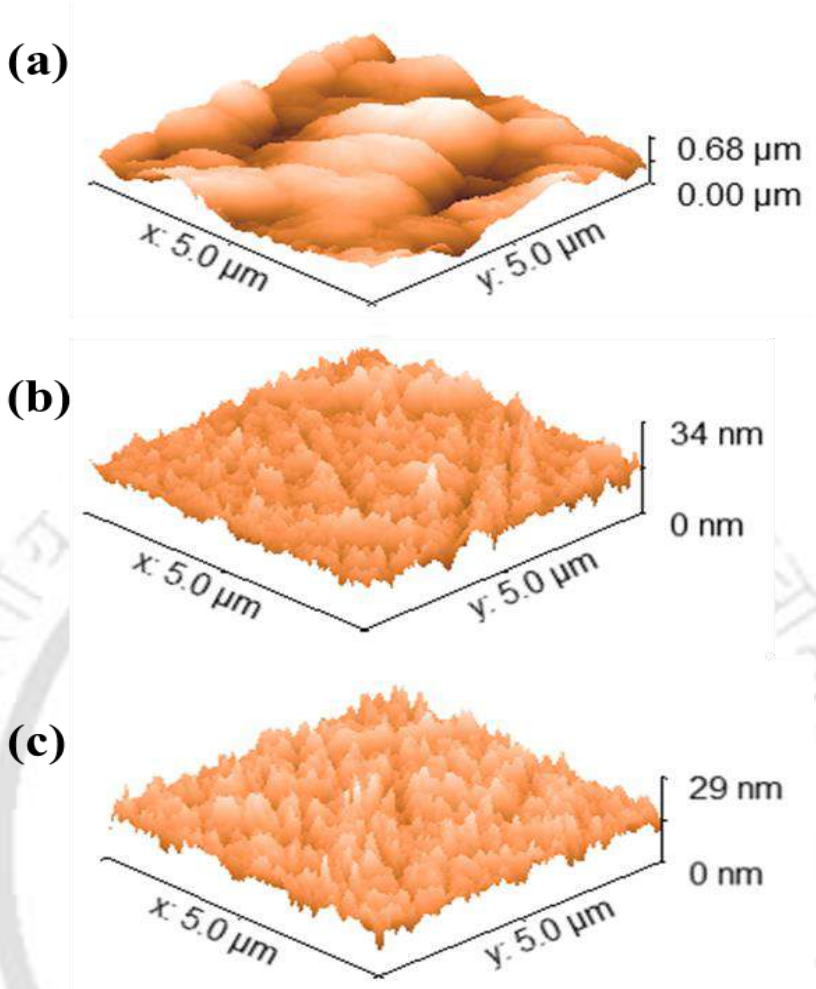

Fig. 5.16 AFM images of a) uninhibited MS, b) and c) MS with PLPE and PLSE, respectively, after 3 h immersion in 1 M HCl.

XRD pattern for MS degradation in the acidic medium with PLSE is depicted by Fig. 5.17 (c) exhibits several peaks at 44.59°, 64.8°, 82.2°, and 98.84° with reduced intensity, which correspond to Fe. Moreover, it was observed that the iron chloride peak had vanished, signifying the formation of a protecting layer on the metallic surface due to the adsorption of PLSE. This technique depicts potential interactions between the metal and *Phaseolus lunatus* extract molecules. Furthermore, these results are well aligned with the discoveries of FESEM, EDX, and AFM techniques.

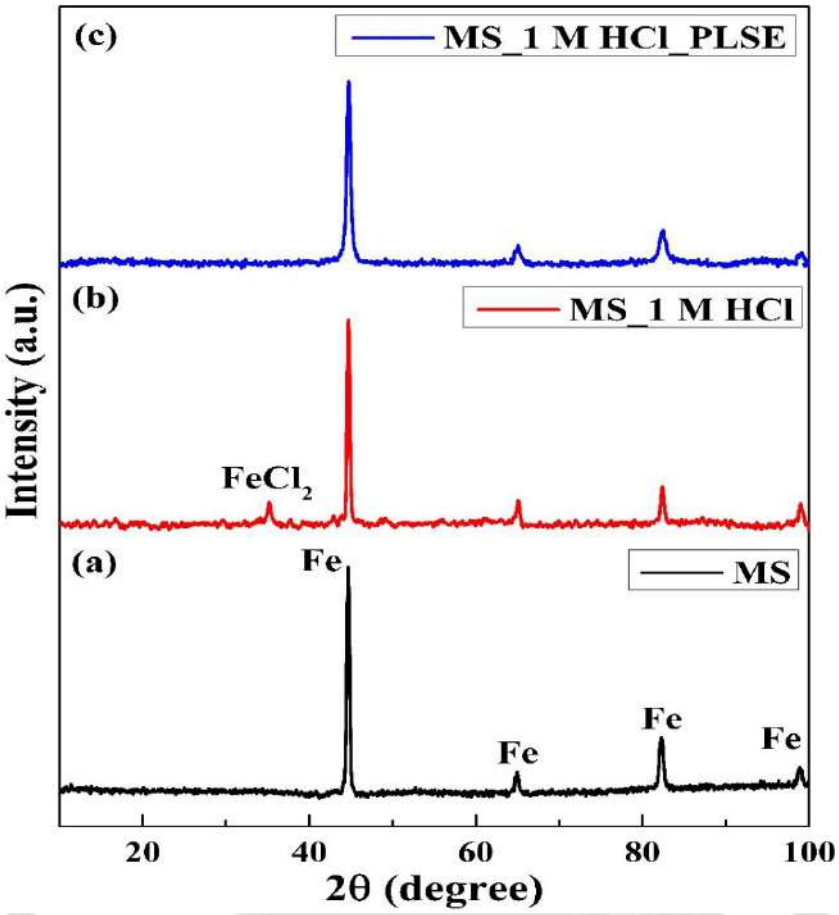

Fig. 5.17 XRD graphs for a) polished MS, (b) uninhibited MS, and (c) MS with PLSE after 2 h immersion in 1 M HCl.

5.6 Corrosion mitigation mechanism

The mechanism for MS dissolution in 1 M HCl is proposed as follows:

The mechanism for the anodic deterioration of MS is given by the following reactions (Eqs. 5.2 – 5.5):

$$Fe + Cl^- \leftrightarrow (FeCl^-)_{ads} \quad (5.2)$$

$$(FeCl^-)_{ads} \leftrightarrow (FeCl)_{ads} + e^- \quad (5.3)$$

$$(FeCl)_{ads} \rightarrow (FeCl^+)_{ads} + e^- \quad (5.4)$$

$$(FeCl^+)_{ads} \leftrightarrow Fe^{2+} + Cl^- \quad (5.5)$$

The mechanism for cathodic hydrogen evolution is given by the following reactions (Eqs. 5.6 – 5.8):

$$Fe + H^+ \leftrightarrow (FeH^+)_{ads} \quad (5.6)$$

$$(FeH^+)_{ads} + e^- \rightarrow (FeH)_{ads} \quad (5.7)$$

$$(FeH^+)_{ads} + H^+ + 2e^- \rightarrow Fe + H_2 \quad (5.8)$$

The corrosion mitigating effect of *Phaseolus lunatus* extracts in 1 M HCl depends on interactions between metal and extracts (Alao et al., 2023). Electrostatic interactions happen between the molecules of the extract and Cl^- ions that are already adsorbed on the metal surface. This interaction results in the adsorption of protonated inhibitor molecules through the physical adsorption process. On the metallic surface, competition builds between protonated inhibitor molecules and H^+ for electrons. Positively charged inhibitor molecules revert to their neutral state by taking required electrons from the metal surface. The unbound lone pairs of inhibitor molecules facilitate its chemical adsorption on the MS surface. Metal becomes more negative due to the accumulation of electrons on it. To remove this excess of negative charge, electrons jump from iron's d-orbital to the vacant π antibonding orbital of inhibitor molecules (retro-donation), which enhances the adsorption of inhibitor on metal (Srivastava et al., 2018).

Results from Tafel measurements reveal that both extracts (PLPE and PLSE) exhibit a mixed-type inhibition mechanism, and these extracts were adsorbed over the MS through a mixed-type adsorption phenomenon, as suggested by the adsorption isotherms study. Moreover, surface investigations indicate that *Phaseolus lunatus* extracts make a protective layer on the MS surface, which effectively protect it from the corrosive solution (Eddahhaoui et al., 2024).

5.7 Literature comparison

The anticorrosive behavior of *Phaseolus lunatus* extracts was investigated by several corrosion-measuring techniques such as PDP, EIS, and weight loss methods. The obtained inhibitory efficiencies from these methods were compared with the reported inhibitory efficiencies of several plant extracts such as *petroselinum crispum* leaves extract (Al-Senani et al., 2015), *Dysphania ambrosioides* leaves extract (Daoudi et al., 2022), *Taxus baccata* extract (Hanini et al., 2019), *Chromolaena odorata* leaf extract (Mbamalu and Chinedu, 2023), *Uvaria chamae* leaves extract (AI et al., 2018), *Ipomoea batatas* extract (Anyiam et al., 2020), *Prunus dulcis* seeds extracts (Oshomogho et al., 2020), *Senna Obtusifolia* Leaves Extract (Abdulbasit et al., 2023), *Curcuma. L* extract (Abidli et al., 2023), Bitter leaves (*Vernonia amygdalina*) extract (Onukwulia and Omotioma, 2019), English yew (*Taxus baccata*) extract (Hanini et al., 2019), and many others (Table 5.7). The present work exhibited a clear dominance among all tabulated studies in Table 5.7. This study is limited by its focus on the corrosion inhibition efficiency of PLPE and PLSE, which were only tested in a 1 M HCl acidic medium, leaving the effectiveness of the extracts in other corrosive environments, such as H_2SO_4 or other acidic solutions. Additionally, the corrosion inhibition efficiency of PLPE and PLSE was not tested at varying concentrations of HCl.

Table 5.7 Comparison of corrosion inhibition efficiencies of *Phaseolus lunatus* extracts with the recently published plant-based extracts.

Inhibitor	Metal	*Corrosive medium*	Optimum concentration	*Experimental techniques*	*Inhibition efficiency*	References
Petroselinum crispum (Parsley) leaves extract	Carbon steel	1 M HCl	60 % (v/v)	WL	81.39	(Al-Senani et al., 2015)
Thymus Vulgari plant extract	Stainless Steel	1 M HCl	2 % (v/v)	EIS	62.15	(Ehsani et al., 2017)
Uvaria chamae leaves extract	Mild steel	2.5 M HCl	4000 mg L^{-1}	WL	84.60	(Al et al., 2018)
Bitter leaves (*Vernonia amygdalina*) extract	Mild steel	HCl	1000 mg L^{-1}	WL	85.40	(Onukwulia and Omotioma, 2019)
English yew (*Taxus baccata*) extract	Carbon steel	1 M HCl	700 mg L^{-1}	PDP	83.28	(Hanini et al., 2019)
	Carbon steel	1 M HCl	800 mg L^{-1}	EIS	74.26	
	Carbon steel	1 M HCl	700 mg L^{-1}	WL	61.78	
Ipomoea batatas extract (physically modified Starch)	Galvanized steel	1 M HCl	700 mg L^{-1}	PDP	60.44	(Anyiam et al., 2020)
	Galvanized steel	1 M HCl	700 mg L^{-1}	WL	64.26	
Prunus dulcis seeds extracts	Mild steel	1.5 M HCl	1500 mg L^{-1}	WL	69.95	(Oshomogho et al., 2020)
Dysphania ambrosioides (DA) leaves extract	Mild steel	1 M HCl	1500 mg L^{-1}	PDP	81.69	(Daoudi et al., 2022)
	Mild steel	1 M HCl	1500 mg L^{-1}	EIS	81.18	

	Mild steel	1 M HCl	1500 mg L^{-1}	WL	84.00	
Sarampa wood (*Xylocarpus Moluccensis*) extract	Mild steel	1 M HCl	500 mg L^{-1}	PDP	68.00	(Prifiharni et al., 2022)
	Mild steel	1 M HCl	500 mg L^{-1}	EIS	68.00	
Curcuma. L extract	Mild steel	0.1 M HCl	50 mg L^{-1}	EIS	81.10	(Abidli et al., 2023)
Chromolaena odorata Leaf Extract	Mild steel	1 M HCl	700 mg L^{-1}	PDP	81.60	(Mbamalu and Chinedu, 2023)
	Mild steel	1 M HCl	700 mg L^{-1}	WL	83.33	
Senna Obtusifolia Leaves Extract	Mild steel	0.5 M HCl	800 mg L^{-1}	PDP	75.55	(Abdulbasit et al., 2023)
	Mild steel	0.5 M HCl	800 mg L^{-1}	EIS	76.32	
	Mild steel	0.5 M HCl	800 mg L^{-1}	WL	85.67	
	Mild steel	1 M HCl	200 mg L^{-1}	PDP	85.69	
Phaseolus lunatus peel extract (PLPE)	Mild steel	1 M HCl	200 mg L^{-1}	EIS	84.97	Present work
	Mild steel	1 M HCl	200 mg L^{-1}	WL	85.50	
	Mild steel	1 M HCl	200 mg L^{-1}	PDP	90.78	
Phaseolus lunatus seed extract (PLSE)	Mild steel	1 M HCl	200 mg L^{-1}	EIS	88.60	
	Mild steel	1 M HCl	200 mg L^{-1}	WL	90.54	

5.8 Summary

In this work, *Phaseolus lunatus* peel extract (PLPE) and *Phaseolus lunatus* seed extracts (PLSE) were prepared and utilized separately as a novel corrosion inhibitor for mitigating the dissolution of MS in 1 M HCl. The electrochemical and weight loss methods were used to evaluate the anticorrosive behaviors of *Phaseolus lunatus* extracts (PLPE and PLSE). These extracts exhibited excellent corrosion-inhibiting properties due to the presence of several active ingredients, such as lysine, leucine, linoleic acid, oleic acid, 9-Octadecenoic acid (Z)-, methyl ester, and ascorbic acid, which were identified by LC-MS and FTIR analyses. From all analysis, the following conclusions can be drawn:

- Corrosion current densities were decreased with the addition of *Phaseolus lunatus* extracts.
- *Phaseolus lunatus* extracts display excellent anticorrosive performance with maximum inhibition efficiencies of about 85.69 % and 90.78 % at 200 mg L^{-1} of PLPE and PLSE, respectively.
- Positive shift (< ± 85 mV) was observed for E_{corr} (corrosion potential) in the presence of *Phaseolus lunatus* extracts as compared to uninhibited systems, which means the inhibitor works as a mix-type of inhibitor.
- The values of R_{ct} were significantly increased from 25.89 Ωcm^2 (blank system) to 172.31 Ωcm^2 (PLPE) and 227.07 Ωcm^2 (PLSE) at 200 mg L^{-1}, signifying higher hindrance for corrosive ions to reach the MS for inhibited systems as compared to blank.
- Weight loss measurements show the similar inhibiting effect of *Phaseolus lunatus* extracts (PLPE and PLSE) as obtained in electrochemical studies.

- *Phaseolus lunatus* extracts (PLPE and PLSE) showed prominent inhibitory effects with 71.92 and 78.43 % inhibitory efficiencies at 323 K. The values of E_a, ΔH, and ΔS displayed a positive shift than that of the uninhibited system.
- The evaluated standard Gibbs free energies for PLPE and PLSE lie in the range of -40 kJ mol^{-1} to -20 kJ $mol^{-1,}$ but these values were near to -20 kJ mol^{-1}, confirming that they favored physical adsorption (mix-type adsorption) on metal.
- Surface characterization revealed that *Phaseolus lunatus* extracts adsorbed on MS to build a defensive layer, which significantly mitigates MS dissolution.

5.9 References

Abdulbasit, Y., Abdullahi, B., Bishir, U., 2023. Experimental and theoretical evaluation of corrosion inhibition performance of senna obtusifolia leaves extract on mild steel in 0.5M HCl. Moroccan J. Chem. 11, 282–299. https://doi.org/10.48317/IMIST.PRSM/morjchem-v11i2.38203

Abidli, I., Souissi, N., Essalah, K., Novoa, X.R., 2023. A combined experimental and theoretical approach effect of Curcuma. L extract as a corrosion inhibitor on iron in acidic solution. Can. Metall. Q. 63,1–19. https://doi.org/10.1080/00084433.2023.2240113

AI, O., KJ, U., MC, E., PC, O., EC, O., 2018. Thermodynamic and kinetic studies of powerful eco friendly green inhibitors; Costus afer, Uvaria chamae and Xylopia aethiopia for the control of mild steel corrosion in HCl solution. J. Phys. Chem. Biophys. 08, 2161-0398. https://doi.org/10.4172/2161-0398.1000264

Al-Moubaraki, A.H., Awaji, H., 2020. 1-X-4-[4´-(–OCH3)-Styryl] pyridinium iodides, potent inhibitors for stainless steel corrosion in 2 M HCl acid solutions. Int. J. Corros. Scale Inhib. 9, 460–501. https://doi.org/10.17675/2305-6894-2020-9-2-5

Al-Moubaraki, A.H., Chaouiki, A., Alahmari, J.M., Al-hammadi, W.A., Noor, E.A., Al-Ghamdi, A.A., Ko, Y.G., 2022. Development of natural plant extracts as sustainable inhibitors for efficient protection of mild steel: Experimental and first-principles multi-level computational methods. Materials (Basel). 15, 8688. https://doi.org/10.3390/ma15238688

Al-Senani, G., Al-Saeedi, S., Almufarij, R., 2015. Green corrosion inhibitors for carbon steel

by green leafy vegetables extracts in 1 M HCl. Orient. J. Chem. 31, 2077–2086. https://doi.org/10.13005/ojc/310428

Alao, A.O., Popoola, A.P., Dada, M.O., Sanni, O., 2023. Utilization of green inhibitors as a sustainable corrosion control method for steel in petrochemical industries: A review. Front. Energy Res. 10, 1–21. https://doi.org/10.3389/fenrg.2022.1063315

Ali Asaad, M., Sarbini, N.N., Sulaiman, A., Ismail, M., Huseien, G.F., Abdul Majid, Z., Bothi Raja, P., 2018. Improved corrosion resistance of mild steel against acid activation: Impact of novel Elaeis guineensis and silver nanoparticles. J. Ind. Eng. Chem. 63, 139–148. https://doi.org/10.1016/j.jiec.2018.02.010

Amegroud, H., Boudalia, M., Elhawary, M., Garcia, A.J., Bellaouchou, A., Amin, H.M.A., 2024. Electropolymerized conducting polyaniline coating on nickel-aluminum bronze alloy for improved corrosion resistance in marine environment. Colloids Surfaces A Physicochem. Eng. Asp. 691, 133909. https://doi.org/10.1016/j.colsurfa.2024.133909

Ameh, P.O., 2018. Electrochemical and computational study of gum exudates from Canarium schweinfurthii as green corrosion inhibitor for mild steel in HCl solution. J. Taibah Univ. Sci. 12, 783–795. https://doi.org/10.1080/16583655.2018.1514147

Anyiam, C.K., Ogbobe, O., Oguzie, E.E., Madufor, I.C., Nwanonenyi, S.C., Onuegbu, G.C., Obasi, H.C., Chidiebere, M.A., 2020. Corrosion inhibition of galvanized steel in hydrochloric acid medium by a physically modified starch. SN Appl. Sci. 2, 520. https://doi.org/10.1007/s42452-020-2322-2

Bhan, C., Golder, A.K., 2024. ZnO nanorods aligned in a vertical configuration for targeted electrochemical detection of aniline. ACS Appl. Bio Mater. 7, 7413–7428. https://doi.org/10.1021/acsabm.4c01050

Bhan, C., Kumar Golder, A., 2023. Bio-based hierarchical vertically aligned 2D ZnO nanostructures for ultra selective electrochemical sensing of p-Chloroaniline. Chem. Eng. J. 475, 146122. https://doi.org/10.1016/j.cej.2023.146122

Bhan, C., Ravi, R., Golder, A.K., 2025. Phyto-analytic formation of Ag nanostructures for targeted electrocatalytic sensing of ciprofloxacin. J. Environ. Chem. Eng. 13, 115140. https://doi.org/10.1016/j.jece.2024.115140

Boudalia, M., Laourayed, M., El Moudane, M., Sekkat, Z., Campos, O.S., Bellaouchou, A., Guenbour, A., José Garcia, A., Amin, H.M.A., 2023. Phosphate glass doped with niobium and bismuth oxides as an eco-friendly corrosion protection matrix of iron steel in HCl medium: Experimental and theoretical insights. J. Alloys Compd. 938, 168570.

https://doi.org/10.1016/j.jallcom.2022.168570

Boutoumit, A., Elhawary, M., Bellaouchou, A., Boudalia, M., Hammani, O., José Garcia, A., Amin, H.M.A., 2024. Electrochemical, structural and thermodynamic investigations of methanolic Parsley extract as a green corrosion inhibitor for C37 Steel in HCl. Coatings 14, 783. https://doi.org/10.3390/coatings14070783

Daoudi, W., El Aatiaoui, A., Falil, N., Azzouzi, M., Berisha, A., Olasunkanmi, L.O., Dagdag, O., Ebenso, E.E., Koudad, M., Aouinti, A., Loutou, M., Oussaid, A., 2022. Essential oil of Dysphania ambrosioides as a green corrosion inhibitor for mild steel in HCl solution. J. Mol. Liq. 363, 119839. https://doi.org/10.1016/j.molliq.2022.119839

Dhongde, N.R., Das, N.K., Hazarika, J., Park, J.-G., Banerjee, T., Rajaraman, P.V., 2025. Azoles as corrosion inhibitors in alkaline medium for ruthenium chemical mechanical planarization applications:Electrochemical and theoretical analysis. J. Mol. Struct. 1320, 139651. https://doi.org/10.1016/j.molstruc.2024.139651

Eddahhaoui, F.-Z., Najem, A., Elhawary, M., Boudalia, M., Campos, O.S., Tabyaoui, M., José Garcia, A., Bellaouchou, A., Amin, H.M.A., 2024. Experimental and computational aspects of green corrosion inhibition for low carbon steel in HCl environment using extract of Chamaerops humilis fruit waste. J. Alloys Compd. 977, 173307. https://doi.org/10.1016/j.jallcom.2023.173307

Ehsani, A., Mahjani, M.G., Hosseini, M., Safari, R., Moshrefi, R., Mohammad Shiri, H., 2017. Evaluation of Thymus vulgaris plant extract as an eco-friendly corrosion inhibitor for stainless steel 304 in acidic solution by means of electrochemical impedance spectroscopy, electrochemical noise analysis and density functional theory. J. Colloid Interface Sci. 490, 444–451. https://doi.org/10.1016/j.jcis.2016.11.048

El Khatib, L.W., Rahal, H.T., Abdel-Gaber, A.M., 2020. Synergistic effect between Fragaria ananassa and Cucurbita pepo L leaf extracts on mild steel corrosion in hydrochloric acid solutions. Prot. Met. Phys. Chem. Surfaces 56, 1096–1106. https://doi.org/10.1134/S2070205120050111

Hanini, K., Merzoug, B., Boudiba, S., Selatnia, I., Laouer, H., Akkal, S., 2019. Influence of different polyphenol extracts of Taxus baccata on the corrosion process and their effect as additives in electrodeposition. Sustain. Chem. Pharm. 14, 100189. https://doi.org/10.1016/j.scp.2019.100189

Haque, J., Verma, C., Srivastava, V., Nik, W.B.W., 2021. Corrosion inhibition of mild steel in 1 M HCl using environmentally benign Thevetia peruviana flower extracts. Sustain.

Chem. Pharm. 19, 100354. https://doi.org/10.1016/j.scp.2020.100354

Hermoso-Diaz, I.A., Foroozan, A.E., Flores-De los Rios, J.P., Landeros-Martinez, L.L., Porcayo-Calderon, J., Gonzalez-Rodriguez, J.G., 2019. Electrochemical and quantum chemical assessment of linoleic acid as a corrosion inhibitor for carbon steel in sulfuric acid solution. J. Mol. Struct. 1197, 535–546. https://doi.org/10.1016/j.molstruc.2019.07.085

Hidalgo, J., Hidalgo, L., Serrano Aguiar, C.D., García Madroñero, D.B., Galambos, I., Vilasó-Cadre, J.E., Reyes-Domínguez, I.A., Brânzanic, A.M. V., Ignat, N., Turdean, G.L., 2025. Study of Caesalpinia spinosa extracts as green corrosion inhibitor for mild steel. Langmuir 41, 9406–9421. https://doi.org/10.1021/acs.langmuir.5c00224

Ishnava, K.B., Patel, K.S., 2020. In vitro study of Praecitrulus fistulosus (Stocks) Pangalo (Cucurbitaceae) fruit – A potential candidate of Anthelmintic activity. Bull. Natl. Res. Cent. 44, 130. https://doi.org/10.1186/s42269-020-00365-1

Kumar, A., Bhattacharya, B., Das, C., 2025. Studies on the inhibitive effect of ferrozine on the corrosion of mild steel in hydrochloric acid. J. Taiwan Inst. Chem. Eng. 174, 106221. https://doi.org/10.1016/j.jtice.2025.106221

Kumar, A., Das, C., 2024. Corrosion inhibition of mild steel by Praecitrullus fistulosus (tinda fruit and peel) extracts. Sci. Total Environ. 929, 172569. https://doi.org/10.1016/j.scitotenv.2024.172569

Lavanya, M., Machado, A.A., 2024. Surfactants as biodegradable sustainable inhibitors for corrosion control in diverse media and conditions: A comprehensive review. Sci. Total Environ. 908, 168407. https://doi.org/10.1016/j.scitotenv.2023.168407

Li, D., Zhang, P., Guo, X., Zhao, X., Xu, Y., 2019. The inhibition of mild steel corrosion in 0.5 M H_2SO_4 solution by radish leaf extract. RSC Adv. 9, 40997–41009. https://doi.org/10.1039/C9RA04218K

Ma, Y., Han, F., Li, Z., Xia, C., 2016. Acidic-functionalized ionic liquid as corrosion inhibitor for 304 stainless steel in aqueous sulfuric acid. ACS Sustain. Chem. Eng. 4, 5046–5052. https://doi.org/10.1021/acssuschemeng.6b01492

Mahgoub, F.M., Hefnawy, A.M., Abd Alrazzaq, E.H., 2019. Corrosion inhibition of mild steel in acidic solution by leaves and stem extract of Acacia nilotica. Desalin. WATER Treat. 169, 49–58. https://doi.org/10.5004/dwt.2019.24681

Masuku, M., Ouma, L., Pholosi, A., 2021. Microwave assisted synthesis of oleic acid modified magnetite nanoparticles for benzene adsorption. Environ. Nanotechnology, Monit.

Manag. 15, 100429. https://doi.org/10.1016/j.enmm.2021.100429

Matad, P.B., Mokshanatha, P.B., Hebbar, N., Venkatesha, V.T., Tandon, H.C., 2014. Ketosulfone Drug as a green corrosion inhibitor for mild steel in acidic medium. Ind. Eng. Chem. Res. 53, 8436–8444. https://doi.org/10.1021/ie500232g

Mbamalu, E.E., Chinedu, A.P., 2023. Assessment of the corrosion inhibitory potentials of chromolaena odorata leaf extract on mild steel in hydrogen chloride acid environment. Moroccan J. Chem. 11, 188–204. https://doi.org/doi.org/10.48317/IMIST.PRSM/morjchem-v10i3.30521

Naik, M., Lee, Y.-S., Qurashi, A., 2018. Chemically grafted aminated carbon nanotubes and l-lysine in ultramodified conditions for carbon dioxide storage. ACS Omega 3, 10442–10448. https://doi.org/10.1021/acsomega.8b00597

Onukwulia, O.D., Omotioma, M., 2019. Study of bitter leaves extract as inhibitive agent in HCL medium for the treatment of mild steel through pickling. Port. Electrochim. Acta 37, 115–121. https://doi.org/10.4152/pea.201902115

Oshomogho, F.O., Akhihiero, T.E., Edokpayi, O., Ossai, J.E., 2020. Green corrosion inhibition of mild steel using Prunus Dulcis seeds extract in an acidic medium. Glob. J. Pure Appl. Sci. 26, 171–178. https://doi.org/10.4314/gjpas.v26i2.9

Pal, A., Das, C., 2023. Novel use of kitchen waste: Protection of boiler quality steel from corrosion in acidic media using onion waste. Chem. Pap. 77, 1107–1127. https://doi.org/10.1007/s11696-022-02549-7

Pal, A., Das, C., 2022a. New eco-friendly anti-corrosion inhibitor of purple rice bran extract for boiler quality steel: Experimental and theoretical investigations. J. Mol. Struct. 1251, 131988. https://doi.org/10.1016/j.molstruc.2021.131988

Pal, A., Das, C., 2022b. Investigations on corrosion inhibition in acidic media for BQ steel using banana flower bract, an eco-friendly novel agro-waste: Experimental and theoretical considerations. Inorg. Chem. Commun. 145, 110024. https://doi.org/10.1016/j.inoche.2022.110024

Prifiharni, S., Mashanafie, G., Priyotomo, G., Royani, A., Ridhova, A., Elya, B., Soedarsono, J.W., 2022. Extract sarampa wood (Xylocarpus Moluccensis) as an eco-friendly corrosion inhibitor for mild steel in HCl 1M. J. Indian Chem. Soc. 99, 100520. https://doi.org/10.1016/j.jics.2022.100520

Shah, A., Akhtar, S., Mahmood, F., Urooj, S., Siddique, A.B., Irfan, M.I., Naeem-ul-Hassan, M., Sher, M., Alhoshani, A., Rauf, A., Amin, H.M.A., Abbas, A., 2024. Fagonia arabica

extract-stabilized gold nanoparticles as a highly selective colorimetric nanoprobe for Cd^{2+} detection and as a potential photocatalytic and antibacterial agent. Surfaces and Interfaces 51, 104556. https://doi.org/10.1016/j.surfin.2024.104556

Srivastava, V., Chauhan, D.S., Joshi, P.G., Maruthapandian, V., Sorour, A.A., Quraishi, M.A., 2018. PEG-Functionalized Chitosan: A biological macromolecule as a novel corrosion inhibitor. ChemistrySelect 3, 1990–1998. https://doi.org/10.1002/slct.201701949

Tang, M., Li, X., Deng, S., Lei, R., 2021. Synergistic inhibition effect of Mikania micrantha extract with KI on steel corrosion in H_2SO_4 solution. J. Mol. Liq. 344, 117926. https://doi.org/10.1016/j.molliq.2021.117926

Thomas, A., Prajila, M., Shainy, K.M., Joseph, A., 2020. A green approach to corrosion inhibition of mild steel in hydrochloric acid using fruit rind extract of Garcinia indica (Binda). J. Mol. Liq. 312, 113369. https://doi.org/10.1016/j.molliq.2020.113369

Varvara, S., Caniglia, G., Izquierdo, J., Bostan, R., Găină, L., Bobis, O., Souto, R.M., 2020. Multiscale electrochemical analysis of the corrosion control of bronze in simulated acid rain by horse-chestnut (Aesculus hippocastanum L.) extract as green inhibitor. Corros. Sci. 165, 108381. https://doi.org/10.1016/j.corsci.2019.108381

Wang, Q., Zhang, Q., Zheng, H., Liu, L., Wu, X., Zhao, C., Zhou, X., Sun, Y., Yan, Z., Li, X., 2023. Insight into anti-corrosion behavior of protein extract as eco–friendly corrosion inhibitor. Sustain. Chem. Pharm. 34, 101177. https://doi.org/10.1016/j.scp.2023.101177

Yin, H., Wei, C., Ye, Y., Wang, Z., Zhou, S., 2025. Synergistic lanthanum /nitrogen co-modified carbon dots as steel corrosion inhibitor. Mater. Today Commun. 42, 111106. https://doi.org/10.1016/j.mtcomm.2024.111106

Chapter 6:

Duranta erecta fruit and leaves extracts as green corrosion inhibitors for mild steel protection in hydrochloric acid

Duranta erecta fruit and leaves extracts as green corrosion inhibitors for mild steel protection in hydrochloric acid

This chapter displays the anticorrosive behaviour of Duranta erecta fruit and seed extracts for protecting mild steel in 1 M HCl. These extracts were characterized by LC-MS and FTIR analyses, which confirm the presence of Ethanone, 1-(2-hydroxy-5-methylphenyl)-, 4,7-Dimethoxy-2-methyl-2,3-dihydro-1 H-inden-1-one, Isopropyl Myristate, 9-Octadecenamide, n-Hexadecanoic acid, and 7,10,13-Eicosatrienoic acid, methyl ester. The corrosion inhibiting efficiencies were evaluated by weight loss and electrochemical methods. Results showed that values of corrosion current density and inhibition efficiency were decreased and increased with increasing inhibitor concentration. The highest inhibition efficiencies of 90.82% (DEFE) and 91.82% (DELE) were achieved at 200 mg L^{-1}. Langmuir adsorption isotherm possesses the best fit, and extracts followed the preferential physical (mixed-type) adsorption. Thermodynamic parameters suggest a spontaneous and endothermic corrosion process. Surface analyses (FESEM, EDX, AFM) further validate the above findings.

Submitted Article: Kumar, A., Das, C., *Duranta erecta* fruit and leaves extracts as green corrosion inhibitors for mild steel protection in hydrochloric acid (**Submitted to journal)**.

6.1 Characterizations of DEFE and DELE

6.1.1 LC-MS analysis

Duranta erecta fruit and seed extracts (DEFE and DELE) were analyzed by liquid chromatography-mass spectroscopy to identify the active phytochemicals. Figs. 6.1 (a) and 6.1 (b) present the mass spectra of DEFE and DELE, respectively, showing various peaks at different m/z values. These spectra reveal that both extracts exhibit the abundance of the following compounds: Ethanone, 1-(2-hydroxy-5-methylphenyl)- (m/z: 151.07), 4,7-Dimethoxy-2-methyl-2,3-dihydro-1 H-inden-1-one (m/z: 207.10), Isopropyl Myristate (m/z: 271.24), and 9-Octadecenamide (m/z: 282.27). Additionally, DEFE contained n-Hexadecanoic acid (m/z: 257.24), while DELE exhibited the presence of 7,10,13-Eicosatrienoic acid, methyl ester (m/z: 321.27). Few studies have also reported the presence of the above compounds in *Duranta erecta* extracts (R et al., 2019; Shadrack Donkor et al., 2022). These compounds possess all required structural characteristics, such as double bonds, aromatic rings, heteroatoms, and long carbon chains, to be a suitable candidate for corrosion inhibition.

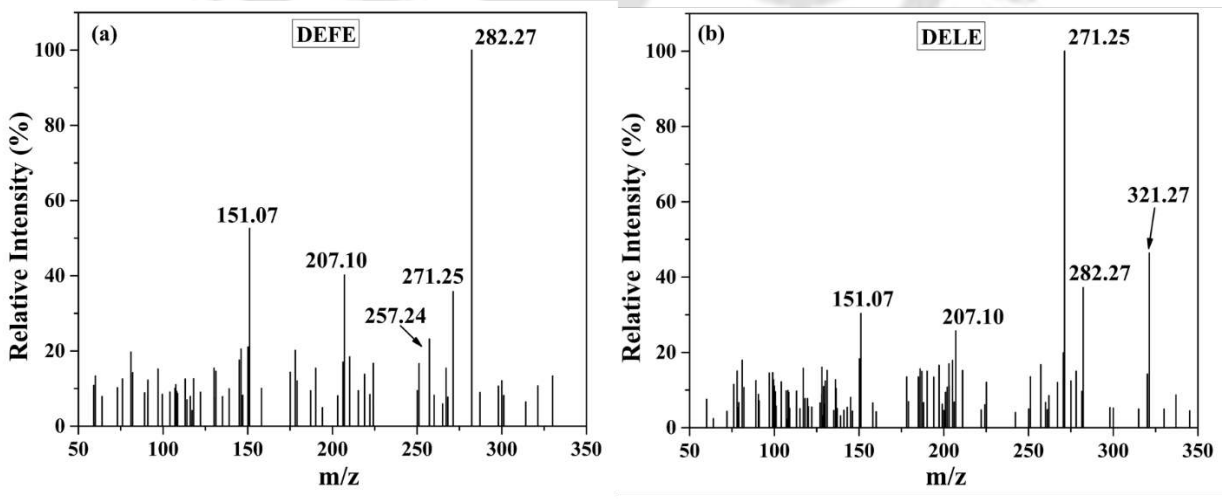

Fig. 6.1 Mass spectra of DEFE (a) and DELE (b).

6.1.2 FTIR analysis

The FTIR spectroscopy was carried out to find available functional groups in DEFE and DELE (Fig. 6.2). In these plots, bands in the region 3200-3540 cm^{-1} correspond to –OH of alcohol, phenols, etc. A band at 2978 cm^{-1} (DEFE) and 2980 cm^{-1} (DELE) is attributed to N−H stretching (Naik et al., 2018; Shah et al., 2024). Furthermore, the bands around 2904 cm^{-1} correspond to C–H stretching in alkanes, while the band near 1645 cm^{-1} may be attributed to C=O bending vibrations. The bands at 1400 cm^{-1} represent the alkene bending vibrations in extracts (Ishnava and Patel, 2020). The bands at 1085 and 878 in both *Duranta erecta* extracts can be due to –C-O stretching and C-C bending, respectively (Golder et al., 2021; Mittal et al., 2020). These observations illustrate that both *Duranta erecta* extracts (DEFE and DELE) contained oxygen and nitrogen in their functional groups (O–H, –C-O, C=O, C-C, C=C, and NH), which are well aligned with the findings of LC-MS analysis (Agomuo et al., 2017; Mittal et al., 2020). These compounds have all the properties of typical corrosion inhibitors.

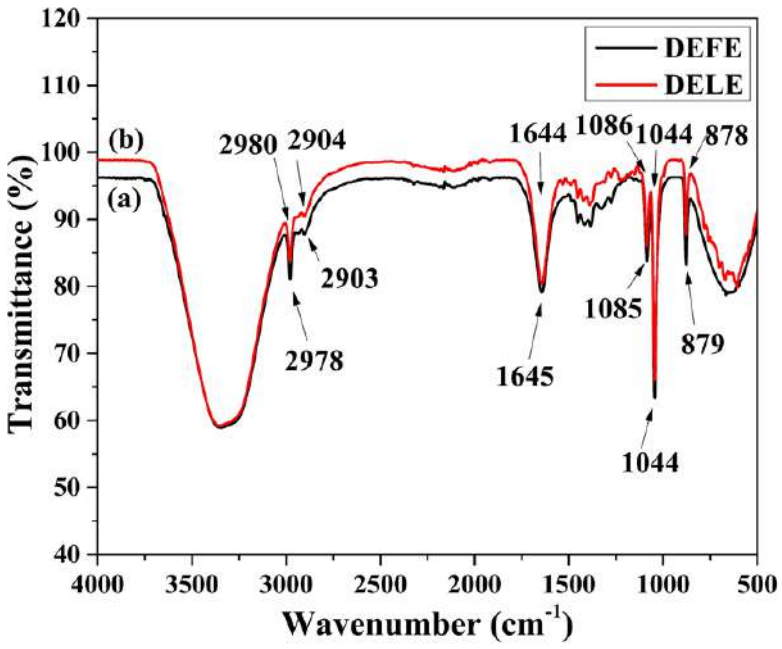

Fig. 6.2 FTIR spectra of, (a) DEFE and (b) DELE.

6.2 Corrosion test

6.2.1 Weight loss investigations

6.2.1.1 Influence of *Duranta erecta* extract's concentration

The weight loss experiments were performed with a 24 h immersion time. The MS electrodes were immersed in 1 M HCl at several dosages (0, 50, 100, 150, 200, and 250 mg L^{-1}) of *Duranta erecta* extracts. These experiments were executed in environmental conditions without stirring. According to the changes in the sample's weight in inhibited or uninhibited systems, corrosion rate (CR) and inhibition efficiency values were calculated. During the weight loss observations, it was recorded that values of corrosion rate declined with the amount of *Duranta erecta* extracts (DEFE and DELE) up to 200 mg L^{-1}, which depicts the formation of a corrosion inhibitory layer by the adsorption of extract molecules on the metallic surface. Layer's compactness was enhanced with the addition of both *Duranta erecta* extracts up to 200 mg $L^{-1,}$ but on higher concentrations up to 250 mg L^{-1}, inhibitory efficiency showed an insignificant improvement (~1%), which illustrates that the adsorption of inhibitors on MS exhibits equilibrium above 200 mg L^{-1} concentrations of inhibitors (Al-Amiery et al., 2022). These findings indicate that at lower concentrations, the availability of inhibitor molecules is limited. At this stage, the number of inhibitor molecules is insufficient to cover the entire active surface of the metal, resulting in a lower inhibitory effect. However, as the concentration of inhibitors increases, more molecules adsorb onto the metal surface. Eventually, at a certain inhibitor concentration, all active sites on the MS surface become fully occupied by adsorbed molecules. This saturation leads to the maximum inhibitory efficiency, which remains constant above a certain concentration of inhibitor (Al-Amiery et al., 2023).

In this work, the inhibitory efficiency of both *Duranta erecta* extracts was constant above their 200 mg L^{-1} concentration, which signifies equilibrium of surface coverage with extract molecules, so this system showed the highest inhibitory effect at this dose. These

findings suggest that 200 mg L^{-1} is the optimal dose of DEFE and DELE for their corrosion-inhibiting behavior (Fig. 6.3). In the literature, some work has also reported a similar trend of inhibition efficiency with inhibitor dose (Betti et al., 2023). Herein, 90.79 % (DEFE) and 91.17 % (DELE) inhibitory efficiencies were achieved after 24 h exposure at the optimum dosages of DEFE and DELE, respectively. Similar immersion times of 24 h have been reported by a few studies that have examined the impact of inhibitor concentration (Haldhar et al., 2021).

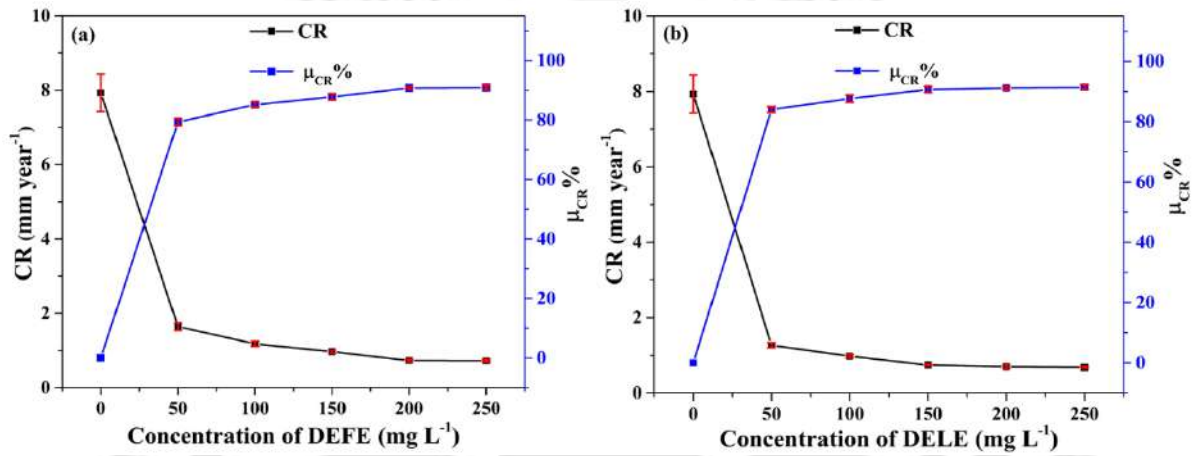

Fig. 6.3 Variations in CR and μ_{CR} % with increasing DEFE a) and DELE b) concentration.

6.2.1.2 Effect of immersion time

The effect of immersion time on the corrosion inhibition efficiency of *Duranta erecta* extracts was investigated by immersing MS coupons in 1 M HCl with and without 200 mg L^{-1} of inhibitor for durations ranging from 4 to 48 h at 28 ± 2 °C. The variation in inhibiting efficiency of *Duranta erecta* extracts is displayed in Fig. 6.4. A rapid increase in the corrosion inhibiting efficiency was seen for the initial exposure period of 4 to 12 h. Thereafter, values of inhibiting efficiencies exhibited a slow improvement up to 24 h. After 24 h, there is a minute increase (≤ 1 %) in inhibition efficiency up to 48 h. These observations signify that the adsorption of DEFE and DELE on metal was accomplished within 24 h and reached an

equilibrium stage. During 24-48 h, the available molecules of inhibitor in 1 M HCl solution participate in repairing the adsorbed inhibiting layer, which deteriorated due to the attack of corrosive species. This inhibitory behavior can be explained by the fact that inhibitor molecules adsorb onto metal and form an inhibitory layer. Its thickness and compactness were increased with time and reached a steady state within 24 h of exposure (Faustin et al., 2015).

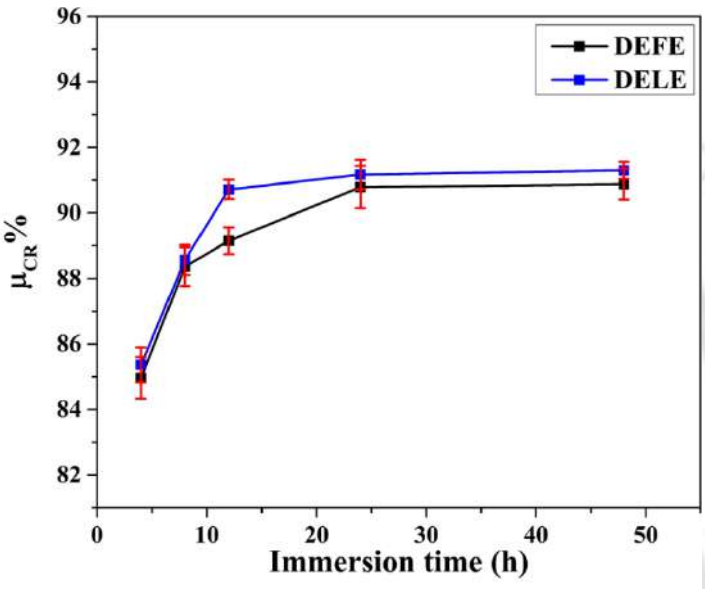

Fig. 6.4 The variation in the inhibitory efficiencies of DEFE and DELE with exposure time.

6.2.2 Electrochemical studies

Electrochemical analysis is most commonly used to study the corrosion-inhibiting behavior of materials. This work used *Duranta erecta* extracts to reduce MS dissolution in 1 M HCl. Each observation was executed thrice for several dosages (0-200 mg L^{-1}) of DEFE and DELE at 30 ºC.

6.2.2.1 Open circuit potential

Open circuit potential was measured for MS corrosion at several dosages of DEFE and DELE, separately. These values were utilized in their respective electrochemical tests, such as EIS and PDP. The obtained OCP plots are demonstrated in Figs. 6.5 (a) and (b). These figures illustrate that OCP values reach study state values within 1 h of exposure of MS to corrosive solution in the presence or absence of inhibitor. It was also noticed that OCP curves shifted positively in inhibiting systems compared to the blank.

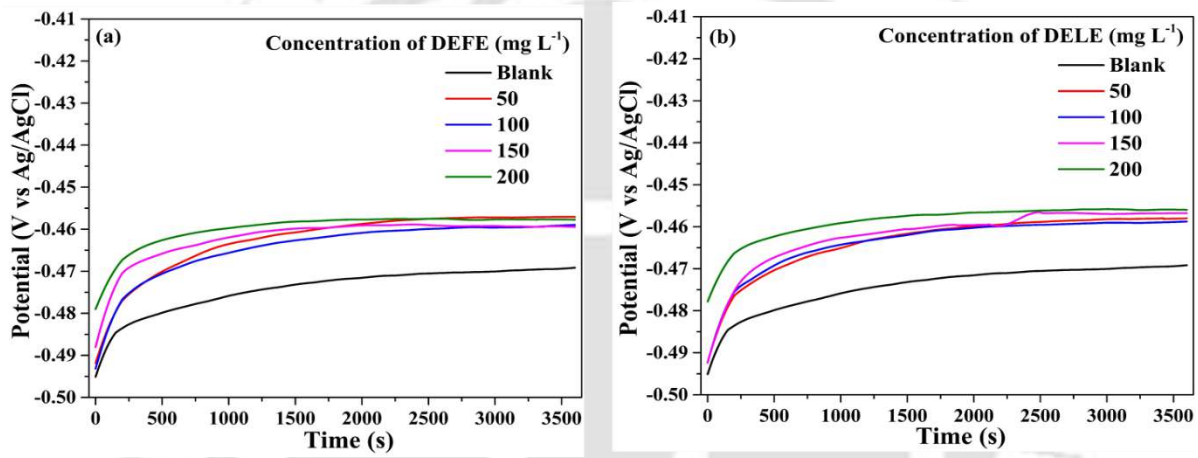

Fig. 6.5 OCP plots for MS immersed in 1 M HCl in the presence and absence of DEFE a), and DELE b).

6.2.2.2 Potentiodynamic polarization

The Tafel plots for MS degradation in an acidic medium with and without *Duranta erecta* extracts were recorded and shown in Fig. 6.6. The addition of *Duranta erecta* extracts to the corrosive solution triggered the shifting of both the cathodic and anodic current to lesser current density values compared to those observed in the absence of the inhibitor. Quantitative information on the kinetics of the corrosion process was derived by determining electrochemical parameters (corrosion current density (i_{corr}), corrosion potential (E_{corr}), cathodic (β_c), and anodic (β_a) Tafel slopes) from the fitting Tafel plots in the Nova 1.1.0

software, and they are listed in Table 6.1. From this table, it can be seen that E_{corr} shifted positively for inhibited systems compared to blank systems. Still, this shift remained within ± 85 mV, indicating that *Duranta erecta* extracts (DEFE and DELE) exhibited mix-type inhibiting behavior (Pal and Das, 2022a).

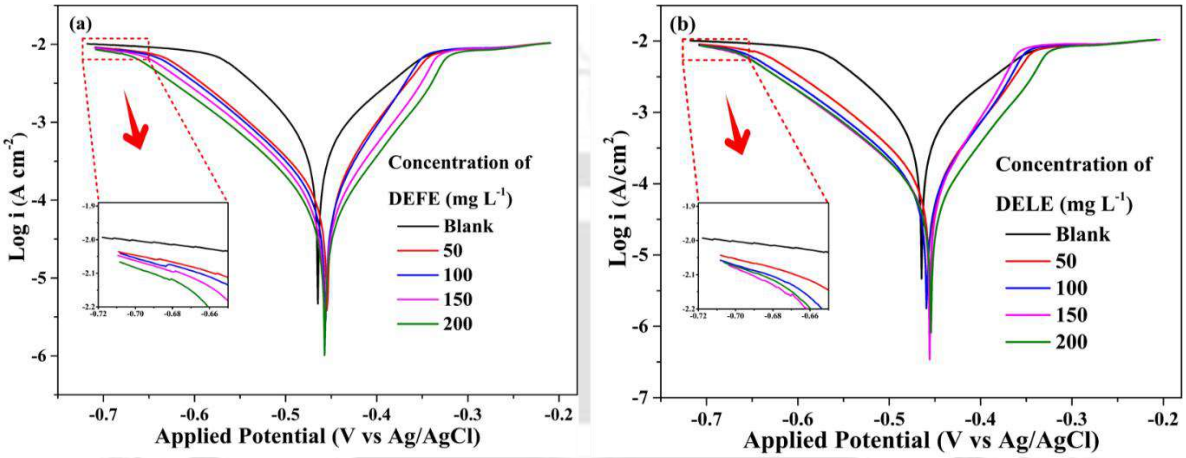

Fig. 6.6 Tafel plots for MS immersed in 1 M HCl with and without several concentrations of DEFE a) and DELE b).

Moreover, it was also noticed that E_{corr} values were very close to their OCP values (Canales et al., 2021), which were recorded before each electrochemical test. Table 6.1 also shows that anodic and cathodic currents declined with the addition of *Duranta erecta* extracts compared to the blank, depicting a reduction in metal deterioration and H_2 gas formation. Furthermore, on careful observation, it was found that two simultaneous processes (reduction in the values of corrosion current densities and improvement in polarization resistance) were occurring with the addition of *Duranta erecta* extracts (DEFE and DELE) (Pang et al., 2024). These processes explain the construction of an inhibiting layer on the metallic surface due to the adsorption of DEFE and DELE, which exhibited strong corrosion-inhibiting properties with the following efficiency of 90.82 and 91.82 %, respectively, at their optimum concentration (200 mg L^{-1}) (Ali Asaad et al., 2018). Additionally, Table 6.2 shows that corrosion rate values

were decreased with the addition of duranta erecta extracts. These values are well aligned with the corrosion rate values obtained from weight loss method, as presented in Table 6A.1 of Appendix 6A.

Table 6.1 The obtained parameters from Tafel analysis for MS with and without several concentrations of DEFE and DELE in 1 M HCl.

Inhibitor	Conc. (mg L^{-1})	b_a (mV dec^{-1})	$-b_c$ (mV dec^{-1})	*OCP* (mV vs. Ag/AgCl)	E_{corr} (mV vs. Ag/AgCl)	i_{corr} (µA cm^{-2})	R_p (Ω cm^2)	*CR* (mm $Year^{-1}$)	μ_P (%)
Blank	0	110.59 ± 0.52	120.25 ± 1.04	-468.15 ± 5.68	-465.25 ± 5.56	734.98 ± 5.23	34.04 ± 0.12	8.54 ± 0.45	_
DEFE	50	106.21 ± 0.51	60.91 ± 0.40	-457.11 ± 2.23	-454.60 ± 3.65	141.47 ± 0.82	118.83 ± 0.34	1.64 ± 0.11	80.75 ± 0.87
	100	85.08 ± 1.00	59.20 ± 0.90	-458.99 ± 1.97	-456.69 ± 3.04	105.22 ± 1.65	144.08 ± 0.18	1.22 ± 0.10	85.68 ± 0.47
	150	79.58 ± 0.79	71.39 ± 1.07	-459.44 ± 3.52	-456.72 ± 2.27	88.59 ± 1.09	197.24 ± 0.44	0.96 ± 0.06	87.95 ± 1.01
	200	81.21 ± 0.39	79.28 ± 1.55	-457.76 ± 2.82	-457.48 ± 2.62	67.49 ± 0.90	258.14 ± 0.53	0.78 ± 0.02	90.82 ± 0.16
Blank	0	110.59 ± 0.52	120.25 ± 1.04	-468.15 ± 5.68	-465.25 ± 5.56	734.98 ± 5.23	34.04 ± 0.12	8.54 ± 0.45	_
DELE	50	92.56 ± 0.87	65.55 ± 0.83	-457.98 ± 3.36	-455.45 ± 1.82	116.04 ± 1.43	143.63 ± 0.15	1.35 ± 0.12	84.21 ± 0.40
	100	83.58 ± 0.79	60.47 ± 0.51	-458.77 ± 4.10	-458.73 ± 2.01	81.52 ± 0.89	186.92 ± 0.54	0.95 ± 0.05	88.91 ± 0.91
	150	89.22 ± 0.33	45.32 ± 0.20	-456.76 ± 3.96	-455.54 ± 4.04	66.39 ± 0.31	196.58 ± 0.25	0.77 ± 0.02	90.97 ± 0.70
	200	78.49 ± 0.62	67.27 ± 0.53	-455.96 ± 2.52	-454.56 ± 3.13	60.15 ± 0.63	261.53 ± 0.68	0.70 ± 0.04	91.82 ± 0.97

6.2.2.3 Electrochemical impedance spectroscopy

Electrochemical impedance spectroscopy (EIS) is another effective approach for studying events happening at the electrical interface of metal and electrolyte in inhibited or uninhibited metal corrosion [47]. EIS results of MS degradation in HCl solution with and without various dosages (0-200 mg L^{-1}) of *Duranta erecta* extracts are obtained as Nyquist and Bode plots. Nyquist curves have the same depressed semicircles (Fig. 6.7), which depict the heterogeneity of the metallic surface. At higher frequencies, a huge capacitive loop appeared, which signifies the transfer of charges across the double layer. In uninhibited systems, an inductive loop appeared at low frequencies, which completely disappeared in the presence of inhibitor.

This inductive loop is related to the relaxation of adsorbed intermediate ions, for instance, H^{+}_{ads}, Cl^{-}_{ads}, and others, confirming the existence of corrosion product on metallic surface, but the disappearance of the inductive loop for inhibited systems is considered as a process of deuteriation in EIS studies (Pal and Das, 2022b). The Nyquist pattern of MS corrosion in electrolytes with and without *Duranta erecta* extracts shows the typical nature of electrochemical reactions occurring at the metal-electrolyte interface, which are primarily controlled by charge transfer resistance. In each Nyquist curve, the semicircle's diameter represents the value of R_{ct} (charge transfer resistance) (Bhan and Kumar Golder, 2023). It was enlarged with the amount of inhibitors up to 200 mg L^{-1} (Figs. 6.7 (a) and 6.7 (b)), which signifies that charge transfer resistance was enhanced with the concentration of inhibitors.

Bode magnitude and Bode phase graphs of metal corrosion in HCl solution for inhibited or uninhibited systems are demonstrated in Fig. 6.8. These Bode phase curves exhibited different values of phase angles, which lie in the range of 0° and 90°, suggesting the capacitive or resistive properties of the metal-electrolyte interface, but all these values are smaller than 90°, confirming the non-pure capacitive behavior (Kumar and Das, 2024). Furthermore, the

peak height of phase plots was increased with the addition of extracts (Figs. 6.8 c and d), depicting the capacitive behavior on the metal-electrolyte interface (Pal and Das, 2023).

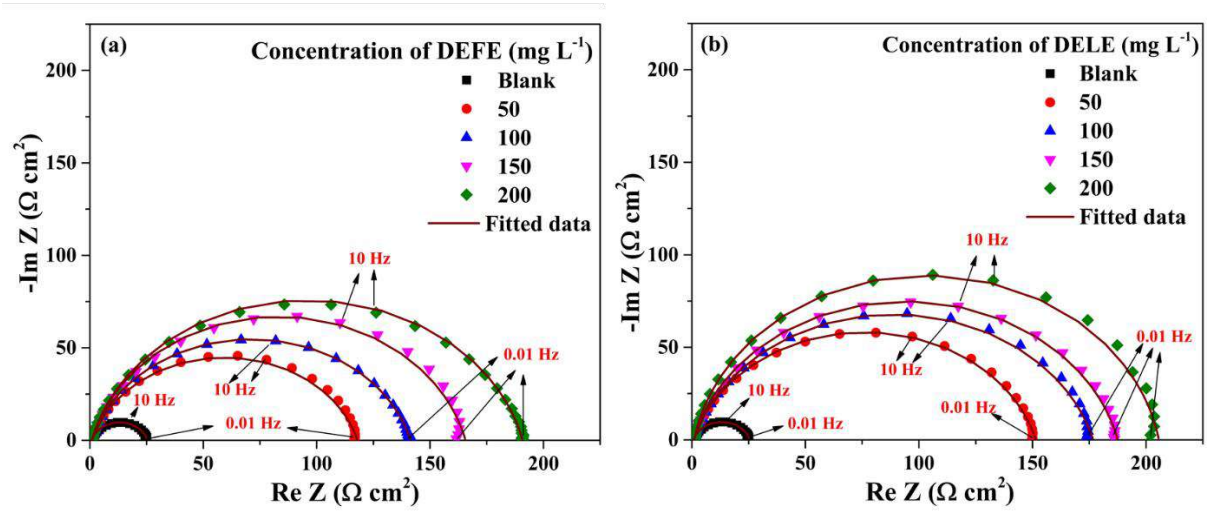

Fig. 6.7 Nyquist diagrams of MS exposed to 1 M HCl with and without several concentrations of DEFE a) and DELE b).

A simple Randle circuit model (Fig. 6.9) was used to understand the electrochemical insight of the Nyquist plot. R_s is the solution resistance, R_{ct} is the charge transfer resistance, and *CPE* is the constant phase element (Pal and Das, 2022a). Several Nyquist parameters (R_{ct}, Y_0, C_{dl}, n, goodness of fit (χ^2), and μ_{Rct} (%)) were obtained by fitting the Nyquist plots to the proposed electrochemical circuit using Nova 1.1.0 software, and their values were tabulated in Table 6.2. The obtained values of χ^2 varied from 1.12×10^{-3} to 3.24×10^{-3}, signifying the decent fitting of EIS data to an equivalent circuit model (Goswami et al., 2024; Tang et al., 2021). Table 6.2 shows that the value of R_{ct} was significantly enhanced for inhibited systems compared to the blank, signifying that corrosive species face higher hindrance to reach the metallic surface from the bulk of electrolyte (Dhongde et al., 2025). It was due to the development of a corrosion-inhibiting layer on the metallic surface that separates the metallic bodies and electrolytes.

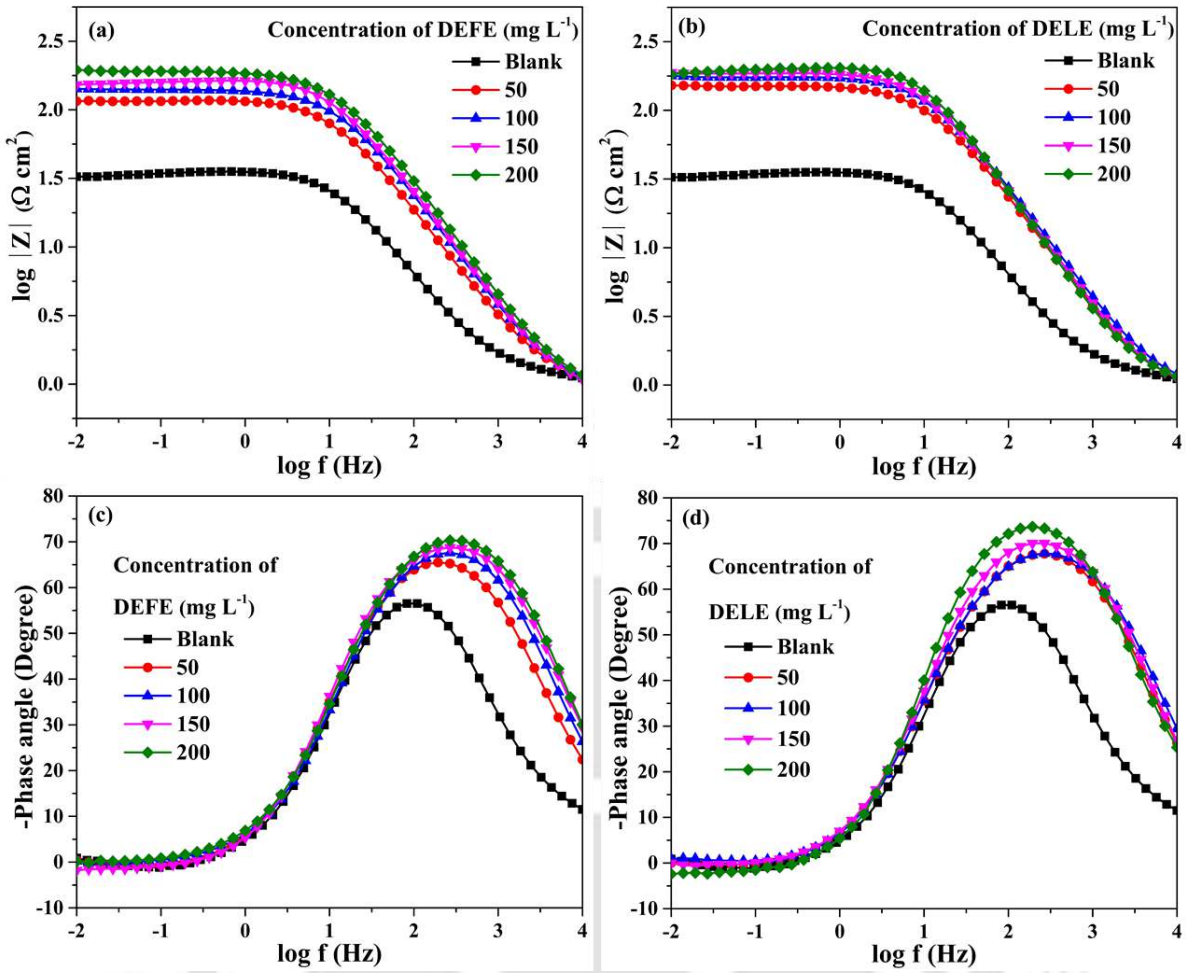

Fig. 6.8 Bode magnitude and phase plots for MS corrosion in 1 M HCl with and without several concentrations of DEFE (a,c) and DELE (b,d).

On comparing the corrosion-inhibiting behavior of both *Duranta erecta* extracts, it was observed that DELE exhibited a stronger inhibiting nature than DEFE at 200 mg L^{-1}. Additionally, these R_p values were compared with those obtained from PDP measurements, as represented in Table 6A.1 of the Appendix 6A, this comparison suggests that EIS findings have good agreement with PDP analysis. The obtained inhibitory efficiencies from electrochemical and weight loss analysis are tabulated in Table 6A.2 of Appendix 6A. Furthermore, in PDP measurements, the obtained inhibitory efficiencies are slightly higher than those achieved in EIS and weight loss investigations, and calculated p-values confirm that electrochemical data are highly statistically significant ($p < 0.0001$).

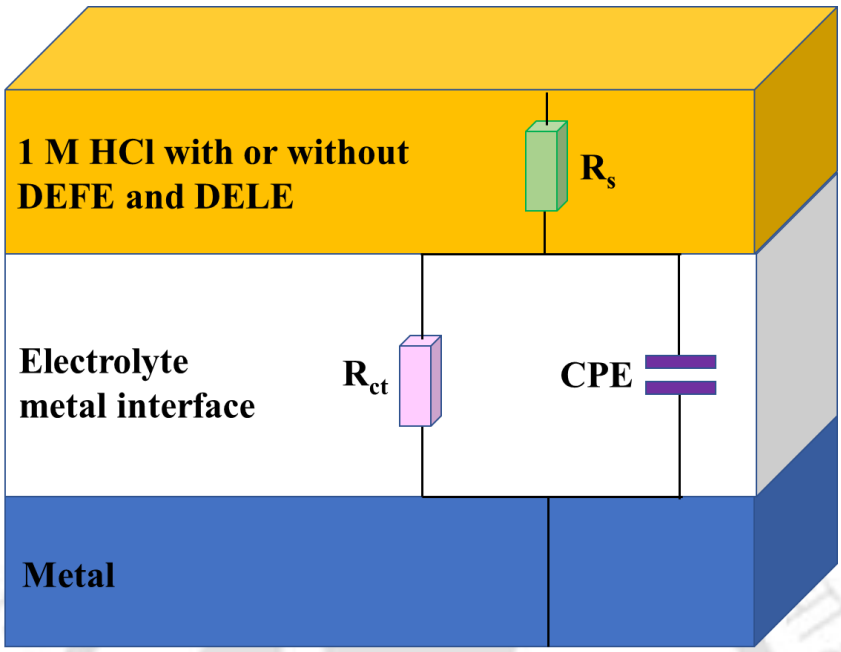

Fig. 6.9 Equivalent circuit model for MS corrosion in 1 M HCl in presence or absence of DEFE and DELE.

Table 6.2 Nyquist parameters for MS corrosion in 1 M HCl with and without several concentrations of DEFE and DELE.

Inhibitor	Conc. (mg L^{-1})	R_s (Ω cm^2)	R_{ct} (Ω cm^2)	CPE parameters		C_{dl} (µF cm^{-2})	Goodness of fit	μ_{Rct} (%)
				n	Y_0 (µMho cm^{-2})		(χ^2) ×10^{-3}	
Blank	0	0.84 ± 0.001	25.89 ± 0.14	0.81 ± 0.001	875.67 ± 6.29	348.06 ± 0.46	1.12	_
DEFE	50	0.98 ± 0.001	117.01 ± 0.62	0.83 ± 0.002	240.67 ± 1.41	120.38 ± 0.22	1.76	77.87 ± 0.15
	100	0.92 ± 0.002	140.44 ± 0.50	0.84 ± 0.001	177.41 ± 0.80	88.12 ± 0.41	1.24	81.56 ± 0.34
	150	0.84 ± 0.001	163.16 ± 0.82	0.85 ± 0.001	156.41 ± 0.86	84.29 ± 0.19	2.59	84.13 ± 0.11
	200	0.90 ± 0.001	189.90 ± 0.75	0.86 ± 0.001	128.55 ± 0.62	68.07 ± 0.32	2.31	86.37 ± 0.25
Blank	0	0.84 ± 0.001	25.89 ± 0.14	0.81 ± 0.001	875.67 ± 6.29	348.06 ± 0.46	1.12	_
DELE	50	0.92 ± 0.001	150.53 ± 0.48	0.84 ± 0.001	186.94 ± 0.92	95.66 ± 0.36	1.57	82.80 ± 0.21
	100	0.92 ± 0.001	175.76 ± 1.06	0.84 ± 0.002	160.31 ± 0.83	86.23 ± 0.15	2.98	85.27 ± 0.31
	150	0.92 ± 0.002	186.54 ± 0.76	0.86 ± 0.001	146.21 ± 0.73	82.18 ± 0.33	3.02	86.12 ± 0.22
	200	0.97 ± 0.002	202.64 ± 0.65	0.89 ± 0.001	117.10 ± 0.55	75.78 ± 0.48	1.52	87.22 ± 0.42

6.3 Effect of the temperature

In this study, the effect of the temperature was studied using the optimum concentration of inhibitors at different temperatures (313 and 323 K). Before starting the electrochemical test, MS electrodes were dipped in an acidic solution to measure OCP values for a period of 1 h. The obtained OCP graphs for 303, 313, and 323 K are shown in Figs. 6.10 a, b, and c, and their steady-state values are listed in Table 6.3.

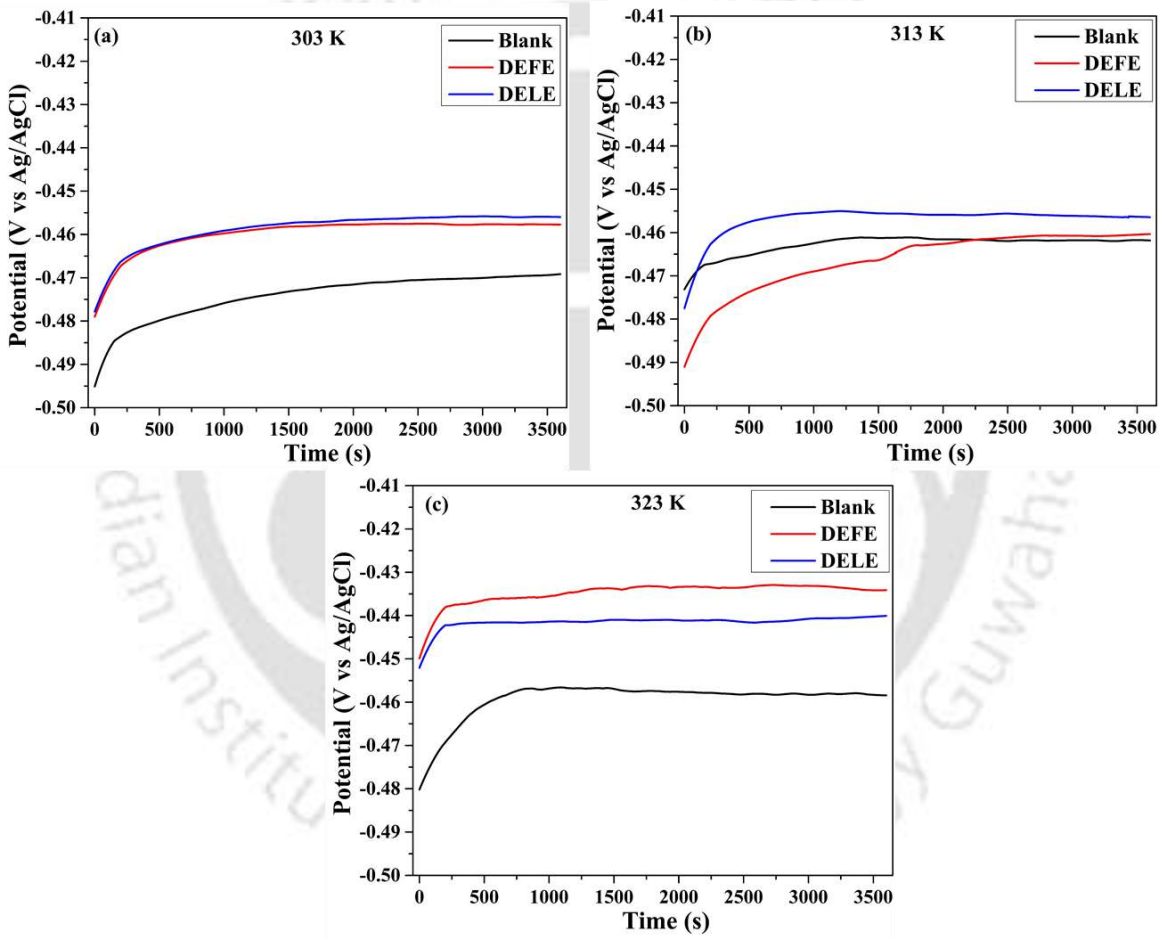

Fig. 6.10 OCP graphs for MS immersed in 1 M HCl at (a) 303, (b) 313, and (c) 323 K, in the presence and absence of DEFE and DELE.

Tafel plots for the dissolution of MS with and without *Duranta erecta s* extracts at 303 K, 313 K, and 323 K are shown in Figs. 6.11 (b), 6.11 (d), and 6.11 (f). Tafel parameters are assembled in Table 6.3, which illustrates that corrosion current density rises with increasing temperature, which signifies that temperature rise accelerates the dissolution of MS.

Nyquist patterns of MS degradation in corrosive solution with and without *Duranta erecta* extracts are represented by Figs. 6.11 (a), 6.11 (c), and 6.11 (e). These Nyquist patterns exhibited a depressed semicircle, signifying the heterogeneity of the metallic surface. At higher frequencies, a single capacitive loop appeared in each semicircle. It depicts the transfer of corrosive ions through the capacitance double layer. A small inductive loop was found in blank systems at low frequency, demonstrating the relaxation of species, such as H^{+}_{ads}, and Cl^{-}_{ads}, which confirms the formation of unstable corrosion products on MS. This inductive loop completely disappeared in inhibited systems, but a single capacitive loop remained there. These Nyquist plots were fitted to the Randle circuit by Nova 1.1.0, for evaluating the Nyquist parameters, and all obtained Nyquist parameters are tabulated in Table 6.4. The values of R_{ct} and μ_P (%) were declined with temperature, which means a rise in temperature promotes metal corrosion. Still, DEFE and DELE exhibited the strong inhibitory effect with inhibition efficiency of 77.79 and 78.96 %, respectively, at 323 K.

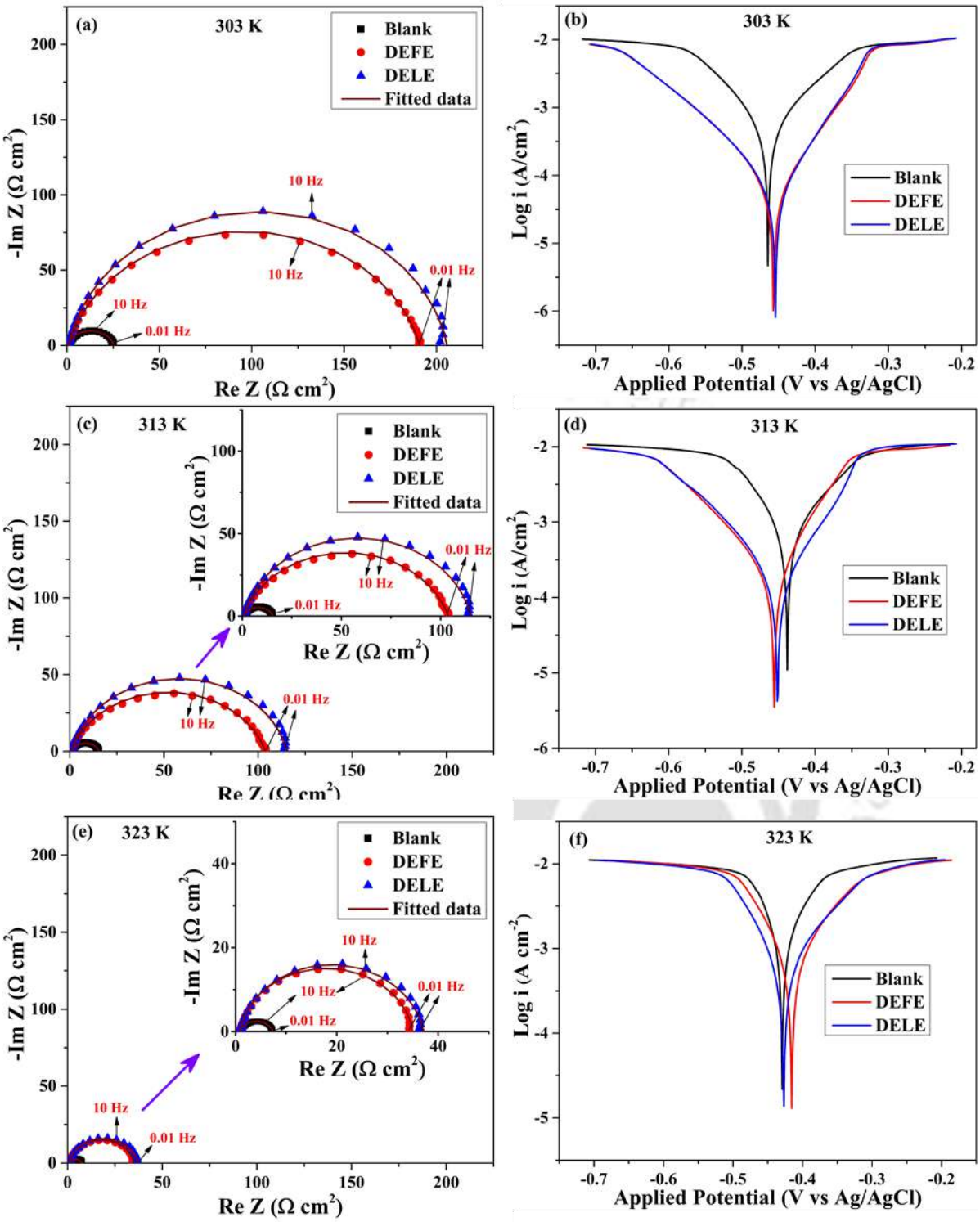

Fig. 6.11 Nyquist plots (a, c, e) and Tafel plots (b, d, f) for blank, DEFE, and DELE at 303, 313, and 323 K.

Table 6.3 Tafel parameters for MS degradation in 1 M HCl with and without several concentrations of DEFE and DELE at 303, 313, and 323 K.

Temperature (K)	Inhibitor	Conc. (mg L^{-1})	b_a (mV dec^{-1})	$-b_c$ (mV dec^{-1})	*OCP* (mV vs. Ag/AgCl)	E_{corr} (mV vs. Ag/AgCl)	i_{corr} (µA cm^{-2})	R_p (Ω cm^2)	*CR* (mm $Year^{-1}$)	μ_P (%)
303	Blank	0	110.59 ± 0.52	120.25 ± 1.04	-468.15 ± 5.68	-465.25 ± 5.56	734.98 ± 5.23	34.04 ± 0.12	8.54 ± 0.45	–
	DEFE	200	81.21 ± 0.39	79.28 ± 1.55	-457.76 ± 2.82	-457.48 ± 2.62	67.49 ± 0.90	258.14 ± 0.53	0.78 ± 0.02	90.82 ± 0.16
	DELE	200	78.49 ± 0.62	67.27 ± 0.53	-455.96 ± 2.52	-454.56 ± 3.13	60.15 ± 0.63	261.53 ± 0.68	0.70 ± 0.04	91.82 ± 0.97
313	Blank	0	105.06 ± 1.08	165.79 ± 2.35	-461.76 ± 6.93	-437.85 ± 6.52	1302.48 ± 11.03	21.44 ± 0.04	15.13 ± 0.94	–
	DEFE	200	97.26 ± 2.14	62.63 ± 0.89	-460.34 ± 3.40	-456.37 ± 2.46	201.03 ± 2.32	82.30 ± 1.51	2.34 ± 0.10	84.57 ± 0.31
	DELE	200	82.83 ± 1.53	80.05 ± 2.18	-456.45 ± 2.21	-451.36 ± 3.88	175.72 ± 1.68	100.61 ± 0.25	2.04 ± 0.05	86.51 ± 0.53
323	Blank	0	146.54 ± 1.38	285.84 ± 1.51	-458.16 ± 5.43	-429.41 ± 6.35	4429.22 ± 36.40	9.50 ± 0.01	51.45 ± 2.96	–
	DEFE	200	84.44 ± 0.40	115.07 ± 1.62	-434.33 ± 2.96	-415.32 ± 4.01	937.14 ± 4.69	22.57 ± 0.05	10.89 ± 0.65	78.84 ± 0.51
	DELE	200	88.05 ± 0.32	130.63 ± 1.85	-440.07 ± 4.31	-426.31 ± 3.53	850.19 ± 6.59	26.87 ± 0.13	9.88 ± 0.68	80.80 ± 0.18

Table 6.4 EIS parameters for the exposure of MS to 1 M HCl with and without several concentrations of DEFE and DELE at temperatures of 303, 313, and 323 K.

Temperature (K)	Inhibitor	Conc. (mg L^{-1})	R_s (Ω cm^2)	R_{ct} (Ω cm^2)	*CPE* parameters		C_{dl} (μF cm^{-2})	Goodness of fit (χ^2) $\times 10^{-3}$	μ_{Rct} (%)
					n	Y_0 (μMho cm^{-2})			
303	Blank	0	0.84 ± 0.001	25.89 ± 0.14	0.81 ± 0.001	875.67 ± 6.29	348.06 ± 0.46	1.12	–
	DEFE	200	0.90 ± 0.001	189.90 ± 0.75	0.86 ± 0.001	128.55 ± 0.62	68.07 ± 0.32	2.31	86.37 ± 0.25
	DELE	200	0.97 ± 0.002	202.64 ± 0.65	0.89 ± 0.001	117.10 ± 0.55	75.78 ± 0.48	1.52	87.22 ± 0.42
313	Blank	0	0.85 ± 0.002	16.51 ± 0.07	0.77 ± 0.001	1492.67 ± 16.43	446.72 ± 1.74	1.68	–
	DEFE	200	0.73 ± 0.001	103.08 ± 0.59	0.82 ± 0.001	222.09 ± 2.21	104.03 ± 0.43	3.12	84.12 ± 0.17
	DELE	200	0.94 ± 0.001	113.22 ± 0.28	0.87 ± 0.002	181.23 ± 1.07	100.02 ± 0.29	2.59	85.54 ± 0.30
323	Blank	0	0.88 ± 0.003	7.67 ± 0.04	0.71 ± 0.002	3744.06 ± 28.06	865.87 ± 2.57	2.23	–
	DEFE	200	0.83 ± 0.002	34.40 ± 0.18	0.89 ± 0.001	1987.66 ± 14.68	850.33 ± 1.95	2.86	77.79 ± 0.82
	DELE	200	0.81 ± 0.001	36.31 ± 0.26	0.89 ± 0.001	1504.19 ± 11.29	808.37 ± 2.31	1.37	78.96 ± 0.14

6.3.1 Effect of activation energy

To understand the kinetics of the corrosion inhibition process in the presence of *Duranta erecta* extracts (DEFE and DELE), PDP data (i_{corr} of 303, 313, and 323 K) was utilized to evaluate several thermodynamic parameters, such as activation energy, enthalpy, and entropy of the corrosion process. The values of ln (i_{corr}) (µA cm^{-2}) were plotted with 1/T (K^{-1}) to evaluate E_a of MS corrosion in inhibited or uninhibited systems (Fig. 6.12 (a)). This figure shows a straight line for uninhibited or inhibited MS corrosion with DEFE and DELE, where slope and intercept correspond to $-E_a/R$ and ln A, respectively. The obtained values of E_a are shown in Table 6.5.

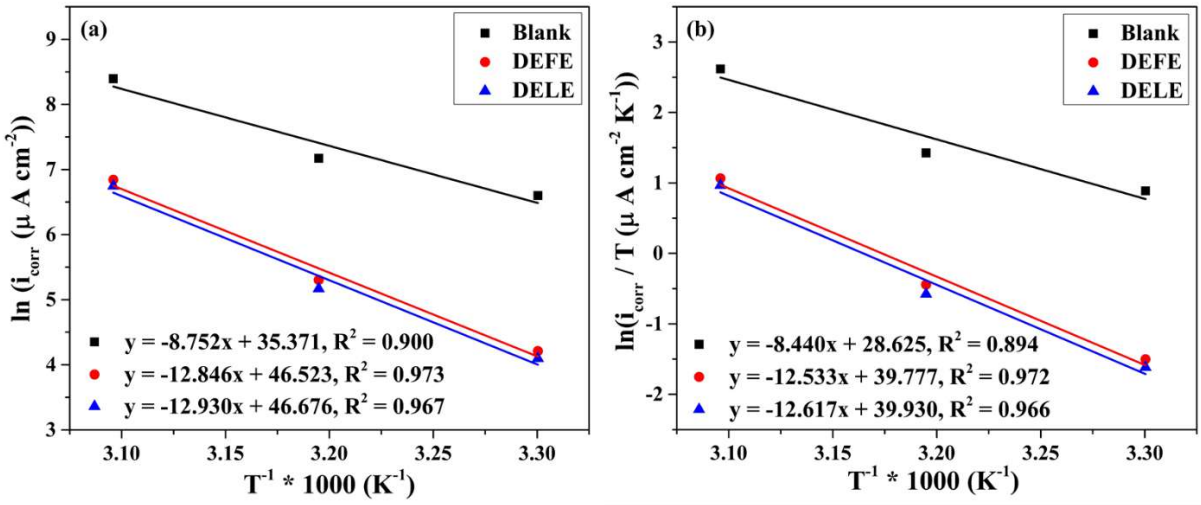

Fig. 6.12 Arrhenius plots (a) and Transition state plots (b) for MS corrosion with and without optimum concentrations of DEFE and DELE.

The kinetic-thermodynamic model was employed to further elucidate the inhibitor's interaction with the MS surface. In this model, to determine the enthalpy and entropy of the degradation phenomenon, values of ln (i_{corr}/T) (µA cm^{-2} K^{-1}) were plotted against 1/T (K^{-1}) (Fig. 6.12 (b)). This figure contained three straight lines for uninhibited or inhibited MS corrosion with DEFE and DELE. The slope and intercept of these lines correspond to the (-ΔH

/R) and ($\ln\frac{k_B}{h} + \frac{\Delta S}{R}$), respectively. The obtained entropy and enthalpy are tabulated in Table 6.5.

It was noticed that inhibited systems exhibited higher E_a than blank systems, which means that corrosion of the metal is more difficult in the presence of both *Duranta erecta* extracts. Few studies reported that inhibitors follow the physical adsorption to adsorb on metal if two events occur: a decrease in inhibition efficiency with temperature elevation along with the rise in activation energy of the inhibited system compared to the blank. On the other hand, it will adsorb by chemisorption if the values of inhibition efficiency are increased by lowering the temperature with a decrease in activation energy for the inhibited system compared to that of the blank (Aslam et al., 2022). Herein, inhibitory efficiencies of both extracts declined with temperature elevation, with the rise in activation energies for DEFE and DELE as compared to blank, which illustrates the physical adsorption of *Duranta erecta* extracts on the MS surface. Positive enthalpy values were obtained for MS corrosion in HCl solution with extracts, depicting that MS dissolution is an endothermic process, and these values were increased for inhibitor-containing systems relative to the blank, which means the addition of the inhibitor leads to the formation of a strong protective layer. The difference between activation energy and enthalpy change is equal to the product of R and T in each system, which signifies that MS corrosion follows the unimolecular-type process. Furthermore, the values of ΔS for metal corrosion exhibited a positive shift for *Duranta erecta* extracts; this positive shift of ΔS is linked to the formation of the activated complex in the rate-determining step of the metal dissolution process.

The values of ΔS increased as reactants converted to activated complexes, which replaced the pre-adsorbed water molecule from the surface of metallic bodies. Therefore, *Duranta erecta* extract's molecules interacted with MS and formed a compact film, which is encouraged by their electrostatic interaction of inhibitor with MS. If the values of ΔS are

reduced in inhibitor-containing systems than that of the blank, inhibitor molecules recommend their association rather than dissociation in the rate-determining step (Jeeja et al., 2022).

Table 6.5 Kinetic parameters of MS degradation in 1 M HCl with and without optimum concentration of DEFE and DELE.

Inhibitor	Conc. (mgL^{-1})	Pre-exponential factor, A ($\mu A\ cm^{-2}$)	E_a ($KJ\ mol^{-1}$)	ΔH ($KJ\ mol^{-1}$)	ΔS ($J\ mol^{-1}\ K^{-1}$)	$(E_a - \Delta H)$ ($KJ\ mol^{-1}$)
Blank	0	$(2.30 \pm 0.21) \times 10^{15}$	72.76 ± 0.25	70.17 ± 0.27	40.45 ± 0.78	2.59
DEFE	200	$(1.60 \pm 0.08) \times 10^{20}$	106.80 ± 1.10	104.20 ± 0.93	133.16 ± 0.86	2.60
DELE	200	$(1.87 \pm 0.11) \times 10^{20}$	107.50 ± 0.94	104.90 ± 1.02	134.44 ± 0.81	2.60

6.4 Adsorption studies

The adsorption isotherm analysis is a valuable tool for studying the interactions between inhibitor molecules and the metal surface. This analysis was conducted by utilizing surface coverage (θ) data obtained from the PDP test, to check the suitability of various adsorption isotherms, for instance, Langmuir (Figs 6.13 (a and b), Temkin (Figs 6.13 (c and d), Frumkin (Figs 6.13 (e and f)). Based on these plots, the data exhibited the best fit to the Langmuir isotherm due to its high R^2 value with the slope near to 1 for both *Duranta erecta* extracts (DEFE and DELE), which indicates that the corrosion inhibitors formed a monolayer on the MS surface (Pal and Das, 2022a). Data from Langmuir plots were used to evaluate the equilibrium adsorption constant (K_{ads}) values, which were obtained as 100.00 and 142.86 L g^{-1} for DEFE and DELE, respectively.

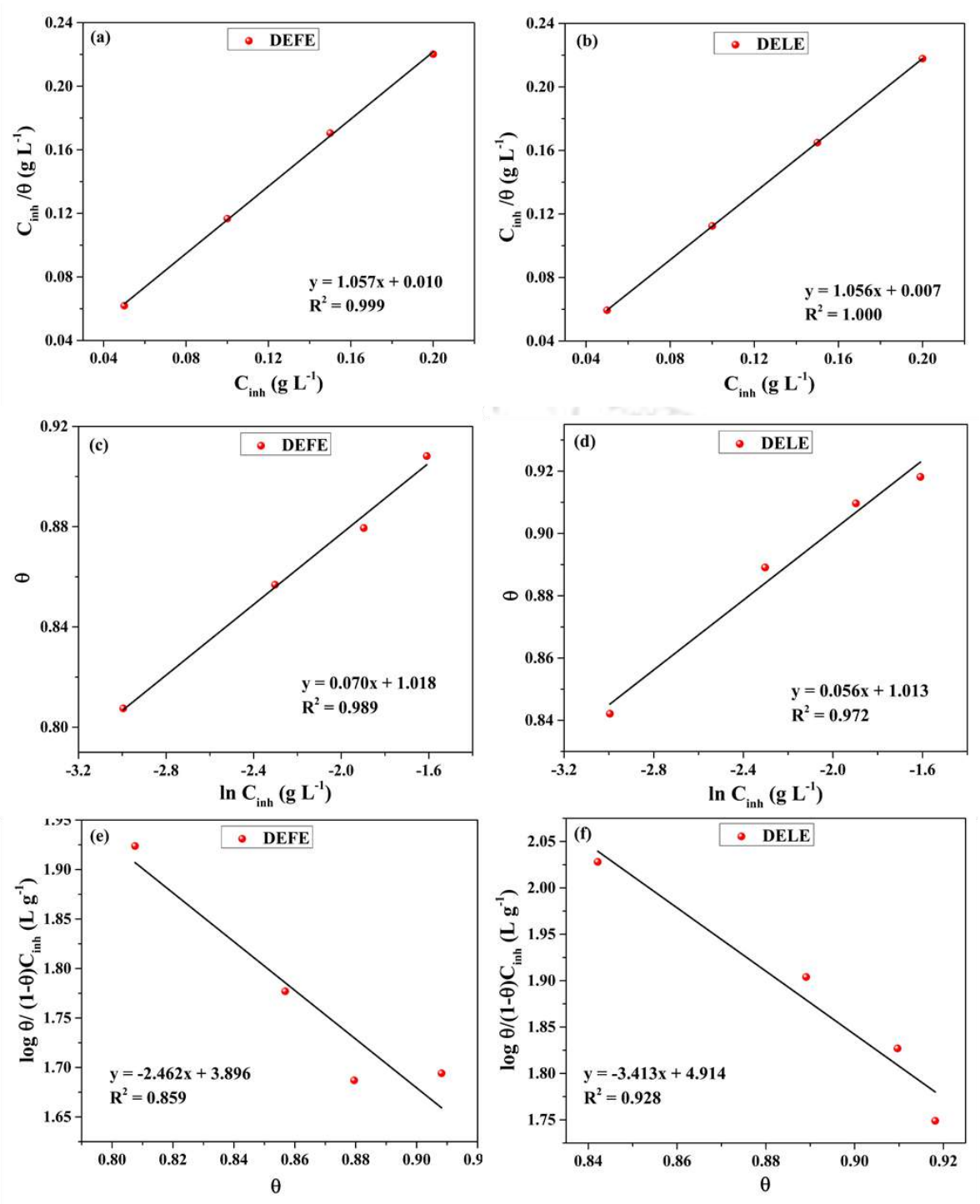

Fig. 6.13 (a, b) Langmuir, (c,d) Temkin, and (e,f) Frumkin isotherms of DEFE and DELE, respectively.

Thereafter, these values were used to calculate the Standard Gibbs free energy (ΔG^{o}_{ads}) of inhibited systems of DEFE and DELE, which were estimated using Eq. (6.1).

$$\Delta G^{o}_{ads} = -RTln(C_{water}\, K_{ads}) \quad (6.1)$$

where K_{ads} represents the equilibrium adsorption constant (L g^{-1}), C_{water} is H_2O concentration in the mixture (1000 g L^{-1}) (Kaya et al., 2023). Several studies have reported that the interaction of extract molecule with metal occurs by physisorption process, chemisorption, or mixed type process only if the values of standard Gibbs free energy lie in the following ranges $\Delta G^{o}_{ads} \geq$ -20 kJ mol^{-1}, $\Delta G^{o}_{ads} \leq$ -40 kJ mol^{-1}, and -40 kJ $mol^{-1} \leq \Delta G^{o}_{ads} \leq$ -20 kJ mol^{-1}, respectively (Kartal et al., 2025). In this work, the obtained ΔG^{o}_{ads} values lie in the range of -40 to -20 kJ mol^{-1}, but closer to -20 kJ $mol^{-1,}$ signifying that both *Duranta erecta* extracts favored physical adsorption (mix-type adsorption). Moreover, the negative sign depicts that DEFE and DELE tend to self-adsorb on metal from 1 M HCl solution.

Table 6.6 Adsorption isotherm parameters.

Inhibitor	$\frac{1}{K_{ads}}$ (g L^{-1})	K_{ads} (L g^{-1})	ΔG^{o}_{ads} (KJ mol^{-1})
DEFE	0.010	100.00 ± 2.92	-29.00 ± 0.061
DELE	0.007	142.86 ± 4.52	-29.90 ± 0.036

6.5 Surface analysis

6.5.1 FESEM

The FESEM analysis was performed to learn about the corrosion-inhibiting process of inhibitors on the MS surface. Fig. 6.14 portrays the FESEM picture of the MS before and after 2 h immersion in HCl solution with and without *Duranta erecta* extracts (200 mg L^{-1}). FESEM pictures of MS before and after dipping in acidic solution are depicted in Figs. 6.14 (a) and (b), respectively. These images illustrate that the MS surface was severely damaged and cracked due to free acidic attack. Figs. 6.14 (c) and (d) show the FESEM picture of inhibited MS with

DEFE and DELE, respectively, after its 2 h exposure to the acid solution. These FESEM pictures show that a strongly corroded MS surface was visible for the blank sample. However, a nearly smooth surface was seen for MS-inhibited corrosion, and a smoother surface was found for DELE, implying that DELE exhibited a stronger inhibiting effect than DEFE (Pal and Das, 2022c). Extract molecules adsorbed on the MS to form a strong inhibiting film that hinders the transfer of corrosive species from the electrolyte to the MS surface. These findings are in good agreement with electrochemical studies.

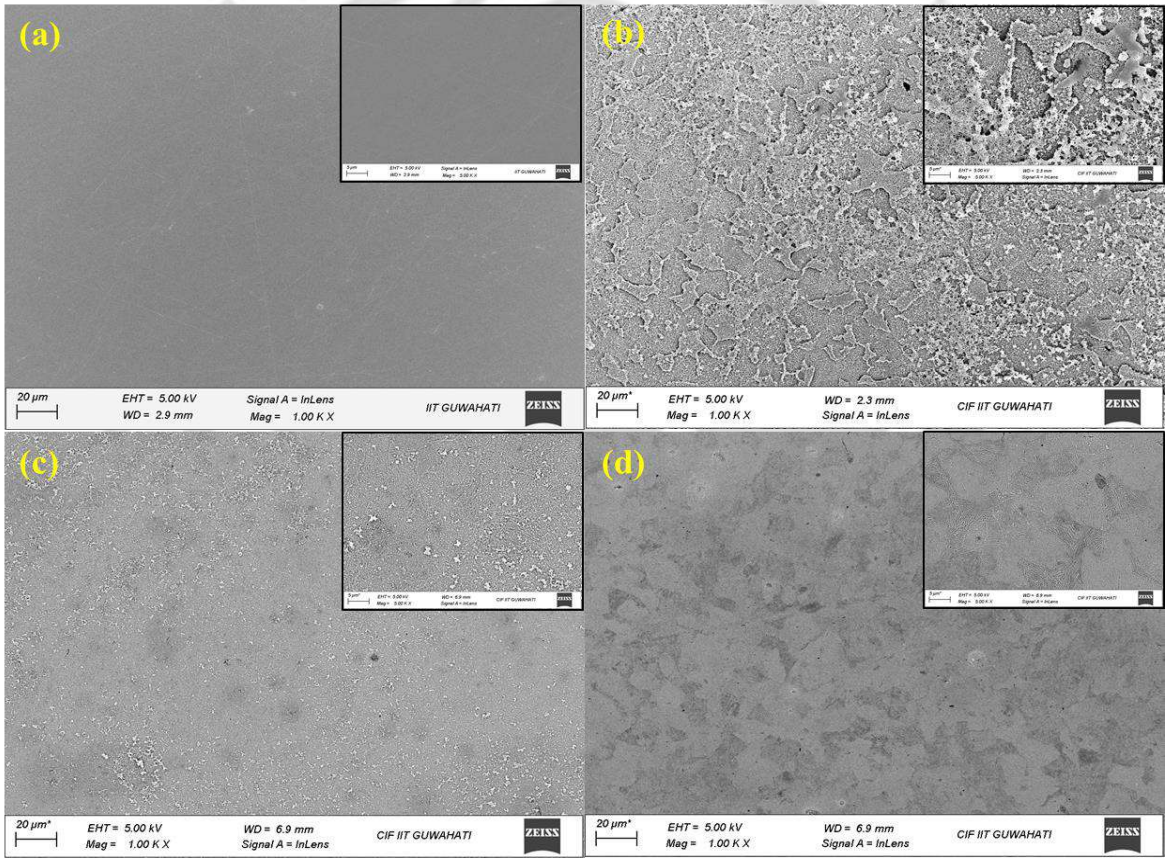

Fig. 6.14 FESEM pictures of a) polished MS, b) uninhibited MS after acid immersion, c) and d) inhibited MS corrosion in 1 M HCl with DEFE and DELE, respectively.

6.5.2 EDX

Fig. 6.15 shows the EDX spectra of the MS coupons, which provide information about the existing elements on the surface of MS. This information gives valuable insights about the inhibitory nature of plant extracts for metal protection in corrosive solution. EDX spectra of MS corrosion without extracts and a pit from uninhibited MS after their 4 h acid immersion are demonstrated in Figs. 6.15 (a) and (b), respectively. From these plots, it was observed that the wt% of Cl was higher inside the pit, indicating that corrosion occurred rapidly in pits compared to the plan surface. Figs. 6.15 (c) and (d) represent the EDX spectra of inhibited MS with DEFE and DELE, respectively. On observing all these spectra, it was found that the wt% of Cl and Fe was decreased and increased, respectively, in the presence of inhibitors. It implies that extract molecules are adsorbed on the MS and create a strong inhibiting film, which affects the transfer of corrosive species from the bulk of the electrolyte to the metallic surface.

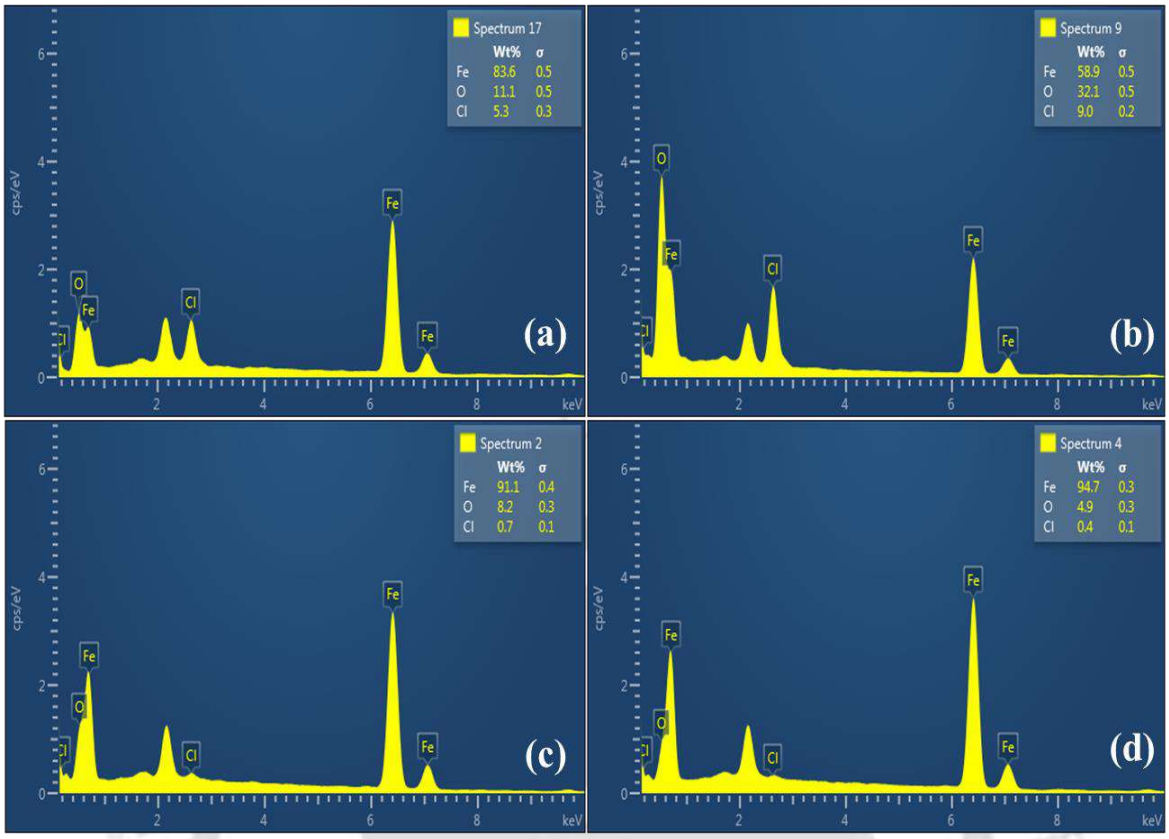

Fig. 6.15 EDX spectra for a) uninhibited MS, b) selected pits from the uninhibited spectrum, c) and d) inhibited with DEFE and DELE, respectively.

6.5.3 AFM

The atomic force microscope is a highly effective tool for analyzing metal microstructure. During the analysis, surface roughness was computed on area scales of 5.0 µm × 5.0 µm after 3 h immersion of MS coupons. Fig. 6.16 shows three-dimensional AFM images of the MS surface after 3 h immersion in the acidic medium with and without *Duranta erecta* extracts (DEFE and DELE) at an optimum dosage of 200 mg L^{-1}. Gwyddion software was used to estimate the roughness of metallic surfaces. The average roughness of MS after immersion in 1.0 M HCl is 420.90 nm, which was decreased to 32.62 nm and 26.77 nm due to adding an

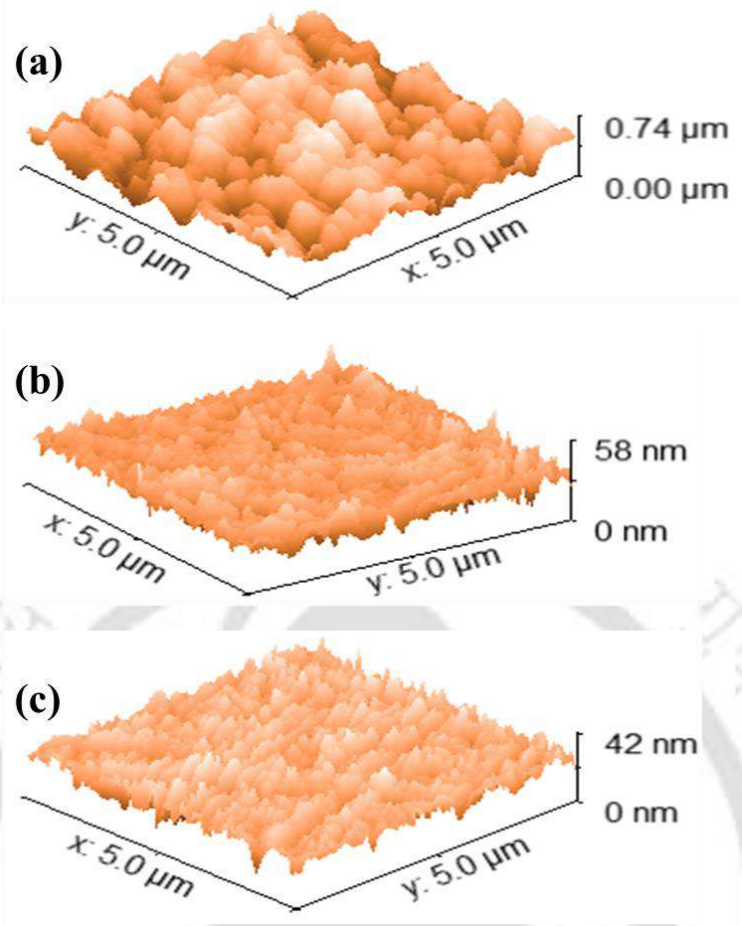

Fig. 6.16 AFM images of a) uninhibited MS, b) and c) MS with DEFE and DELE, respectively, after their 3 h immersion in 1 M HCl.

optimum amount of DEFE and DELE, respectively. MS surface suffers from very little damage in the presence of *Duranta erecta* extracts, confirming the creation of a strong corrosion-inhibiting film over MS, which separates the metal from the electrolyte. These findings are well concurred with the outcomes of FESEM and EDX analyses.

6.6 Corrosion inhibiting mechanism

The mechanism for MS degradation in 1 M HCl is proposed as follows:

Anodic MS dissolution is proposed by the following reactions (Eqs. 6.2-6.5):

$$Fe + Cl^- \leftrightarrow (FeCl^-)_{ads} \quad (6.2)$$

$$(FeCl^-)_{ads} \leftrightarrow (FeCl)_{ads} + e^- \quad (6.3)$$

$$(FeCl)_{ads} \rightarrow (FeCl^+)_{ads} + e^- \quad (6.4)$$

$$(FeCl^+)_{ads} \leftrightarrow Fe^{2+} + Cl^- \quad (6.5)$$

Cathodic hydrogen evolution is represented by the following reactions (Eqs. 6.6-6.8):

$$Fe + H^+ \leftrightarrow (FeH^+)_{ads} \quad (6.6)$$

$$(FeH^+)_{ads} + e^- \rightarrow (FeH)_{ads} \quad (6.7)$$

$$(FeH^+)_{ads} + H^+ + 2e^- \rightarrow Fe + H_2 \quad (6.8)$$

The corrosion-inhibiting effect of *Duranta erecta* extracts in 1 M HCl depends on interactions of metal and extracts (Alao et al., 2023; Pal and Das, 2020). Electrostatic interactions occurred between the extract's molecules and preabsorbed Cl^- ions on the MS. This type of interaction encourages the physical adsorption of protonated inhibitors. Over the MS surface, the protonated inhibitor molecule competes with H^+ ions for electrons. Therefore, positively charged inhibitor molecules accept the electron from the metal to become neutral. The available unbound lone pairs of inhibitor molecules are responsible for its chemisorption on metallic surfaces. Therefore, electrons accumulate on the metallic surface over time. So, to get rid of this electron excess, electrons move from iron's d-orbital to the vacant π antibonding orbital of the extract's molecule (retro-donation), which enhances the adsorption of extract molecules on the metal surface (Srivastava et al., 2018).

Findings from the PDP test depict that both *Duranta erecta* extracts (DEFE and DELE) possess a mixed-type inhibiting nature, and these extracts were adsorbed over MS through mixed-type adsorption, which was validated by adsorption isotherms investigations. Moreover, surface analysis reveals that *Duranta erecta* extracts create a corrosion-inhibiting film on the MS, which efficiently reduces metal corrosion.

6.7 Summary

Duranta erecta fruit extract (DEFE) and *Duranta erecta* leaves extract (DELE) were prepared and employed separately in MS corrosion in 1 M HCl for the protection of MS. The corrosion-inhibiting behavior of both *Duranta erecta* extracts was scrutinized by electrochemical as well as weight loss analysis, and these extracts possess excellent corrosion-inhibiting properties due to the presence of several active compounds such as, Ethanone, 1-(2-hydroxy-5-methylphenyl)-, 4,7-Dimethoxy-2-methyl-2,3-dihydro-1 H-inden-1-one, Isopropyl Myristate, 9-Octadecenamide, n-Hexadecanoic acid, and 7,10,13-Eicosatrienoic acid, methyl ester, which were identified by LC-MS and FTIR analyses. Based on all investigations, the following conclusions were made:

- *Duranta erecta* extracts exhibited outstanding anticorrosive properties with maximum inhibition efficiencies of 90.82 % and 91.82 % at 200 mg L^{-1} of DEFE and DELE, respectively.
- E_{corr} value was slightly varied (< ± 85 mV) for extracts containing systems relative to blank, which signifies the mix-type behavior of *Duranta erecta* extracts.
- The value of R_{ct} shows a huge jump from 25.89 Ω cm^2 (blank system) to 189.90 Ω cm^2 (DEFE) and 202.64 Ω cm^2 (DELE) at 200 mg L^{-1} of *Duranta erecta* extracts, which implies that corrosive species faced higher resistance to reach the metallic surface.
- Weight loss observation also represents similar corrosion-inhibiting behavior of *Duranta erecta* extracts (DEFE and DELE) as obtained in electrochemical studies.
- DEFE and DELE exhibited strong inhibitory effects with 78.84 and 80.80% inhibitory efficiencies at 323 K. Ea, ΔH, and ΔS values displayed a positive shift compared to the blank.

- Obtained ΔG^{o}_{ads} values were -29.00 kJ mol^{-1} and -29.90 kJ mol^{-1} for inhibited MS corrosion with DEFE and DELE, respectively, confirming that they favored physical adsorption (mix-type adsorption) over the MS surface.
- Surface analyses confirmed that *Duranta erecta* extracts formed a corrosion-inhibiting film on MS surface, which effectively reduced MS degradation.

6.8 References

Agomuo, E., Amadi, P., Ogunka-Nnoka, C., Amadi, B., Ifeanacho, M., Njoku, U., 2017. Characterization of oils from Duranta repens leaf and seed. OCL 24, A601. https://doi.org/10.1051/ocl/2017048

Al-Amiery, A., Isahak, W.N.R.W., Al-Azzawi, W.K., 2023. ODHI: A promising isatin-based corrosion inhibitor for mild steel in hydrochloric acid. J. Mol. Struct. 1288, 135829. https://doi.org/10.1016/j.molstruc.2023.135829

Al-Amiery, A.A., Al-Azzawi, W.K., Isahak, W.N.R.W., 2022. Isatin schiff base is an effective corrosion inhibitor for mild steel in hydrochloric acid solution: gravimetrical, electrochemical, and computational investigation. Sci. Rep. 12, 17773. https://doi.org/10.1038/s41598-022-22611-4

Alao, A.O., Popoola, A.P., Dada, M.O., Sanni, O., 2023. Utilization of green inhibitors as a sustainable corrosion control method for steel in petrochemical industries: A review. Front. Energy Res. 10, 1–21. https://doi.org/10.3389/fenrg.2022.1063315

Ali Asaad, M., Sarbini, N.N., Sulaiman, A., Ismail, M., Huseien, G.F., Abdul Majid, Z., Bothi Raja, P., 2018. Improved corrosion resistance of mild steel against acid activation: Impact of novel Elaeis guineensis and silver nanoparticles. J. Ind. Eng. Chem. 63, 139–148. https://doi.org/10.1016/j.jiec.2018.02.010

Aslam, R., Mobin, M., Shoeb, M., Aslam, J., 2022. Novel ZrO_2-glycine nanocomposite as eco-friendly high temperature corrosion inhibitor for mild steel in hydrochloric acid solution. Sci. Rep. 12, 9274. https://doi.org/10.1038/s41598-022-13359-y

Betti, N., Al-Amiery, A.A., Al-Azzawi, W.K., Isahak, W.N.R.W., 2023. Corrosion inhibition properties of schiff base derivative against mild steel in HCl environment complemented with DFT investigations. Sci. Rep. 13, 8979. https://doi.org/10.1038/s41598-023-36064-w

Bhan, C., Kumar Golder, A., 2023. Bio-based hierarchical vertically aligned 2D ZnO nanostructures for ultra selective electrochemical sensing of p-Chloroaniline. Chem. Eng. J. 475, 146122. https://doi.org/10.1016/j.cej.2023.146122

Canales, C., Galarce, C., Rubio, F., Pineda, F., Anguita, J., Barros, R., Parragué, M., Daille, L.K., Aguirre, J., Armijo, F., Pizarro, G.E., Walczak, M., De la Iglesia, R., Navarrete, S.A., Vargas, I.T., 2021. Testing the Test: A comparative study of marine microbial corrosion under laboratory and field conditions. ACS Omega 6, 13496–13507. https://doi.org/10.1021/acsomega.1c01762

Dhongde, N.R., Das, N.K., Hazarika, J., Park, J.-G., Banerjee, T., Rajaraman, P.V., 2025. Azoles as corrosion inhibitors in alkaline medium for ruthenium chemical mechanical planarization applications:Electrochemical and theoretical analysis. J. Mol. Struct. 1320, 139651. https://doi.org/10.1016/j.molstruc.2024.139651

Donkor, S., Larbie, C., Gustav Komlaga, G., Emikpe, B.O., 2022. Safety evaluation of hydroethanolic fruit extracts of Duranta erecta Linn. GSC Biol. Pharm. Sci. 18, 154–167. https://doi.org/10.30574/gscbps.2022.18.2.0067

Faustin, M., Maciuk, A., Salvin, P., Roos, C., Lebrini, M., 2015. Corrosion inhibition of C38 steel by alkaloids extract of Geissospermum laeve in 1 M hydrochloric acid: Electrochemical and phytochemical studies. Corros. Sci. 92, 287–300. https://doi.org/10.1016/j.corsci.2014.12.005

Golder, A.K., Chauhan, S., Ravi, R., 2021. Synthesis of low-cost bentonite/Duranta erecta's fruit powder imbedded alginate beads and its application in surfactant removal. Environ. Sci. Pollut. Res. 28, 58945–58957. https://doi.org/10.1007/s11356-021-14306-6

Goswami, R.N., Saini, R., Mehta, S., Verma, G., Ray, A., Khatri, O.P., 2024. $Ti_3C_2T_x$ M Xene-Polyaniline nanocomposites for redesigning epoxy coatings to improve anticorrosive performance. ACS Appl. Eng. Mater. 2, 1396–1410. https://doi.org/10.1021/acsaenm.4c00167

Haldhar, R., Prasad, D., Kamboj, D., Kaya, S., Dagdag, O., Guo, L., 2021. Corrosion inhibition, surface adsorption and computational studies of Momordica charantia extract: A sustainable and green approach. SN Appl. Sci. 3, 25. https://doi.org/10.1007/s42452-020-04079-x

Ishnava, K.B., Patel, K.S., 2020. In vitro study of Praecitrulus fistulosus (Stocks) Pangalo (Cucurbitaceae) fruit – A potential candidate of anthelmintic activity. Bull. Natl. Res. Cent. 44, 130. https://doi.org/10.1186/s42269-020-00365-1

Kartal, A., Yıldız, R., Döner, A., Baran, M.F., 2025. Thorough examination of Polygonum aviculare L. plant leaf extract as a green corrosion inhibitor for mild steel in 1 M HCl: Synthesis, characterization, observations from surface analysis, experimental and DFT studies. Inorg. Chem. Commun. 176, 114241. https://doi.org/10.1016/j.inoche.2025.114241

Kaya, F., Solmaz, R., Halil Geçibesler, İ., 2023. The use of methanol extract of Rheum Ribes (Işgın) flower as a natural and promising corrosion inhibitor for mild steel protection in 1 M HCl solution. J. Ind. Eng. Chem. 122, 102–117. https://doi.org/10.1016/j.jiec.2023.02.013

Kumar, A., Das, C., 2024. Corrosion inhibition of mild steel by Praecitrullus fistulosus (tinda fruit and peel) extracts. Sci. Total Environ. 929, 172569. https://doi.org/10.1016/j.scitotenv.2024.172569

Mittal, P., Goswami, M., Airi, M., 2020. Phytochemical , FTIR and NMR analysis of crude extract of duranta plumieri leaves. J. Pharm. Sci. Res. 12, 182–185.

Naik, M., Lee, Y.-S., Qurashi, A., 2018. Chemically grafted aminated carbon nanotubes and L-Lysine in ultramodified conditions for carbon dioxide storage. ACS Omega 3, 10442–10448. https://doi.org/10.1021/acsomega.8b00597

Pal, A., Das, C., 2023. Novel use of kitchen waste: protection of boiler quality steel from corrosion in acidic media using onion waste. Chem. Pap. 77, 1107–1127. https://doi.org/10.1007/s11696-022-02549-7

Pal, A., Das, C., 2022a. Investigations on corrosion inhibition in acidic media for BQ steel using banana flower bract, an eco-friendly novel agro-waste: Experimental and theoretical considerations. Inorg. Chem. Commun. 145, 110024. https://doi.org/10.1016/j.inoche.2022.110024

Pal, A., Das, C., 2022b. New eco-friendly anti-corrosion inhibitor of purple rice bran extract for boiler quality steel: Experimental and theoretical investigations. J. Mol. Struct. 1251, 131988. https://doi.org/10.1016/j.molstruc.2021.131988

Pal, A., Das, C., 2022c. New eco-friendly anti-corrosion inhibitor of purple rice bran extract for boiler quality steel: Experimental and theoretical investigations. J. Mol. Struct. 1251, 131988. https://doi.org/10.1016/j.molstruc.2021.131988

Pal, A., Das, C., 2020. A novel use of solid waste extract from tea factory as corrosion inhibitor in acidic media on boiler quality steel. Ind. Crops Prod. 151, 112468. https://doi.org/10.1016/j.indcrop.2020.112468

Pang, M., Ma, X., Jin, S., Wu, R., Yu, Z., Zhong, T., Zou, C., 2024. Mechanical property and corrosion performance in the as-rolled Mg-8Li-4Gd-1.5Ni alloy. Appl. Mater. Today 41, 102446. https://doi.org/10.1016/j.apmt.2024.102446

Rajeswari, r., Prabhakaran, v., Saravanakumar a., 2019. Phytochemical screening, gas chromatography–mass spectrometry profiling, in vitro cytotoxicity, and anthelmintic activity of hydroalcoholic extract of duranta erecta leaves. Asian J. Pharm. Clin. Res. 13, 63–68. https://doi.org/10.22159/ajpcr.2020.v13i1.35592

Jeeja, R., A., Thomas, A., Arshad, M., Joseph, A., 2022. The influence of aqueous and alcoholic extracts of Garcinia cambogia fruit rind in the management of mild steel corrosion in hydrochloric acid: Theoretical and electroanalytical studies. J. Mol. Liq. 346, 117873. https://doi.org/10.1016/j.molliq.2021.117873

Shah, A., Akhtar, S., Mahmood, F., Urooj, S., Siddique, A.B., Irfan, M.I., Naeem-ul-Hassan, M., Sher, M., Alhoshani, A., Rauf, A., Amin, H.M.A., Abbas, A., 2024. Fagonia arabica extract-stabilized gold nanoparticles as a highly selective colorimetric nanoprobe for Cd^{2+} detection and as a potential photocatalytic and antibacterial agent. Surfaces and Interfaces 51, 104556. https://doi.org/10.1016/j.surfin.2024.104556

Srivastava, V., Chauhan, D.S., Joshi, P.G., Maruthapandian, V., Sorour, A.A., Quraishi, M.A., 2018. PEG-functionalized chitosan: a biological macromolecule as a novel corrosion inhibitor. ChemistrySelect 3, 1990–1998. https://doi.org/10.1002/slct.201701949

Tang, M., Li, X., Deng, S., Lei, R., 2021. Synergistic inhibition effect of Mikania micrantha extract with KI on steel corrosion in H_2SO_4 solution. J. Mol. Liq. 344, 117926. https://doi.org/10.1016/j.molliq.2021.117926

Chapter 7:

Anti-corrosive behavior of a novel ternary RGO-ZnO-PANI nanocomposite reinforced epoxy coating on mild steel in the marine environment

Anti-corrosive behavior of a novel ternary RGO-ZnO-PANI nanocomposite reinforced epoxy coating on mild steel in the marine environment

This chapter explores the formation of a novel RGO-ZnO-PANI nanocomposite through ultrasonication and in situ polymerization process to enhance the barrier and corrosion-inhibiting properties of epoxy coatings. The anti-corrosive performance of EP/RGO-ZnO-PANI nanocomposite coatings was assessed using potentiodynamic polarization (PDP), electrochemical impedance spectroscopy (EIS), and salt spray tests. The EP/RGO-ZnO-PANI coating exhibited outstanding corrosion resistance, achieving 99.98% inhibition efficiency after 1-day immersion in 3.5 wt% NaCl solution. Furthermore, EIS findings demonstrate that EP/RGO-ZnO-PANI nanocomposite coating exhibited higher anti-corrosive properties than that of EP, EP/RGO, EP/RGO-ZnO, and EP/RGO-ZnO-PANI up to their 45 days immersion. Similar findings were obtained in salt spray analysis. Additional analyses, including FESEM, TGA, and contact angle measurements, confirmed its enhanced morphology, thermal stability, and hydrophobicity as compared to other coatings.

Published Article: Kumar, A., Das, C., 2025. Anti-corrosive behavior of a novel ternary RGO-ZnO-PANI nanocomposite reinforced epoxy coating on mild steel in marine environment. ***Adv. Eng. Mater***. 2500949. https://doi.org/10.1002/adem.202500949.

7.1 Characterizations of prepared materials

7.1.1 FESEM and EDX analyses

Figs. 7.1 (a) and (b) show the nanosheet-like morphology of graphene oxide and reduced graphene oxide, respectively. Fig. 7.1 (c) shows the rode shape morphology of ZnO (Garg et al., 2021). FESEM images of prepared RGO/ZnO composites at various ratios of RGO:ZnO, such as 4:0.5, 4:1, and 4:2, are shown in Figs. 7.1 (d), (e), and (f), respectively, which clearly demonstrated that a more homogeneous distribution of ZnO on RGO surface was obtained at 4:1 ratio. Therefore, the RGO-ZnO composite with this optimized ratio was used in this work, and its FESEM image is shown in Fig. 7.1 (e) (Tai et al., 2016). Fig. 7.1 (g) demonstrated the FESEM images of polyaniline (PANI), which have nanofiber type morphology. Fig. 7.1 (h) displays the FESEM pictures of RGO-ZnO-PANI nanocomposite. In this picture, RGO-ZnO composites are wrapped with PANI nanofiber, and this image also shows the distribution of RGO-ZnO nanocomposites in PANI. Furthermore, EDX analysis was conducted to characterize the RGO-ZnO and RGO-ZnO-PANI nanocomposites. Figs. 7.2 (a) and (c) present the EDX spectra of RGO-ZnO and RGO-ZnO-PANI, respectively. These spectra display several characteristic peaks corresponding to C, O, and Zn in RGO-ZnO and to C, O, Zn, and N in RGO-ZnO-PANI, confirming the successful formation of the respective composites. Additionally, Figs. 7.2 (b) and (d) show the elemental mapping images of RGO-ZnO and RGO-ZnO-PANI, respectively. The mapping in Fig. 7.2 (b) reveals a uniform distribution of C, O, and Zn elements, indicating a homogeneous dispersion of ZnO on the RGO surface. Similarly, Fig. 7.2 (d) shows an even distribution of C, O, Zn, and N in the RGO-ZnO-PANI composite, which confirms the formation of the RGO-ZnO-PANI composite. These results are consistent with the morphological observations of FESEM analysis.

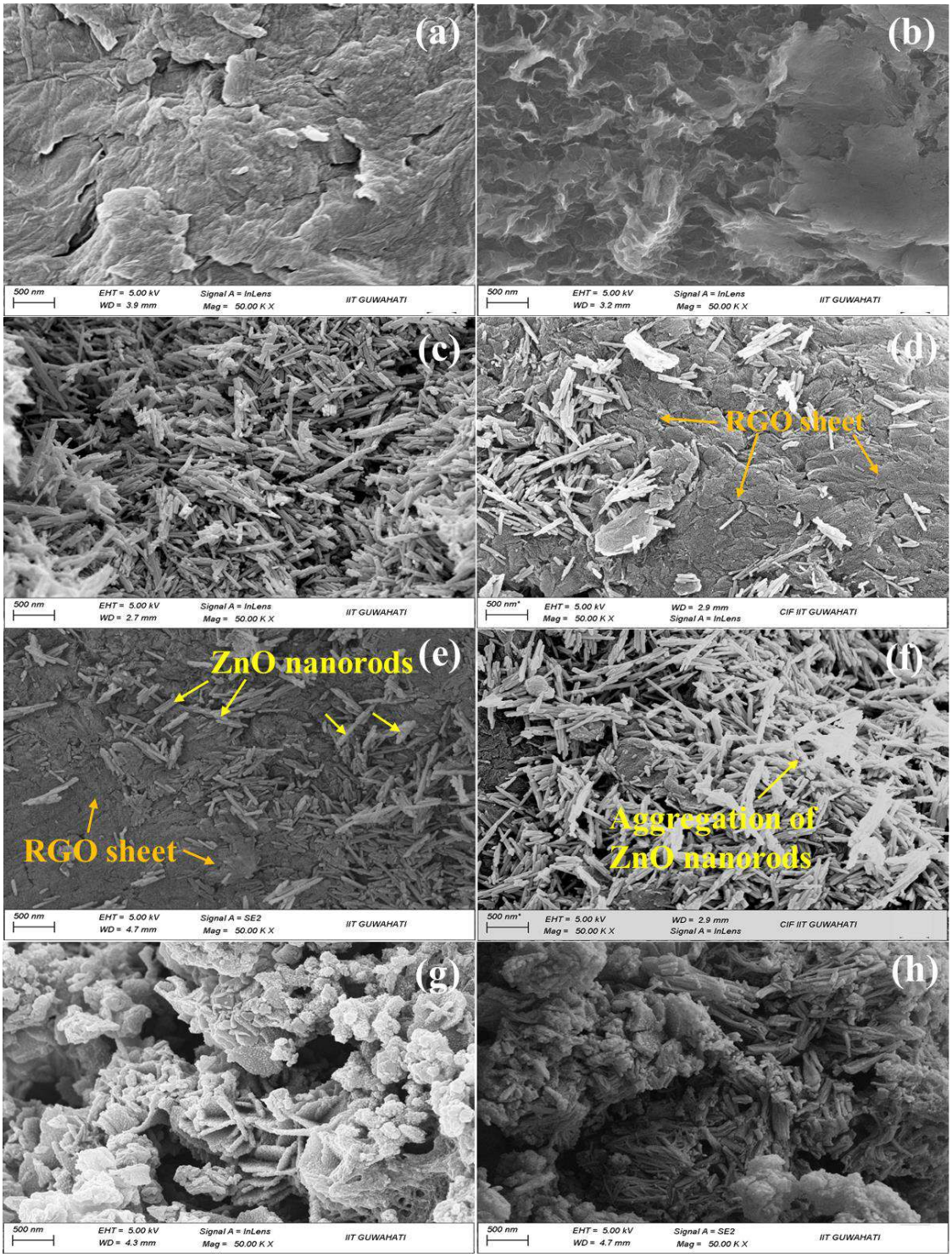

Fig. 7.1 FESEM images of prepared material: (a) GO, (b) RGO, (c) ZnO, (d) RGO-ZnO (4:0.5), (e) RGO-ZnO (4:1), (f) RGO-ZnO (4:2), (g) PANI, and (h) RGO-ZnO-PANI nanocomposite.

7.1.2 X-ray diffraction analysis

The structural and phase information of prepared graphite, GO, RGO, ZnO, RGO-ZnO, PANI, and RGO-ZnO-PANI were examined by XRD analysis. XRD spectra of all materials are shown in Fig. 7.3. XRD of graphite powder shows two diffractions at 2θ values of 26.55º and 54.67º, corresponding to (002) and (004) planes, respectively (Ain et al., 2019). Graphene oxide (GO) shows two diffractions at 2θ values of 10.16º and 42.48º, corresponding to the (001) and (100) planes, respectively. During the reduction of graphene, few oxygens were removed, and XRD patterns of RGO show one new peak at 24.54º corresponding to the (002) plane, which indicates the formation of RGO. XRD patterns of ZnO show sharp and intense peaks at 31.69º, 34.40º, 36.37º, 47.52º, 56.67º, 62.89º, 66.4º, 67.99º, 69.14º, 72.67º, 77.07º, 81.45º and their corresponding planes (100), (002), (101), (102), (110), (103), (200), (112), (201), (202), (104), which are well-matched with JCPDS no 036-1451. RGO-ZnO composite shows all ZnO Peaks but one RGO peak at 42.89º with (100) planes. Similar XRD patterns of RGO, ZnO, and RGO-ZnO have been reported in the literature (Jayachandiran et al., 2018). The XRD spectra of PANI show two broad peaks at around 20º and 25.57º, corresponding to the (020) and (200) planes, indicating the formation of semi-crystalline polyaniline fiber (Zhang et al., 2017). Semicrystalline PANI exhibits superior chain packing properties, which promote the formation of a more compact and cohesive polymer network within the epoxy matrix. This increased structural density effectively minimizes the diffusion of corrosive species and provides strong barrier properties. Furthermore, the redox-active characteristics of semicrystalline PANI facilitate the formation of stable, protective oxide layers on the metal surface, contributing to its passivation. Due to these properties, PANI significantly enhances the corrosion resistance of epoxy coatings (Siva et al., 2014). In XRD pattern of RGO-ZnO-PANI nanocomposite, several peaks were found at 2θ values of 31.69º, 34.40º, 36.31º, 47.52º, 56.67º, 62.89º, 66.4º, 67.99º, 69.14º, 72.67º, 77.07º, which confirm the presence of ZnO, and

one low peak was recorded at 42.48º, which corresponds to RGO. This spectrum also displayed the two peaks at 2θ values of 20º and 25.57º, which confirms the presence of PANI. All these peaks confirm the formation of the ternary RGO-ZnO- PANI nanocomposite. Furthermore, deconvolution of the most prominent peak was performed using the Gaussian in the range of 35 to 38º for XRD plots of ZnO, RGO-ZnO, and RGO-ZnO-PANI composite (Mehto et al., 2016), deconvoluted plots are shown in Fig. 7A.1. of the Appendix 7A. The obtained XRD patterns and diffraction parameters were further used to study the variations in the lattice strain, dislocation density, and crystallite size during composite formation (Table 7.1). The crystallite size, lattice strain, and dislocation density were calculated using Eqs. (2), (3), and (4)(Bhan and Kumar Golder, 2023).

$$d = \frac{k\lambda}{\beta cos\theta_B} \tag{2}$$

$$\varepsilon = \frac{\beta}{4Tan\theta_B} \tag{3}$$

$$\delta = \frac{1}{d^2} \tag{4}$$

Where d, ε, θ_B, β, δ, k, and λ represent the crystal size (nm), lattice strain, half-width at full maxima (FWHM), Bragg angle, and dislocation density (lines/nm^2), respectively. The constant parameters of the XRD diffractometer, k and λ, have values of 0.94 and 0.154 nm, respectively (Ravi et al., 2025).

The crystallite size of RGO-ZnO-PANI is smaller as compared to ZnO and RGO-ZnO, indicating a higher surface area of the RGO-ZnO-PANI coating, enhancing interaction with the coating matrix and improving dispersion. Additionally, the dislocation density and lattice strain of RGO-ZnO-PANI are higher than ZnO and RGO-ZnO, suggesting stronger matrix-filler bonding (enhanced toughness) and better crack resistance (improved structural integrity), respectively.

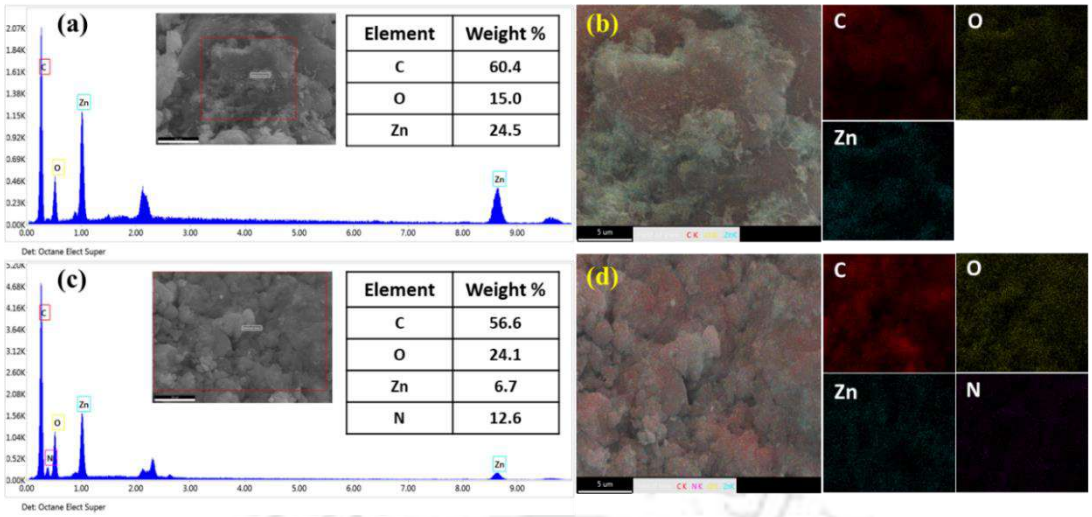

Fig. 7.2 EDX spectra and mapping images of (a, b) RGO-ZnO and (c, d) RGO-ZnO-PANI.

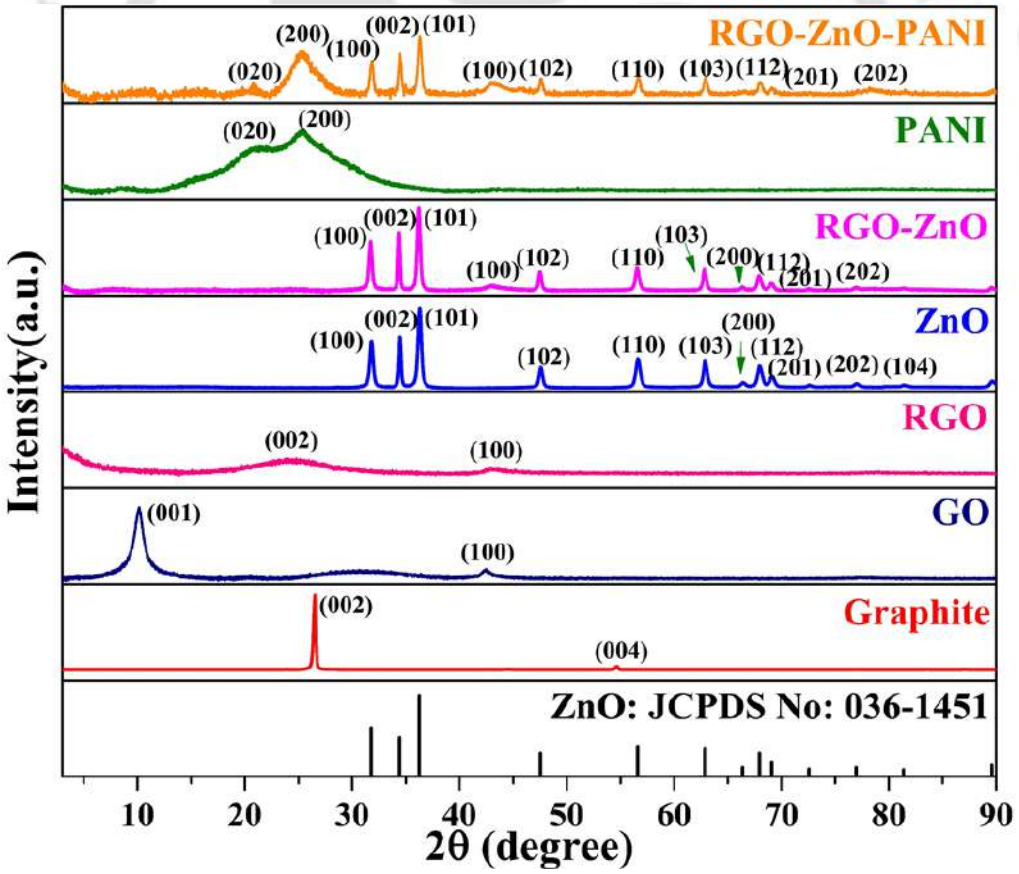

Fig. 7.3 XRD patterns for graphite, GO, RGO, ZnO, RGO-ZnO, PANI, RGO-ZnO-PANI nanocomposites.

Table 7.1 The XRD diffraction parameters.

Sample code	Peak position, 2θ (degree)	Crystallite size (nm)	d-spacing (Å)	Lattice strain (e)	Dislocation densities (Lines/nm^2)
ZnO	36.26	50.47	2.47	2.31×10^{-3}	3.93×10^{-4}
RGO-ZnO	36.21	25.50	2.48	4.57×10^{-3}	1.54×10^{-3}
RGO-ZnO-PANI	36.31	22.87	2.47	5.08×10^{-3}	1.91×10^{-3}

7.1.3 Raman analysis

Raman spectra of graphite, GO, RGO, ZnO, RGO-ZnO, and RGO-ZnO-PANI are shown in Fig. 7.4. Raman spectra of graphite show two peaks at 1578.6 and 2664.9 cm^{-1}. A peek at ~ 1578.6 cm^{-1} corresponds to the planer stretching of the C-sp^2 bond. After the oxidation of graphite, a new peak appeared at ~ 1360 cm$^{-1,}$ which indicates the change in graphite structures due to oxidation; this is associated with the C-sp^3 bond vibration. The peak at 1578.9 cm^{-1} shifted to ~ 1587.0 cm^{-1}. These changes are characteristic peaks of GO, and I_D/I_G ratio for graphene oxide is 1.33 (Das et al., 2020). In the case of RGO, two peaks are obtained at 1322.6 cm^{-1} and 1587.0 cm^{-1} with I_D/I_G (1.5). This increment from 1.33 to 1.5 indicated that defects and disorders increased during the reduction, which is consistent with XRD data. In the Raman spectrum of ZnO, an intense peak at 437.55 cm^{-1} corresponds to wurtzite hexagonal ZnO. Furthermore, Raman spectra of RGO-ZnO nanocomposite show the shifting of the G band to lower wave number 1589.50 cm^{-1} due to the hybridization of ZnO. I_D/I_G ratio also decreased from 1.5 (RGO) to 1.47 (RGO-ZnO). Furthermore, a low intensive peak appears at 432.51 cm^{-1}, corresponding to ZnO in the RGO-ZnO composite (Jayachandiran et al., 2018). Raman spectra of RGO-ZnO-PANI nanocomposite is also similar to PANI, but it has a low intense peak at 432.51 cm^{-1}. From these spectra, it was observed that the I_D/I_G ratio was decreased from

1.47 (RGO-ZnO) to 1.29 (RGO-ZnO-PANI) due to the overlapping of G and D bands of RGO and PANI (Wu et al., 2016).

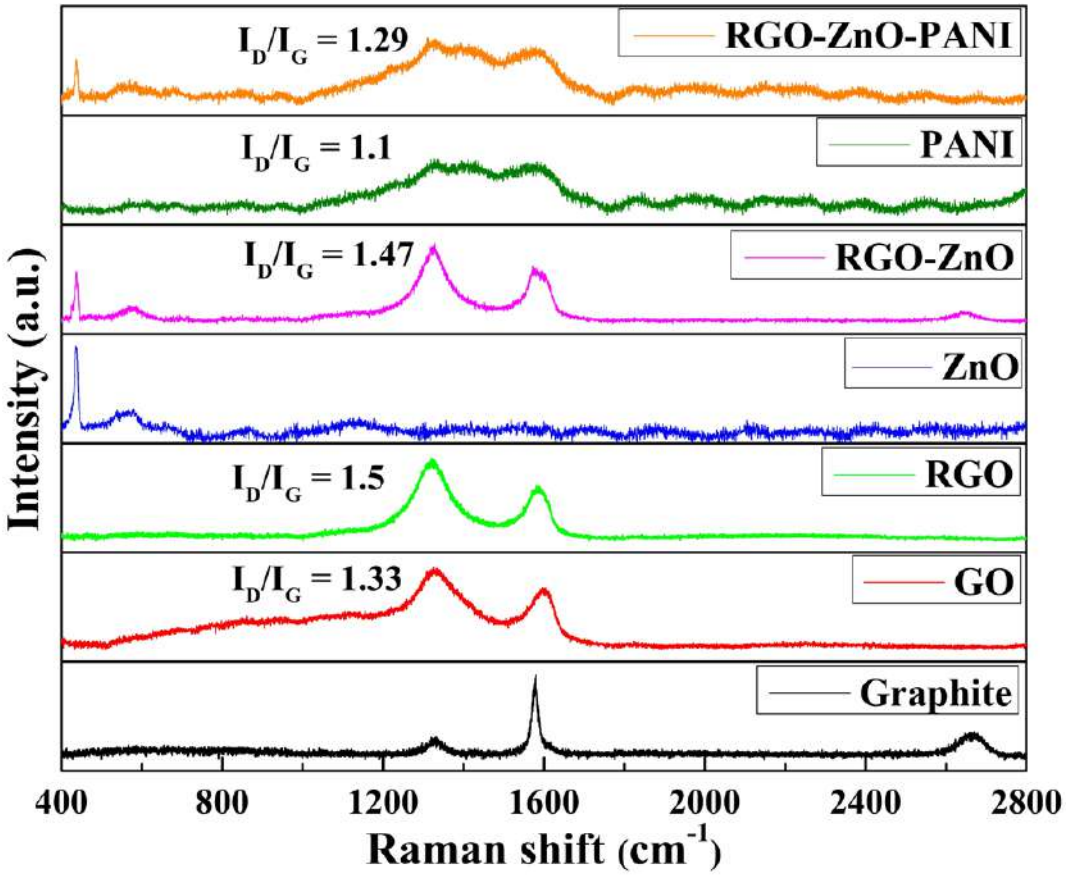

Fig. 7.4 Raman spectra of graphite, GO, RGO, RGO-ZnO, PANI, and RGO-ZnO-PANI.

7.2 Characterizations of EP, 0.5 wt% EP/RGO, EP/RGO-ZnO, and EP/ RGO-ZnO-PANI coatings

7.2.1 FESEM analysis

The morphology of several coatings on the MS surface was investigated using the FESEM analysis. Fig. 7.5 (a) displays the FESEM image of pure epoxy (EP), which shows a rough surface with few micropores and microcracks. Fig. 7.5 (b) shows the FESEM image of EP/RGO coating, which has cracks and holes free surface, but it still has a slightly rough

surface due to the agglomeration of RGO sheets in the epoxy matrix (Aradhana et al., 2018). To enhance the coating properties, ZnO decorated RGO was utilized in the epoxy matrix for preparing the EP/RGO-ZnO coating, which improves the morphology of the coated surface and provides a smoother surface (Fig. 7.5 (c)) than that of EP/RGO coating. The presence of ZnO on the RGO nanosheet's surface hindered the agglomeration of RGO nanosheets (Rajitha et al., 2020). Coatings properties were further improved by the modification of the RGO-ZnO nanocomposite by PANI to obtain the RGO-ZnO-PANI ternary nanocomposite. This composite was utilized to prepare EP/ RGO-ZnO-PANI nanocomposite coating, which exhibited a smoother surface, as shown in Fig. 7.5 (d), compared to all other coatings. The uniform dispersion of the RGO-ZnO-PANI nanocomposite within the epoxy matrix resulted in a smoother surface and increased coating compactness, indicating strong interfacial compatibility and interaction between the nanocomposite and the epoxy, leading to a denser, more cohesive coating. Similar changes in the surface morphology of coatings with nanofiller addition have been reported by several studies (Dhongde et al., 2023; Lv et al., 2023).

7.2.2 FTIR analysis

The FTIR spectra of all prepared coatings (EP, EP/RGO, EP/RGO-ZnO, and EP/RGO-ZnO-PANI nanocomposite) are shown in Fig. 7.6, all of which revealed nearly similar absorption curves. This should be due to the fact that the addition of a small amount (0.5 wt%) of nanofillers had a low influence on the FTIR spectrum of the epoxy. In FTIR spectra of pure epoxy (EP), a band around at 3487 cm^{-1} was found for O–H stretching vibration, and bands at 2968 and 2928 cm^{-1} ascribed to asymmetric and symmetric C–H stretching vibration, respectively. The peaks at 1630, 1587, and 1502 cm^{-1} correspond to the benzene ring of epoxy. Furthermore, the band at 1243 cm^{-1} was designated for the epoxy group, at 1182 cm^{-1} (due to C–O–C asymmetric stretching vibration for ester), at 1033 cm^{-1} ascribed to aromatic C–O

stretching vibration and the most intensive peak at 827 cm^{-1} can be appointed to the oxirane group of epoxy resin (Aradhana et al., 2019). Similar adsorption bands were obtained in FTIR spectra of all nanocomposite coatings, such as EP/RGO, EP/RGO-ZnO, and EP/RGO-ZnO-PANI. On comparing these spectrums, peak shifting was observed at 1033 cm^{-1} and 1630 cm^{-1} for composite coatings as compared to pure EP coating. These shifting can be ascribed to the strong interaction between the epoxy matrix and added nanofillers through hydrogen bonding and chemical bonding (Ahmad et al., 2018).

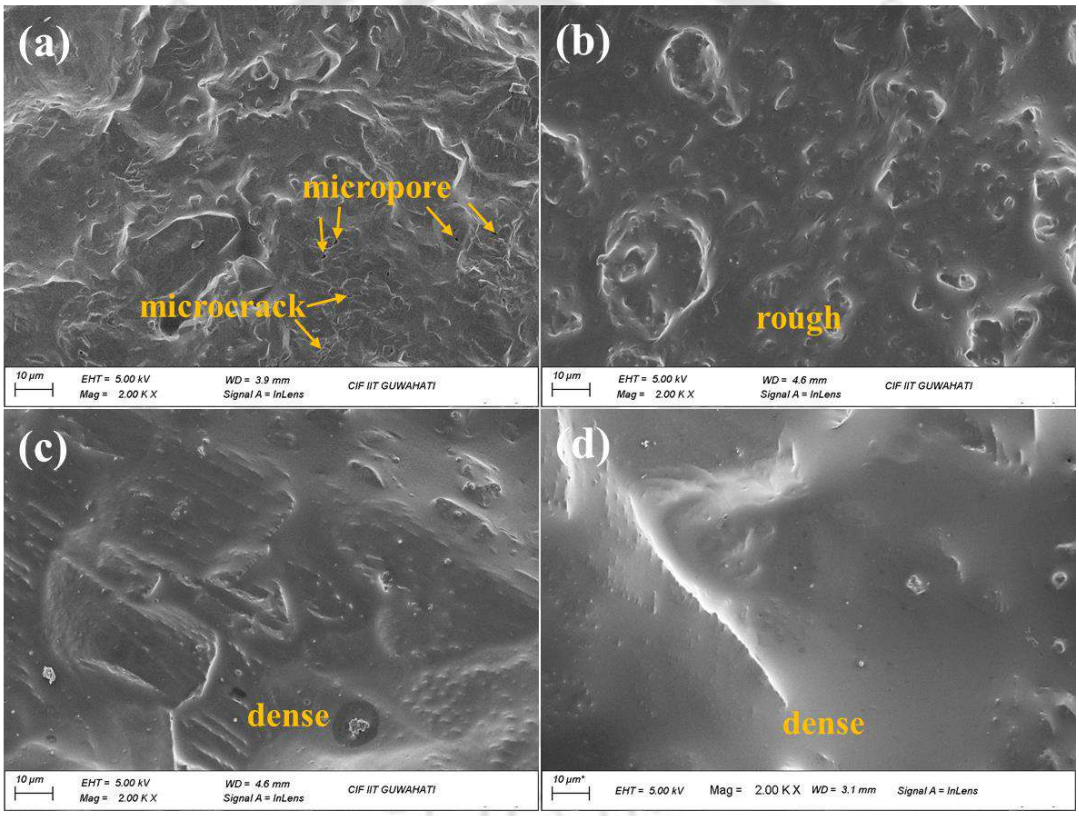

Fig. 7.5 FESEM images of prepared coatings: (a) EP, (b) EP/RGO, (c) EP/RGO-ZnO, and (d) EP/RGO-ZnO-PANI nanocomposite on MS substrates.

Furthermore, in the case of EP/RGO-ZnO-PANI coatings, the intensity of peaks around 3480 was significantly reduced compared to pure epoxy (S. Guo et al., 2020). These results of

the FTIR analysis demonstrated that RGO-ZnO-PANI nanofillers exhibited a strong interaction with epoxy resin and formed a more compact coating than other coatings.

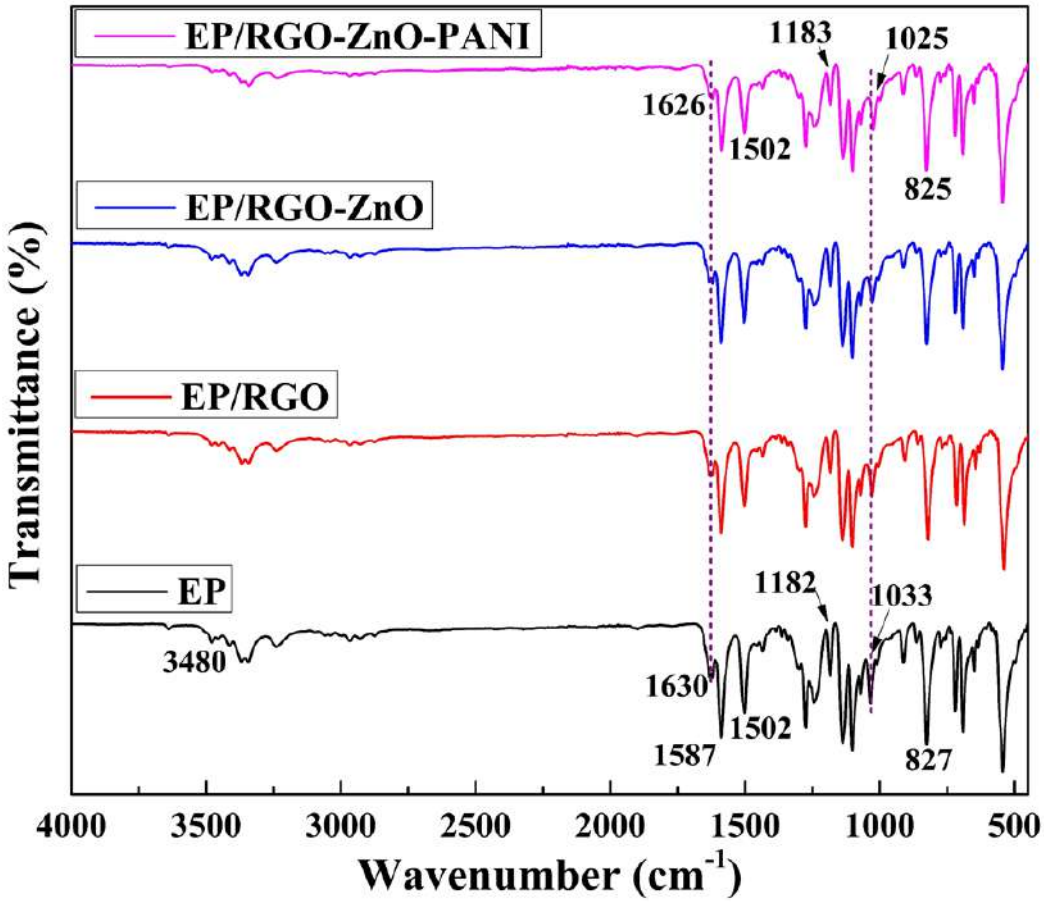

Fig. 7.6 FTIR spectra of EP, EP/RGO, EP/RGO-ZnO, and EP/RGO-ZnO-PANI nanocomposite coatings.

7.2.3 TGA analysis

TGA plots for all prepared coatings (EP, EP/RGO, EP/RGO-ZnO, and EP/RGO-ZnO-PANI nanocomposite) are shown in Fig. 7.7 (a). In each coating, early weight loss was seen when they heated up to 100 ℃. This weight loss was mainly due to the evaporation of adsorbed moisture and the release of gases trapped within the matrix. Furthermore, at higher temperatures from 100 ℃ to 300 ℃, the amount of weight loss of about 8.10 %, 2.06 %, 1.51

%, and 1.26 % was found for EP, EP/RGO, EP/RGO-ZnO, and EP/RGO-ZnO-PANI nanocomposite coating. The weight loss observed in these nanocomposite coatings was because of the degradation and decomposition of their molecular networks. During the heating, these materials can undergo thermal decomposition, leading to the breakdown of chemical bonds within the polymer matrix (Ji et al., 2022b). A significant weight loss was observed at temperatures between 300°C and 600°C, likely due to the presence of RGO, RGO-ZnO, and RGO-ZnO-PANI separately in the epoxy coating which facilitates the breakdown process by forming char. The char layer helps to prevent the decomposition of the epoxy resin. The incorporation of nanofillers into the epoxy matrix enhanced their thermal stability and tendency to generate the char. As obtained, RGO-ZnO has better distribution than RGO in epoxy coatings, which also exhibited higher thermal stability of EP/ RGO coating. This figure shows that EP/RGO-ZnO-PANI exhibited higher thermal stability during the heating process than other coatings. The excellent interaction of composite and matrix and the uniform dispersion of RGO-ZnO-PANI may explain this effect (Huang et al., 2011), which delayed the deterioration of the epoxy resin. Similar degradation patterns were observed in the literature (Zhang et al., 2023).

7.2.4 Contact angle analysis

The coating failure is primarily caused by the penetration of H_2O, O_2, Cl^-, and other corrosive electrolyte. These corrosive species penetrate through the coating and try to reach the metallic surface, leading to the continuous accumulation of the aqueous phase near the metallic substrate. So, water adsorption and wetting properties are vital characteristics to check the coating performance (Pan et al., 2024). Wetting properties of all prepared (EP, EP/RGO, EP/RGO-ZnO, and EP/RGO-ZnO-PANI) coatings were evaluated by measuring the water contact angle, as shown in Fig. 7.7 (b). The reported contact angles are based on the average

of three measurements made on each sample, and the error bar is determined by comparing the average reported data to the three measurements. The contact angle of the mild steel covered with pure epoxy was 67.37º, indicating the hydrophilic behavior due to the presence of a few micropores and microcracks, as shown in Fig. 7.5 (a). The value of the contact angle was significantly increased to 81.88º with the addition of RGO in epoxy, indicating enhanced hydrophobic properties attributed to 2-D surface of RGO, which makes holes and a pore-free surface of the coating (Fig. 7.5 (b)). It was further increased to 85.77º in the presence of zinc oxides doped reduced graphene oxide (RGO-ZnO), which depicts improvement in hydrophobicity due to uniform distribution of RGO-ZnO in epoxy coatings, resulting in a smoother surface (Fig. 7.5 (c)) than pure EP and EP/RGO coatings. The highest contact angle of 88.46º was obtained for the ternary EP/RGO-ZnO-PANI coating, indicating superior water-repelling properties. This improvement is attributed to the formation of a smoother surface and a denser structure resulting from the homogeneous distribution of the RGO-ZnO-PANI nanocomposite within the epoxy matrix (Fig. 7.5 (d)). The higher values of the contact angles on the nanocomposite coatings would limit the access of the corrosive agents into the coatings and provide the enhanced corrosion resistance properties of the coating (Zhang et al., 2019; Zhou et al., 2025).

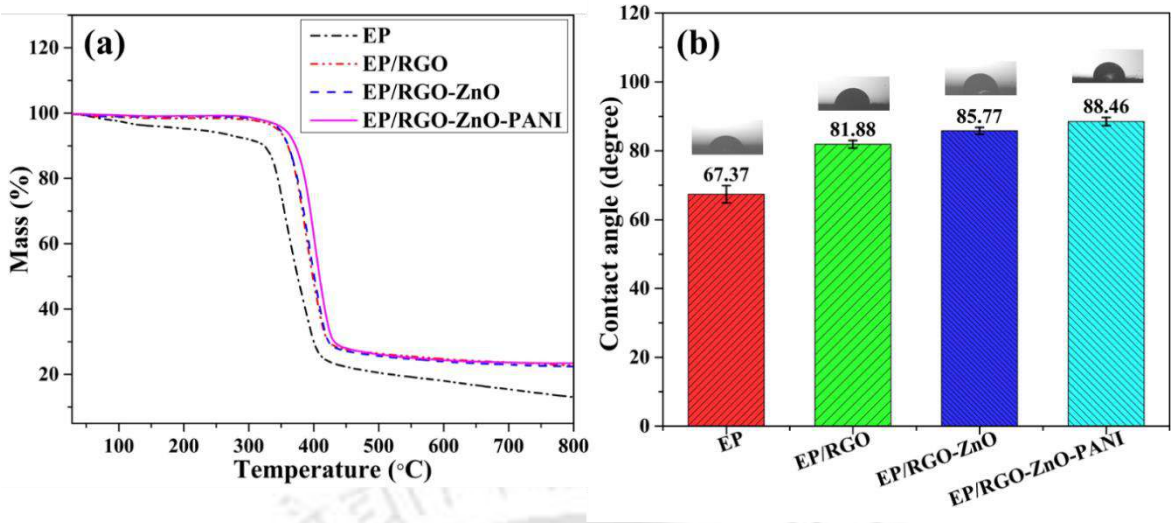

Fig. 7.7 (a) Thermogravimetric and (b) contact angle plots for EP, EP/RGO, EP/RGO-ZnO, and EP/RGO-ZnO-PANI (error bars represent the standard deviation from the mean values, based on three replicate measurements).

7.3 Corrosion inhibiting behavior of coating

7.3.1 PDP measurements

The corrosion protection behavior of EP, 0.5 wt% EP/RGO, EP/RGO-ZnO, and EP/RGO-ZnO-PANI nanocomposite coatings on MS against 3.5 wt% NaCl was studied using the Potentiodynamic polarization test (Dhongde et al., 2024). Before each PDP test, coated and uncoated coupons were immersed in 3.5 wt% NaCl for 1 day, and OCP measurements were conducted for 30 min to achieve the steady state (equilibrium) potential (Kobbekaduwa et al., 2024). Fig. 7.8 demonstrates the Tafel plots for uncoated and coated MS with EP, EP/RGO, EP/RGO-ZnO, and EP/RGO-ZnO-PANI nanocomposite coatings. Furthermore, Tafel parameters ((corrosion potential (E_{corr}), corrosion current density (i_{corr}), anodic Tafel slop (b_a), cathodic Tafel slop (b_c), polarization resistance (R_p)) were estimated from these Tafel plots via Nova 1.10. software. The mean values and standard deviations of these parameters, obtained from triplicate experiments, are presented in Table 7.2.

Fig. 7.8 and Table 7.2 demonstrate that the value of E_{corr} was positively shifted for EP, EP/RGO, EP/RGO-ZnO, and EP/RGO-ZnO-PANI with differences of 27.67, 66.22, 70.64, and 82.47 as compared to blank (-663.80 mV). This positive shift illustrates the strong anti-corrosive behavior of the above coatings. Moreover, a significant drop was seen in the value of i_{corr} for epoxy-coated MS as compared to uncoated MS. This drop was further increased with EP/RGO, EP/RGO-ZnO, and EP/RGO-ZnO-PANI nanocomposite coatings. The Tafel plots illustrate that both anodic and cathodic current density decline significantly, resulting in the decrease of i_{corr}. It shows that EP, EP/RGO, EP/RGO-ZnO, and EP/RGO-ZnO-PANI nanocomposite coatings significantly reduce the anodic (MS degradation) and cathodic (oxygen reduction) reactions. The highest decline was obtained for EP/RGO-ZnO-PANI nanocomposite-coated MS samples, which implies that this coating exhibited the strongest anti-corrosive properties among all prepared coatings (Bian et al., 2023; L. Guo et al., 2020). It provided impermeable barrier resistance against corrosive species to reach the metallic surface from corrosive solution and provided 99.98% corrosion inhibiting efficiency. These values were used to calculate p-values, which confirm that electrochemical data are highly statistically significant ($p< 0.0001$) (Table 7A.1 of the Appendix 7A). Furthermore, the anti-corrosive behavior of EP/RGO-ZnO-PANI nanocomposite coatings with 1 wt% of RGO-ZnO-PANI was also studied after 1-day immersion in 3.5 wt% NaCl and their Tafel plots and Tafel parameters are shown in Fig. 7A.2 and Table 7A.2 respectively, of the Appendix 7A. It was observed that this ternary coating with 1 wt % of RGO-ZnO-PANI in epoxy has lesser corrosion protection properties as compared to its 0.5 wt% based nanocomposite coatings due to the agglomeration of RGO-ZnO-PANI nanocomposite at higher loading. This decline in anticorrosive properties of EP/RGO-ZnO-PANI (1 wt %) nanocomposite coating was furthered validated by FESEM analysis, Fig. 7A.3 of the Appendix 7A, shows the FESEM images of EP/RGO-ZnO-PANI (0.5 and 1 wt %) nanocomposite coating. From these images, it was

observed that a smooth and crack-free surface was found at 0.5 wt% but few pores and cracks were seen in a coating containing 1 wt% of RGO-ZnO-PANI due to the agglomeration of nanofillers at higher loading. Therefore, further investigations were done with pure epoxy (EP) and 0.5 wt% nanofillers (EP/RGO, EP /RGO-ZnO, and EP/RGO-ZnO-PANI) based nanocomposite coatings.

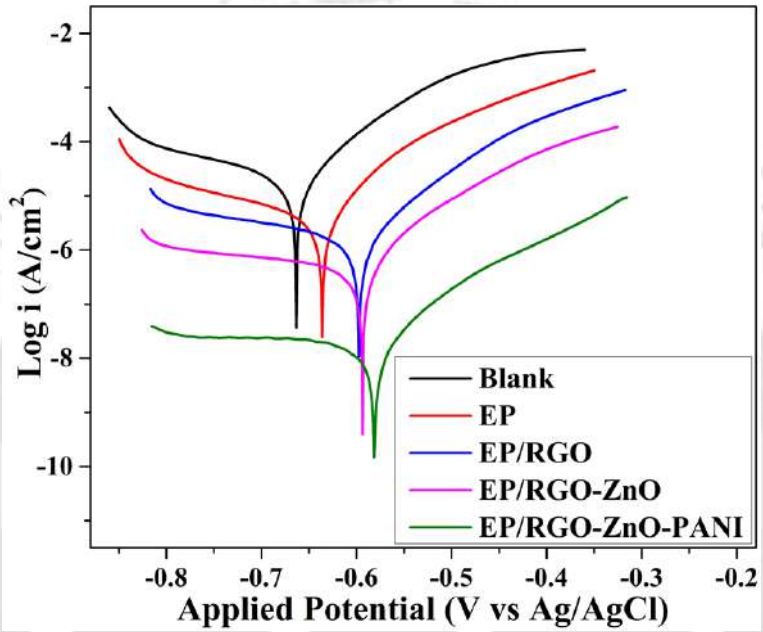

Fig. 7.8. Tafel plots for Blank, EP, EP/RGO, EP/RGO-ZnO, and EP/RGO-ZnO-PANI after 1-day immersion in 3.5 wt% NaCl.

Table 7.2 Tafel parameters for blank, EP, EP/RGO, EP/RGO-ZnO, and EP/RGO-ZnO-PANI coatings after 1-day immersion in 3.5 wt% NaCl.

System	b_a (mVdec^{-1})	$-b_c$ (mVdec^{-1})	E_{corr} (mV vs. Ag/AgCl)	i_{corr} (µA cm^{-2})	R_p (Ω cm^2)	CR (mm Year^{-1})	μ_P (%)
Blank	393.60 ± 9.20	89.31 ± 0.89	-663.80 ± 6.27	28.21 ± 0.83	(1.12 ± 0.02) ×10^3	(3.28 ± 0.04) ×10^{-1}	-
EP	361.49 ± 4.02	70.33 ± 0.48	-636.13 ± 6.47	5.03 ± 0.14	(5.08 ± 0.10) ×10^3	(5.84 ± 0.05) ×10^{-2}	82.17 ± 0.20
EP/RGO	160.27 ± 1.21	66.19 ± 1.07	-597.58 ± 5.06	1.39 ± 0.05	(1.46 ± 0.04) ×10^4	(1.62 ± 0.03) ×10^{-2}	95.05 ± 1.10
EP/RGO-ZnO	425.58 ± 2.13	54.24 ± 1.00	-593.16 ± 5.37	0.44 ± 0.02	(4.70 ± 0.03) × 10^4	(5.17 ± 0.04) ×10^{-3}	98.42 ± 0.93
EP/ RGO-ZnO-PANI	44.78 ± 1.73	31.71 ± 0.93	-581.33 ± 4.86	0.0053	(1.51 ± 0.01) × 10^6	(6.22 ± 0.13) ×10^{-5}	99.98 ± 0.01

7.3.2 EIS measurements

EIS experiments were also performed to study the anti-corrosive behavior of prepared coatings (EP, 0.5 wt% EP/RGO, EP/RGO-ZnO, and EP/RGO-ZnO-PANI nanocomposite). Before each EIS test, the uncoated and coated MS samples with these coatings were immersed in 3.5 wt% NaCl for 1, 15, 30, and 45 days, and OCP was measured to achieve the steady state potential. The variations in the OCP with immersion time are shown in Fig. 7.9. From this figure, it is observed that the OCP value of all coatings negatively shifted with the immersion time, which indicated the deuteriation of coatings with immersion time. However, results show that the OCP values are higher for nanofillers-based coatings relative to bare epoxy coating even after exposure of 45 days. The maximum was obtained for EP/ RGO-ZnO-PANI, which signifies the superior anti-corrosive properties of EP/ RGO-ZnO-PANI as compared to other coatings (Yao et al., 2023).

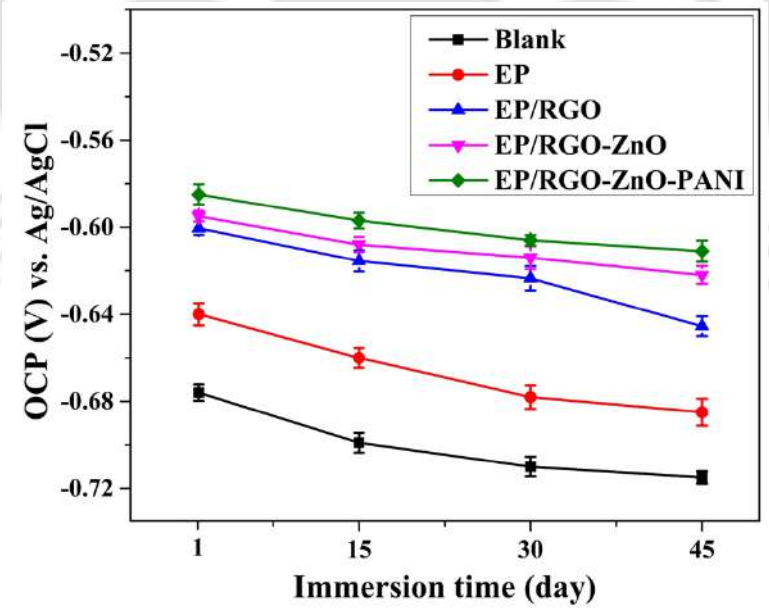

Fig. 7.9 OCP variation with immersion time for blank, EP, EP/RGO, EP/RGO-ZnO, and EP/RGO-ZnO-PANI.

Fig. 7.10 displays Nyquist and Bode plots for Blank (a, b), EP (c, d), EP/RGO (e, f), EP/ RGO-ZnO (g, h), and EP/ RGO-ZnO-PANI (i, j), respectively. In these Nyquist plots, capacitive arcs decrease with the immersion time (1- 45 days) for each system, and its higher value was recorded for initial exposure, which frequently represents the higher effectiveness of prepared coatings (Ji et al., 2022a). Moreover, obtained Bode patterns (Fig. 7.10 d, f, and j) after 1-day exposure exhibited the different impedance modulus values for each coating at 0.01 Hz, which were in the following sequence: EP <EP/RGO < EP/RGO-ZnO < EP/RGO-ZnO-PANI nanocomposite coating. It illustrates the corrosion resistance of coatings enhanced with the incorporation of RGO, RGO-ZnO, and RGO-ZnO-PANI. Furthermore, these results imply that the coating's barrier characteristics were also enhanced by the good dispersion of RGO, RGO-ZnO, and RGO-ZnO-PANI. It was highest for RGO-ZnO-PANI (Dhongde et al., 2023). On careful observing Nyquist and Bode plots for epoxy coating at different immersion times, it was found that epoxy coating exhibited the one-time constant during its immersion from 1 to 30 days, which signifies that corrosive solution penetrates through the epoxy coating at its initial exposure but did not reach the coating/metal interface. The EIS data at this stage can be illustrated by the physical model, and its corresponding equivalent circuit (R(QR)) (Jayakumar and Karimbintherikkal Gopalan, 2024) is shown in Fig. 7.11 (a). Furthermore, on higher immersion time (from 30 to 45 days), epoxy coatings showed a two-time constant, which implies that corrosive solution has penetrated the coating and reached the coating/metal interface, resulting in metal corrosion. This EIS data was fitted to another equivalent circuit model R(Q(R(QR))) (Goswami et al., 2024), which is shown in Fig.7.11 (b). These fittings of EIS data were performed using Nova 1.1.0 software to evaluate the EIS parameters. The mean values and standard deviations of these parameters, obtained from triplicate experiments, are shown in Table 7.3. As represented in Fig. 7.11 (a), the R(QR) equivalent circuit model is made of three key parameters; for instance, R_s and R_c represent solution resistance and coating

resistance, respectively, and coating capacitance is denoted by Q_c (Castela and Simões, 2003). Few studies have reported that this equivalent circuit model was utilized when a one-time constant remained during the immersion process (Meng et al., 2021; Xia et al., 2024). Usually, R_c is considered a an indicator to estimate the barrier property of a coating, which impedes corrosive medium penetration into the coating (Liu et al., 2018). Furthermore, R(Q(R(QR))) model (Fig. 7.11 (b)) consisted of two additional parameters, such as R_{ct} and Q_{dl}, which represent charge transfer resistance and double layer capacitance, respectively (Han et al., 2025). From Table 7.3, it was observed that after 1-day immersion, the epoxy coating exhibited R_c values around $1.61 \times 10^4\ \Omega\ cm^{2,}$ which was significantly decreased to $4.06 \times 10^2\ \Omega\ cm^2$ after its 45 days immersion. The obtained values of R_{ct} and Q_{dl} were $9.00 \times 10^2\ \Omega\ cm^2$ and $4.02 \times 10^3\ \mu F\ cm^{-2}$, respectively. This decrease in R_c values by 97.48 % implies that Epoxy coating demonstrated poor barrier and anti-corrosive properties. It can not effectively hinder the transfer of corrosive species, resulting in the failure of epoxy coating. Furthermore, all other coatings, such as EP/RGO, EP/RGO-ZnO, and EP/RGO-ZnO-PANI, exhibited one-time constant during the whole immersion period (1-45 days). Their EIS data was analyzed using the R(QR) model as described above for Epoxy coating up to 30 days immersion. The obtained values of R_c for EP/RGO coating at different immersion times are also plotted in Fig 7.11 (c), which displays similar patterns of R_c decline. Herein, the value of R_c declined from 3.2×10^4 (after 1-day exposure) to $5.1 \times 10^3\ \Omega\ cm^2$ (after its 45 days immersion). This decline of R_c was about 84.06 %, which implies that EP/RGO exhibited poor anti-corrosive properties.

Furthermore, the values of R_c for EP/ RGO-ZnO, and EP/ RGO-ZnO-PANI coated MS in 3.5 wt% NaCl were dropped from 1.78×10^5 and $1.12 \times 10^6\ \Omega\ cm^2$ to 2.28×10^4 and $2.1 \times 10^5\ \Omega\ cm^2$ respectively, during 45-day immersion (Fig 7.11 (c)), which depicts the declined corrosion inhibiting properties of coatings (Cheng et al., 2022). Few studies have also reported the similar declining behaviour of R_c with immersion time (Liu et al., 2018). In this work, the

EP/RGO-ZnO-PANI nanocomposite coating still exhibited the highest R_c values ($2.1 \times 10^5\ \Omega$ cm^2) after 45 days of exposure to NaCl solution among the all prepared coating, which signifies that EP/RGO-ZnO-PANI nanocomposite coating provides the highest barrier and anti-corrosive properties as compared to other coatings (Liu et al., 2022). In the last few years, Q_c (coating capacitance) is generally used to assess the water uptake in organic coatings (Hu et al., 2022). It describes the diffusion of corrosive solution into the coatings, and its value increases with the increase in the amount of diffused water inside the coatings. Herein, Q_c (µF cm^{-2}) value for each coating increased with their immersion in the marine environment, and a minimum was obtained for EP/RGO-ZnO-PANI nanocomposite coating during the entire immersion period (1- 45 days), confirming the outstanding corrosion inhibiting properties of EP/RGO-ZnO-PANI as compared to other coatings.

The variations in the values of Log (Q_c (µF cm^{-2})) with immersion time are also shown in Fig. 7.11 (d). Similar variations in R_c and Q_c with immersion time were also reported by few studies (Cui et al., 2023). Based on variations of the above two parameters (R_c and Q_c) with immersion period, the order of corrosion inhibiting performance of all above coatings is as follows: EP <EP/RGO < EP/RGO-ZnO < EP/RGO-ZnO-PANI nanocomposite coating. The lower values of Q_c, for binary and ternary composite-based coatings denote the low penetration of the electrolyte through the coatings (Tang et al., 2022), which implies strong anti-corrosive properties of coatings. After 1-day exposure, EP/RGO-ZnO-PANI coating exhibited 98.48 % more effective properties as compared to bare epoxy coating, and findings from PDP measurement showed its outstanding corrosion inhibiting efficiency of about 99.98% with respect to blank. Therefore, the electrochemical test demonstrates the greater anti-corrosive and barrier properties of EP/RGO-ZnO-PANI coatings.

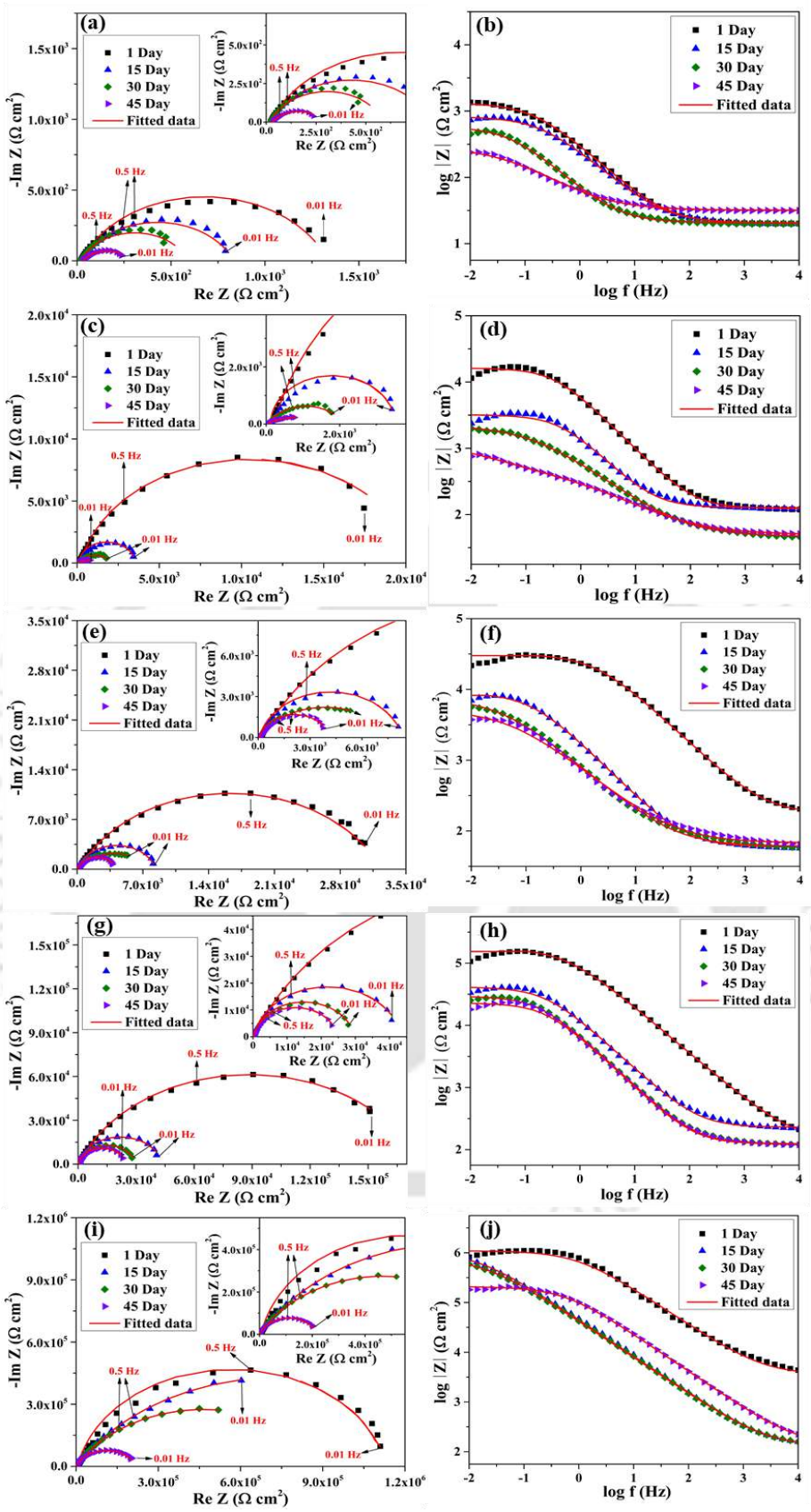

Fig. 7.10 Nyquist and Bode plots for Blank (a, b), EP (c, d), EP/RGO (e, f), EP/ RGO-ZnO (g, h), and EP/RGO-ZnO-PANI (i, j).

Table 7.3 Nyquist parameters for blank, EP, 0.5 wt% EP/RGO, EP/RGO-ZnO, and EP/RGO-ZnO-PANI coatings after 1, 15, 30, and 45 days immersion in 3.5 wt% NaCl.

System	Time (day)	R_s (Ω cm^2)	R_c (Ω cm^2)	CPE_c parameters		Q_c (μF cm^{-2})	R_{ct} (Ω cm^2)	CPE_{dl} parameters		Q_{dl} (μF cm^{-2})	Goodness of fit (χ^2) ×10^{-3}
				n_{coat}	Y_0 (μMho cm^{-2})			n_{dl}	Y_0 (μMho cm^{-2})		
Blank	1	20.19 ± 1.02	-	-	-	-	(1.32 ± 0.01) × 10^3	0.77 ± 0.01	772.00 ± 2.40	738.22 ± 1.99	3.21
	15	20.41 ± 0.51	-	-	-	-	(8.14 ± 0.02) × 10^2	0.75 ± 0.02	965.25 ± 4.63	919.99 ± 4.10	2.00
	30	20.61 ± 1.34	-	-	-	-	(5.69 ± 0.01) × 10^2	0.77 ± 0.02	3822.10 ± 9.25	3659.57 ± 9.10	4.17
	45	31.90 ± 2.07	-	-	-	-	(2.58 ± 0.02) × 10^2	0.64 ± 0.01	7851.50 ± 15.03	7302.81 ± 13.87	1.89
EP	1	122.67 ± 1.81	(1.61 ± 0.01) × 10^4	0.84 ± 0.01	31.73 ± 0.18	29.25 ± 0.45	-	-	-	-	4.02
	15	126.70 ± 1.95	(3.10 ± 0.01) × 10^3	0.84 ± 0.02	138.16 ± 0.01	126.81 ± 0.74	-	-	-	-	3.11
	30	46.10 ± 0.38	(2.20 ± 0.01) × 10^3	0.83 ± 0.01	490.28 ± 2.34	474.48 ± 5.02	-	-	-	-	5.03
	45	49.80 ± 1.20	(4.06 ± 0.01) × 10^2	0.56 ± 0.02	807.65 ± 6.13	742.04 ± 9.58	(9.00 ± 0.01) × 10^2	0.52 ± 0.01	4407.10 ± 9.58	4017.13± 0.01	2.13
EP/RGO	1	80.89 ± 0.61	(3.20 ± 0.02) × 10^4	0.74 ± 0.03	4.86 ± 0.02	2.79 ± 0.05	-	-	-	-	3.32
	15	58.49 ± 0.31	(8.96 ± 0.07) × 10^3	0.78 ± 0.01	129.99 ± 1.09	124.67 ± 0.79	-	-	-	-	4.15
	30	60.60 ± 0.22	(7.60 ± 0.02) × 10^3	0.84 ± 0.01	352.29 ± 2.31	340.28 ± 2.01	-	-	-	-	3.18
	45	67.75 ± 1.25	(5.10 ± 0.02) × 10^3	0.78 ± 0.02	387.33 ± 3.42	371.34 ± 1.96	-	-	-	-	2.33
EP/RGO-ZnO	1	139.09 ± 3.19	(1.78 ± 0.02) × 10^5	0.75 ± 0.01	2.20 ± 0.02	2.09 ± 0.03	-	-	-	-	4.31
	15	137.82 ± 1.06	(4.10 ± 0.03) × 10^4	0.82 ± 0.01	16.90 ± 0.04	16.32 ± 0.20	-	-	-	-	1.15
	30	123.88 ± 0.32	(2.90 ± 0.01) × 10^4	0.83 ± 0.03	30.35 ± 0.19	29.39 ± 0.32	-	-	-	-	3.72
	45	122.71 ± 0.80	(2.28 ± 0.01) × 10^4	0.84 ± 0.01	30.77 ± 0.26	29.84 ± 0.22	-	-	-	-	1.33
EP/ RGO-ZnO-PANI	1	210.12 ± 4.83	(1.12 ± 0.01) × 10^6	0.74 ± 0.02	0.23 ± 0.01	0.15 ± 0.01	-	-	-	-	4.22
	15	128.49 ± 0.96	(1.06 ± 0.01) × 10^6	0.79 ± 0.01	5.62 ± 0.05	5.40 ± 0.04	-	-	-	-	3.57
	30	129.98 ± 1.85	(7.86 ± 0.04) × 10^5	0.81 ± 0.02	6.06 ± 0.03	5.84 ± 0.07	-	-	-	-	2.65
	45	138.00 ± 2.02	(2.10 ± 0.01) × 10^5	0.81 ± 0.01	7.12 ± 0.04	6.06 ± 0.10	-	-	-	-	1.53

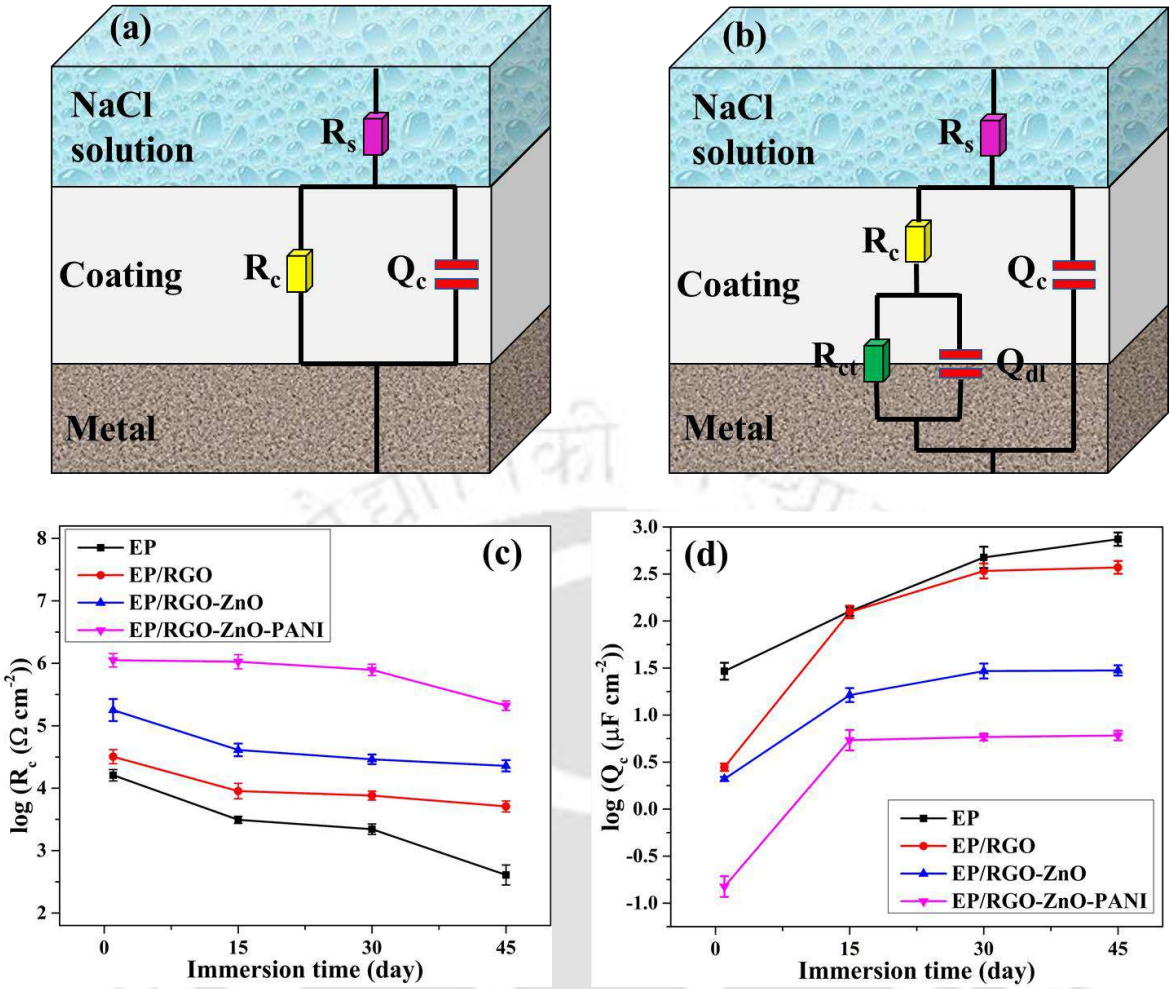

Fig. 7.11 Equivalent circuit model (a) R(QR) and (b) R(Q(R(QR))), variations in (c) R_c and (d) Q_c value for EP, EP/RGO, EP/ RGO-ZnO, and EP/RGO-ZnO-PANI (g, h) at different immersion times (error bars represent the standard deviation from the mean values, based on three replicate measurements).

7.3.3 Salt spray analysis

Salt spray analysis was utilized to investigate the corrosion resistance properties of coated MS samples and optical photography was also performed to take the picture of coated samples at different exposure times, which displays the changes in the morphology at and around the scratched coated surface due to NaCl attack (Fig. 7.12). After 48 h of salt spray, corrosion starts near the scratches of the epoxy-coated MS. To study its deterioration behavior,

the exposure time was extended to 1000 h. This coating deterioration increased with time due to the penetration of corrosive species through the pores of epoxy coating. EP/RGO-coated MS, relative to pure epoxy coating, showed better corrosion resistance properties. The amount of corrosion rust increases with time after 500 h. Coated MS with EP/RGO coating showed deficient anti-corrosion behavior. However, there was no corrosive rust seen in the EP/RGO-ZnO coating up to 500 h exposure, which implies that the anti-corrosive property of the coating was improved due to the decoration of ZnO on the RGO surface, which hindered the restacking of RGO sheets and provided better distribution as compared to RGO. Furthermore, EP/RGO-ZnO-PANI nanocomposite coating shows very less red rust for the period of 750-1000 h of immersion, which signifies that the addition of ternary nanocomposite RGO-ZnO-PANI significantly enhanced the anti-corrosive properties of epoxy coating as compared to other coatings.

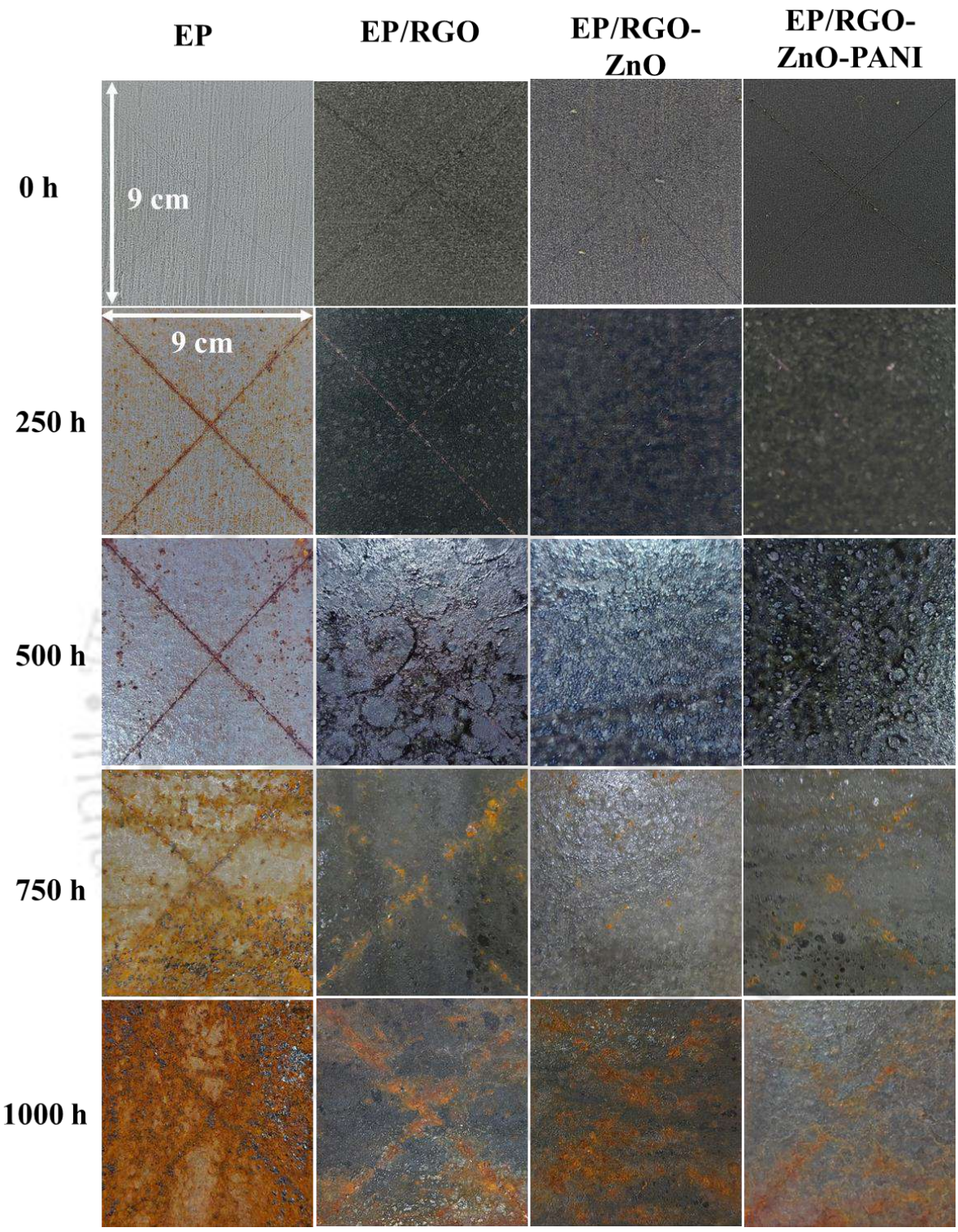

Fig. 7.12 Optimized images of the salt spray analysis of MS coated with EP, 0.5 wt% EP/RGO, EP/RGO-ZnO, and EP/RGO-ZnO-PANI after 0, 250, 500, 750, 1000 h of salt spray and dimension MS plate is 9 × 9 × 0.5 cm^3.

7.4 Corrosion inhibition mechanism

Fig. 7.13 shows the schematic diagram of the interaction of EP, EP/RGO, EP/RGO-ZnO, and EP/RGO-ZnO-PANI coatings and corrosive electrolyte during the exposure of coated MS. Some fractures and micropores were formed in the epoxy coating, as illustrated in Fig. 7.5 (a). Additionally, dissolved oxygen and other corrosive fluids contribute to common defects in epoxy coatings (Wang et al., 2022, 2016). Corrosive electrolytes can easily penetrate the epoxy coating through these defects, reaching the surface of the MS substrate and causing severe corrosion (Zhang et al., 2022). The incorporation of inorganic or organic nanofillers into the epoxy matrix usually creates a solid barrier that obstructs the path of corrosive molecules that travel through the epoxy. Therefore, these corrosive species faced higher hindered and traveled more tortuous paths during their propagation through the polymer matrix, and these obstructions slowed down the penetration process (Wei et al., 2013; Weng et al., 2010). The number of defects was decreased in the epoxy coating with the incorporation of RGO nanosheets, which form compact structures, as shown in Fig. 7.5 (b). This compact structure hindered the penetration of corrosive species and provided better corrosion protection than pure epoxy, but still, this coating exhibited some pores due to the agglomeration of the RGO sheet. To resolve this issue, ZnO nanorods were decorated on the RGO nanosheet, which hindered their restacking and resulted in a large uniform distribution of RGO-ZnO in the polymer matrix, creating a smoother surface (Fig. 7.5 (c)) and significantly enhanced corrosion-protecting properties as compared to EP/RGO coating. Moreover, adding RGO-ZnO-PANI into the epoxy matrix makes a denser and more intact structure, as shown in Fig. 7.5 (d), than all other prepared coatings. EP/RGO-ZnO-PANI coating provided superior corrosion protecting and adhesion properties to MS surface against 3.5 wt% NaCl solution. These findings are also supported by the FTIR analysis (Fig. 7.6).

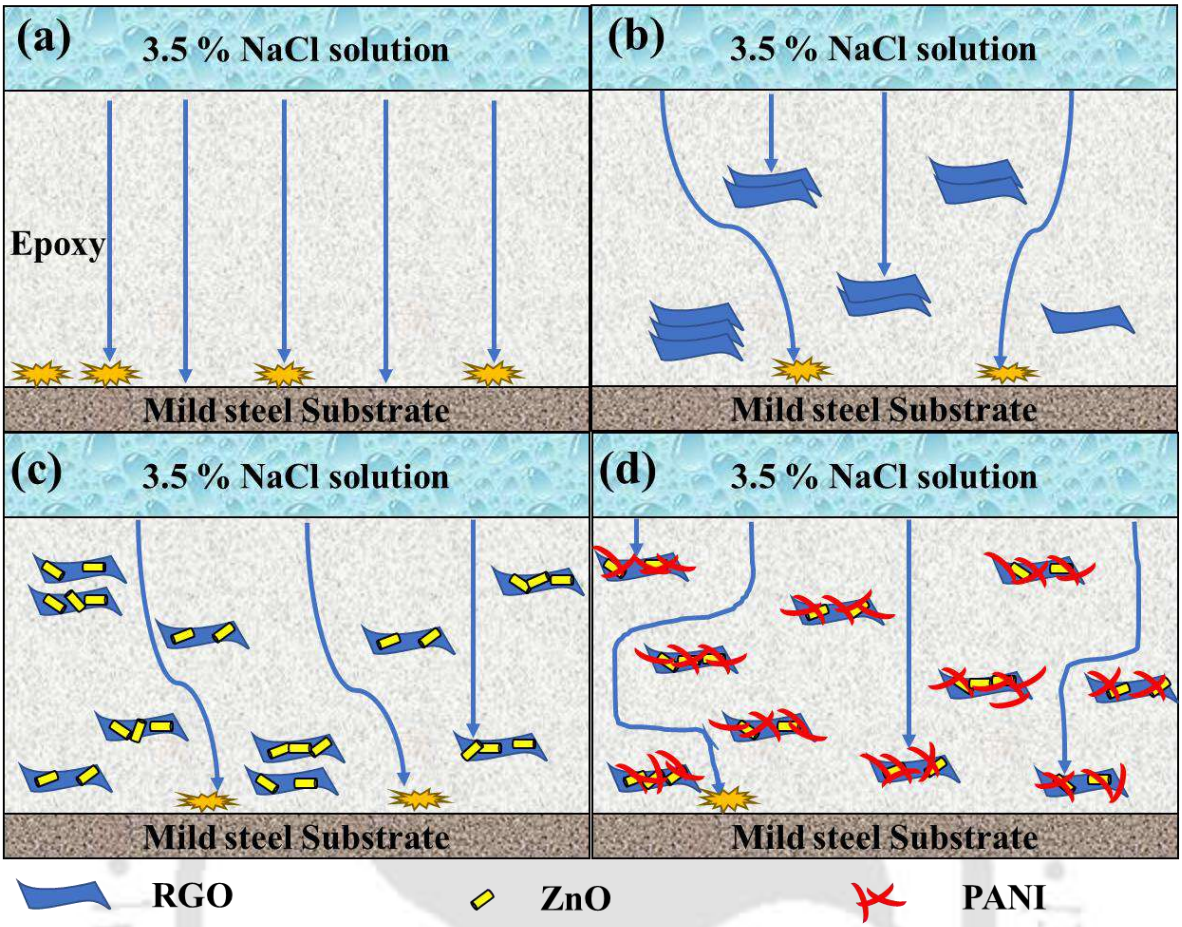

Fig. 7.13 Schematic diagram of the corrosion protective mechanism for (a) pure EP coating, (b) EP/RGO coating, (c) EP/RGO-ZnO coating, and (d) EP/RGO-ZnO-PANI coating.

7.5 Literature comparison

In this work, the anticorrosive behavior of prepared coatings was investigated by potentiodynamic polarization tests after one day of immersion in 3.5% NaCl. The obtained inhibition efficiency of EP/RGO-ZnO-PANI nanocomposite coatings was compared with recently reported coatings, such as epoxy/FGO (Dhongde et al., 2023), CS-g-SA/epoxy (Shamsheera et al., 2019), RHQD/epoxy(Dhongde et al., 2024), and Bt@PDA@LM(Zhang et al., 2022). For example, Dhongde et al., have used Epoxy/FGO composite coating to mitigate the carbon steel corrosion in 3.5% NaCl solution. They found that corrosion current density

significantly decreased for the coated sample and achieved 99.90% inhibition efficiency at a 2 wt% loading of FGO in epoxy coating (Dhongde et al., 2023). Shamsheera et al. have prepared the CS-g-SA/epoxy coatings to reduce mild steel corrosion. During corrosion studies, CS-g-SA/epoxy coatings demonstrated outstanding anticorrosive properties and exhibited 94.94% inhibition efficiency compared to blank(Shamsheera et al., 2019). The comparison of all these studies with the present work is represented in Table 7.4, and this Table displays that the present work exhibited a clear superiority among all listed studies.

Table 7.4 Comparison of Tafel parameters for EP/RGO-ZnO-PANI coatings with recently reported studies after 1-day immersion in 3.5 wt% NaCl.

Metal	*Optimum loading (wt%)*	*Coating*	E_{corr} (mV vs. Ag/AgCl)	i_{corr} (µA cm^{-2})	R_p (Ω cm^2)	μ_P (%)	Source
Carbon steel	2	Epoxy/FGO	-211.00	0.10	2.52×10^6	99.90	(Dhongde et al., 2023)
Carbon steel	_	Bt@PDA@LM	-0.838	2.05	_	82.63	(Zhang et al., 2022)
Mild steel	_	CS-g-SA/epoxy	-337.08	0.0016	12.19×10^3	94.94	(Shamsheera et al., 2019)
Carbon steel	0.5	RHQD/epoxy	-547.00	0.01	1.45×10^7	99.88	(Dhongde et al., 2024)
Mild steel	0.5	EP/ RGO-ZnO-PANI	-581.33	0.0053	1.51×10^6	99.98	**Present work**

7.6 Summary

In this study, a ternary RGO-ZnO-PANI nanocomposite was successfully prepared by wrapping PANI on RGO-ZnO composite through an in-situ polymerization process, and it was incorporated into epoxy coating through the solution blending technique. The corrosion

protection properties of coated mild steel (MS) with nanofiller-containing coatings were investigated by potentiodynamic polarization (PDP), electrochemical impedance spectroscopy (EIS), and salt spray tests. Based on all analysis following conclusions can be drawn:

- The morphology, chemical structure, thermal stability, and wettability of EP, EP/RGO, EP/RGO-ZnO, and EP/RGO-ZnO-PANI nanocomposite coatings were investigated using FESEM, FTIR, TGA, and contact angle measurements.
- Results revealed that the EP/RGO-ZnO-PANI coating exhibited the smoothest surface, superior thermal stability, and enhanced hydrophobicity. These improvements are attributed to the formation of a more compact and robust structure between the RGO-ZnO-PANI composite and epoxy matrix.
- PDP results revealed that EP/RGO-ZnO-PANI nanocomposite coating exhibited the highest inhibitory efficiency of about 99.98% against 3.5 wt% NaCl after its 1-day immersion.
- EIS findings demonstrated the better anti-corrosive behavior of EP/RGO-ZnO-PANI nanocomposite coating even after 45 days of immersion in 3.5 wt% NaCl compared to other coatings.
- Salt spray analysis show that EP/RGO-ZnO-PANI coating provided superior protection to MS up to 1000 h as compared to other coatings.

7.7 References

Ahmad, A.F., Ab Aziz, S., Abbas, Z., Obaiys, S.J., Khamis, A.M., Hussain, I.R., Zaid, M.H.M., 2018. Preparation of a chemically reduced graphene oxide reinforced epoxy resin polymer as a composite for electromagnetic interference shielding and microwave-absorbing applications. Polymers (Basel). 10, 1180. https://doi.org/10.3390/polym10111180

Ain, Q.T., Haq, S.H., Alshammari, A., Al-Mutlaq, M.A., Anjum, M.N., 2019. The systemic effect of PEG-nGO-induced oxidative stress in vivo in a rodent model. Beilstein J. Nanotechnol. 10, 901–911. https://doi.org/10.3762/BJNANO.10.91

Aradhana, R., Mohanty, S., Nayak, S.K., 2019. High performance electrically conductive epoxy/reduced graphene oxide adhesives for electronics packaging applications. J. Mater. Sci. Mater. Electron. 30, 4296–4309. https://doi.org/10.1007/s10854-019-00722-5

Aradhana, R., Mohanty, S., Nayak, S.K., 2018. Comparison of mechanical, electrical and thermal properties in graphene oxide and reduced graphene oxide filled epoxy nanocomposite adhesives. Polymer (Guildf). 141, 109–123. https://doi.org/10.1016/j.polymer.2018.03.005

Bhan, C., Kumar Golder, A., 2023. Bio-based hierarchical vertically aligned 2D ZnO nanostructures for ultra selective electrochemical sensing of p-Chloroaniline. Chem. Eng. J. 475, 146122. https://doi.org/10.1016/j.cej.2023.146122

Bian, H., Zhang, G., Zhai, Q., Du, Y., Ma, Y., Yang, B., Tang, S., Bin, D., Meng, X., Lu, H., 2023. Enhanced corrosion resistance by polypyrrole and $Ti_3C_2T_x$-acrylic epoxy double-layer coating for 304SS bipolar plates of PEMFC. J. Ind. Eng. Chem. 122, 520–528. https://doi.org/10.1016/j.jiec.2023.03.015

Castela, A.S., Simões, A.M., 2003. An impedance model for the estimation of water absorption in organic coatings. Part I: A linear dielectric mixture equation. Corros. Sci. 45, 1631–1646. https://doi.org/10.1016/S0010-938X(03)00014-3

Cheng, L., Liu, C., Wu, H., Zhao, H., Wang, L., 2022. Interfacial assembled mesoporous polydopamine nanoparticles reduced graphene oxide for high performance of waterborne epoxy-based anticorrosive coatings. J. Colloid Interface Sci. 606, 1572–1585. https://doi.org/10.1016/j.jcis.2021.08.150

Cui, J., Bao, Y., Sun, Y., Wang, H., LI, J., 2023. Critical factors on corrosion protective waterborne coatings containing functionalized graphene oxide: A review. Compos. Part A Appl. Sci. Manuf. 174, 107729. https://doi.org/10.1016/j.compositesa.2023.107729

Das, P., Mandal, B., Gumma, S., 2020. Engineering of structural and surface functional characteristics of graphite oxide nanosheets by controlling oxidation temperature. Appl. Surf. Sci. 504, 144444. https://doi.org/10.1016/j.apsusc.2019.144444

Dhongde, N.R., Baranwal, P.K., Rajaraman, P.V., 2023. Functionalization of graphene oxide with an ionic liquid (1-butyl-3-methylimidazolium acetate): Preparation of epoxy-based coating on carbon steel for anticorrosive applications. J. Appl. Polym. Sci. 140, 1–17. https://doi.org/10.1002/app.54026

Dhongde, N.R., Das, N.K., Banerjee, T., Rajaraman, P.V., 2024. Synthesis of carbon quantum dots from rice husk for anti-corrosive coating applications: Experimental and theoretical

investigations. Ind. Crops Prod. 212, 118329. https://doi.org/10.1016/j.indcrop.2024.118329

Garg, R., Gupta, R., Singh, N., Bansal, A., 2021. Characterization and performance evaluation of synthesized ZnO nanoflowers, nanorods, and their hybrid nanocomposites with graphene oxide for degradation of Orange G. Environ. Sci. Pollut. Res. 28, 57009–57029. https://doi.org/10.1007/s11356-021-14511-3

Goswami, R.N., Mourya, P., Saini, R., Pandey, A., Konathala, L., Ray, A., Khatri, O.P., 2024. Polyaniline-wrapped h-boron nitride nanosheets as anticorrosive filler in epoxy coatings for substantially enhanced protection of mild steel. J. Ind. Eng. Chem. 140, 285–297. https://doi.org/10.1016/j.jiec.2024.05.048

Guo, L., Gu, C., Feng, J., Guo, Y., Jin, Y., Tu, J., 2020. Hydrophobic epoxy resin coating with ionic liquid conversion pretreatment on magnesium alloy for promoting corrosion resistance. J. Mater. Sci. Technol. 37, 9–18. https://doi.org/10.1016/j.jmst.2019.06.024

Guo, S., Lu, Y., Wan, X., Wu, F., Zhao, T., Shen, C., 2020. Preparation, characterization of highly dispersed reduced graphene oxide/epoxy resin and its application in alkali-activated slag composites. Cem. Concr. Compos. 105, 103424. https://doi.org/10.1016/j.cemconcomp.2019.103424

Han, Q., Xu, J., Shi, J., Zhou, M., Wang, H., Geng, L., Xiong, J., Du, Z., 2025. Structural and hetero-interfacial engineering of magnetic bimetallic composites based polyurethane microwave absorbing coating for marine environment. Compos. Part A Appl. Sci. Manuf. 192, 108770. https://doi.org/10.1016/j.compositesa.2025.108770

Hu, D., Jiang, P., Huang, X., 2022. Mixed-dimensional engineering of 3D MXene ultralight hybrid aerogel for anticorrosive and microwave absorption applications. Compos. Part A Appl. Sci. Manuf. 156, 106865. https://doi.org/10.1016/j.compositesa.2022.106865

Huang, T.-C., Yeh, T.-C., Huang, H.-Y., Ji, W.-F., Chou, Y.-C., Hung, W.-I., Yeh, J.-M., Tsai, M.-H., 2011. Electrochemical studies on aniline-pentamer-based electroactive polyimide coating: Corrosion protection and electrochromic properties. Electrochim. Acta 56, 10151–10158. https://doi.org/10.1016/j.electacta.2011.08.114

Jayachandiran, J., Yesuraj, J., Arivanandhan, M., Raja, A., Suthanthiraraj, S.A., Jayavel, R., Nedumaran, D., 2018. Synthesis and electrochemical studies of rGO/ZnO nanocomposite for supercapacitor application. J. Inorg. Organomet. Polym. Mater. 28, 2046–2055. https://doi.org/10.1007/s10904-018-0873-0

Jayakumar, N., Gopalan, N.K., 2024. Improved anticorrosive performance of epoxy coating by

introducing a one-pot synthesised nano-ceria embedded lamellar polyaniline/kaolinite hybrid. J. Ind. Eng. Chem. 139, 313–324. https://doi.org/10.1016/j.jiec.2024.05.010

Ji, X., Seif, A., Duan, J., Rashidi, A., Zhou, Z., Pourhashem, S., Mirzaee, M., Zhai, X., Zhao, X., Hou, B., 2022a. Experimental and DFT studies on corrosion protection performance of epoxy/graphene quantum dots@TiO_2 nanotubes coatings. Constr. Build. Mater. 322, 126501. https://doi.org/10.1016/j.conbuildmat.2022.126501

Ji, X., Wang, W., Zhao, X., Wang, L., Ma, F., Wang, Y., Duan, J., Hou, B., 2022b. Poly(dimethyl siloxane) anti-corrosion coating with wide pH-responsive and self-healing performance based on core−shell nanofiber containers. J. Mater. Sci. Technol. 101, 128–145. https://doi.org/10.1016/j.jmst.2021.06.014

Kobbekaduwa, D., Nanayakkara, O., Krevaikas, T., Di Sarno, L., 2024. Effect of organic corrosion inhibitors on the behaviour of repair mortars and reinforcement corrosion. Constr. Build. Mater. 451, 138787. https://doi.org/10.1016/j.conbuildmat.2024.138787

Liu, C., Du, P., Zhao, H., Wang, L., 2018. Synthesis of L-Histidine-attached graphene nanomaterials and their application for steel protection. ACS Appl. Nano Mater. 1, 1385–1395. https://doi.org/10.1021/acsanm.8b00149

Liu, S., Wang, X., Yin, Q., Xiang, X., Fu, X.-Z., Wang, X.-Z., Luo, J.-L., 2022. A facile approach to fabricating graphene/waterborne epoxy coatings with dual functionalities of barrier and corrosion inhibitor. J. Mater. Sci. Technol. 112, 263–276. https://doi.org/10.1016/j.jmst.2021.07.061

Lv, Y., Zhao, W., Qiang, Y., Zhao, J., 2023. Constructing the interface of g-C_3N_4/epoxy composites using carbon quantum dots to achieve self-repairing, early corrosion monitoring and superior anticorrosion performance. Corros. Sci. 225, 111601. https://doi.org/10.1016/j.corsci.2023.111601

Mehto, V.R., Mehto, A., Gupta, D.K., Pandey, R.K., 2016. Synthesis and characterization of PANI/ZnO nanocomposites. J. Chinese Chem. Soc. 63, 935–946. https://doi.org/10.1002/jccs.201600069

Meng, F., Liu, L., Cui, Y., Wang, F., 2021. Evaluation of coating resistivity for pigmented/unpigmented epoxy coatings under marine alternating hydrostatic pressure. J. Mater. Sci. Technol. 64, 165–175. https://doi.org/10.1016/j.jmst.2019.09.011

Pan, K., Yang, S., Tao, X., Xi, Z., Lin, Y., Wang, L., Huang, C., Li, X., 2024. Enhancing corrosion resistance and toughness of solvent-free epoxy coatings with low-viscosity fluorine-containing hyperbranched polyether. Prog. Org. Coatings 187, 108149.

https://doi.org/10.1016/j.porgcoat.2023.108149

Rajitha, K., Mohana, K.N.S., Hegde, M.B., Nayak, S.R., Swamy, N.K., 2020. Fabrication of ZnO/rGO and ZnO/MWCNT nanohybrids to reinforce the anticorrosion performance of polyurethane coating. FlatChem 24, 100208. https://doi.org/10.1016/j.flatc.2020.100208

Ravi, R., Bhan, C., Golder, A.K., 2025. Bio-analytic synthesis of Cu-doped TiO_2 for photocatalytic degradation of ciprofloxacin under visible light. Opt. Mater. (Amst). 159, 116577. https://doi.org/10.1016/j.optmat.2024.116577

Shamsheera, K.O., Prasad, A.R., Garvasis, J., Basheer, S.M., 2019. Stearic acid grafted chitosan / epoxy blend surface coating for prolonged protection of mild steel in saline environment. J. Adhes. Sci. Technol. 33, 2250–2264. https://doi.org/10.1080/01694243.2019.1637170

Siva, T., Kamaraj, K., Sathiyanarayanan, S., 2014. Epoxy curing by polyaniline (PANI) – characterization and self-healing evaluation. Prog. Org. Coatings 77, 1095–1103. https://doi.org/10.1016/j.porgcoat.2014.03.019

Tai, H., Yuan, Z., Zheng, W., Ye, Z., Liu, C., Du, X., 2016. ZnO nanoparticles/reduced graphene oxide bilayer thin films for improved NH_3-sensing performances at room temperature. Nanoscale Res. Lett. 11, 3-8. https://doi.org/10.1186/s11671-016-1343-7

Tang, G., Hou, X., Wang, Y., Yan, Z., Ren, T., Ma, L., Huang, X., Wang, C., 2022. Hexagonal boron nitride/polyaniline nanocomposites for anticorrosive waterborne epoxy coatings. ACS Appl. Nano Mater. 5, 361–372. https://doi.org/10.1021/acsanm.1c03173

Wang, X., Li, C., Zhang, M., Lin, D., Yuan, S., Xu, F., Zhou, Y., Wang, C., Zhu, Y., Wang, H., 2022. A novel waterborne epoxy coating with anti-corrosion performance under harsh oxygen environment. Chem. Eng. J. 430, 133156. https://doi.org/10.1016/j.cej.2021.133156

Wang, Z., Yu, J., Zhang, X., Li, N., Liu, B., Li, Yanyan, Wang, Y., Wang, W., Li, Yezhou, Zhang, L., Dissanayake, S., Suib, S.L., Sun, L., 2016. Large-scale and controllable synthesis of graphene quantum dots from rice husk biomass: A comprehensive utilization strategy. ACS Appl. Mater. Interfaces 8, 1434–1439. https://doi.org/10.1021/acsami.5b10660

Wei, H., Ding, D., Wei, S., Guo, Z., 2013. Anticorrosive conductive polyurethane multiwalled carbon nanotube nanocomposites. J. Mater. Chem. A 1, 10805. https://doi.org/10.1039/c3ta11966a

Weng, C.-J., Huang, J.-Y., Huang, K.-Y., Jhuo, Y.-S., Tsai, M.-H., Yeh, J.-M., 2010. Advanced

anticorrosive coatings prepared from electroactive polyimide–TiO_2 hybrid nanocomposite materials. Electrochim. Acta 55, 8430–8438. https://doi.org/10.1016/j.electacta.2010.07.063

Wu, H., Lin, S., Chen, C., Liang, W., Liu, X., Yang, H., 2016. A new ZnO/rGO/polyaniline ternary nanocomposite as photocatalyst with improved photocatalytic activity. Mater. Res. Bull. 83, 434–441. https://doi.org/10.1016/j.materresbull.2016.06.036

Xia, Y., Tong, L., Feng, X., Xiang, H., He, Y., Liu, X., 2024. Effects of polydopamine functionalized graphitic carbon nitride-cerium oxide nanofiller on the corrosion resistance of epoxy coating. Prog. Org. Coatings 187, 108111. https://doi.org/10.1016/j.porgcoat.2023.108111

Yao, H., Bi, W., Yin, X., Mu, S., Sha, S., Wang, N., 2023. Effect of boron nitride modified by sodium tripolyphosphate on the corrosion resistance of waterborne epoxy coating. J. Coatings Technol. Res. 20, 1513–1527. https://doi.org/10.1007/s11998-022-00637-7

Zhang, C., Dai, X., Wang, Y., Sun, G., Li, P., Qu, L., Sui, Y., Dou, Y., 2019. Preparation and corrosion resistance of ETEO modified graphene oxide/epoxy resin coating. Coatings 9, 46. https://doi.org/10.3390/coatings9010046

Zhang, H.-L., Liu, J.-Y., Zuo, X.-B., Tian, J.-L., Zou, Y.-X., 2023. A composite epoxy coating with a newly synthetic BN@SiO_2 filler and its improvement on the durability of cement-based materials. Constr. Build. Mater. 404, 133272. https://doi.org/10.1016/j.conbuildmat.2023.133272

Zhang, M., Xu, F., Lin, D., Peng, J., Zhu, Y., Wang, H., 2022. A smart anti-corrosion coating based on triple functional fillers. Chem. Eng. J. 446, 137078. https://doi.org/10.1016/j.cej.2022.137078

Zhang, Yuefang, Liu, Jia, Zhang, Yahong, Liu, Jin, Duan, Y., 2017. Facile synthesis of hierarchical nanocomposites of aligned polyaniline nanorods on reduced graphene oxide nanosheets for microwave absorbing materials. RSC Adv. 7, 54031–54038. https://doi.org/10.1039/c7ra08794b

Zhou, Z., Wang, Z., Niu, R., Huang, S., Cairney, J.M., Fan, X., Chen, E.Y.-S., 2025. Enhancing maritime corrosion resistance of epoxy coating on steels by using rust conversion and graphene-based composites. Compos. Part A Appl. Sci. Manuf. 192, 108793. https://doi.org/10.1016/j.compositesa.2025.108793

Chapter 8:

Overall conclusions and scope for future works

Overall conclusions and scope for future works

This chapter summarizes the conclusions of the work presented in this thesis, based on the obtained findings from the anticorrosive behavior of the used inhibitors and coating. Additionally, it offers some valuable recommendations for future research in this field.

8.1 Overall conclusions

The work presented in this thesis exhibited the preparation, characterization, and anticorrosive behaviors of green corrosion inhibitors and epoxy-based coatings. Herein, we have successfully developed ecofriendly corrosion inhibitor and EP/RGO-ZnO-PANI coatings to protect the mild steel in 1 M HCl and 3.5% NaCl solutions, respectively.

Results of weight loss and electrochemical techniques confirmed the excellent corrosion-inhibiting behavior of all developed inhibitors. These corrosion inhibitors behaved as a mixed-type of inhibitors because corrosion potential was not significantly sifted in inhibitor-containing systems compared to their absence. These inhibitors showed a decline in their inhibition efficiency with increasing the temperature, but they were effective in attaining a satisfactory inhibition efficiency at 323K temperature. A rise in E_a values was recorded in the presence of inhibitors, which signifies that higher energy is required to corrode the metal in inhibited systems than in blank. Adsorption studies explored that used inhibitors followed the Langmuir adsorption model to adsorb on metal surfaces. Obtained values of thermodynamic parameters confirmed that metal corrosion is a spontaneous and endothermic process.

Furthermore, electrochemical and salt spray techniques were used to investigate the corrosion-inhibiting behavior of coatings. PDP test displayed that EP/RGO-ZnO-PANI nanocomposite coatings exhibited higher corrosion inhibition efficiency among all other prepared coatings after 1-day immersion in 3.5% NaCl. EIS and Salt spray tests revealed that EP/RGO-ZnO-PANI nanocomposite coatings exhibited the strongest corrosion inhibiting properties during the whole exposure as compared to other coatings. Some major conclusions from the study are summarized as follows:

8.1.1 Corrosion inhibition by chayote extracts

- The presence of ascorbic acid in chayote extract was confirmed by FTIR analysis.
- The values of i_{corr} were reduced with the addition of chayote extracts.

- Maximum inhibitory efficiencies of 76.82 and 85.72% were achieved at 2000 mg L^{-1} of CE and CEPH3, respectively.
- R_{ct} using CE and CEPH3 inhibitor were determined to be about 3.38 and 5.63 times higher than blank.
- CEPH3 inhibitor showed remarkable inhibition efficiency of 71.88 % at 323 K.
- ΔG^{o}_{ads} value of CE (-53.046 < -40) and CEPH3 (-50.278 < -40) indicated the chemisorption of inhibitors.
- Surface investigations confirmed that chayote extracts form a strong protective layer over the metal, which significantly hinders MS corrosion.

8.1.2 Corrosion inhibition by Tinda extracts

- Phenol, 3,5-bis (1,1-dimethylethyl)-, 9-octadecenoic acid, methyl ester, hexadecanoic acid 15-methyl-, methyl ester, 9, 12-octadecadienoic acid, methyl ester, 9, 12, 15-octadecatrienoic acid, methyl ester, (Z,Z,Z-), ascorbic acid, and phytol, were identified in TPE and TFE by LC-MS and FTIR analysis.
- The values of i_{corr} and inhibition efficiencies were decreased and increased, respectively, with increasing inhibitor concentration.
- Maximum inhibitory efficiencies of 83.73 and 87.11% were achieved at 200 mg L^{-1} of TPE and TFE, respectively.
- R_{ct} was increased from 25.89 to 125.18 Ω cm^2 (TPE) and 142.69 Ω cm^2 (TFE) at 200 mg L^{-1}.
- TPE and TFE exhibited significant inhibitory effects with 70.71 and 72.74 % inhibition efficiency at 323 K.
- TFE has greater inhibition efficiency than TPE.

- ΔG°_{ads} for TPE and TFE confirmed preferentially physical adsorption (mix-type adsorption).
- Surface investigations demonstrated the formation of a corrosion inhibiting layer by adsorbed extract molecules on the metal surface.

8.1.3 Corrosion inhibition by *Phaseolus lunatus* extracts

- Lysine, leucine, linoleic acid, oleic acid, 9-Octadecenoic acid (Z)-, methyl ester, and ascorbic acid were identified in PLPE and PLSE by LC-MS and FTIR analyses.
- i_{corr} was decreased with the addition of PLPE or PLSE.
- 85.69% and 90.78% inhibition efficiencies were obtained at 200 mg L^{-1} of PLPE and PLSE, respectively.
- R_{ct} was increased from 25.89 to 172.31 Ω cm^2 (PLPE) and 227.07 Ω cm^2 (PLSE) at 200 mg L^{-1}.
- PLPE and PLSE demonstrate good inhibitory effects with 71.92 and 78.43% inhibitory efficiencies at 323 K.
- Surface characterizations revealed that PLPE and PLSE adsorbed on MS surface and build a defensive layer, which significantly mitigate MS dissolution.

8.1.4 Corrosion inhibition by *Duranta erecta* extracts

- Presence of *Ethanone, 1-(2-hydroxy-5-methylphenyl)-, 4,7-Dimethoxy-2-methyl-2,3-dihydro-1 H-inden-1-one, Isopropyl Myristate, 9-Octadecenamide, n-Hexadecanoic acid, and 7,10,13-Eicosatrienoic acid, methyl ester in Duranta erecta extracts* was identified by LC-MS and FTIR analyses.
- Maximum inhibitory efficiencies of 90.82% and 91.82% were obtained at 200 mg L^{-1} of DEFE and DELE, respectively.

- R_{ct} shows a huge jump from 25.89 to 189.90 Ω cm^2 (DEFE) and 202.64 Ω cm^2 (DELE) at 200 mg L^{-1}.
- DEFE and DELE exhibited strong inhibitory effects with 78.84 and 80.80% at 323 K
- DELE has greater inhibition efficiency than DEFE.
- ΔG^{o}_{ads} (-29.00 kJ mol^{-1} for DEFE and -29.90 kJ mol^{-1} for DELE) demonstrated that inhibitor favored physical adsorption.
- Surface analyses confirmed that *Duranta erecta* extracts formed a corrosion-inhibiting film on MS surface, which effectively reduced MS degradation.

Obtained inhibition efficiency of CEPH3, TFE, PLSE, and DELE at their optimum concentration and different temperature were compared and assembled in the following Tables 8.1 and 8.2, respectively, which showed that inhibition efficiencies were decreased with temperature, and DELE exhibited superiority of among the all inhibitors.

Table 8.1 Tafel parameters of CEPH3, TFE, PLSE, and DELE at their optimum concentrations.

Inhibitor	Conc. (mg L^{-1})	i_{corr} (µA cm^{-2})	μ_P (%)
Blank	0	734.98 ± 5.23	_
CEPH3	2000	104.92 ± 1.66	85.72 ± 0.40
TFE	200	95.29 ± 1.51	87.11 ± 0.50
PLSE	200	67.77 ± 0.85	90.78 ± 0.44
DELE	200	60.15 ± 0.63	91.82 ± 0.97

Table 8.2 Inhibition efficiencies from Tafel analysis for the optimum concentration of CEPH3, TFE, PLSE, and DELE at 303, 313, and 323 K.

Inhibitor	Inhibition efficiency (μ_P (%))	Temperature		
		303 K	313 K	323 K
CEPH3		85.72 ± 0.40	74.18 ± 0.44	71.88 ± 0.13
TFE		87.11 ± 0.50	77.80 ± 0.48	72.74 ± 0.15
PLSE		90.78 ± 0.44	84.90 ± 0.76	78.43 ± 0.30
DELE		91.82 ± 0.97	86.51 ± 0.53	80.80 ± 0.18

8.1.5 Corrosion inhibition by EP/RGO-ZnO-PANI nanocomposite coating

- We have successfully synthesized a ternary RGO-ZnO-PANI nanocomposite by wrapping of PANI onto the RGO-ZnO surface via an in-situ polymerization process.
- PDP results showed EP/RGO-ZnO-PANI nanocomposite coating exhibited the highest inhibitory efficiency of about 99.98% against 3.5 wt% NaCl after its 1-day immersion.
- EIS findings demonstrated the better anti-corrosive behavior of EP/RGO-ZnO-PANI nanocomposite coating after 45 days of immersion in 3.5 wt% NaCl compared to other coatings.
- Salts spray analysis shows that EP/RGO-ZnO-PANI coating provided superior protection to MS up to 1000 h as compared to other prepared coatings.

In this work, all developed inhibitors demonstrated strong corrosion inhibiting potential to mitigate mild steel corrosion in the acidic medium at their optimum concentration. Among these inhibitors, DELE showed the highest inhibition effect and demonstrated maximum thermal stability. Furthermore, electrochemical analysis, surface characterizations, and salt spray tests confirm that epoxy coating containing RGO-ZnO-PANI nanocomposite exhibited

the highest anti-corrosion performance in NaCl solutions as compared to other coatings. The findings of this research provide valuable reference data for future research in developing economically viable and sustainable corrosion inhibitors and epoxy coatings. The proposed bio-extracts and nanocomposite coatings demonstrate significant potential for industrial scalability due to the availability of natural resources, low-cost synthesis routes, and compatibility with existing coating processes. Moreover, the use of plant-based bio-extracts ensures biodegradability and minimizes ecological impact. The developed materials are inherently non-toxic and environmentally safe, aligning with green chemistry principles and sustainable materials development as reported by previous literature findings for green synthesized nanomaterials. Although a detailed study on the life cycle assessment of the nanocomposite could be a part of the future scope of the present research work.

8.2 Scope for future works

Based on the findings of this thesis, the following future research directions are proposed:

- Corrosion inhibiting potential of proposed inhibitors can be further explored in different corrosive environments, including sulfuric acid, phosphoric acid, nitric acid, sodium hydroxide, and sodium chloride solutions.
- These extracts also can be used to mitigate the corrosion of various metals, such as copper, zinc, and brass.
- The anticorrosive behavior of EP/RGO-ZnO-PANI coatings can be tested in H_2S, CO_2, and acidic environments.
- The adsorption mechanisms and surface interactions of the inhibitors and coatings with metal can be further studied using density functional theory, molecular dynamics, and Monte Carlo simulations to gain molecular-level insights into their corrosion inhibition behavior.

- Long-term durability of proposed inhibitors and coatings can be further investigated in real-world conditions including variations in process parameters like temperature, pressure, and composition of electrolyte, to assess their industrial applicability and stability.
- A comprehensive life-cycle assessment of the developed green inhibitors and coatings will be carried out to evaluate their possible emissions to air, water, and soil, and to assess their overall environmental impacts, including global warming potential (GWP) and marine and terrestrial ecotoxicity potentials (MAEP/TEP).

Appendix

Appendix 3A

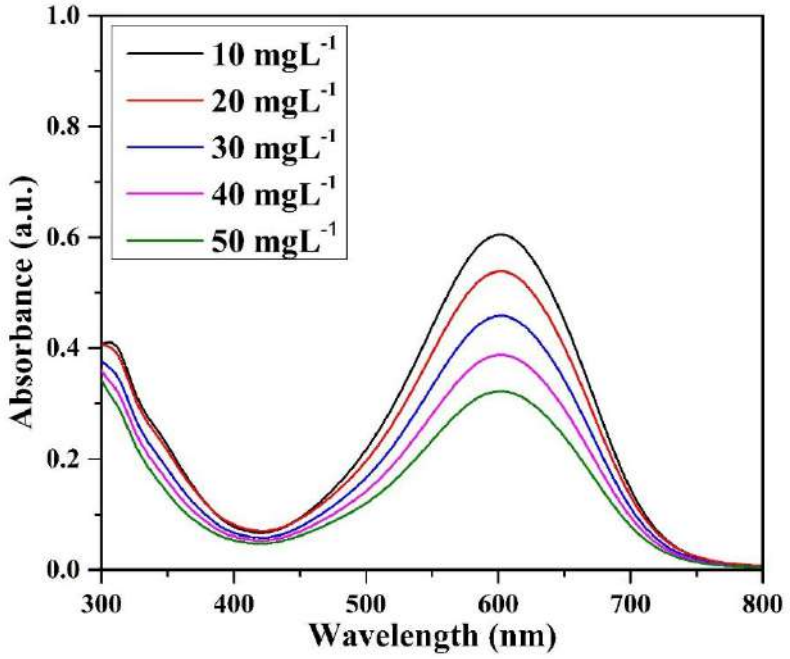

Fig. 3A.1 UV-Vis spectrum of standard ascorbic acid.

Table 3A.1 Preparation of chayote extract solutions.

Initial CE conc. (mg L^{-1})	CE volume (µL)	Distilled water volume (mL)	HCl volume (mL) [12.178 M]	Final CE conc. (mg L^{-1})	Final HCl Conc. (M)
7,50,000	46.67	64.205	5.748	500	1.0
7,50,000	93.33	64.159	5.748	1,000	1.0
7,50,000	140.00	64.112	5.748	1,500	1.0
7,50,000	186.67	64.065	5.748	2,000	1.0

Table 3A.2 Comparison of CR values determined by WL and PDP methods, along with R_p values obtained from PDP and EIS techniques.

Inhibitor	Concentration (mg L^{-1})	*CR* (mm $year^{-1}$)		R_p (Ω cm^2)	
		WL	PDP	PDP	EIS
Blank	0	7.93 ± 0.50	8.54 ± 0.45	34.04 ± 0.12	25.89 ± 0.14
CE	500	4.81 ± 0.51	4.77 ± 0.50	58.41 ± 0.03	42.80 ± 0.12
	1000	3.61 ± 0.43	3.55 ± 0.44	68.23 ± 0.05	56.66 ± 0.15
	1500	2.52 ± 0.28	2.60 ± 0.31	79.55 ± 0.18	68.60 ± 0.21
	2000	1.88 ± 0.10	1.98 ± 0.12	109.74 ± 0.08	87.48 ± 0.29
CEPH3	500	4.44 ± 0.33	4.43 ± 0.35	54.94 ± 0.13	48.25 ± 0.14
	1000	2.89 ± 0.34	3.28 ± 0.38	72.34 ± 0.02	72.43 ± 0.28
	1500	2.12 ± 0.14	1.97 ± 0.12	92.21 ± 0.13	96.29 ± 0.54
	2000	1.26 ± 0.04	1.21 ± 0.03	177.48 ± 0.18	145.87 ± 0.81

**CR = Corrosion rate, WL= Weight loss, PDP= Potentiodynamic palarization, and EIS = Electrochemical impedance spectroscopy.*

Table 3A.3 The comparison Table for obtained inhibition efficiencies from weight loss, EIS, and PDP analysis, ANOVA (Single factor) test results.

Inhibitor	Conc. (mg L^{-1})	μ_{CR} (%)	μ_{Rct} (%)	μ_P (%)	*p-value*
Blank	0	-	-	-	-
CE	500	39.34 ± 0.93	39.50 ± 0.17	44.08 ± 0.27	1.73×10^{-11}
	1000	54.48 ± 0.94	54.30 ± 0.12	58.41 ± 0.73	
	1500	68.22 ± 0.58	62.25 ± 0.11	69.48 ± 0.76	
	2000	76.29 ± 0.50	70.40 ± 0.10	76.82 ± 0.54	
CEPH3	500	44.01 ± 0.39	46.34 ± 0.16	48.07 ± 0.49	1.34×10^{-13}
	1000	63.56 ± 0.72	64.25 ± 0.14	61.58 ± 0.44	
	1500	73.27 ± 0.94	73.11 ± 0.15	76.90 ± 0.07	
	2000	84.11 ± 0.58	82.25 ± 0.10	85.72 ± 0.40	

**p≤0.0001 indicates the reliability of the PDP data obtained from triplicate experiments at a confidence interval of 99.99%.*

Appendix 4A

Table 4A.1 Comparison of CR values determined by WL and PDP methods, along with R_p values obtained from PDP and EIS techniques.

Inhibitor	Concentration (mg L^{-1})	*CR* (mm $year^{-1}$)		R_p (Ω cm^2)	
		WL	PDP	PDP	EIS
Blank	0	7.93 ± 0.50	8.54 ± 0.45	34.04 ± 0.12	25.89 ± 0.14
TPE	50	3.25 ± 0.22	3.39 ± 0.23	62.00 ± 0.05	65.83 ± 0.19
	100	2.29 ± 0.11	2.27 ± 0.09	95.17 ± 0.08	90.30 ± 0.26
	150	1.79 ± 0.10	1.74 ± 0.08	153.52 ± 0.39	109.84 ± 0.37
	200	1.46 ± 0.07	1.40 ± 0.06	147.92 ± 0.13	125.18 ± 0.44
TFE	50	2.92 ± 0.15	2.97 ± 0.16	69.13 ± 0.17	74.08 ± 0.20
	100	1.97 ± 0.06	2.00 ± 0.05	104.81 ± 0.03	97.16 ± 0.33
	150	1.49 ± 0.09	1.44 ± 0.08	124.86 ± 0.23	127.97 ± 0.68
	200	1.11 ± 0.06	1.11 ± 0.05	158.47 ± 0.19	142.69 ± 0.84

**CR = Corrosion rate, WL= Weight loss, PDP= Potentiodynamic palarization, and EIS = Electrochemical impedance spectroscopy.*

Table 4A.2 The comparison Table for obtained inhibition efficiencies from gravimetric, EIS, and PDP analysis, ANOVA (Single factor) test results.

Inhibitor	Conc. (mg L^{-1})	μ_{CR} (%)	μ_{Rct} (%)	μ_P (%)	*p-value*
Blank	0	-	-	-	-
TPE	50	59.02 ± 1.10	60.81 ± 0.29	60.49 ± 0.36	1.10×10^{-9}
	100	71.12 ± 0.49	71.43 ± 0.18	73.51 ± 0.83	
	150	77.43 ± 0.46	76.51 ± 0.13	79.68 ± 0.97	
	200	81.59 ± 0.53	79.39 ± 0.12	83.73 ± 0.61	
TFE	50	63.18 ± 0.54	65.51 ± 0.25	65.35 ± 0.68	1.03×10^{-10}
	100	75.16 ± 0.95	73.45 ± 0.16	76.67 ± 0.56	
	150	81.21 ± 0.76	79.84 ± 0.13	83.22 ± 0.11	
	200	86.00 ± 0.30	81.92 ± 0.15	87.11 ± 0.50	

**p≤0.0001 indicates the reliability of the PDP data obtained from triplicate experiments at a confidence interval of 99.99%.*

Appendix 5A

Table 5A.1 Comparison of CR values determined by WL and PDP methods, along with R_p values obtained from PDP and EIS techniques.

Inhibitor	Concentration (mg L^{-1})	*CR* (mm $year^{-1}$)		R_p (Ω cm^2)	
		WL	PDP	PDP	EIS
Blank	0	7.93 ± 0.50	8.54 ± 0.45	34.04 ± 0.12	25.89 ± 0.14
PLPE	50	2.61 ± 0.12	2.81 ± 0.15	82.84 ± 0.22	75.97± 0.45
	100	1.97 ± 0.05	2.07 ± 0.11	114.58 ± 0.15	97.11 ± 0.30
	150	1.51 ± 0.07	1.57 ± 0.07	146.30 ± 0.27	129.95 ± 0.52
	200	1.15 ± 0.02	1.22 ± 0.04	153.23 ± 0.42	172.31 ± 0.88
PLSE	50	2.38 ± 0.13	2.50 ± 0.14	90.45 ± 0.19	83.87 ± 0.24
	100	1.65 ± 0.06	1.72 ± 0.06	126.05 ± 0.15	127.30 ± 0.38
	150	1.01 ± 0.03	1.08 ± 0.05	179.71 ± 0.42	190.52 ± 0.65
	200	0.75 ± 0.02	0.79 ± 0.03	204.08 ±0.21	227.07 ± 1.18

**CR = Corrosion rate, WL= Weight loss, PDP= Potentiodynamic palarization, and EIS = Electrochemical impedance spectroscopy.*

Table 5A.2 The comparison Table for obtained inhibition efficiencies of PLPE and PLSE from weight loss, EIS, and PDP analysis, ANOVA (Single factor) test results.

Inhibitor	Conc. (mgL^{-1})	μ_{CR} (%)	μ_{Rct} (%)	μ_P (%)	*p-value*
Blank	0	0	-	-	-
PLPE	50	67.09 ± 0.98	65.92 ± 0.23	67.11 ± 0.71	1.52×10^{-9}
	100	75.16 ± 0.75	73.34 ± 0.16	75.78 ± 0.44	
	150	80.96 ± 0.88	80.08 ± 0.21	81.66 ± 0.12	
	200	85.50 ± 0.65	84.97 ± 0.13	85.69 ± 0.87	
PLSE	50	69.99 ± 1.10	69.13 ± 0.17	70.74 ± 0.82	2.74×10^{-9}
	100	79.19 ± 0.97	79.66 ± 0.37	79.83 ± 0.61	
	150	87.26 ± 0.88	86.41 ± 0.14	87.33 ± 0.91	
	200	90.54 ± 0.45	88.60 ± 0.16	90.78 ± 0.44	

**p≤0.0001 indicates the reliability of the PDP data obtained from triplicate experiments at a confidence interval of 99.99%.*

Appendix 6A

Table 6A.1 Comparison of CR values determined by WL and PDP methods, along with R_p values obtained from PDP and EIS techniques.

Inhibitor	Concentration (mg L^{-1})	*CR* (mm $year^{-1}$)		R_p (Ω cm^2)	
		WL	PDP	PDP	EIS
Blank	0	7.93 ± 0.50	8.54 ± 0.45	34.04 ± 0.12	25.89 ± 0.14
DEFE	50	1.64 ± 0.10	1.64 ± 0.11	118.83 ± 0.34	117.01 ± 0.62
	100	1.18 ± 0.07	1.22 ± 0.10	144.08 ± 0.18	140.44 ± 0.50
	150	0.97 ± 0.04	0.96 ± 0.06	197.24 ± 0.44	163.16 ± 0.82
	200	0.73 ± 0.03	0.78 ± 0.02	258.14 ± 0.53	189.90 ± 0.75
DELE	50	1.27 ± 0.07	1.35 ± 0.12	143.63 ± 0.15	150.53 ± 0.48
	100	0.98 ± 0.03	0.95 ± 0.05	186.92 ± 0.54	175.76 ± 1.06
	150	0.74 ± 0.02	0.77 ± 0.02	196.58 ± 0.25	186.54 ± 0.76
	200	0.70 ± 0.04	0.70 ± 0.04	261.53 ± 0.68	202.64 ± 0.65

**CR = Corrosion rate, WL= Weight loss, PDP= Potentiodynamic palarization, and EIS = Electrochemical impedance spectroscopy.*

Table 6A.2 The comparison Table for obtained inhibition efficiencies from weight loss, EIS, and PDP analysis, ANOVA (Single factor) test results.

Inhibitor	Conc. (mg L^{-1})	μ_{CR} (%)	μ_{Rct} (%)	μ_P (%)	*p-value*
Blank	0	-	-	-	_
DEFE	50	79.32 ± 1.20	77.87 ± 0.15	80.75 ± 0.87	8.74×10^{-7}
	100	85.12 ± 0.85	81.56 ± 0.34	85.68 ± 0.47	
	150	87.77 ± 1.10	84.13 ± 0.11	87.95 ± 1.01	
	200	90.79 ± 0.45	86.37 ± 0.25	90.82 ± 0.16	
DELE	50	83.98 ± 0.98	82.80 ± 0.21	84.21 ± 0.40	9.32×10^{-6}
	100	87.64 ± 1.23	85.27 ± 0.31	88.91 ± 0.91	
	150	90.67 ± 1.10	86.12 ± 0.22	90.97 ± 0.70	
	200	91.17 ± 0.55	87.22 ± 0.42	91.82 ± 0.97	

**p≤0.0001 indicates the reliability of the PDP data obtained from triplicate experiments at a confidence interval of 99.99%.*

Appendix 7A

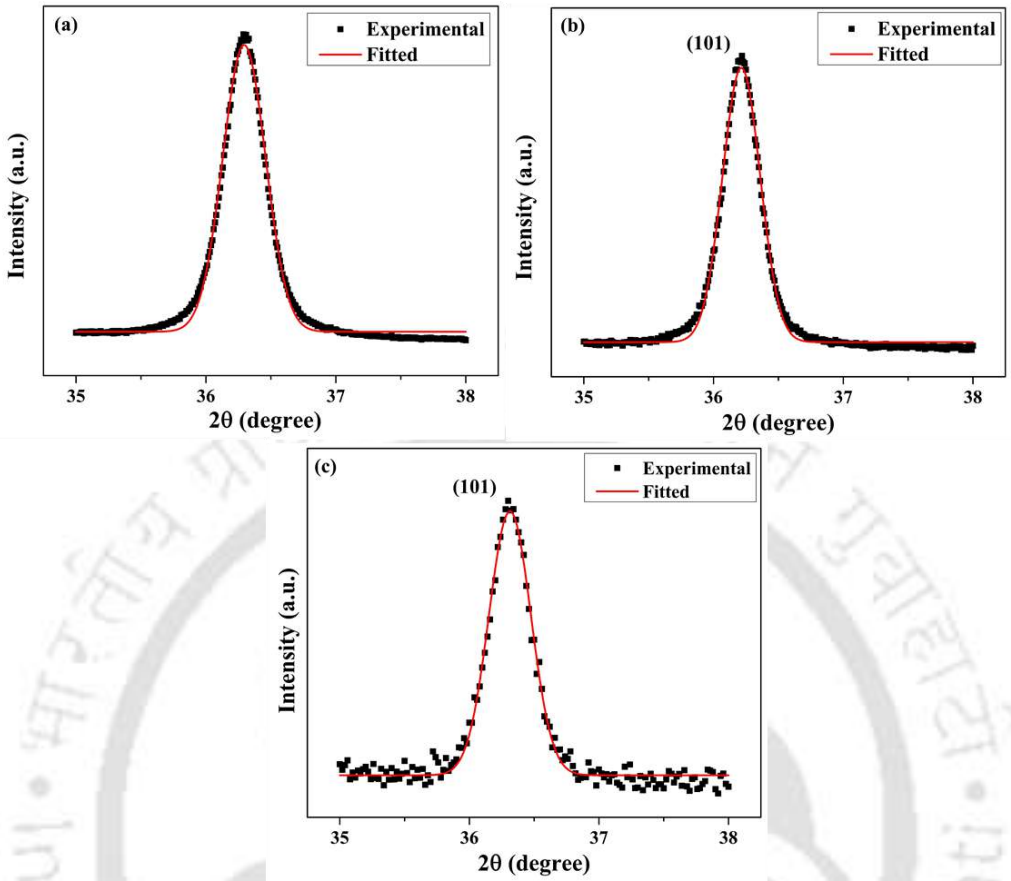

Fig. 7A.1. Deconvolution plots of (a) ZnO, (b) RGO-ZnO, and (c) RGO-ZnO-PANI for most prominent peak.

Table 7A.1 Tafel parameters for blank, EP, EP/RGO, EP/RGO-ZnO, and EP/RGO-ZnO-PANI coatings after 1-day immersion in 3.5 wt% NaCl, ANOVA (Single factor) test results.

System	μ_P (%)	p-value
Blank	-	-
EP	82.17 ± 0.20	6.6×10^{-9}
EP/RGO	95.05 ± 1.10	
EP/RGO-ZnO	98.42 ± 0.93	
EP/ RGO-ZnO-PANI	99.98 ± 0.01	

**p≤0.0001 indicates the reliability of the PDP data obtained from triplicate experiments at a confidence interval of 99.99%.*

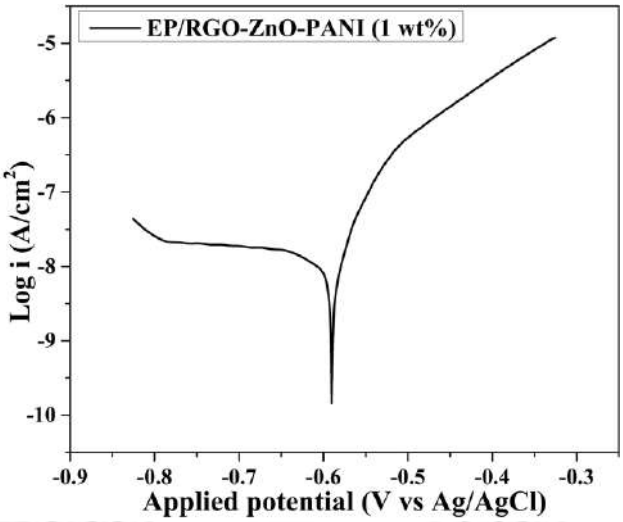

Fig. 7A.2 Tafel plot for EP/RGO-ZnO-PANI (1 wt%) after 1-day immersion in 3.5% NaCl.

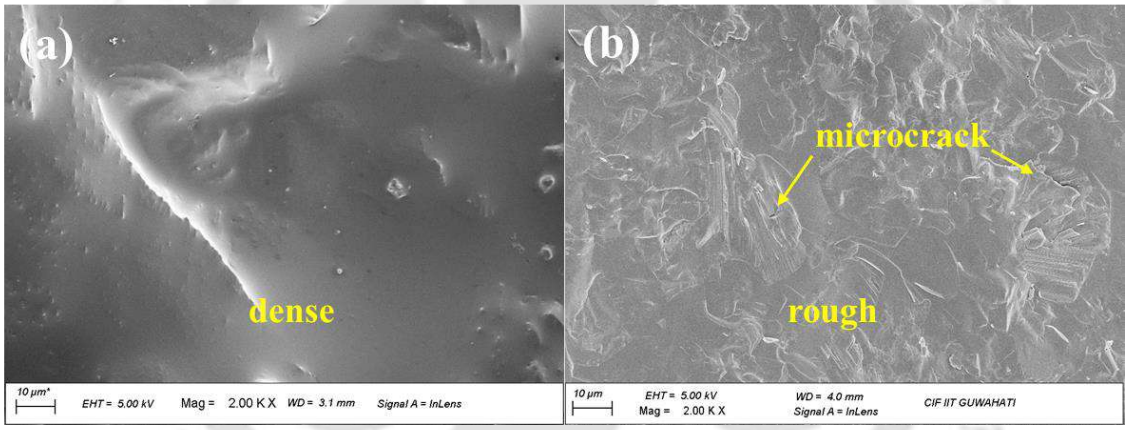

Fig. 7A.3 FESEM images for (a) 0.5 wt% and (b) 1 wt% of RGO-ZnO-PANI in epoxy coatings.

Table 7A.2 Tafel parameters for Blank, EP/RGO-ZnO-PANI (1 wt%) after 1-day immersion in 3.5% NaCl.

System	b_a (mVdec^{-1})	$-b_c$ (mVdec^{-1})	E_{corr} (mV vs. Ag/AgCl)	i_{corr} (µA-cm^{-2})	R_p ×10^{-6} (Ω-cm^2)	μ_P (%)
EP/ RGO-ZnO-PANI (1 wt%)	68.60 ± 2.69	36.19 ± 1.10	-589.13 ± 5.04	0.0080	1.28 ± 0.01	99.97 ± 0. 01

Research output

Research output

Journal Publications (thesis):

1. **A. Kumar**, C. Das, 2023. A novel eco-friendly inhibitor of chayote fruit extract for mild steel corrosion in 1 M HCl: Electrochemical, weight loss studies, and the effect of temperature. ***Sustain. Chem. Pharm***. 36, 101261. https://doi.org/10.1016/j.scp.2023.101261 (Elsevier) **[IF = 6.0]**
2. **A. Kumar**, C. Das, 2024. Corrosion inhibition of mild steel by *Praecitrullus fistulosus* (tinda fruit and peel) extracts. ***Sci. Total Environ***. 929, 172569. https://doi.org/10.1016/j.scitotenv.2024.172569 (Elsevier) [**IF = 9.8**]
3. **A. Kumar**, C. Das, 2025. Investigations on corrosion inhibition of mild steel in acid medium using *Phaseolus lunatus* peel and seed extracts. ***Mater. Today Commun.*** 49, 113752. https://doi.org/10.1016/j.mtcomm.2025.113752 (Elsevier) [**IF = 4.5**]
4. **A. Kumar**, C. Das, 2025. Anti-corrosive behavior of a novel ternary RGO-ZnO-PANI nanocomposite reinforced epoxy coating on mild steel in marine environment, ***Adv. Eng. Mater.*** 27, 2500949. https://doi.org/10.1002/adem.202500949 (Wiley) [**IF = 3.3**]
5. **A. Kumar**, C. Das, 2025. *Duranta erecta* fruit and leaves extracts as green corrosion inhibitors for mild steel protection in hydrochloric acid, **(Submitted to Journal)**
6. **A. Kumar**, C. Das, 2025. Advances in green corrosion inhibitors and protective coatings for metal corrosion control in various media: A comprehensive review, **(Submitted to Journal)**

Journal publications (other):

1. **A. Kumar,** B. Bhattacharya, and C. Das, 2025. Studies on the inhibitive effect of ferrozine on the corrosion of mild steel in hydrochloric acid, ***J. Taiwan Inst. Chem. Eng.*** 174 106221. https://doi.org/10.1016/j.jtice.2025.106221 (Elsevier) **[IF = 6.3]**

2. Z. Farhat, **A. Kumar**, C. Das, 2024. Fabrication of used-tea embedded alginate beads for cationic dye remediation: Synergistic effect of surface adsorption and intraparticle diffusion. ***Surfaces and Interfaces*** 51, 104601. https://doi.org/10.1016/j.surfin.2024.104601 (Elsevier) **[IF = 6.3]**

Book chapter:

1. **A. Kumar**, P. Das, C. Das, A review on corrosion inhibition potential of expired pharmaceutical drugs **(Submitted).**

Conferences attended:

1. **A. Kumar**, C. Das, 2023. Electrochemical and and weight loss studies of polyurethane coated and uncoated mild steel in 1 M HCl and 0.5 M H_2SO_4, **International Conference on Corrosion and Coating (i3C) – 2022**, 07-08th Dec, held at TATA Steel, Jamshedpur, India ***(Oral)***
2. **A. Kumar**, C. Das, 2023. Anticorrosive Behavior of PU in Acidic Environment**, IIChE-CHEMCON 2023**, 27-30th Dec, held at Heritage Institute of Technology, Kolkata, India. ***(Oral)***
3. **A. Kumar,** B. Bhattacharya, and C. Das, 2024. Studies on the inhibitive effect of ferrozine on the corrosion of mild steel in hydrochloric acid, **Research & Industrial Conclave - Integration'24**, 09-11th Aug, held at IIT Guwahati, Assam, India ***(Oral)***
4. **A. Kumar**, C. Das, 2024. Plant extracts as a green inhibitor in acidic environments: A review, **Research & Industrial Conclave – Integration'24**, 09-11th Aug, held at IIT Guwahati, Assam, India ***(Oral)***
5. **A. Kumar**, C. Das, 2024. Development of green corrosion inhibitor using *Duranta erecta* leaves, **ENVIRONMENT 2024,** 09-11th Dec, held at IIT Guwahati, Assam, India. ***(Oral)***

6. P. Das, **A. Kumar**, and C. Das, 2025. Corrosion inhibition potential of expired pharmaceutical drugs: A review, **Research & Industrial Conclave – Integration 25**, 10-12th Oct., held at Indian Institute of Technology Guwahati, Assam, India. (***Oral***).

Workshop/Symposiums attended:

1. **A. Kumar,** A. K. Golder, 2020. Studies on photocatalysts recovery and flux behavior by membrane separation, ***Workshop cum Symposium on Bio-inspired Nanomaterials for Environment Applications,*** 12 -13th Feb 2020, organized by IIT Guwahati, Assam, India ***(Poster)***
2. ***Three-day Training Program on Industrial Corrosion and Its Control***, 12 -14th Feb 2024, organized by The Electrochemical Society of India, Indian Institute of Science Campus & Dept. of Metallurgical & Materials Engineering, National Institute of Technology Karnataka Surathkal, Mangalore
3. ***Three-days National Workshop on Recent Advances in Food Engineering in North-East India conducted***, 17 - 19th Dec. 2020, organized by IIT Guwahati under the Technical Education Quality Improvement Program (TEQIP) sponsored by the Ministry of Human Resource Development, Government of India.
4. ***Two-days International seminar on Challenges and Opportunities of Medical Plant based Industries in BIMSTEC Countries (IChaMP)***, 26 - 27th Aug. 2022, organized by School of Agro and Rural Technology, IIT Guwahati, Assam, India.